UNIVERSITÀ
DEGLI STUDI
FIRENZE

dottorato di ricerca

International Doctorate in
Atomic and Molecular Photonics

Ciclo XXIX

Coordinatore Prof. Righini Roberto

Pressure-induced reactivity in confined systems

Settore Disciplinare CHIM/02

Candidato
Dott. Scelta Demetrio

Tutore
Prof. Bini Roberto

Coordinatore
Prof. Righini Roberto

Anni 2013-2016

Wo aber Gefahr ist, wächst
Das Rettende auch.
(F. Hölderlin, “Patmos”)

Contents

Introduction

Every chemical or physical process is ruled by thermodynamic variables like pressure, temperature and chemical potential [1]. Acting on one of these variables allows to affect the equilibrium composition of simple molecular systems and the kinetics of their transformations. In particular, pressure is a powerful tool to govern the behaviour of molecular systems, because of their "softness" (or, in other words, because of their high compressibility) [1, 2]. Pressure has a wide range of variation in nature, from the absolute vacuum of the interstellar spaces to the huge pressure at the center of neutron stars, passing through the hundreds of GPa (365 GPa, actually, and at least 5000 K of estimated temperature) at the core of our planet: laboratory equipment allows to perform experiments in a wide range of pressures (up to the megabar) and temperatures (up to thousand of Kelvin), making possible to exploit pressure versatility to promote phase transitions from fluid to crystalline phases, or even insulator-metal transitions, and also reactivity on simple molecular systems. An external high pressure has the general effect to reduce the molar volume of the molecular systems, increasing their density. The very interesting part is that by changing pressure one can achieve drastic variation of molar volume (up to 50% with few tenth of GPa), and this is not the same acting on temperature (it could take hundreds of degrees to achieve contraction of the 8% on the molar volume), see figure 1.

In fact, it takes relatively low pressure to significantly reduce the intermolecular distances in the system, leading to an enhanced interaction and, from an energetic point of view, to a high energy state. Molecular systems

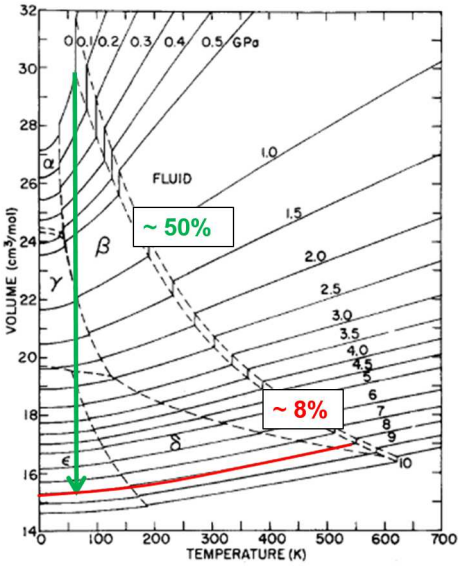

Figure 1: *Effect of pressure (green) and temperature (red) on the molar volume of molecular systems. Figure taken by Mills et al., see ref. [3].*

can this way explore different region of their potential energy surfaces, reaching previously unaccessible new local or global energy minima (figure 2). For molecular crystals, this can correspond to transitions to new dense phases [4], amorphisation and ionisation processes or, in more drastic conditions, to a complete reorganisation of the chemical bonding structure, leading to the formation of new products [5]. Particularly, the application of high pressures in the range from 1 to 10 GPa, together with temperature and laser irradiation, allows to overcome the energetic barriers for the synthesis of compounds such as polymers, avoiding the use of catalysts and any other substance than the reactants [6–8].

This is a general feature for high pressure reactivity, and an interesting point for what concern the so called *Green Chemistry*: exploiting physical tools, we do not require the use of solvents, catalyzers or other chemical coadiuvants. Nevertheless, chemical reactivity at high pressure is a largely unexplored field of study, although really important for fundamental issues and novel material synthesis too: the high pressure synthesis of polymeric

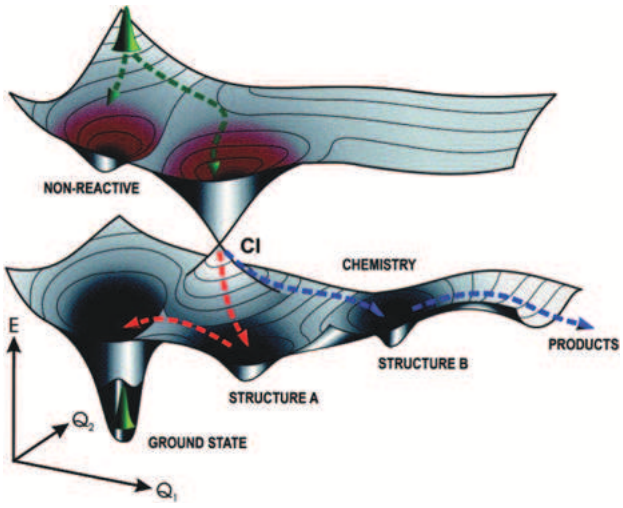

Figure 2: *Schematic representation of the effect of pressure on potential surfaces of a molecular system. Different local minima in the low-lying potential energy surface can be experienced through variation in the density conditions, or even by electronic excitation to higher potential energy surfaces and, then, through conical intersection leading to different structure and, consequently, to different chemical products.*

nitrogen [5], extended CO_2 phases [9] or benzene-derived carbon nanothreads [10, 11] are good examples of this general statement. Moreover, some of these pressure-triggered reactions are reversible but others are irreversible processes, allowing to recover their products at ambient conditions. These products can be really promising for practical applications, and the high pressure reactions, typically small volume processes, can be scaled up to larger volumes in order to fully exploit the appealing characteristics of several of these compounds [12].

In this framework, even more intriguing is to investigate the effect of combined high pressure and extreme confinement on ordinary matter, a condition that is really common in nature but far less studied in laboratory. At different pressures, geochemical and geophysical properties of earth's crust, mantle and core show the recurring of elements like carbon and silicon (see figure 3), whose high pressure behaviour is of great interest even in con-

fined conditions, and of system in which the effects of confinement cannot be neglected, like, for instance, clathrate hydrates. On the other hand, extreme confinement conditions can, in perpective, be exploited to drive the synthesis of new materials and devices with specific and tunable characteristics. "Classic" confinement chemistry is related to the use of active zeolites (zeolites having metallic, catalytic centers) [13–21] or, anyway, to catalysis in spatially confined conditions for several kind of applications, ranging from polymer science [22] to energy vectors storage [23], resulting in a huge amount of literature about this and others related arguments. In our case, we are interested in deepen the understanding about chemistry in confined conditions in absence of any coadiuvant effect, so to exclude the presence of active or catalytic sites and to exploit only physical tools to promote and foster reactivity. In other words, we are interested in exploiting reduced dimensionality so to direct a chemical reactivity fostered only by physical tools (pressure, temperature, laser irradiation).

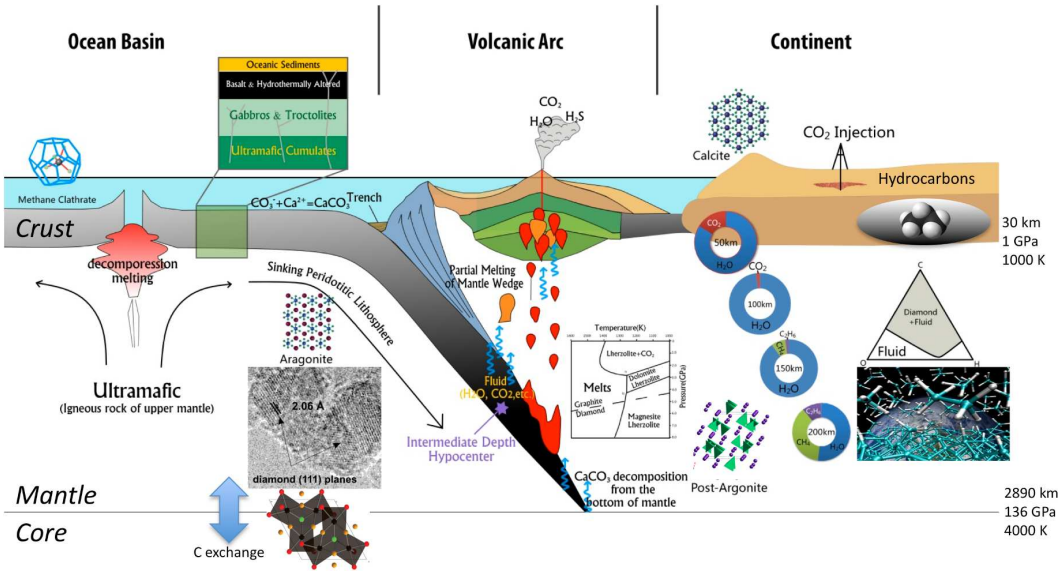

Figure 3: *The role of deep carbon in geological processes is controlled at a fundamental level by atomic-scale structure and bonding. Image from "Physics and Chemistry", DCO directorate final proposal.*

We took into examination three different systems that show a great funda-

mental interest (ranging from cosmology, to geology to life science) and that could exhibit also powerful technological applications deriving both from the synthesis of nanocomposites (starting from our materials) and from their high pressure functionalization. These model system are **a)** nanocomposite inclusion materials based on C/Si constituents, **b)** nanostructured carbon-based materials such as graphite, graphene oxide or carbon nanotubes and **c)** the reactivity and the structural behaviour of red and black phosphorus (and its derivatives such as phosphorene). We have also studied clathrate hydrates of simple hydrocarbon molecules, and particularly methane clathrate hydrates: these studies are still ongoing. The specific goals of these studies are to provide general contributions to a deeper understanding of fundamental chemistry and physics of densified systems in small spaces and reduced dimensionality and to develop novel, high pressure, *Green Chemistry*-oriented routes for the synthesis of nanocomposite materials.

The first class of materials we have studied is that of nanocomposites inclusion materials based on C/Si constituents. C and Si are two of the main constituents of earth interiors, and some interesting studies have underlined the effect of pressure in clarifying the affinities between CO_2 and SiO_2 [9], and even the possibility to have a reactivity between a molecular form of Carbon, CO_2, and its Si-counterpart SiO_2, in the form of Silicalite: the product of this reaction is a mixed carbonate-silicate phase that can be quenched and recovered at ambient conditions [24]. In the framework of this research project, we have studied high pressure polymerization of simple organic molecules in meso/micro-porous materials. The idea is simple: by exploiting the density increase due to the high pressure and, if necessary, light absorption to help trigger the polymerization reaction, avoiding any catalytic effect due to the pore walls (this has been ensured by using non-catalytic porous materials as confining systems), it is possible to synthesize and even stabilize specific polymers embedded in a protecting inorganic scaffold, that allows to recover them and, potentially, to apply them for technological purposes. The high pressure polymerization of simple organic molecules inside the zeolite allows

to obtain nanocomposite materials with finely tunable mechanical properties such as a perfect, ideal zero thermal expansion coefficient material, or ideal conducting, embedded polymers (PolyAcetylene, for instance), or even high density energetic materials (polyCO) trapped in the inorganic framework. Furthermore, high pressure functionalization of the pore walls of nano-porous materials could be of great importance for obtaining composites with potential applications as optical sensors and in non-linear optics. Here zeolites are used as micro-chemical reactors and for this purpose we have selected two different kind of synthetic, non catalytic and electrically neutral pure SiO_2 zeolites, the one with a 3D porosity (named Silicalite, structure type MFI) and the other with a 1D porosity (named ZSM-22, structure type TON). We have then performed high pressure polymerization of acetylene and carbon monoxide in these zeolite matrices, with the twofold purpose to stabilize the polymers and to recover these unique nanocomposite materials at ambient conditions.

The second main field of study has been that of nanostructured carbon-based materials, and particularly Graphite Oxide (GO). Carbon plays a key role on Earth: it's involved in several, different useful materials; it spans over a wide range of oxidation states, giving place to the formation of several different compounds; its near-surface cycle (atmosphere, oceans, crustal surface) profoundly affects climate changing and the health of ecosystems; and also its deep cycle, even if it's not so well known, has a tremendous importance for a complete understanding of its chemistry [25]. The most recurring allotropes of carbon in nature are sp^2 and sp^3 graphite-like and diamond-like phases: these phases have a wide range of metastability that, for instance, allows diamond to be undefinitely stable at room conditions, where graphite is the thermodinamically stable phase. Metastable allotropes of Carbon include fullerenes, nanotubes and graphene, as well as other disordered or amorphous forms like glassy carbons. Between all these allotropes, graphene has reached a wide audience and gained a lot of attention in the past 10 years since its discovery and due to its possible practical applications [26].

In the framework of high pressure reactivity in confined conditions, it's more interesting to starting from a particular graphite derivative, called Graphite Oxide (GO), a layered material whose single layer is named Graphene Oxide. Graphite Oxide shows a larger d-spacing between the single layers in respect to that of Graphite (7-12 Å, depending on the degree of hydration of the samples, versus about 3 Å) and this make it a good candidate for the inclusion of small molecules in perspective of studying its structural stability and possible functionalization (particularly using N-bearing molecules, because of the many, useful N-doped graphene applications). The presence of small, penetrating gas molecules (Ar, molecular nitrogen, ammonia) and of small hydrocarbons such as ethylene, along with pressure application and laser irradiation, allows to trigger a reactivity that could lead to graphene oxide layer functionalization (N-doped graphene planes) and to the synthesis of interesting nanocomposites in which insulating polymer chains (polyethylene, in our case) could form in between the layers, enlarging the d-spacing and indefinitely separating the layers.

The last model system we took into account is Phosphorus. Phosphorus is another key element for chemistry, physics, Earth and planetary sciences and, of course, biology [27]. The major part of Phosphorus on Earth can be found in the crust and mantel, as phosphate, phosphosilicate and other minerals. Phosphorus belongs to the *pnictogen* group (VA, Group 15 in the periodic table) together with Nitrogen, Arsenic, Antimony and Bismuth; its chemistry, and the chemistry of nitrogen, are of paramount importance in several different fields. From a technological point of view, the most used allotropic form of Phosphorus is the white, molecular one (P_4), that is toxic, unstable and highly reactive. Applying high pressure methods to the reactivity of Phosphorus has the twofold utility of **a)** try to find the conditions to switch from the white allotrope, currently used for the majority of the industrial applications, to the more stable and less toxic red polymeric form and black layered one; **b)** deepen the understanding about reaction mechanism for these two different allotropes, that are really interesting for diverse

reasons. Red, polymeric Phosphorus (P-red) offers in fact a high contact surface to other reactants: it's of great interest to exploit this feature to foster reactivity with small molecules in the perspective of obtaining new P-N functionalized materials of some industrial and technological appeal. Conversely, black Phosphorus (P-black), with its layered structure, is an ideal candidate for the inclusion of small molecules, and has been recently rediscovered by the scientific community [28]. In perspective, the layered structure of P-black is ideal for exploiting nanoconfinement conditions to functionalize Phosphorus and to understand the behaviour of the single sheet of P-black, named Phosphorene in analogy with the system Graphite-Graphene. Phosphorene is particularly promising as a 2D platform material [29–31], even in respect to Graphene, for its inherent bandgap, that made it suitable for several possible applications in diverse field, and this versatility explains the growth of interest of the scientific community, that led to a great number of published papers about it and the bulk P-black in the last two years (see figure 4).

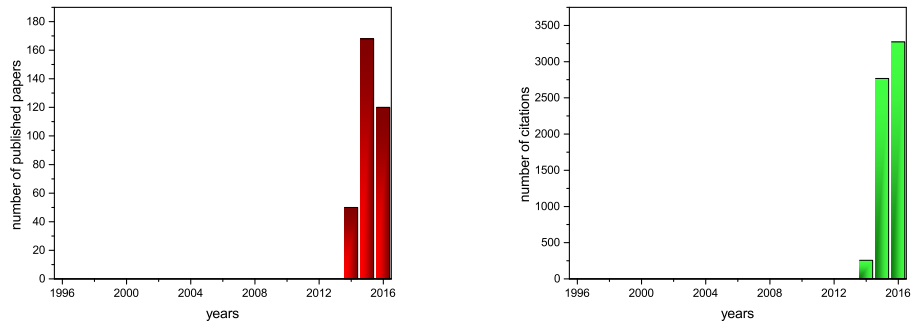

(a) (b)

Figure 4: *Number of published papers (figure 4a) and citations (figure 4b) per year on Phosphorene and black Phosphorus. Data taken from Web of Science (http://apps.webofknowledge.com).*

In conclusion, the behaviour of P-black in presence of small molecules could be interesting for functionalization of the single Phosphorene layer and

for the intercalation of molecules both in the bulk P-black or in the few layers Phosphorene (FLP).

These three systems are of great interest because of their recurrence in geophysical context: Si, C and P are all involved in minerals structures, and constitute three ideal cases of study for the implications of high pressure application on simple molecular systems.

A fourth, important system is that of clathrate hydrates of simple hydrocarbons, that represents at the same time a perfect model for **a)** highly confined conditions, **b)** a technological issue (as instance, for the choke of pipelines for oil and gas transportation) and **c)** an incredible resource for gas storage [32]. Clathrate hydrates are supramolecular compounds in which water molecules are arranged in cage structures that can host different types of guest molecules, from simple gases and small chain hydrocarbons to n-alkanes [33]. Most of the scientific literature studies concern with structure and stability of these clathrate hydrates, whereas chemical reactivity inside clathrates cages is a largely unexplored field of study. Recently, the possibility to use water as a radical initiator and a reactant in this kind of processes by means of near-UV two-photon absorption, that promotes water to dissociative excited states, has been explored at LENS [34]. Some of the products of chemical reactions, starting from simple hydrocarbons clathrate hydrates, are of great importance in the context of *green chemistry* (particularly for storage of molecular hydrogen and *in situ* sequestration of CO_2, typical products of this reactivity, through the formation of the corresponding clathrate hydrates [35]) and also for prebiotic chemistry [36]. In this project, the high-pressure reactivity in methane clathrate hydrate should have been studied in three different phases, that are structurally different, ranging from cage structures for MH-I and MH-II phases to filled-ice-like structure for MH-III phase, in order to understand the influence of cage geometry and occupancy on the reactivity of these systems. In the case of methane clathrate hydrate, we have characterized the structure and phase transitions between the cage structured phases MH-I and MH-II and the filled-ice-like structure MH-III

by means of Raman spectroscopy. We have performed some preliminary experiments about photo-induced reactivity in the MH-II phase, that have revealed a low tendency of the clathrate hydrate to react starting from this phase. The reaction, probably related to the occupancy of the larger cages in the MH-II structure, led to the formation of small amounts of products like ethane, ethanol, 2-methylpropanal and, likely, formic acid (all assigned by their Raman spectra). We are currently working on a reactivity study in the MH-III phase, in order to better understand the influence of cage geometry and occupancy on the reactivity of these systems, and in a newly discover mixed phase where methane and water show a high miscibility [37]. These experiments are still ongoing at the moment, and no definitive results have been already obtained.

Outline

In this thesis, several new experimental results about the synthesis of novel nanocomposite materials with tunable and specific characteristics and the functionalization of 2D platform materials of potential technological interest will be shown.

In the first chapter, the polymerization of simple guest molecules inside the nanopores of non catalytc zeolites, and the obtainment of interesting nanocomposite materials will be discussed.

In the second chapter, the effects of the intercalation of simple molecules between the layers of Graphite Oxide will be taken into account, with a twofold interest for structural and reactivity features. Moreover, some new interesting results regarding high pressure, high temperature polymerization of fluid ethylene (a preliminary work for some experiments to be performed on GO) will be shown.

The third chapter will be focused on the high pressure chemistry of P-red and P-black in presence of small (H_2, He) and N-bearing (N_2, NH_3) molecules, with the twofold purpose of studying the structural behaviour of

the two allotropes with pressure and of synthesizing new P-N functionalized materials.

In the experimental section, a detailed description of the techniques and of the instrumentations used for the experiments will be given.

Chapter 1

C/Si based nanocomposite inclusion materials

In this chapter, we will present our data for the synthesis and characterization of novel nanocomposite inclusion materials based on C/Si constituents. These nanocomposites are good models to understand the influence of low dimensionality on fostering and directing reactivity of small hydrocarbons, and to design new synthetic routes for systems of appealing practical and technological application.

1.1 An intriguing micro-chemical reactor: synthetic zeolites

A large variety of nanoporous materials have been used so far to custom design new appealing materials or just to drive their synthesis, being used as catalyzers. The best class of compounds for these purposes is that of zeolites. These materials are micro-porous, crystalline inorganic solids made up of corner-sharing SiO_4 and AlO_4 tethraedra, which typically show a strong acid character and enhanced catalytic properties, so to be used as coadiuvant in many different synthetic processes. In the perspective of driving synthesis of new materials exploiting only physical tools, the first requirement is to

use *non-catalytic* zeolites as micro-chemical reactors. For our experiments, we choose two types of non-catalytic zeolites, differing in their nanochannels arrangement and dimensionality: *silicalite* (structure type MFI, with a 3D network of channels) [38] and *ZSM-22* (structure type TON, with a 1D porosity) [39, 40]. Both of these zeolites, apart from being non catalytic ones, are synthetic, electrically neutral and constituted only by pure silica SiO_2 units.

Silicalite (framework type MFI, monoclinic space group $P2_1/n$ at room temperature with cell parameters a = 19.8352(2) Å, b = 20.0903(2) Å and c = 13.3588(1) Å) is characterized by a framework of 4-, 5-, 6- and 10-membered rings of corner sharing SiO_4 tethaedra forming **a 3D network** of internal, mutual interconnected nanochannels, the one linear, parallel to the crystallographic (010) direction with dimensions of 5.4 x 5.6 Å, and the other sinusoidal and parallel to the crystallographic direction (100) with dimensions of 5.1 x 5.3 Å[38, 41] (see figure 1.1a). At higher temperature, monoclinic silicalite reversibly turns to an orhorombic *Pnma* structure with cell parameters a = 20.0511(1) Å, b = 19.8757(1) Å and c = 13.36823(9) Å. Silicalite has brute formula $Na_n[Al_nSi_{96-n}O_{192}]$ with $n = 0$, and there are two different kind of silicalite, Silicalite-1-OH and Silicalite-1-F. The first one contains a significant amount of -OH groups, while the second one is obtained via calcination in the so called *fluorine route* [42], revealing a low concentration of surviving fluorine ions.

High pressure behaviour of silicalite is well known, and it has been studied with several compression media both experimentally (silicon oil, CO_2 and Ar [43]) and theoretically [44]. The most important feature is that, if compressed without pressure transmitting medium or with non penetrating silicone oil [43], silicalite structure tends to collapse at a pressure slightly above 8 GPa for effect of a *Pressure Induced Amorphization* (PIA), while this mechanism is deactived up to higher pressures if silicalite is filled with guest molecules. In the latter case, with CO_2 or Ar filled nanochannels, PIA is deactivated up to 25 GPa and a *bulk modulus* B_0 of 35.9(4) GPa, near to the bulk modulus

value for α-Quartz [43], is obtained, whereas a B_0 of 26.7 GPa is found with ethylene/polyethylene filled cavities [45]). Of course, this enhanced resistence to PIA is due to the penetration of small molecules inside the channels: if this penetration can not take place due to the dimensions of the guest molecules, as in the case of silicone oil, the PIA mechanism is not deactivated. We have performed our experiments starting both from powder and from single crystal silicalite: the single crystal has dimensions of 80 µm x 40 µm x 40 µm (see figure 1.1b).

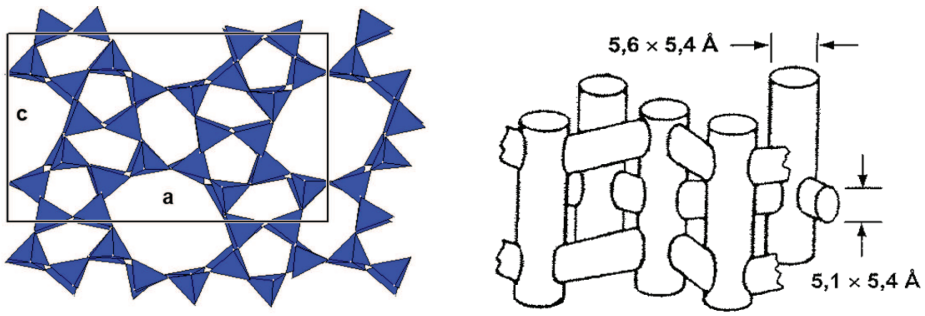

(a)

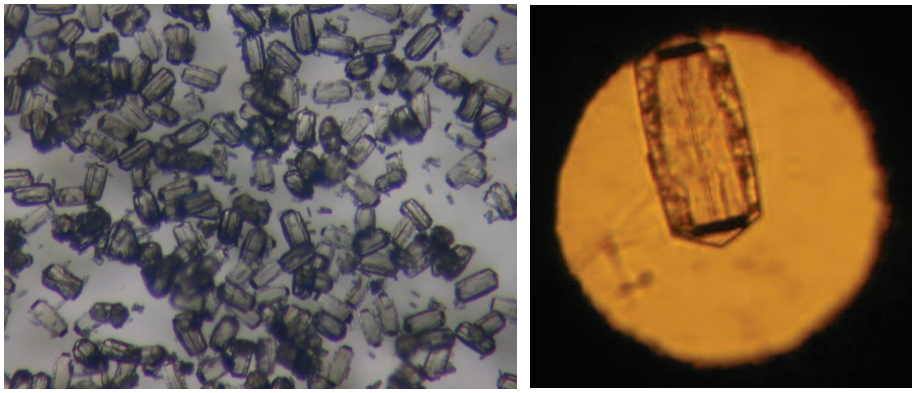

(b)

Figure 1.1: *Silicalite (framework type MFI). In 1.1a, the structure of silicalite is reported: a projection of the structure along the ac plane, and a representation of the 3D network of inteerconnected nanochannels. In 1.1b, two optical images of single crystals of silicalite (MFI) on a microscope glass (left) and inside the gasket hole in a DAC (right).*

All-silica ZSM-22 (framework type TON, orthorhombic space group $Cmc2_1$ with cell parameters $a = 13.859(3)$ Å, $b = 17.420(4)$ Å and $c = 5.038(2)$ Å) is constituted by SiO_4 tetrahedra that are corner-linked to build up a 3-dimensional 4-connected framework made up by 5-, 6- and 10-membered rings. The 5-membered rings of SiO_4 tetrahedra form a zig-zag chain along the crystallographic direction **a-**, and these chains are linked through oxygen atoms along **b-** and **c-** directions by the remaining free corners of the SiO_4 tetrahedra, giving rise to 10-membered rings channels parallel to the (001) direction with no interconnection and therefore representing a **1D channel system** (see figure 1.2). These unidirectional, 1D channels have elliptical cross sections of 4.6 and 5.7 Å axes. ZSM-22 crystals show twinning nature with (110) as twin plane [39]. The twinning phenomenon is responsible for the presence of another kind of 10-membered-rings, quite similar to the one described above, and it is assumed to cause only slight distortions of the Si-O bond and angles structure. Anyway, the twinning occurs frequently because there's probably a very small difference in the binding energy between twinned and untwinned structure, and it's quite common to find no untwinned crystals in a batch of these zeolite [39]. ZSM-22 is prepared by sol-gel techniques using triethylenetetramine as structure directing agent, followed by crystallization at 170°C under hydrothermal conditions [40]. The sample is then calcined in air at about 550°C to remove the organic template.

The high pressure behaviour of all-silica ZSM-22 is currently under investigation. We have designed and performed several experiments of simple compression/decompression using pressure transmitting media such as silicone oil (Daphne Oil 7474), Ne and NaCl. The results are currently on elaboration. In our experiments, only powder ZSM-22 has been employed, due to the complexity of the synthetic routes leading to the growth of a good quality single crystal of this zeolite.

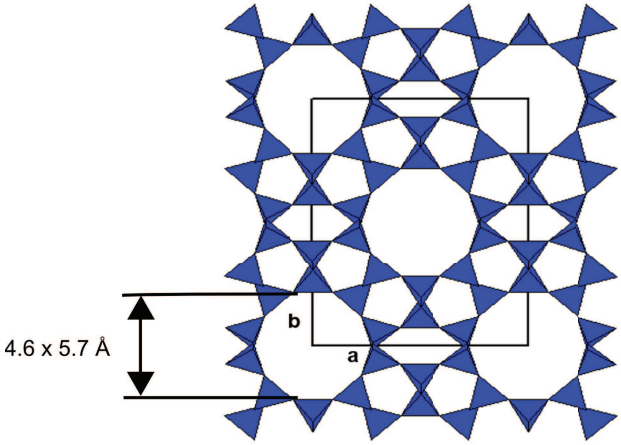

Figure 1.2: *The structure of ZSM-22 (framework type TON) is reported in this projection along the ab plane. The dimensions of the elliptical 1D nanochannels are also reported.*

1.2 High pressure polymerization of Acetylene in silicalite

The first experiment designed to exploit confinement conditions in a zeolite in order to drive polymerization reactions of simple hydrocarbon molecules using only physical tools (pressure and laser irradiation) was about the polymerization of ethylene inside silicalite [45]. Among the remarkable results of this experiment, it's appropriate to recall the obtainement of a completely filled silicalite crystal (with a bulk modulus $B_0 = 26.7$ GPa, and an enhanced resistance to external uniform compression up to 24 GPa). Furthermore, the filling of silicalite pores with synthesized PolyEthylene (PE) has the effect of changing the thermal expansion coefficient from negative [46] to positive value, and constitutes a good starting point in the quest for ideal, zero thermal expansion coefficient materials, as one could argue that a good balancing of the amount of polymerized molecules inside the pores would allow to calibrate this thermal coefficient to the desired value. The specific structure of polyethylene favours its complete polymerization inside

the channels: polyethylene is in fact constituted by a chain of single-bonded C atoms, and it can stretch freely in order to adapt and fit into the silicalite pores. The synthesized material is named PESIL (acronymous for PolyEthylene filled SILicalite).

The natural extension of this work relates to the synthesis of some nanocomposite material with specific, tunable and interesting properties. Polyacetylene constitutes a textbook model for organic linear, ideal conductive chains, a sort of prototype for 1D conductive polymers. Acetylene high pressure behaviour is well-known [6, 47–51], and its polymerization treshold at ambient temperature is relatively low (between 3 and 4 GPa). Polymerization starts from the solid, orthorhombic phase of avetylene, where the molecules show the correct alignment that leads to a *transoid*-polymer. Unfortunately, polyacetylene (PA) obtained from bulk polymerization of its monomer is difficult to recover at ambient conditions due to its high reactivity in respect to the atmospheric moisture, and the synthsis of an all-conjugated form of this polymer is prevented by the occurring of branching of the chains (that is also favoured, for instance, by laser irradiation) [6].

This experiment has a twofold purpose: to synthesize a new nanocomposite material made up of a conductive nanowire embedded in a protecting, inorganic scaffold; and to stabilize the synthesized polyacetylene avoiding its reaction with moisture and the branching of the chains, so to preserve conjugation.

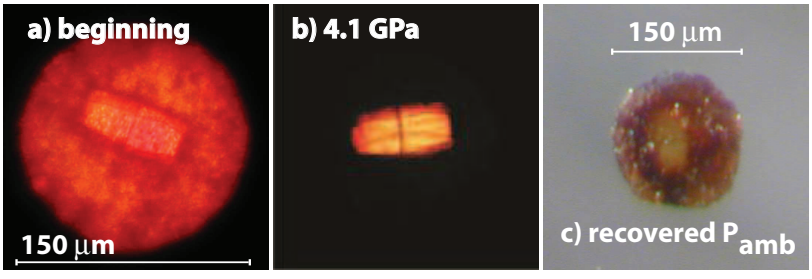

Figure 1.3: *Optical images of the sample at three different stages of the reaction: at the beginning (left); at about 4.1 GPa, where polymerization completes (center); the recovered PASIL surrounded by bulk polyacetylene (right).*

Samples of acetylene (see figure 1.3 for optical images at different stages of the experiment) were loaded in DAC together with powder or single crystal silicalite by the *spray loading* method (see section 4.2). The time evolution of the pressure induced polymerization of acetylene in the presence of silicalite and the evaluation of the unreacted monomer in the reaction mixture at the end of the process have been tracked using FTIR spectroscopy (see figure 1.4). Reactions kinetics are strictly dependent on the crystalline quality of the starting acetylene sample: the more the defects, the faster the reaction up to a stabilization when the 80-90% of the initial monomer has undergone polymerization. Typical times for the reaction to complete are between few hours and more than one day at about 4-5 GPa, depending on the sample. From the ratio between the integrated intensity of the combination bands of monomer at different times of the reaction, it's possible to evaluate the percentage of unreacted monomers and so to quantify the advancement of the reaction. The so synthesized novel nanocomposite has been called PASIL (standing for *PolyAcetylene filled SILicalite*).

The spectral region of C-H stretching modes of polyacetylene-like chains has been studied at about 2.7 GPa in the bulk polymer (surrounding the silicalite crystal, see figure 1.3 above) and inside the silicalite crystal, exploiting the high spatial resolution provided by synchrotron FTIR (20-30 μm spot on 80 x 40 x 40 μm crystal almost bridging between the anvils). The spectra, reported in figure 1.5, are normalized with respect to the integrated intensity of combination bands of the residual acetylene. Here, the ratio between the integrated intensity of confined PA and that of bulk PA is about 0.48, and this means that the amount of confined polymerized material is about half than that of the bulk, probably due to the unfavourable 3D character of the host crystal (i.e., for its particular geometrical constraints, polyacetylene does obviously not fit well in sinusoidal channels). Peaks above 3000 cm^{-1} are assigned to modes of C-H groups with sp^2 carbons (PA-like chains) while peaks below 3000 cm^{-1} are assigned to C-H groups with sp^3 hybridized carbon, related to terminations and branching of the chains. More

in detail, peaks at about 2870 cm^{-1} and 2940 cm^{-1} are related to -CH_2- and R_3C-H groups respectively, with this last directly related to branching of the PA-like chains. The sp^2 peak in the confined material (3025-3042 cm^{-1}) is much broader than that of bulk PA, indicating that PA chains inside the zeolite host are highly strained due to confinement. The ratio between the integrated intensity of all the sp^2 and sp^3 peaks in confined and bulk polyacetylene is 0.46 and 0.35, respectively. Taking into account the different absorption cross sections for sp^2 and sp^3 sites (see reference [52]), these values leads to an sp^2/sp^3 ratio of 0.67 in confined PA, and of 0.52 in bulk PA. So, both the confined and the bulk polyacetylene are made of highly branched chains, but the confined one exhibits a slightly higher sp^2 content for effect of

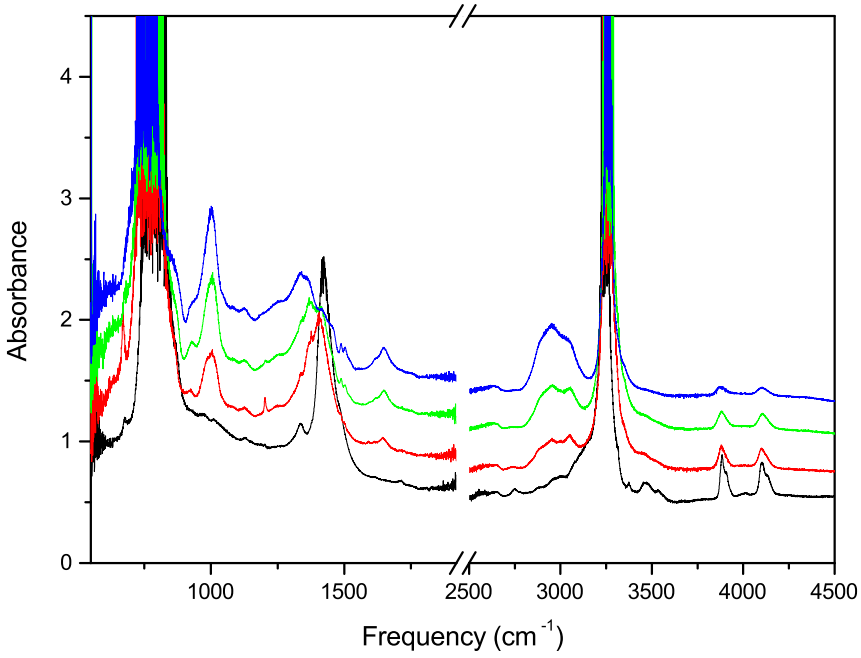

Figure 1.4: *Polymerization progress in acetylene/silicalite samples. From bottom to top, FTIR spectra referring to the sample at the beginning of the reaction (black curve), after 24 hours (red curve), after 49.5 hours (green curve) and after 144 hours (blue curve).*

confinement. Micro-raman spectroscopy has been used to identify and map differences between bulk and confined PA-like conjugated chains. Despite of the huge background fluorescence, the strong resonance Raman spectrum of PA was always clearly observed [53, 54]. In bulk PA we observe up to seven active Raman mode, related to *cis* and *trans* species (see table 1.1), while in the confined PASIL we only see the peaks from the trans isomer [49,53,55–59] and the peaks from the cis one are really weak or even absent (figure 1.6). Furthermore, we observed a systematic blue-shift (estimated in 5-10 cm^{-1}) for the polymer-related bands inside the silicalite crystal in respect to the bulk PA, likely due to the interaction between the confined chains and the walls of the nanochannels.

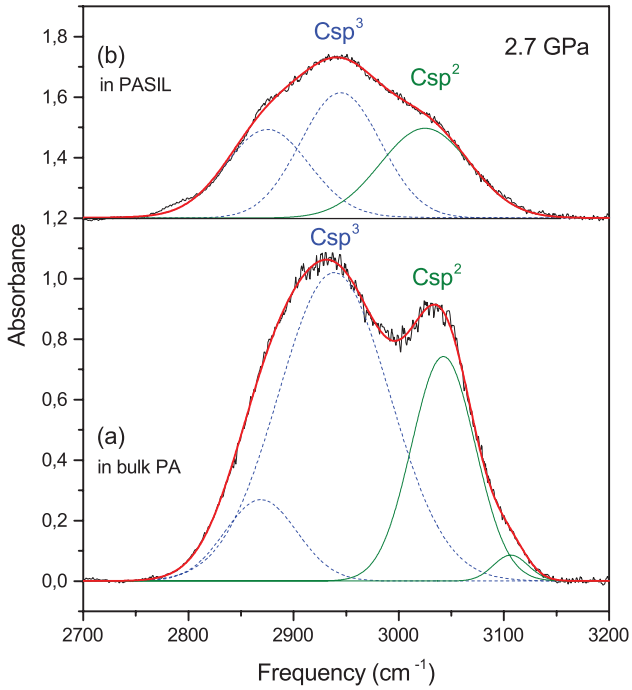

Figure 1.5: *Synchrotron FTIR absorption spectra of bulk (a) and nanoconfined (b) PA in PASIL in the frequency range of C-H stretching modes at 2.7 GPa. Conjugated (C sp^2) chains are identified by olive peaks, while branching and terminations (C sp^3) are indicated in dashed blue. The absorbances of the two spectra were normalize to the same integrated intensity of combination bands of residual acetylene.*

Active Raman Mode	Frequency, cm^{-1}	Isomer
CH bending in-plane + C-C and C=C stretching	925	cis
CH bending out-of-plane	1010	trans
C-C stretching + CH bending in-plane	1120	trans
C=C stretching + C-C stretching	1255	cis
C-C stretching (?)	1300	trans/cis
C=C stretching	1497	trans
C-C stretching	1543	cis

Table 1.1: *Assignments for the Raman bands in polyacetylene.*

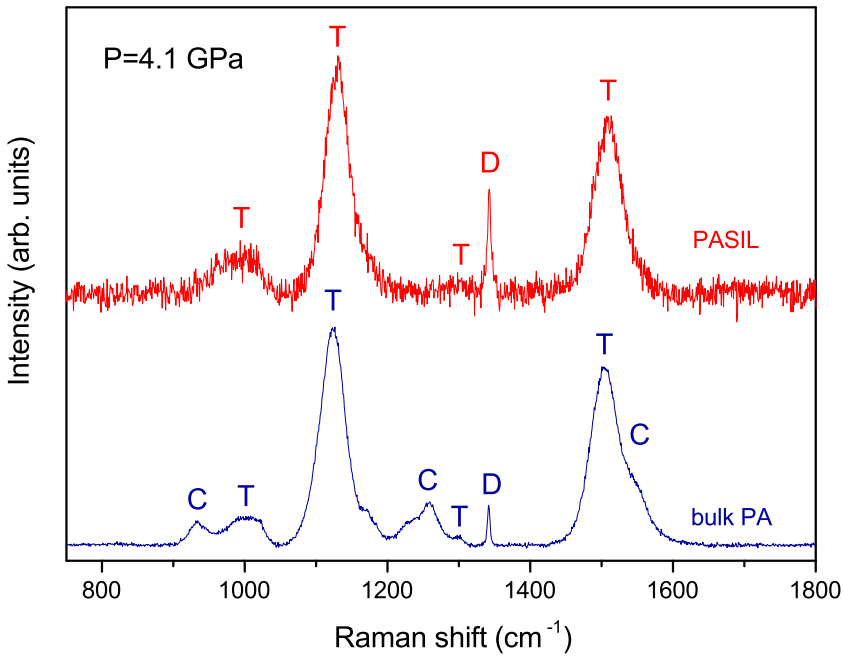

Figure 1.6: *Raman spectra of the PA-like chains at 4.1 GPa in the bulk (blue curve) and in the silicalite (red curve) crystal. The spectra have been normalized to the same integrated intensity and vertically shifted for the sake of clarity. T and C refer to peaks of Trans and Cis PA, respectively; D indicates the diamond peak.*

Although the resonance effect is related to the wavelength excitation and

to the experimental pressure (optimal conditions seems to be 1.9 eV and 0.7 GPa, where *cis* and *trans* isomers have almost the same resonance), making difficult to correctly estimate the relative abundance of the two isomers, there is a good evidence of the selection of only one of these two isomers due to the nanochannel dimensionality of the zeolite. In PASIL, we observe a stronger fluorescence background than in the bulk PA, probably due to the presence of structural defects in the nanocomposite leading to a lower S/N ratio. A better understanding of the polymer properties inside and outside of the single crystal silicalite is derived by the map of the spatial distribution of the different isomers using the relative intensity of two corresponding Raman peaks. This is possible thanks to the high spatial resolution of our Raman setup. We took into account the integrated intensity, I_T of the *trans* peak at 1503 cm^{-1} and that of the *cis* peak, I_C, at 1548 cm^{-1}. In figure 1.7 we report a map of the quantity $\eta = I_T/(I_T + I_C)$ after polymerization in the selected sample region (white framework) at about 4.1 GPa through a 5 μm, 95 x 95 μm^2 square mesh. η of course does not provide reliable values for relative concentrations of the two species, because the intensity of Raman signal strictly depends on the different scattering cross section of the species took into account, but the map allows to visualize the relative spatial distribution of the isomers. As a result, it can be seen that a major abundance of *trans* isomer is found in the zeolite region or, in other words, that confined PA in PASIL exhibit a much higher *trans* character than the bulk PA, and this is clearly an effect of confinement.

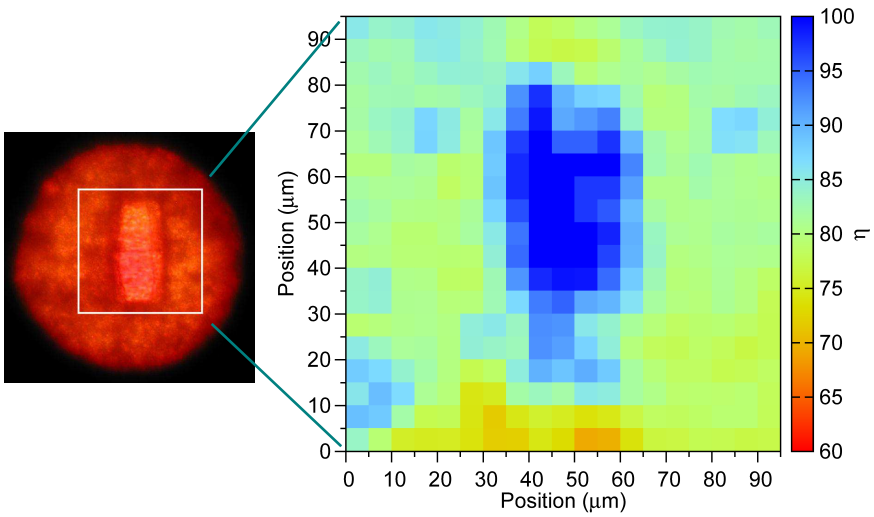

Figure 1.7: *Optical and spectroscopic images of PASIL: Raman mapping of a selected portion of the sample. On the left, optical image of the sample at the beginning of the polymerization (photo taken in transmitted light), with the silicalite crystal clearly embedded in the bulk, reddish PA/acetylene mixture; on the right, the Raman microscopy mapping of the sample, referring to the selected, square region in the optical image. The color scale refers to the quantity* $\eta = I_T/(I_T + I_C)$*, where* I_T *is the integrated intensity of the trans peak at 1503* cm^{-1} *and* I_Cm *is the integrated intensity of the cis peak at 1548* cm^{-1}

The recovered PASIL in the gasket hole has been studied by single-crystal XRD (SC-XRD) at 175 and 293 K using Cu Kα radiation ($\lambda = 0.154$ nm). The unit cell of PASIL results to be orthorhombic with space group *Pnma*, and cell parameters $a = 20.01(5)$ Å, $b = 19.969(5)$ Å and $c = 13.477(7)$ Å. The first noticeable thing is the changing in structure from monoclinic in pure silicalite [41] to orthorhombic, as it was in other systems [43, 45] due to the filling of the pores. The unit cell volume at 293 K is 5385(14) Å^3, 0.6% greater that that of empty silicalite (5354.3 Å^3 [41]), confirming the insertion of polymerized acetylene inside the pores. At the temperature of 175 K, the unit cell volume is 5358(5) Å^3. The thermal expansion coefficient, estimated from these two values, is positive over this temperature range: this means that the insertion of polyacetylene in the pores of silicalite changes

its thermal expansion coefficient from negative in unfilled silicalite [46] to positive in PASIL. Insertion of molecules inside the pores deactivates the low energy high amplitude vibrations that are responsible for negative values of thermal expansion coefficient [60]. The unit cell value, compared to that of PESIL (5434 $Å^3$) [45], is lower, thus indicating the lower degree of pore filling in PASIL. The analysis of the intensity data in the SC-XRD patterns was complicated due to the twinned nature of the silicalite crystal, with a 2-fold twin axis along the (110) direction. If the silicalite pores are completely filled, the a and b lattice parameters are almost equal, and so the twinned reflections overlap almost perfectly [43, 45]. Here, due to the varying degrees of partial overlap of the reflections from the twin components, the integration becomes increasingly difficult at higher angles, strongly limiting the number of useful reflections. For the refinement of the structure of PASIL, there were 292 useful reflections at low angle ($\theta < 34°$). The structural refinement has been performed starting from the structural model of PESIL. Due to the low number of available reflections, some constraints were applied on C-C and on Si-O distances, obtaining an R1 agreement factor of about 8.2% with a carbon occupancy fixed to 100%. If the carbon atoms were completely removed, we obtained an R1 of 12%, while with a 50% occupancy of carbon we obtained R1 of 5.7%. These results are in good agreement with the spectroscopic evidences of a low pore filling due to only partial polymerization inside the nanochannels. Trying to put carbon atoms only in the linear channels results in an increase of R1 agreement factor, and this means that, in the lowest R1 configuration, both types of pores are occupied in a completely disordered way by arrangements of carbon atoms that looks very similar to highly strained *transoid*-PA like chains, as seen spectroscopically. In figure 1.8 is shown a representation of the crystal structure of PASIL, corresponding to the best R1 agreement factor of 5.7%, yielding a 50% carbon occupancy of the available sites.

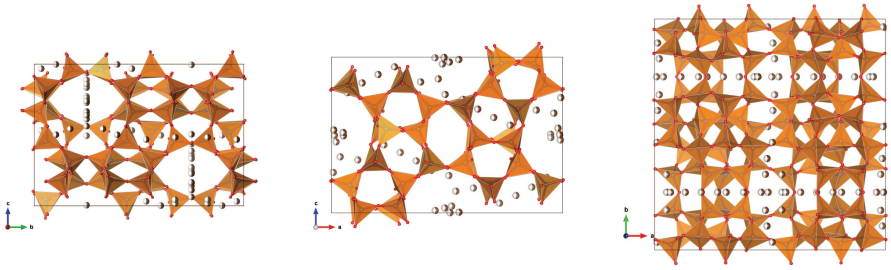

Figure 1.8: *Representation of the crystal structure of PASIL along the three crystallographic directions a, b and c. On the left, the view along the* ***a*** *direction; on the center, the view along the* ***b*** *direction; on the right, the view along the* ***c*** *direction. The framework tetrahedra are shown in orange-brown, the oxygen atoms are red and the carbon atoms with 50% occupancy are half white, half grey.*

Angle dispersive synchrotron XRD (AD-XRD) measurements have been performed to investigate compressibility and resistence of the synthesized PASIL to irreversible pressure induced amorphization (PIA). The XRD patterns were measured on the recovered PASIL at ambient conditions. Once opened the cell, the unreacted acetylene was gone, and PASIL was then compressed again using the bulk PA as compression medium. We perform AD-XRD measurements by oscillating the DAC around $\omega \pm 3°$ during the acquisition to activate different Bragg peaks within the average 2D diffraction image. We found at least two different domains in PASIL, corresponding to different amounts of PA in the channels of silicalite (see figure 1.9). The integrated XRD pattern of PASIL shows the peaks of the host zeolite progressively weakening with increasing pressure but surviving up to 19 GPa. This indicates a progressive PIA even if amorphization is not complete, because two poorly resolved bragg peaks around 2.0° are still observed in the decompressed sample at room conditions. In completely filled silicalite, PIA was deactived up to 24-26 GPa [43, 45, 61], while in empty silicalite PIA is complete at about 8 GPa [43]. The degree of filling of the channels affects the overall compressibility of the crystal [43,45], and so the intermediate PIA value obtained for PASIL is again in good agreement with the picture of a partially filled zeolite. Looking at the integrated pattern, above 3 GPa we

can see four Bragg peaks between θ 1.8° and 2.7°, where there should be only two reflections. The presence of these 4 peaks is related to the presence of two different domains spanned by the x-ray beam within the same cystal during the small angle oscillation of the sample. Each of the two domains observed in the XRD experiments has a pseudotetragonal, *Pnma* orthorhombic unit cell with two Bragg peaks in this angle region. The presence of two main peaks around 2° is consistent with both the structure of PASIL and that of empty silicalite. The splitting of the peaks is not related to a non-hydrostatic compression of the sample, because the bulk PA is a quasi-hydrostatic amorphous soft compression medium over the first few GPa. Therefore, the first and the third peaks are related to the higher specific volume and less compressible domain, while the second and the fourth peaks are related to a softer domain with smaller specific volume. The two peaks left at room conditions in the decompressed sample are originated from what remains of the two crystalline high and low volume domains after the compression/decompression cycle. In the inset of figure 1.9, the relative volume over pressure of the two domains until 4 GPa, where non-hydrostaticity of bulk PA makes it unreliable as compression medium, is shown. These two domains exhibit completely different compression behaviours. The responses of the two domains to the external applied pressure diverge with respect to each other up to 4 GPa, more than the error bars on each single P-V point. Linear equations of state (EOS) fitted through the points yield bulk moduli of 20.1 ± 0.9 GPa and 14.5 ± 1.8 GPa, whereas the PESIL bulk modulus was found to be 26.7 GPa. The stiffer and the softer domains in PASIL therefore correspond to more or less PA confined inside the channels, because it is well-known that pore filling reduces the compressibility of the host framework [43, 45]. A high channel filling and a low compressibility reduce the tendency of the crystal to undergo PIA; nevertheless, the two domains of PASIL do not exhibit a marked difference in PIA, and this clearly indicate that the rigidity of conjugated chains also plays s role in deactivating this amorphization mechanism, and that this effect is predominant here.

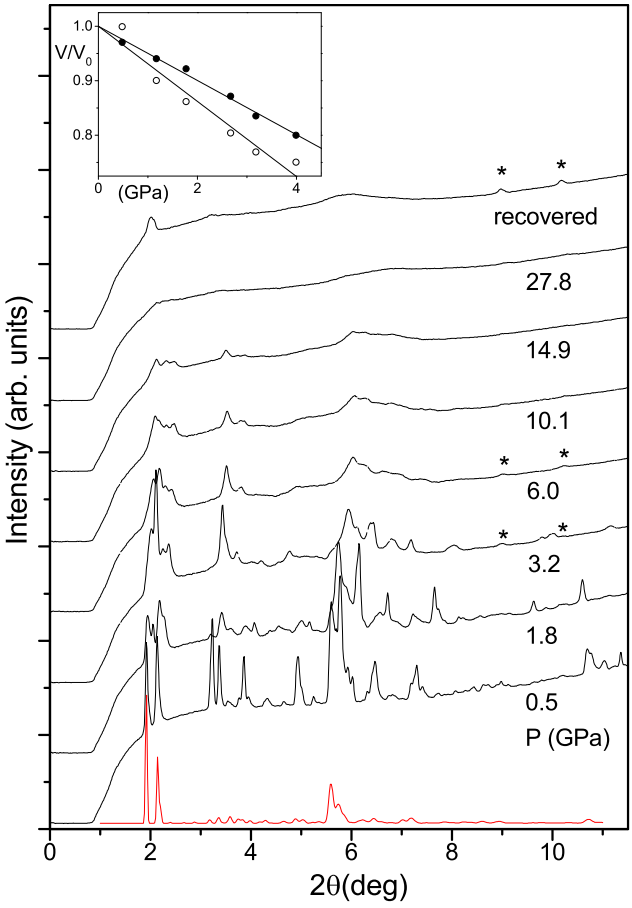

Figure 1.9: *AD-XRD patterns of PASIL as a function of pressure. The stars indicate the peaks from Re gasket. The pressure are written under the relative pattern. Red curve indicates the calculated powder XRD pattern at ambient pressure based on structural model of PASIL. The inset shows the relative volumes of the two domains of PASIL as a function of pressure. The two EOS (empty and solid circle) correspond to two regions of the sample, where polymerization occurred at a different extent. The stiffer EOS correspond to a larger amount of confined PA.* $\lambda = 0.3738$ *Å.*

1.3 From 3D to 1D zeolites: PA/TON

Switching to all-silica ZSM-22, the synthesis of single, ideal nanoconductive chains in the protecting scaffold offered by the zeolite can be significantly improved. In fact ZSM-22 provides an ideal host matrix to exploit the directional properties of polyacetylene, due to its internal 1D nanochannels. As in the case of PASIL, the samples was loaded using the *Spray Loading* technique (section 4.2). The polymerization reaction was triggered only by pressure and conducted in the same way than in PASIL. Polymerization takes few hours to complete at about 5 GPa: timescales are comparable with those of PASIL and of bulk PA, thus ensuring that no catalytic effect due to eventual, residual groups from synthesis of 1D-zeolite is present. Only powder sample of all-silica ZSM-22 has been used for this experiments. The syntehsized nanocomposite material has been called PA/TON [62].

The results of this prothocol are really encouraging. By the comparison of FTIR spectra acquired in the C-H stretching region of PA in the PA/TON composite at high pressure (see figure 1.10) with those of bulk PA and confined PA in PASIL, we observe a significant amount of sp^2 carbons with respect to the sp^3 ones. The peaks assigned to modes of CH groups with C in sp^3 hydridization refers to points of branching or termination of chains, while the peaks assigned to modes of CH groups with C in sp^2 hybridization refers, as in PASIL, to PA chains or oligomers. By a simple qualitative observation, it's fairly seen that the sp^2 to sp^3 ratio is greater than in the previous attempt, indicating an improved conjugation in PA/TON with respect to what we obtained in PASIL. More in detail, the r ratio between the integrated absorbance of sp^2 and sp^3 peaks could give good hints on the deviation of our PA-like chains from the ideal, all conjugated chain of PA. In perfect PA, r would tend to infinite. In bulk PA, PASIL and PA/TON, r is equal to 0.35, 0.46 [63] and 1.1, respectively. Taking into account the different cross section for sp^2 and sp^3 C sites [52], this r values leads to sp^2/sp^3 ratios of 0.52 for bulk PA, 0.67 for PASIL and 1.5 for PA/TON. Given that we used only powdered ZSM-22 for our experiments, we can confidently speculate

that sp^2/sp^3 ratio for the powdered nanocomposite is even higher than 1.5 because the powdered nanocomposite is completely surrounded by bulk PA that likely contributes to the IR absorption lowering the ratio because of its less ordered structure. The final result is that, as a difference with the PASIL case, where the degree of branching inside the zeolite and in the bulk PA was comparable, in PA/TON the monodimensionality of the channels is able to drive the formation of virtually non-branched PA chains, which is a great advancement for potential technological applications.

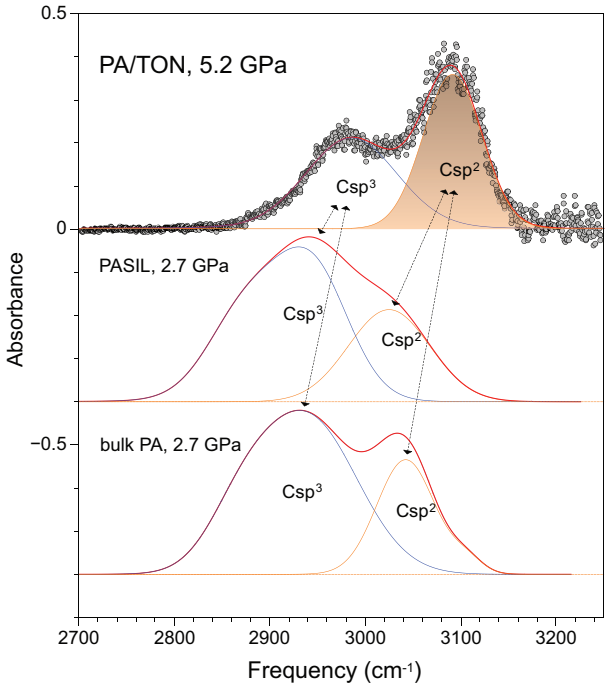

Figure 1.10: *FTIR absorption spectrum of PA/TON in the CH stretching region. On the top panel, the spectrum of PA/TON at 5.2 GPa: conjugated chains are indicated by the C(sp^2)-H peak in orange, with full area, whereas the C(sp^3)-H peak (blue line) is related to branching and terminations fo the chains, and likely arises from the bulk, surrounding PA. On the central and on the bottom panel, spectra from PASIL (at 2.7 GPa) and bulk PA (2.7 GPa) are reported for comparison. All the spectra have been normalized to the same peak intensity and vertically shifted for the sake of clarity.*

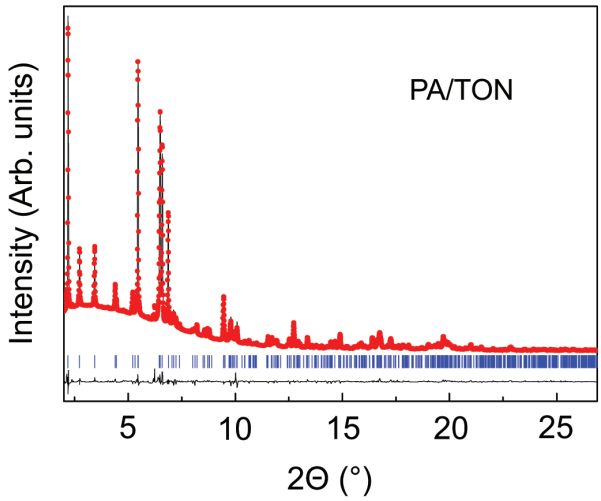

Figure 1.11: *Experimental (dots) and calculated (solid line) XRD profiles from the Rietveld refinement of PA/TON at ambient pressure. Data were collected on sample recovered in the gasket. Black profile: difference XRD profile. Vertical bars: position of the calculated Bragg reflections.*

Unfortunately, Raman measurements on PA/TON composite has been prevented by the huge fluorescence, probably due to the powdered matrix. Anyway, laboratory XRD has been used to qualitatively check the degree of pore filling of TON with acetylene/PA during the high pressure synthesis of the nanocomposite material. The limited data quality of this laboratory XRD and in particular the low signal to noise ratio and the low angular resolution prevented a good, quantitative structure refinement of PA/TON. To overcome this limitation, synchrotron XRD measurements were performed on the PA/TON material recovered at ambient conditions inside the gasket. To better understand the configuration and nature of the 1D embedded polymers, DFT calculations has been also performed.

Starting the Rietveld refinement from the structural model by Marler [39], the first fit was very poor with an R1 factor of 30.1%. The Fourier difference map calculated for this refinement show 4 sites for carbon atoms per unit cell to be located. Each of these 4 sites had a multiplicity of 4 but, lying in the yz plane, they cannot be all simultaneously occupied because the C-C distances

would result to be too short. Conversely, considering 24 SiO_2 formula units from the framework and 16 C atoms in the pores with a chemical occupancy fixed to 50% has been obtained a very good fit, with R1 factor of 4.2%, see figure 1.11. The parameters obtained from the fit are reported in table 1.2.

Cell parameters	
a (Å)	13.8553(1)
b (Å)	17.3992(2)
c (Å)	5.03855(5)
V (Å^3)	1214.64(2)
R_p (%)	10.2 [11.9]
R_{wp} (%)	9.4 [10.7]
R_{Bragg} (%)	4.2 [5.7]

Table 1.2: *Structural Data and Agreement Factors Obtained from Rietveld Refinement on PA/TON (space group $Cmc2_1$, $Z = 8$). The values in square brackets refer to the agreement with the atoms of the embedded polymers fixed to the values obtained from the relaxed DFT structure with fixed cell parameters.*

The improvement in the fit, obtained including 16 C atoms with 50% occupancy, is consistent with the presence of some degree of disorder in the chain isomers and positions: this picture is in better agreement with the residual electron density in the center of the pores that can be seen in the observed Fourier map (the Fourier transform of the intensity distribution in the space of wave vectors, see figure 1.12) than a model with 8 C atoms fully occupying their crystallographic sites. The PA content is therefore 4 chains per unit cell and, consequently, 1 chain per pore, corresponding to 100% pore filling.

In order to obtain more informations on the nature of PA chains inside the pores, a second refinement was performed using the relaxed *cis*-PA chain from DFT calculations with fixed positions. DFT calculations show and confirm that the PA-like chains have a planar zigzag conformation, parallel

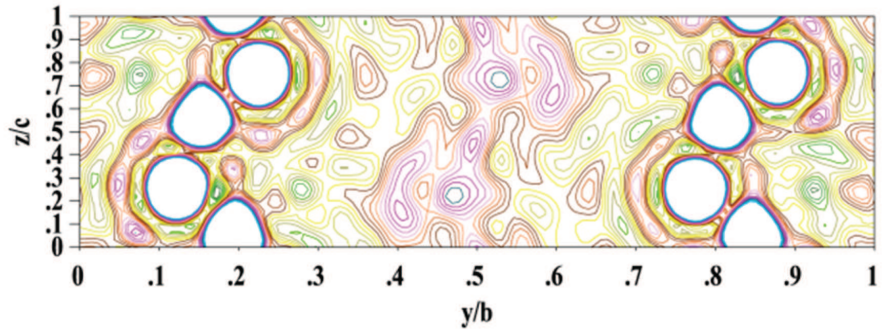

Figure 1.12: *Section of the electron density map at $x/a = 0.5$, obtained by Fourier inversion of observed structure factor amplitudes and model phases (the isocontour interval is 0.1 $e/^3$). The white circles ($y/b = 0.1 - 0.25$ and $y/b = 0.75 - 0.9$) represent the framework atoms, while the polymerized chains of PA are visible in the range $y/b = 0.4 - 0.6$.*

to the *bc* plane (see figure 1.13). In this case, the Bragg R-factor increases to 5.7%, thus indicating that such a model, although much closer to the final model in terms of quality of the fit, does not completely reproduce the data. The parameters obtained for this second fit are reported in the same table 1.2, in square brackets. This result, along with the fact that the observed Fourier map contains additional features out of the four peaks along z in the center of the pores, that are expected for carbon atoms in pure *cis*-PA, indicates that the real structure of the composite is somewhat disordered. Another noticeable thing is that, in the case of PA/TON and differently for the main feature observed in PASIL, an ordered, pure *trans*-PA is not consistent with the simmetry of ZMS-22 (framework type TON). Such a structure for the guest polymer would imply an increase in the size of the unit cell, with a consequent change in symmetry and thus in the X-ray diffraction patterns. No changes in this direction has been observed during our experiments, allowing to neglect this possibility.

Therefore, the use of all-Silica ZSM-22 instead of silicalite as protecting host allows to obtain a major conjugation in the confined PA chains, and

a high degree of filling of the pores (because of the favourable geometry of linear nanochannels), even if some kind of disorder in the confined polymer is not avoided.

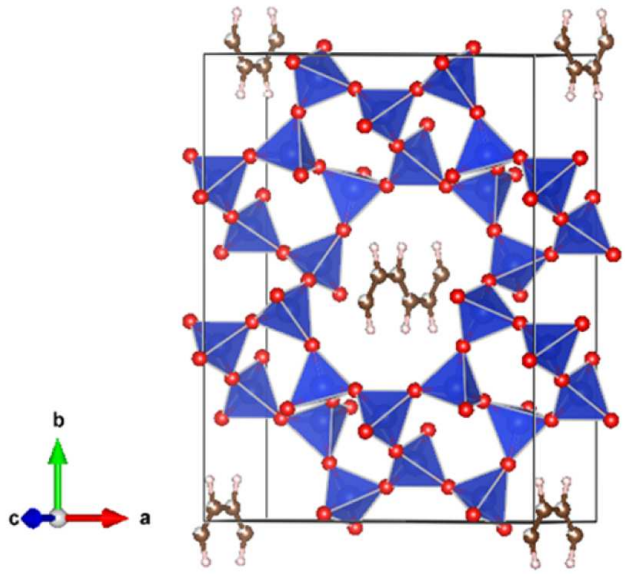

Figure 1.13: *Structure of PA/TON. SiO_4 tetrahedra are represented in blue; black/white and white spheres represent respectively carbon and hydrogen atoms from the relaxed structure of PA obtained from DFT calculations and fixed during the Rietveld refinement.*

1.4 High pressure polymerization of CO in silicalite

Carbon monoxide (CO) is an interesting model system due to its properties and to its simple structure. Several studies have shown, for simple molcules such as CO_2 [9] or N_2 [5], a high pressure reactivity ending in the formation of extended covalently bonded solids: these transformations required drastic pressure conditions, and the products couldn't be recovered at room conditions. On the contrary, CO at high pressure undergoes to an irreversible chemical transformation giving a solid, yellowish to brownish product with a high carbon content, namely a polymeric carbon monoxide (polyCO, or pCO). This is particularly interesting because CO is a very simple molecule with a weak and static dipole moment, isoelectronic and also isostructural with (but much more reactive than) molecular nitrogen, N_2, in a rather wide P,T range. The formation of polymeric CO (pCO) in the high pressure range has been investigated in several experimental and theoretical studies [3, 64–72]. Polymeric CO is an amorphous solid made up of carbonyl groups with structural and orientational disorder, non-stoichiometric and with a tendency to disproportionate with the formation of C and CO_2. The pCO chains are highly photosensitive, hygroscopic, and metastable at ambient conditions, where they can storage energies of several kJ/g [67]. Ceppatelli *et al.* (see reference [72]) have studied the CO polymerization starting from three different crystalline phases (see figure 1.14), rhombohedral ϵ-CO (13 GPa and 100 K), cubic δ-CO (7 GPa and 200 K; 5.9 GPa and 300 K) and hexagonal β-CO (5.8 GPa at 400 K), carefully separating temperature effects from irradiation effects. They found that the polymerization process at low temperature gave rise to polycarbonyl chains containing a considerable amount of anhydride groups. At $T \geq 300$ K, this groups were interconverted in epoxy rings, CO_2 and carbonyl functional groups. The polymerization seemed to proceed essentially in two steps, a first one (the early stage) in which the formation of carbonyl groups was observed, and a second one (a

later stage) in which the formation of carbonyl groups slowed down (or at least stopped) and started to appear CO_2 and apoxy rings signatures in the FTIR spectra. These two steps seems to be strictly consequential, thus suggesting an extended network decomposition of the carbonyl groups, a decarboxylation process that gives a carbon rich solid product (characterized by the presence of epoxy functions) and molecular CO_2. Unfortunately, the product of this reaction could not be recovered: once opened the cell, the contact with the atmospheric moisture determined a sudden conversion of the products, that incorporated water (in form of -OH groups) and showed new spectral signature that could be related to the presence of carboxylic acids [72].

Recently, a DFT study [73] have predicted that orientationally and structurally ordered pCO can be obtained at high pressure in the form of a crystalline, metallic phase made up of 1D $[\text{-(C=O)-}]_n$ chains with an alternate head-to-tail orientation of C=O bonds, or in the form of a 3D insulating CO crystal structures where carbon atoms are all in sp^3 hybridization.

It is quite clear that the exploitation of extreme confinement conditions could represent a unique way to synthesize a completely ordered pCO, at the same time avoiding the reactivity with water and allowing inexpensive storage (considering the hydrophobic nature of silicalite and all-silica ZSM-22 crystals). As it was for PA, pCO is characterized by intriguing properties that could made it a suitable high density energy material, so an improved synthesis could open several potential technological perspectives.

Samples of carbon monoxide in the presence of silicalite crystal or powder were loaded in DAC using the *Cryo loading* technique (see section 4.2). The polymerization has been performed at room temperature and 7.0-7.5 GPa, well above the ambient temperature polymerization threshold pressure of about 5.8 GPa [72]. At this pressure, CO to pCO conversion have typical time constant of about an hour, reaching the 90% completion in several days. The advancement of the polymerization reaction has been followed using FTIR spectroscopy, looking at the appearence of polymer-related bands

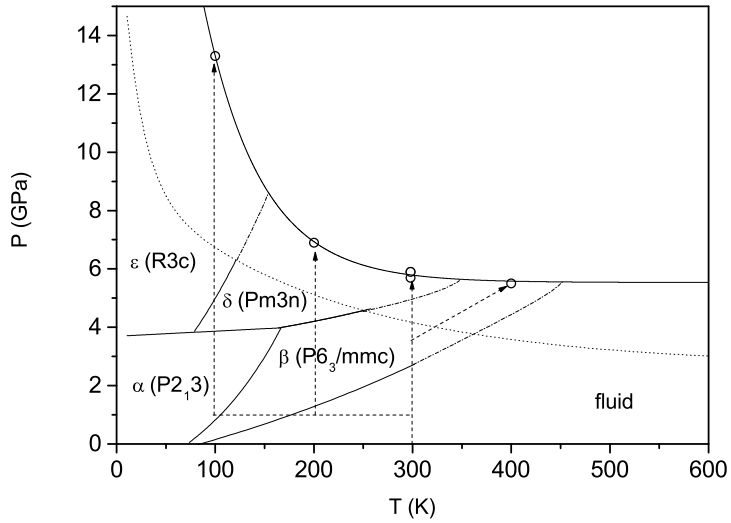

Figure 1.14: *Phase diagram of CO (taken from Ceppatelli et al., see reference [72]). The empty circles indicates the P-T value for the onset of polymerization in the study of Ceppatelli and coauthors. The onsets were observed avoiding visible or higher frequency irradiation of the sample. Upper line is the instability line for CO, traced after that paper. The dotted line is an older instability line, traced by Evans and coauthors [68]. The dashed lines refer to the single paths followed to reach the experimental conditions where the chemical reaction was observed. Dash-dot lines refer to the extrapolated high P-T boundaries of the melting line and of the* β-δ *and* δ-ϵ *phase boundaries with respect to existing literature data (full lines).*

but, mostly, at the consumption of CO monomer, that can be estimated using the integrated intensity of the CO overtones. Once the polymerization was completed, the samples of the pCOSIL (*polyCarbon monOxide filled SILicalite*) nanocomposite were recovered at ambient conditions and infrared spectra and XRD diffraction pattern were acquired on the recovered material on a free-standing gasket. In the recovered samples at ambient pressure, bulk pCO strongly reacted with the atmospheric moisture [72] but this reaction was avoided in pCO confined in silicalite due to the hydrophobic nature of the host inorganic framework. In figure 1.15 we present the FTIR spectra

acquired on the recovered pCOSIL, surrounded by bulk pCO as an embedding medium, along with the spectrum of pure bulk pCO synthesized in the same conditions and of pure silicalite powder pelleted in the gasket. All of these three spectrum were taken out of DACs, so to expose everyone of these three sample to the atmosphere. The spectral region presented in the figure is the C=O stretching region: other section of the MIR spectrum at lower frequencies are dominated by absorption due to silicalite, and the quantitative analysis of the C=O band can be performed only in recovered sample outside DAC, because of the severe limitation due to the close, overwhelming two-phonon peak of the diamond.

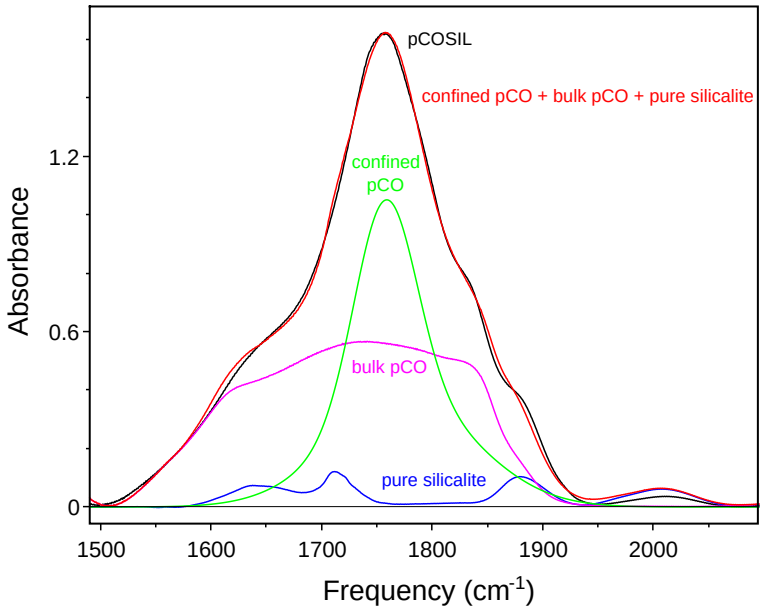

Figure 1.15: *C=O stretching region of the IR spectrum of recovered pCOSIL on gasket, after opening of the cell and exposition to the atmosphere. Black line refers to pCOSIL; magenta (rescaled) to pure, bulk pCO; blue (rescaled) to pure silicalite; green line indicates an analytical peak for confined pCO in pCOSIL; Red line is the sum of the rescaled spectra of bulk pCO, silicalite and confined pCO fitting the experimental spectrum of pCOSIL.*

The composite peak of pCOSIL in the spectral region of interest arises

from the sum of three different absorption component. The spectrum of pCOSIL has been fitted using a linear combination of the experimental spectra of pure, bulk pCO and of pure silicalite and of an analytical, slightly asymmetric peak, assigned to confined pCO. The fit (red line in the figure 1.15) is very good. The single C=O stretching peak assigned to confined pCO is 1758 cm^{-1}, while the broad composite band of bulk pCO is centered at about 1739 cm^{-1}. As it was for PASIL [63], CO_2 [24] and PESIL [45], this frequency shift can be related to the interaction between the confined molecules and the walls of the nanochannels. Such a shift (10-15 cm^{-1}) is so small that it can be suitably assigned to average van der Walls type interaction between pCO and host silicalite. More useful information could be gained looking at the shape of the C=O stretching band. In the bulk pCO, this band is broad and composite, and it can arise from the contribution and the presence of several, different C=O containing groups, underlying the high disorder of the recovered material; in contrast, the confined pCO in pCOSIL exhibits a single peak, which is a strong sign of orientational and structural ordering. The slight asymmetry of this peak, together with its large bandwidth, is indeed an indication of the confinement induced strain of the pCO chains, another clear effect of the interaction between confined pCO and silicalite walls. The total frequency spread of the C=O stretching peak (about 7%) is again compatible with a range of interactions between pCO and silicalite still of the order of van der Walls forces. Another interesting point is that the ideal, infinite $[\text{-(C=O)-}]_n$ chain (sse figure 1.16) shows two C=O groups alternately pointing in opposite directions in each asymmetric unit. This configuration means that there are two different stretching modes for the single unit: one antisymmetric and one symmetric. Due to the presence of an inversion center, the first one is only IR active, while the second one is only Raman active. Therefore, the single C=O stretching peak structure in the FTIR spectrum of confined pCO in pCOSIL is a strong signature for these ideal chains to be synthesized in the highly confined conditions. DFT calculations showed that the frequency of the symmetric Raman mode

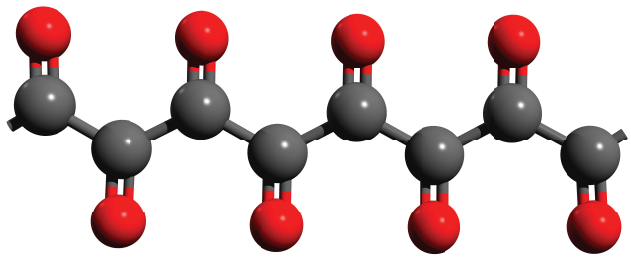

Figure 1.16: *[-(C=O)-]$_n$ polycarbonyl chain structure with alternate head-to-tail orientation of C=O units. Grey spheres indicate C atoms, red spheres indicate O atoms.*

for this structural model should be 55 cm^{-1} lower that the IR frequency. Unfortunately, Raman measurements of pCOSIL samples was prevented by strong photosensitivity and fluorescence of the whole mixture of pCOSIL and bulk, embedding pCO (even using very low laser power densities of about 10^4 W/cm^2).

Single crystal X-ray diffraction (SC-XRD) measurements on the recovered pCOSIL have allowed to determine the crystal structure of the nanocomposite material. The single crystal of pCOSIL, embedded in bulk pCO, was removed from the free-standing gasket and glued on the top of a glass fiber. Starting from the empty silicalite network in the orthorhombic space group *Pnma*, the crystal structure of pCOSIL has been refined obtaining an R factor of 13%. In figure 1.17, the difference Fourier maps for pCOSIL are presented. These maps clearly shows the presence of electron density-rich regions in both linear and sinusoidal channels of silicalite, and this picture is consistent with the presence of single, isolated and disordered pCO chains in both types of pores. Adding C atoms to the model in the same positions where they were found in the refinement of PESIL structure [45], a significant improvement of the refinement can be obtained (new R factor of 10%). Two more C atoms per asymmetric unit were added based on the strongest remaining peaks on the Fourier difference map. The high degree of translational and conformational disorder of confined pCO chains, and the close scattering power of oxygen

and carbon atoms, prevent any attempt to distinguish between C and O: based on the experimental IR results, half of the guest atoms were defined as carbon and the other half as oxygen. For the reasons explained above, this assignement has absolutely no effect on the R factor value. So, we obtained the number of 84 C/O atoms per unit cell, with a final R factor of 9.2%. This R factor corresponds to the structural model presented in figure 1.18.

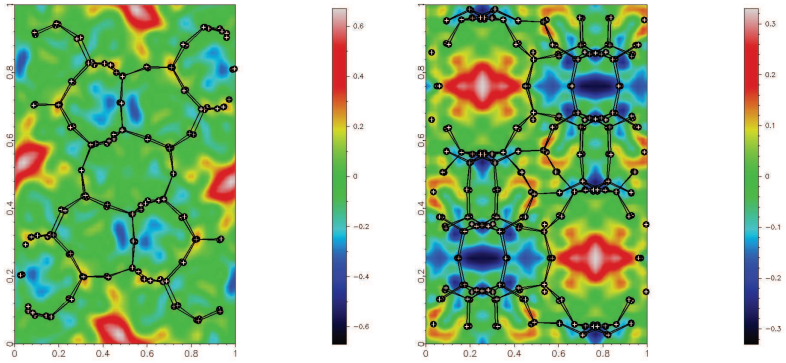

Figure 1.17: *Difference Fourier maps of pCOSIL. Left panel: projection along b; right panel: projection along a. The maps show the presence of regions of electron density due to C and O atoms in both the linear and sinusoidal pores. The linear pores are visible in the left panel, orthogonal to the drawing; the sinusoidal pores can be seen on the right panel.*

If only one type of pores, linear or sinusoidal, is occupied, the resulting R factor is close to 11%, showing a worse agreement with experimental data. From this refinement, we obtained high atomic displacement parameters, due to translational, orientational and conformational disorder of confined pCO chains. These displacement are strictly related to the van der Walls interaction between confined pCO and silicalite walls. Due to this interactions, the unit cell volume of pCOSIL results to be very near to that of unfilled silicalite (5351.5(5) Å^3).

FTIR and SC-XRD results show that the synthesized pCOSIL is made of a silicalite network with the addition of confined, extra-framework pCO chains compatible with the model of ideal, *all-transoid* polycarbonyl [-(C=O)-]$_n$

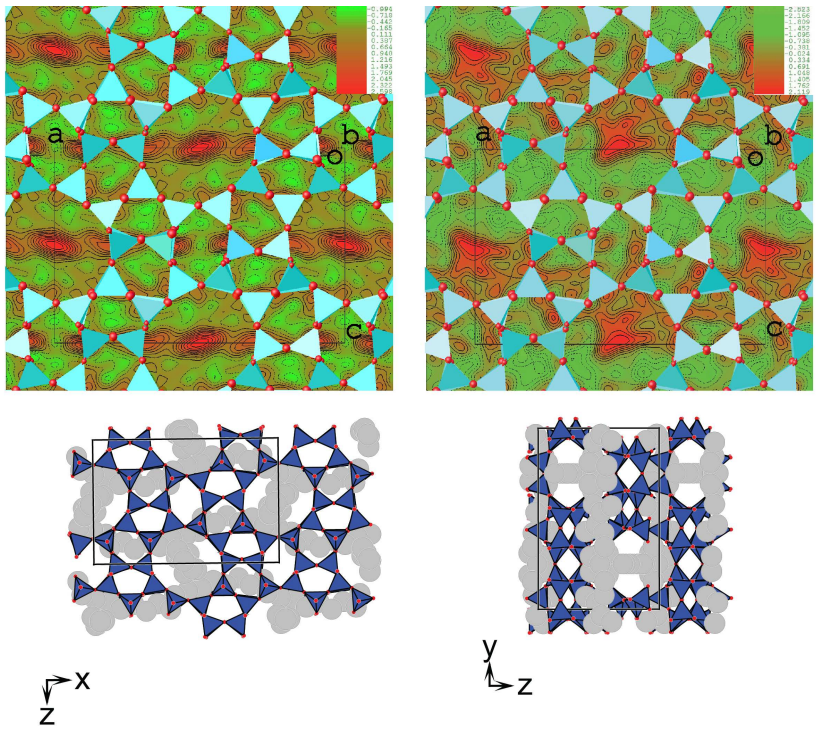

Figure 1.18: *Refined structure of pCOSIL. Top part: cyan tetrahedra and red balls indicate silicalite framework; contour plot indicate charge density distribution for pCO in both the linear (orthogonal to the drawing) and sinusoidal pores of the silicalite framework. Top left, left image: cut along the b axis at* $y = 0$*; top right, right image: cut along the b axis at* $y = 1/4$*. Bottom part: structure of pCOSIL obtained by SC-XRD. Blue tetrahedra and red dots indicate the silicalite framework, gray spheres the confined C and O atoms. Bottom left, left image: view along the b axis, where linear (along y) and sinusoidal (parallel to xz) extra-framework C/O chains can be seen; bottom right, right image: view along the a axis.*

with head-to-tail orientation of the C=O functional groups [73]. As in the case of PASIL, the peculiar nature of silicalite host force the pCO chains to be bent at least in the sinusoidal channels, resulting in a high strain of the confined polymer. This feature may easily prevent the occurrence of the predicted metallic pCO chains in our real system [73].

1.5 From pCOSIL to pCO/TON

The presence of the interconnected channels characterizing the silicalite framework likely affects the development of linear, unbranched polyCO chains, therefore, in order to obtain a better quality confined pCO in a zeolite, to preserve it at ambient conditions and to be able to exploit its characteristics, it is worth to try to perform the polymerization in a more appropriate framework. All-Silica ZSM-22, with its network of internal, linear, slightly elliptical nanochannels, offer the desired 1D framework to drive the polymerization of carbon monoxide in the perspective of obtaining an ideal pCO chain. Carbon monoxide has been loaded in DAC, together with all-silica ZSM-22, through *Cryo loading* technique (see section 4.2). Polymerization has been triggered by pressures between 7 and 10 GPa, and it reached its completion in few days. This pressures are slightly higher than that of the room temperature threshold (5.8 GPa at 300 K, see ref. [72]), but comparable with those of pCOSIL synthesis [74]. The synthesized nanocomposite has been named pCO/TON (*polyCarbon monOxide filled TON*) [62].

Figure 1.19 shows the FTIR spectrum of pCO/TON after exposition to the atmosphere, and the spectrum of pCOSIL in the same conditions [74]. The two spectra have been acquired at room conditions on a free-standing gasket so to avoid the overlap between the C=O stretching region and the two-phonon band of diamond. As in the case of pCOSIL, we see a central peak (marked in blue) with an underlying fine structure superimposed on a much broader band, arising from the contribution of surrounding, bulk pCO and, at a less extent, from the weak peaks of ZSM-22 powder itself. Following what stated about FTIR analysis of pCOSIL, the sharper peak arises from confined pCO. While the broad band of bulk pCO is likely related to different kind of carbonyl groups in the disordered bulk material, the sharp peak of confined pCO constitutes a strong signature of a major chemical order of the confined polymer in the zeolite.

As a difference with the case of pCOSIL, the peak from confined pCO is not a single, slightly asymmetric one but can be splitted in three components,

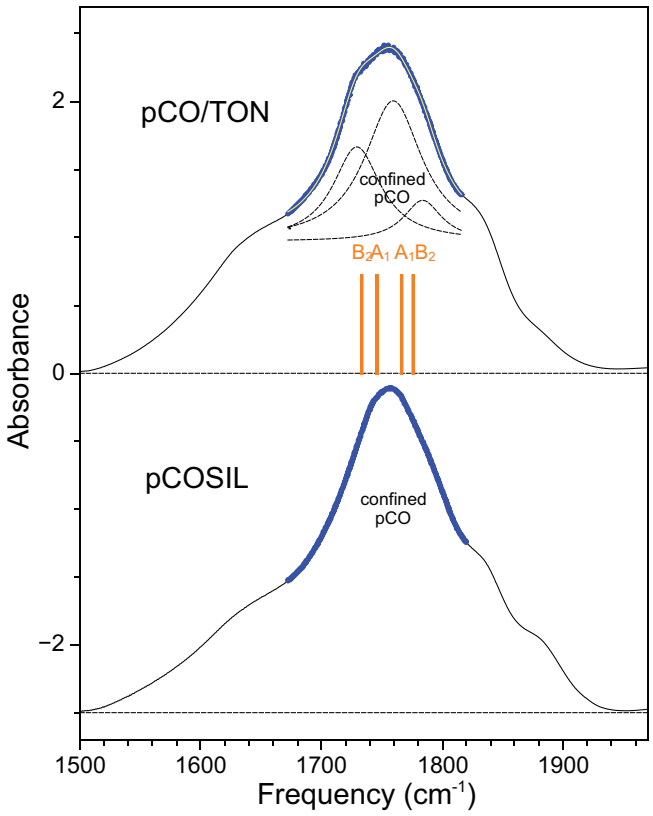

Figure 1.19: *C=O stretching region of the IR spectrum of pCO/TON (top panel) and, for the sake of comparison, pCOSIL (bottom panel, see also figure 1.15). The sample of pCO/TON was recovered in the gasket, taken out of DAC and exposed to the atmosphere. Blue line marks the peak assigned to confined pCO in the host ZSM-22 (top) and in the host silicalite (bottom). Three lorentzian peaks have been fitted to this peak (dashed lines for each one and continuous white line on blue for the sum of the three). Yellow vertical bars refer to DFT calculated frequencies for cisoid-pCO/TON. Absorbance of the two spectra were normalized to the same peak intensity and spectra are vertically shifted by a constant value, for the sake of clarity.*

separated by about 25-30 cm^{-1}. This splitting is related to a more complex structure or to a stronger interaction with the zeolite host than it could be with "isolated" *all-transoid*-polycarbonyl chains. In addition, this *transoid* structure is not compatible with the symmetry of the TON unit cell, whereas

the most simple symmetry-compatible configuration is that with alternating *cisoid*- and *transoid*- C=O conformations, named *cisoid*-pCO/TON. DFT calculations performed of *transoid*-pCO/TON predict eight infrared active A-modes (1606, 1607, 1643, 1656, 1665, 1684, 1690, 1692 cm^{-1}) in this region while the same calculations on *cisoid*-pCO/TON give four infrared modes [1776 (B2), 1766 (A1), 1746 (A1) and 1733 (B2) cm^{-1}]. Taking into account the number and the frequency of the predicted bands, this latter configuration is in good agreement with the experimental results.

Synchrotron XRD measurements have been performed on pCO/TON nanocomposite to refine its structure. The Rietveld procedure gave a very good Bragg R factor of 3.1%. In figure 1.20, the diffraction pattern of pCO/TON is reported, together with its calculated and difference profile. In table 1.3, the structural parameters are reported.

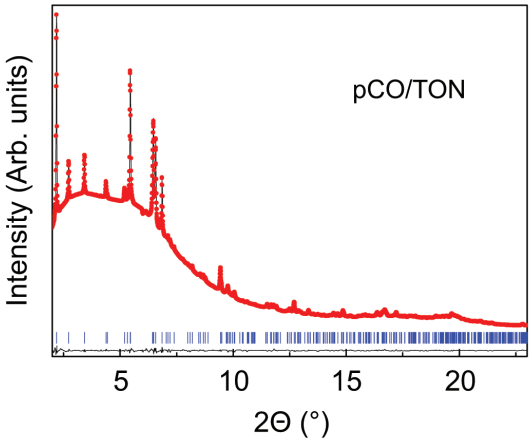

Figure 1.20: *Experimental (dots) and calculated (solid line) XRD profiles from the Rietveld refinement of pCO/TON at ambient pressure. Data were collected on sample recovered in the gasket. Black profile: difference XRD profile. Vertical bars: position of the calculated Bragg reflections.*

C and O atoms can be easily located on the Fourier difference map, but they cannot be chemically distinguished because of their nearly equal scattering power. Anyway, the refined occupations yield a CO content of 2.4 molecules per unit cell, that corresponds to a 30% filling of the pore in a

Cell parameters	
a (Å)	13.8867(4)
b (Å)	17.4430(9)
c (Å)	5.0475(2)
V (Å^3)	1222.63(8)
R_p (%)	9.1 [9.8]
R_{wp} (%)	5.7 [6.3]
R_{Bragg} (%)	3.1 [3.2]

Table 1.3: *Structural Data and Agreement Factors Obtained from Rietveld Refinement on pCO/TON (space group $Cmc2_1$, $Z = 8$). The values in square brackets refer to the agreement with the atoms of the embedded polymers fixed to the values obtained from the relaxed DFT structure with fixed cell parameters.*

statistical distribution. The incomplete filling could be related both to an incomplete polymerization of CO inside the nanochannels, with subsequent loss of the unreacted molecules at the cell opening, or to an unfavourable filling of the same pores by the monomer in the beginning of the reaction. Figure 1.21 shows the observed Fourier map of the pCO/TON nanocomposite: the structural model for the nanocomposite consists in an alternating *cis-* and *transoid* configuration of the polymer. This configuration is commensurate with the host structure of ZMS-22, and it is also consistent with the Fourier map, but gives unreasonable bond lengths and angles.

As in the case of PA/TON, a second refinement has been performed starting from the relaxed pCO chain obtained from DFT calculations, with fixed positions for the atoms. Figure 1.22 reports the structural model of pCO/TON obtained from this second refinement. The Bragg R factor remains the same within this second refinement (see square bracketed values in table 1.3), thus suggesting that the refinement is not very sensitive to a slight shift in the atomic positions. Also this DFT model can thus reproduce the experimental data, both on a structural and on a vibrational level (see infrared spectrum).

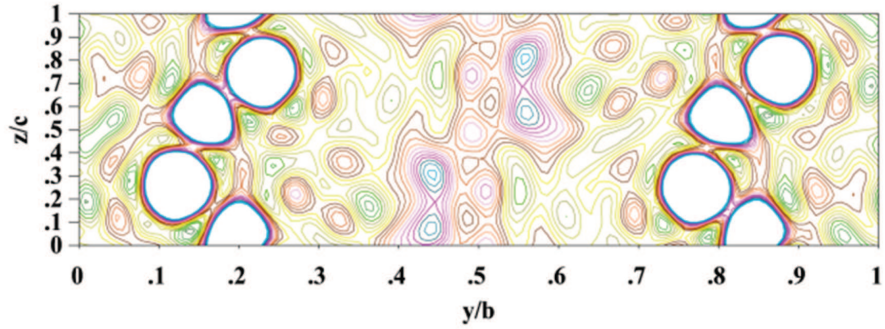

Figure 1.21: *Section of the electron density map at* $x/a = 0.5$*, obtained by Fourier inversion of observed structure factor amplitudes and model phases (the isocontour interval is 0.1* $e/^3$*). The white circles (*$y/b = 0.1 - 0.25$ *and* $y/b = 0.75 - 0.9$*) represent the framework atoms, while the polymerized chains of PA are visible in the range* $y/b = 0.4 - 0.6$*.*

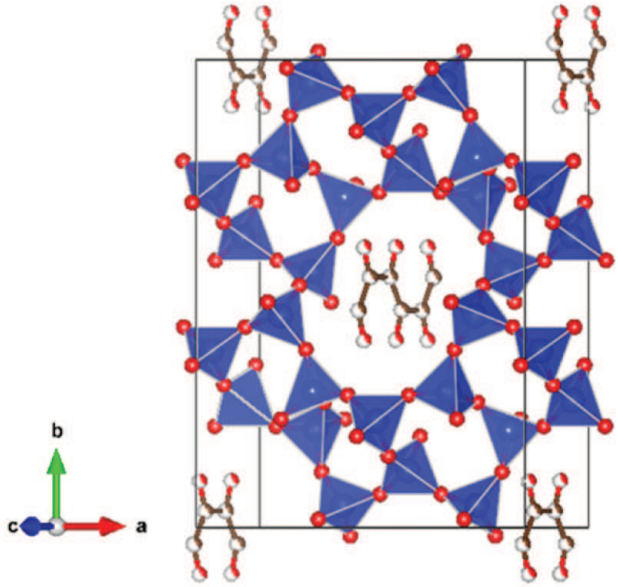

Figure 1.22: *Structure of pCO/TON.* SiO_4 *tetrahedra are represented in blue; black/white and red/white spheres represent respectively carbon and oxygen atoms from the relaxed structure of pCO obtained from DFT calculations and fixed during the Rietveld refinement.*

1.6 Summary

The effect of nanoconfinement on the high pressure polymerization of acetylene and carbon monoxide has been studied, exploiting the host framework of two different synthetic, non catalytic and electrically neutral, pure silica zeolite. These two different zeolite matrices (silicalite, with an internal 3D network of mutual intersecting channels, and all-silica ZSM-22, with a 1D internal structure of linear, slightly elliptical nanochannels) have offered the possibility to evaluate the effect of the host structure in the behaviour of the confined monomers during the polymerization reaction. The purpose of the experiment was twofold: to recover the high pressure synthesized polymers at ambient conditions, avoiding their degradation, and to obtain materials that could be suitable for technological applications.

Polyacetylene is a textbook case for our studies. This polymer is a prototype for a perfect, 1D nanoconductive chain, and it is difficult to recover it from its bulk polymerization because of its tendency to form branching and termination (especially in presence of laser irradiation) and of its high reactivity towards atmospheric moisture [6]. Exploiting the protecting scaffold of the zeolite crystal, it has been possible to synthesize a polymer with specific, high quality characteristics and to recover it at ambient conditions. A new nanocomposite material, named PASIL, has been synthesized under moderate pressure conditions (4 GPa) and avoiding exposure to laser irradiation. The synthesized material has been studied by optical spectroscopy and x-ray diffraction methods. Firstly, confinement conditions are able to drive the polymerization along specific paths: micro-Raman spectra on PASIL show clearly the preferential synthesis of a *transoid* polymer inside the zeolite in respect to the bulk preferential configuration, far less ordered. IR spectra show an increased conjugation for confined PA in the zeolite crystal than in the bulk PA, but a considerable amount of terminations and branchings of the chains, that are highly limited in length (see figure 1.5), is still observed. This data are consistent with the SC-XRD on the recovered sample, from which we obtained a picture of a partially filled silicalite crystal and a car-

bon occupancy inside the nanochannels that ranges up to no more than 50%. This is due to the unfavourable geometry of the channels, that doesn't match with the strict steric requirements of an ideal polyacetylene chain: PA indeed should be planar, because it's constituted by a sequence of conjugated double bonds, but silicalite has two different nanochannels in its 3D network, the one linear and the other sinusoidal, and of course this last type is not good for a polymer that isn't able to stretch as far as necessary to perfectly fit into it (differently from what happened with polyethylene in PESIL [45]). In fact, in PASIL we register only a partial occupancy of nanochannels, and this feature emerges clearly also from the equation of state of the nanocomposite material. During the compression of PASIL, at least two different domains were identified in the crystal, with two different bulk moduli: the first one, almost equal to an empty silicalite; the second one, with intermediate values between empty and completely filled silicalite (as it was for PESIL). To improve the synthesis of the nanocomposite, we switched from silicalite to all-silica ZSM-22, which has only one set of linear, internal nanochannels. The polymerization in this 1D zeolite gives a very good quality of the embedded polymer, with an sp^2/sp^3 ratio far higher than it was in PASIL, thus suggesting an enhanced conjugation in the polymer chains and far less branching and terminations. From XRD, the nanocomposite named PA/TON shows a complete filling of the pores, and the embedded polymer is in an alternate *cisoid* and *transoid* configuration, that is consistent with the structure of the zeolite host. XRD refinement suggests that some degree of disorder in the chain isomers and positions should be present in PA/TON. No Raman characterization was possible due to huge fluorescence.

Polycarbon monoxide is another interesting system for its potential technological applications. Even more than in the case of polyacetylene, the recovery of the polymerization product at ambient conditions is impossible because it readily reacts with the atmosphere [72]. The use of an inorganic, protecting scaffold seems to be the only way to synthesize an ordered material and to recover it once the DAC is opened. In fact, driving the polymeriz-

ation of CO inside silicalite, we obtained a more ordered polymer inside the nanochannels than in bulk CO, as suggested by the FTIR spectra on the recovered sample (see figure 1.15). SC-XRD data on the nanocomposite product, named pCOSIL, show a high filling of the pores of silicalite with the embedded polymer. Furthermore, both FTIR and XRD data are compatible with a specific model configuration of the embedded polyCO, a highly ordered head-to-tail configuration predicted by DFT calculations. Raman measurements was prevented by rapid degradation of the synthesized polyCO under laser light. Switching to ZSM-22 has allowed to obtain even more highly ordered polymer embedded in the zeolite matrix, even if the filling of the pores was not complete (about 30%), due to an incomplete polymerization of the monomer or even to an initial insufficient filling of the pores by fluid CO. The XRD have been refined showing an alternated *cisoid* and *transoid* configuration for embedded pCO, commensurate with the zeolite framework geometric requirements. No significant improve can be obtained refining the XRD data starting from DFT calculations on relaxed polymer chains in the *cisoid* configuration.

For both the ordered models of PA/TON and pCO/TON, DFT calculations of the electronic density of states show van Hove singularities within the band gap of TON, that are related to the 1D nature of the confined polymer chains. It was not possible to estimate this band gap, but we found that the ordered models of PA/TON can be metallic (*trans*-PA/TON) or semiconducting (*cis*-PA/TON), and the same occurs with the ordered models of pCO/TON.

Extreme confinement due to the walls of the nanochannels in silicalite and ZSM-22 is indeed capable to drive the polymerization of guest molecules along preferential path, selecting preferred geometrical configuration and, in the case of 1D zeolites, possibly preventing side effect of branching and terminations, otherwise impossible to avoid in the bulk processes. All the nanocomposites have been recovered at ambient conditions without any signature of degradation due to contact with the atmosphere, and this is particularly

evident in the case of embedded pCO, that is a far more ordered material than the pCO obtained by bulk polymerization.

Chapter 2

High pressure chemistry of Graphite Oxide and simple molecules

In this chapter, the results about high pressure chemistry of Graphene Oxide based systems in the presence of small molecule will be presented. Graphene Oxide, derived from Graphite Oxide (GO), is an interesting carbon based nanostructured material that can be a good 2D platform for the synthesis of modified and doped graphene, in the perspective of possible technological applications.

2.1 Graphite Oxide: structural and spectroscopical features

In the last few years, *chemically modified graphenes* (CMG) have been extensively studied for their peculiar electrical, mechanical and thermal properties, with the perspective of exploiting these features for several applications ranging from polymer composites to metal-free catalysis, energy-related materials, sensors, field-effect transistors (FET) and biomedical applications. In this constantly evolving framework, Graphite Oxide (GO) has rapidly

become a promising starting system for the mass production of CMG and other related 2D platform materials [75]. *Graphite Oxide* (GO) is a largely and cheaply available product of mass oxidation of graphite. GO is a bulk, non stoichiometric high-surface layered material, typically available as water dispersion. Interlayer spacing of GO ranges from 6 to 12 Å , depending on the hydration degree of the dispersed material, and it's sufficient for the insertion of small molecules. This interlayer spacing originates from the oxidation process of graphite and it is related to the molecular structure of the single layers of GO, referred to as *graphene oxide* (in an obvious analogy with graphite/graphene system). The layers of graphene oxide are characterized by the presence of several, different oxigen containing functional groups, that decorate the edges and the basal plane of the material, and contain a variable amount of sp^3 carbon sites. This is the main difference with the fully sp^2 hybdrized "honeycomb" structure of graphene: whereas the latter is a planar sheet, the sp^3 hybridization and the introduction of defects, holes and heteroatoms into the carbon layers determine a loss of planarity of GO sheets and the occurrence of a puckering of the layers (see figure 2.1). The overall structure of GO is generally modelized on that of turbostratic graphite [76, 77].

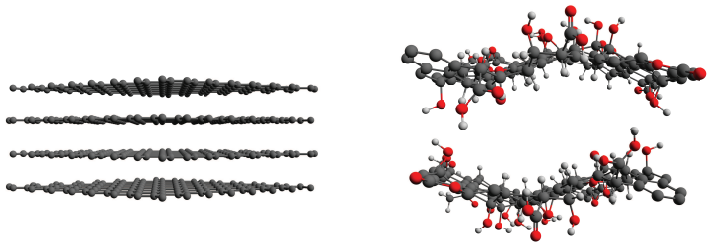

Figure 2.1: *Comparison between graphite (left, space group $P6_3/mmc$, planar layers with a d-spacing of 3.3 Å) and graphite oxide (right, turbostratic packing of highly oxidized puckered layers with d-spacings ranging from 6 to 12 Å) structures.*

Despite of the recent interest for this system, GO synthetic routes have

been extensively studied in the past decades, at the beginning of the chemical interest for graphite-based systems. The principal routes for the synthesis of GO are at least five, namely by Brodie [78], Staudenmeier [79], Hofmann [80], Hummers [81] and Tour [82]. Brodie proposed a reaction involving concentrated sulfuric (H_2SO_4) and nitric (HNO_3) acids together with potassium chlorate ($KClO_3$) as oxidant. Staudenmaier proposed to use fuming HNO_3 only and $KClO_3$ as oxidizing agent. These methods yield a highly oxidized material with a C/O ratio up to 2:1. Staudenmaier method improved the Brodie protocol by stating a multiple adding approach of $KClO_3$ aliquots over the course of the reaction, rather than in a single addition as Brodie had done. After these two pioneering studies, Hofmann proposed a synthesis using non-fuming HNO_3 and $KClO_3$, and later Hummers and coauthors developed a different oxidation method using a mixture of potassium permanganate ($KMnO_4$) and sodium nitrate ($NaNO_3$) and concentrated sulfuric acid. Finally, Tour method uses $KMnO_4$ as an oxidant in a reaction media provided by a mixture of sulfuric and phosphoric (H_3PO_4) acids. The synthetic protocol adopted for the production of the GO used during our experiment was a so called "modified Hummers method", starting from purified natural graphite with the addition of H_2SO_4, $K_2S_2O_8$ and P_2O_5 in the first step, and $KMnO_4$ and H_2O_2 in the subsequent phases [83]. For a more detailed description of the method, see Ceppatelli *et al.*, ref. [84].

The precise chemical structure of GO has been largely debated over the years, and even today no unambiguously assigned model exists. The main reason for this has to be searched in the complexity of this material, that includes sample-to-sample variability, due to its nonstoichiometric, amorphous character. The very first structural models of GO were entirely based on regular lattices composed of discrete, repeated units [75]. Hofmann-Holst structure was based on a spreading of epoxy rings all over the GO basal plane [85], while Ruess model proposed to consider, in addition to the epoxy functions, also hydroxyl group in the edge of the sheets, altering the sp^2 character of the plane with the introduction of sp^3 hybridized carbon atoms

[86]. The Ruess model was based on the idea of an elementar, repeating unit of the complete lattice. The Scholz-Boehm model suggested that the plane was based on quinoidal species in a puckered carbon backbone [87], while Nakajima and Matsuo model relied on the assumption of a lattice framework similar to that of poly(dicarbonomonofluoride), $(C_2F)_n$ [88,89]. Recently, the idea of a lattice-based model has been rejected, and the most widely adopted structure is the one described by Lerf and Klinowski (the Lerf-Klinowski model, see figure 2.2), even if there is actually no complete agreement on this topic. The Lerf-Klinowski model was mainly refined by NMR spectroscopy, giving the picture of a corrugated basal plane with a loss of planarity (due to the presence of several sp^3 hybridized carbon sites) and several, different functional group decorating the basal plane itself (epoxy and alcohol) and its edges (carbonyl and carboxyl) [90]. A further model is that of Dékány, in which no carboxylic acids are presents, composed by two distinct domains, *trans*-linked cyclohexyl species interspersed with tertiary alcohols and 1,3-ethers, and a corrugated network of keto/quinoidal species [91].

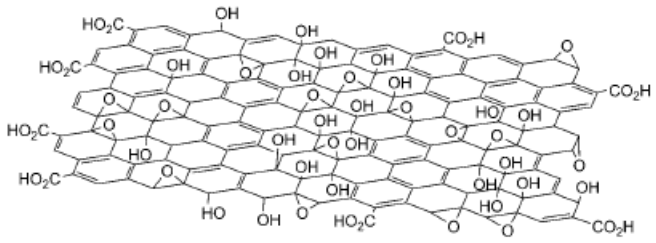

Figure 2.2: *Structural model of GO as proposed by Lerf and Klinowski. Picture taken from Dreyer, et al. see ref [75].*

From a spectroscopical point of view, the huge number of different functional groups on the single layers of GO give rise to very complex spectral features. In the top panel of figure 2.3, we report a typical FTIR spectrum of the GO samples used for this experiments.

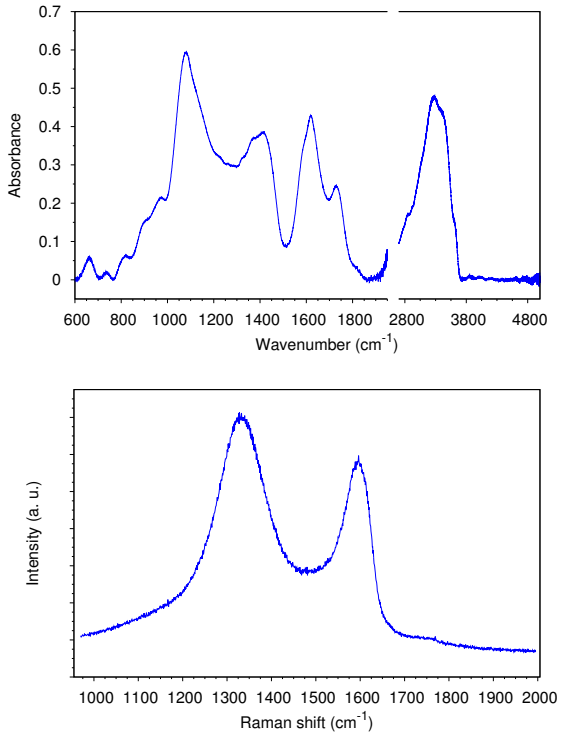

Figure 2.3: *FTIR (top panel) and Raman (bottom panel) spectra of pristine GO at ambient conditions. Infrared spectrum has been acquired in the DAC at ambient pressure; the break in the wavenumber axis corresponds to the region of absorption of diamond anvils. The Raman spectrum instead has been acquired out of the DAC on a free standing gasket, to avoid overlap of the diamond band with the D band of GO. The two broad Raman signals are due to the D band (lower frequency) and to the overlapped G and D' bands (higher frequency).*

The infrared spectrum of GO is dominated by three broad absorption regions: between 800 and 1500 cm^{-1}, between 1500 and 1800 cm^{-1} and between 2600 and 3800 cm^{-1}. The intensity in these regions is related to the presence of O atoms. Due to the extreme difficulty in stating a unique assign-

ment for these very broad bands, the three region refer single bonded C-O functionalities, sp^2 hybridized carbon and carbonyl and carboxyl functionalities, and hydroxyl functionalities (alcoholic, carboxylic and water-related), respectively [92].

In the bottom panel of figure 2.3, we report a typical Raman spectrum of GO in its most characteristic region (between 1000 and 1700 relative cm^{-1}). In this spectral region, the Raman spectrum is dominated by the characteristic D, G and D' bands. A commonly accepted criterion for assessing relative amounts of sp^3 and sp^2 carbon sites in carbon-based graphitic materials is in fact the intensity ratio I_D/I_G between the D (about 1330 cm^{-1}) and the G (about 1600 cm^{-1}) Raman bands. D and G bands are related to C sp^3 and C sp^2 sites, respectively; D' band is related to defects in the honeycomb lattice structure of graphite and again to sp^3 carbon sites. The intensities of D and G bands (and, obviously, the I_D/I_G ratio) are strictly related to the excitation wavelength; furthermore, as a difference in respect to graphite-like, fullerenes and nanotubes, in GO the inherent disorder of the material is responsible for broad Raman signals and a strong overlap between G and D' bands.

In figure 2.4, we report a comparison between the diffraction patterns of graphite (upper curve) and of pure graphite oxide (lower curve). In the pattern from graphite, the main feature is the peak related to the (002) reflection, that gives the characteristic 3.3 Å d-spacing of the graphite layered structure. The pattern from graphite oxide, indexed with respect to the turbostratic model of graphite [76, 77], as discussed above, shows two main Bragg peaks, related to the (001) and the (010) reflections. The (001) peak gives the d-spacing between two adiacent layers of graphene oxide in the GO bulk structure, while the (010) refers to a distance in the basal plane of GO, and it is intimately related to the puckering of the GO sheets. The diffuse, broad signal between 2θ = 5-11° in GO is likely due to the S(Q) structure of H_2O trapped between the GO sheets [77].

Due to the presence of several active sites on its puckered basal plane, GO

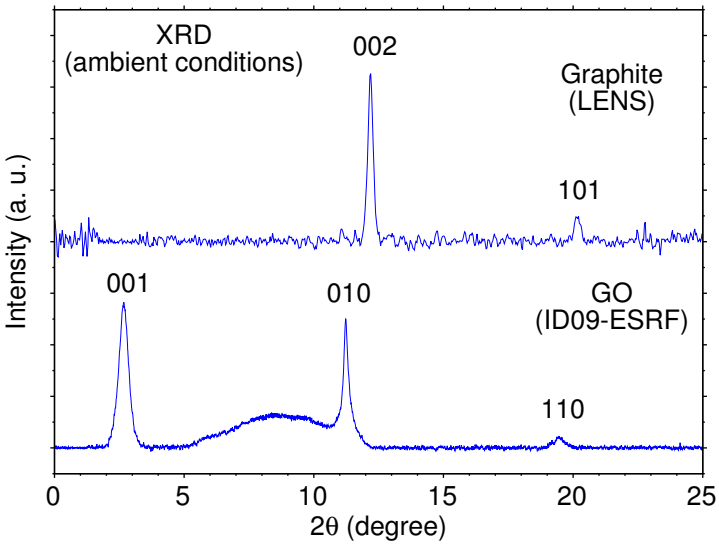

Figure 2.4: *Integrated spectra from the 2D-XRD patterns of graphite (upper curve) and graphite oxide (lower curve). The labels indicate the peaks corresponding to the (002) and (101) reflections in graphite, and to the interlayer (001) and intralayer (010, 110) d-spacings in graphite oxide. The pattern of graphite has been measured at LENS (λ=0.71093 Å), while the pattern of graphite oxide has been measured at ID09, ESRF (λ=0.415352 Å).*

is a very promising platform material to study insertion of simple molecules between the layers in the perspective of separating the graphene oxide layers and of obtaining doped and chemically modified graphenes. There are plenty of experimental and theoretical studies about chemical functionalization of GO [75], about synthesis of reduced GO (rGO, an interesting material for the production of large quantities of graphene) [93], and about the doping with heteroatoms (particulary, the N-doping) [94], but far less studies that investigate high pressure structural and reactive behaviour of GO. There are several work by Talyzin and coauthors investigating lattice expansion of GO by the insertion of small molecules that could interact with the basal plane oxygenated functionalities through the formation of H-bond, like water, alcohols (methanol and ethanol) and acetone. The studies about GO immersed in water have shown a huge auxetic effect on the d-spacing of layered GO

due to the insertion of molecules in the fluid phase, a structural breathing of the lattice with a negative compressibility and an increase of the unit cell volume up to 30% at 1.4 GPa with respect to ambient conditions. At the solidification pressure of water (1.3-1.5 GPa), the compressibility returns to be positive and the pressure dependence of unit cell volume shows the usual characteristics [77]. Talyzin and coauthors have also studied the temperature effetc on this lattice breathing of GO in the presence of water [95]. A similar behaviour, even if to a lesser extent, has been founded in mixtures of GO with protic solvents lik liquid alcohols (methanol, ethanol and methanol/ethanol) [96] and non-protic solvents like liquid acetone [97]. A systematic study of structural breathing of GO in excess of basic or acidic water media has been conducted by the same group, with the result that the lattice spacing of graphite oxide enormously increase in the presence of basic (NaOH) solution up to a value of 85% in respect to "dry" GO at 1.6 GPa, while in contrast this effect is far less pronounced in acidic water (HCl solution) if compared with compression in pure water, stating that pressure induced structural breathing of graphite oxide is strongly enhanced in basic media and suppressed in acidic media [98].

The idea of our study is to exploit high pressure to drive the insertion of simple molecular systems between the GO layers and to foster chemical reactivity in nanoconfined conditions. In this way, we aim to modify the chemical structure of the single graphene oxide sheets achieving at the same time their reduction and, by using suitable molecules, their N- doping. As simple molecular systems we used an inert noble gas (Argon) and two different N-bearing molecules to evaluate the actual experimental conditions for the N-doping: molecular nitrogen (N_2), apolar and non-interacting, and ammonia (NH_3), an highly reactive, polar nucleophile with a basic character according to Brønsted and Lewis. We have also extended this reactivity studies to the possibility of a HP polymerization of ethylene between the GO layers, in the perspective of the synthesis of a nanocomposite insulator/semiconductor material. In order to maximize its insertion between the

GO layers, ethylene should be in the liquid phase: we have performed laser induced polymerization of liquid ethylene in GO, then only pressure induced polymerization and high temperature, high pressure polymerization, whose conditions has been specifically investigated to this purpose.

2.2 GO/Ar, GO/N_2 and GO/NH_3: a closer look to the structure

Samples of pure GO and GO loaded with Argon (cryo-loading), N_2 (cryo-loading) and NH_3 (spray-loading) have been studied during room temperature compression and decompression by XRD technique. Figure 2.4 shows a typical integrated XRD pattern of GO. XRD peaks of GO have been indexed referring to the model structure of turbostratic graphite [76, 77], with the d(001) reflection corresponding to the interlayer d-spacing and the d(010) reflection to the intralayer periodicity.

In figure 2.5, the evolution of the d(001) and d(010) spacings for pure GO, GO/Ar and GO/N_2 samples are reported. For pure GO, two different sets of data are shown, corresponding to different XRD spots on the sample. Black and red circles (full on compression, empty on decompression) mark the equation of state (EOS) of pure GO and show a substantial agreement, taking into account the anisotropic compression conditions, indicating an overall positive compressibility of the system. The pressure evolution of the d(001) spacing indicates a general decrease of the interlayer distance on compression, with a flattening of the curve above 7 GPa. During the decompression step, slightly larger d(001) values were measured. Most important, in the recovered sample at ambient conditions a significantly smaller interlayer spacing was measured (8.02 $\pm$ 0.03 Å for black data and 7.98 $\pm$ 00.3 Å for red data) with respect to the starting GO (8.920 $\pm$ 0.006 Å for the black curve and 8.81 $\pm$ 0.09 Å for the red one), indicating an irreversible modification of the interplanar arrangement. The pressure evolution of the d(010) spacing exhibits the same behaviour up to 7 GPa, but above 8 GPa this distance

slightly increases again. During the decompression, the d(010) values tend to be larger than those acquired during the compression step, while the ambient conditions values are equal to pristine GO before compression (2.121 ± 0.001 Å for black data and 2.124 ± 0.002 Å for red data with respect to the initial values of 2.119 ± 0.005 Å and 2.120 ± 0.007 Å, within the experimental error).

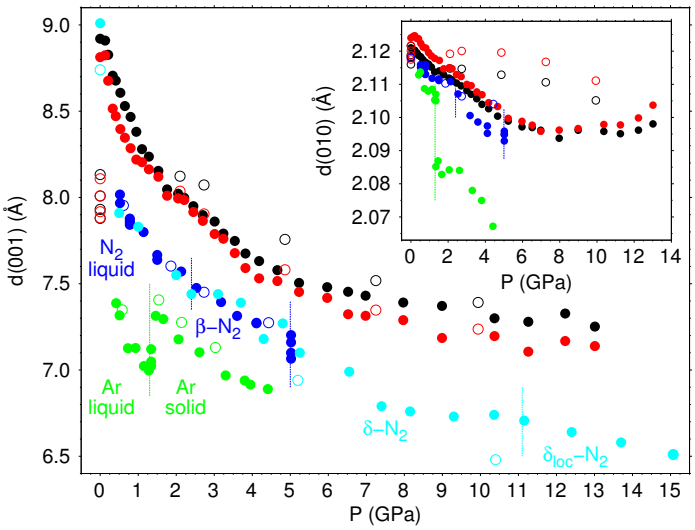

Figure 2.5: *Pressure evolution of the interlayer d(001)-spacing of pure GO, GO/Ar and GO/N_2 samples. Black and red circles refer to pure GO; green circles refer to GO/Ar; blue and cyan circles refer to GO/N_2. Open and empty circles refer to compression and decompression, respectively. Blue and cyan data on GO/N_2 refer to two different experiments. All the data were acquired at ID09 beamline in ESRF (λ= 0.415352 Å), except for cyan data on GO/N_2, acquired at LENS (λ= 0.71093 Å). Inset: pressure evolution of the intralayer d(010)-spacing of GO for the same samples. Same colors summary.*

As for pure GO, also the XRD data acquired on GO/Ar and GO/N_2 samples indicate a positive compressibility, as shown by the reduction of the interlayer d(001) and of the intralayer d(010) spacings with increasing pressure. Anyway, the presence of a compression medium allows several important difference to be noticed. First of all, despite the fact that the

ambient pressure values are the same as in GO without compression medium, the curves for d(001) and d(010) spacings in GO/Ar samples (green circles) and in GO/N_2 samples (blu and cyan circles) are systematically lower than in the pure GO case. It is well known that the interlayer d-spacing of GO strictly depends on the hydration degree of the material. Ar and N_2 are apolar systems unable to form H-bond, but their penetration between the GO layers in high-density conditions is largely favoured by the presence of trapped water molecules enlarging the interlayer spacing, thus allowing Ar and N_2 to accomodate between the sheets [99]. The overall reduction of d(001) spacing suggests a reduction of the H-bonding interactions due to the presence of intercalated, soft non-interacting media.

In the GO/Ar samples, the maximum pressure achieved on compression was limited to 5 GPa, due to the high intensity of the diffraction peaks of solid Ar above this threshold which masks the weak diffraction peaks of GO. The first important thing to notice is a sharp discontinuity in the pressure evolution of both d(001) and d(010) spacings: this discontinuity was observed at the transition pressure of Ar (1.3 GPa) from the liquid to the fcc crystal phase [100, 101], revealed by the appearance of the intense peaks of crystalline Ar in the integrated patterns. The d(001) spacing values show a sudden increase at the phase transition on compression, and a corresponding decrease on decompression. The d(010) values, instead, exhibit a sudden decrease on compression, while on decompression no XRD data could be acquired for this reflection due to the weakening of the peak intensity and its overlap with a reflection from the gasket. This discontinuity in the d(010) spacing suggests a perturbation of the GO basal plane, a puckering of the GO layers induced by the Ar crystallization.

More in detail, the evolution of the unit cell volume of GO/Ar sample during the compression is reported in figure 2.6. The volume behaviour is dominated by the interlayer d(001) expansion over the intralayer d(010) contraction, and show a 3% volume increase at the Ar transition pressure from 35 ± 1 to 36.4 ± 0.3 Å^3. This volume expansion is consistent with the volume

contraction of Ar (about 5%, $\sim$1 mm^3 mmol^{-1}) during the transition from the liquid to the crystal fcc phase [102] and indirectly confirms the insertion of Ar atoms between the GO layers. Considering the $\sim$ 5.59 Å value of the *a* lattice parameter of Ar fcc unit cell, calculated from the 19.5 mm^3 mmol^{-1} volume at the transition pressure [102], only one unit cell of fcc-Ar could fit in the 7.0 Å spacing between the GO layers. Because confined molecules generally experience different transition pressure with respect to their bulk counterpart, confined Ar between the layers likely remains in the liquid phase while its bulk counterpart starts to crystallize with the volume contraction stated above, allowing a free volume to be exploit for the expansion of GO lattice under the pressure exerted by the Ar atoms confined between the layers.

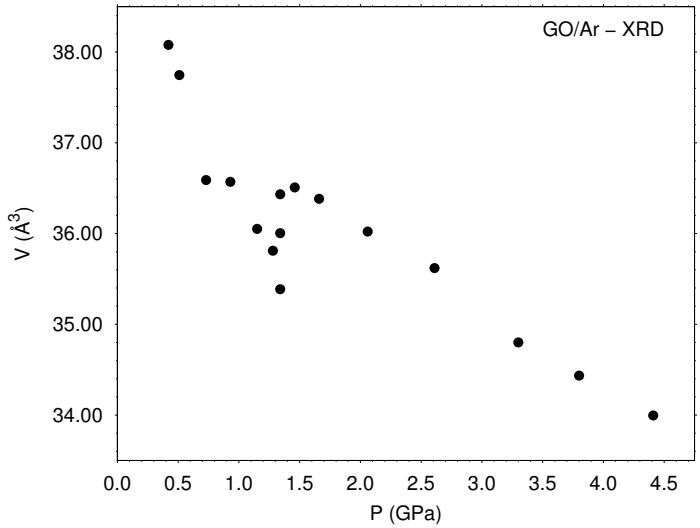

Figure 2.6: *Pressure evolution of the GO/Ar unit cell volume during room temperature compression.*

In the case of GO/N_2 samples, two different compression/decompression XRD experiments were performed. In the first one (performed at LENS, cyan full and empty circles in figure 2.5), the sample was compressed up to 15.1 GPa, while in the second one (performed at ESRF, blue full and empty circles in figure 2.5), the sample was compressed up to 5.0 GPa. In

the first experiment, due to the weakness of the signal, only the (001) peak was followed on compression and decompression; in the second one, both the (001) and (010) reflections were measured. In contrast to what observed in GO/Ar samples, only hardly detectable discontinuities are observed at the pressure values corresponding to the solidification of liquid N_2 into the β-N_2 crystal phase at 2.4 GPa [103], and to the transitions between the β-N_2 and the δ-N_2 (disordered cubic, Pm-3n, 4.9 GPa) [3] and between the δ-N_2 and the δ_{loc}-N_2 (tetragonal, $P4_2/ncm$, 10.5 GPa) [104] crystal phases. However, as it was for the GO/Ar samples, the same interlayer d(001) spacing as in the starting GO was recovered after compression and decompression. This feature is in clear contrast with what observed on pure GO where, in absence of any compression medium, the recovered d(001) spacing at ambient conditions was significantly lower than in the pristine GO.

In contrast to what observed on GO/Ar and GO/N_2, the GO/NH_3 sample exhibits a remarkably different high pressure behaviour. In figure 2.7, the pressure evolution of a selection of the integrated XRD diffraction patterns acquired on GO/NH_3 sample are presented. In the left part of the figure, the pattern evolution upon compression is shown: different colors refer to different NH_3 phases. A more detailed picture of the structural features of this different phases is presented in figure 2.8. For the sake of clarity, the the pressure evolution of d(001), d(010) and unit cell volume of GO/NH_3 system are presented separately from those of pure GO, GO/Ar and GO/N_2 samples (see figure 2.9 below).

The XRD patterns of GO/NH_3 have been acquired in the range between 0.2 and 6.8 GPa, for a complete run of compression/decompression to ambient conditions. Within this pressure range, NH_3 undergoes to the transition between the liquid phase [108, 109] and the orientationally disordered plastic phase III [105, 106] at about 1.0 GPa, and then to the transition between phase III and the ordered phase IV ($P2_12_12_1$) [109]. During the experiment, this phase transitions were clearly detectable by the appearence of characteristic sharp peaks in the integrated pattern (see figure 2.8). The d-spacing

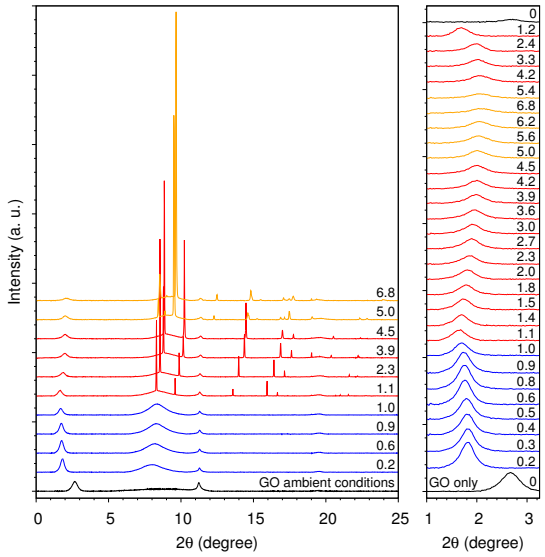

Figure 2.7: *Left panel: pressure evolution of a selection of integrated diffraction patterns from GO/NH_3 sample up to 7 GPa. Right panel: detail of the pressure evolution of the (001) peak during compression and decompression, clearly showing the 2θ shift. Black trace corresponds to GO at ambient conditions; blue traces refer to the pressure range where NH_3 is in the liquid phase; red traces to the pressure range where NH_3 is in the plastic phase III; orange traces to the pressure range where NH_3 is in the crystal phase IV.*

and relative intensities of these peaks are in good agreement with the literature data for NH_3-III [105, 106] and NH_3-IV [107]. The XRD peaks assigned to NH_3 mostly correspond to ring diffraction patterns, thus indicating the formation of powdered, crystalline NH_3 in the excess bulk phase. The phase transitions of NH_3 occur at a slightly higher pressure than in the bulk (1.1 GPa for liquid to NH_3-III, and 4.5-5.0 GPa for NH_3-III to NH_3-IV), as observed in water [77] and ethanol [96]. Figure 2.7 highlights the peculiar behaviour of the (001) peak in this sample: with respect to the pristine GO, in the presence of NH_3 the peak is shifted to lower angles, indicating an increased d-spacing with respect to the starting one. The low angle shift during pressurization is a typical feature of *auxetic materials* and it is related to the insertion of liquid ammonia between the layers of GO. The observed effect

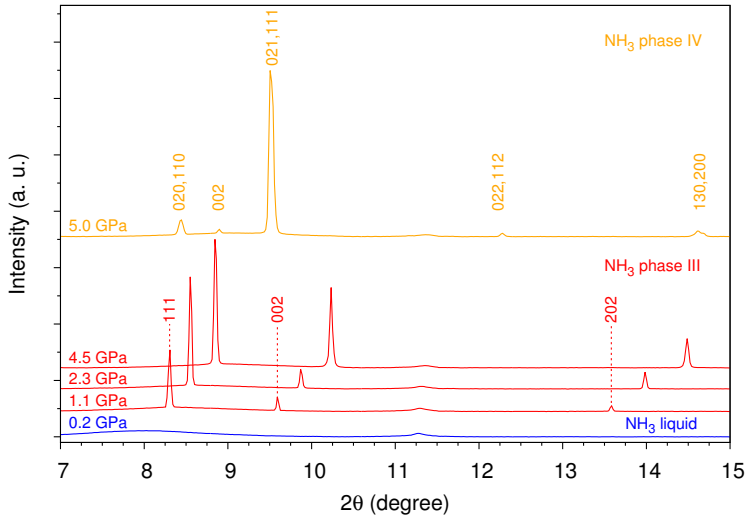

Figure 2.8: *Detail of the XRD integrated patterns acquired during compression of GO/NH_3 sample and showing the phase transitions of NH_3 between liquid (blue), plastic NH_3-III (red) and crystal NH_3-IV (orange) phases. Peak indexing is in accord with literature data [105–107].*

correspond to a 10.8% increase in the d-spacing between 0.2 and 1.1 GPa, where ammonia solidifies into plastic phase-III. Above this pressure, we observe a shift inversion towards high angles with a continuous decrease of the d-spacing up to the maximum investigated pressure.

Figure 2.9, panel *a*, allows to better understand this behaviour. At 0.2 GPa, the XRD pattern provides an interlayer d(001)-spacing of 13.04 Å (46.2% larger than in the pure GO, 8.921 Å). At 1.1 GPa, the interlayer d-spacing reaches its maximum values of 14.45 Å (on compression) and 14.74 Å (on decompression), respectively corresponding to a 62.0% and to a 65.2% increase with respect to ambient pressure value of pure GO. Above 1.1 GPa and up to the maximum investigated pressure, the interlayer d-spacing continuously decrease but always remaining well above 11.27 Å at 6.8 GPa (26.3% larger than in ambient pressure GO). Figure 2.9, panel *b*, shows how the intralayer d(010)-spacing, instead, is much less affected by pressure, slightly and continuously decreasing up to 7 GPa with only a minimal singularity

at 1.1 GPa. The overall unit cell volume (figure 2.9, panel *c*) has a behaviour that reflect perfectly the one of d(001)-spacing, because the intralayer effect is at least two order of magnitude smaller than the interlayer one, and its contribution is almost negligible. The pressure evolution of the unit cell volume closely follows that of the interlayer d(001)-spacing, exhibiting a negative compressibility between 0.2 and 1.1 GPa (*auxetic* behaviour), with a 10.5% volume increase within this range. With respect to pure GO, at 0.2 GPa a 45.2% volume increase is calculated, whereas 60.5% (on compression) and 63.9% (on decompression) increases are achieved at 1.1 GPa. No direct comparison with GO immersed in liquid NH_3 at ambient pressure can be established, because NH_3 is not liquid at room conditions. Nevertheless, a comparison at high pressure indicates that the interlayer d(001)-spacing increases by 10.8% (on compression) and 11.5% (on decompression) with respect to 0.2 GPa, whereas the unit cell volume by 10.5% to 12.8%. It should be remarked that, in the same pressure range, the increases in d(001)-spacing and unit cell volume for GO/H_2O [77] is 8.7% and 7.8%, respectively. In the case of Talyzin work on the GO/water system, the overall maximum lattice expansion occurs to 1.3 GPa, where water starts to solidify, and corresponds to a 19.5% interlayer d-spacing increase and to 18.9% unit cell volume increase in respect to the values at 0.2 GPa. Anyway, the lattice expansion of GO in the presence of NH_3 clearly indicates the insertion of liquid ammonia between the GO layers up to solidification of ammonia into plastic phase III. This suggests that, while part of the NH_3 molecules directly interact with the functional groups of GO layers, other excess molecules can flow in and out the layers. When (1.1 GPa) the external NH_3 solidifies, this molecular insertion is blocked an the NH_3 filled GO starts to behave as expected for a material with positive compressibility.

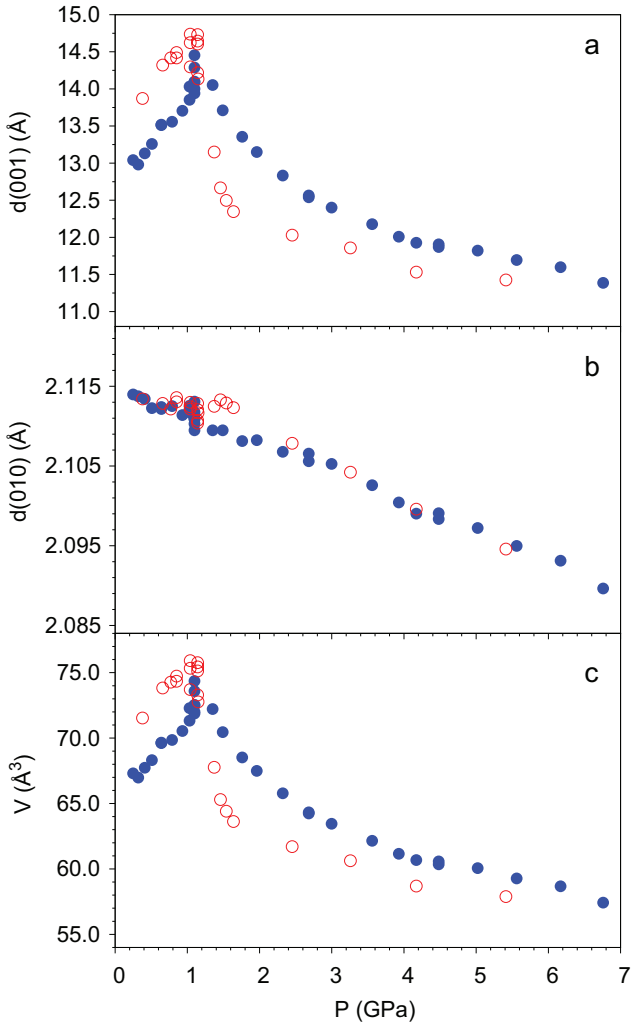

Figure 2.9: *Pressure evolution of the interlayer d(001)-spacing (a), of the intralayer d(010)-spacing (b) and of the unit cell volume calculated from d-spacing (c) for GO/NH_3. Full blue circles indicate data acquired on compression, while red empty circles data acquired on decompression. The maximum lattice expansion coincides with the solidification of NH_3 into plastic phase III (1.1 GPa), whereas only a slight slope variation above 5.0 GPa during compression indicates the transition between phases NH_3-III and NH_3-IV. This behaviour resulted to be reversible with some hysteresis on decompression, with even larger lattice expansion after the melting of NH_3.*

In the investigated pressure range, the interlayer d-spacing of GO oscillates between 13.04 Å at 0.2 GPa, 14.45 Å at 1.1 GPa and 11.16 Å at 6.8 GPa. Considering literature data for the density of liquid ammonia at high pressure and 298 K, we can calculate the volume occupied by a single NH_3 molecule from the corresponding density at 0.25 GPa (0.7223 g cm^{-3}) and 0.95 GPa (0.8287 g cm^{-3}) [110]. The diameter of the sphere containing the tetrahedral NH_3 molecule should range between 4.212 Å at 0.25 GPa and 4.023 Å at 0.95 GPa. Considering that the thickness of GO layers (due to the functional groups pointing in different directions) ranges between 7 and 9 Å [93], the number of NH_3 molecules that can fit between the GO layers at 1.1 GPa ranges from 1.3 to 1.8 in the region where two functional groups of the GO layers are pointing against each other, up to 3.6 in absence of functional groups, whereas at 0.2 GPa this number ranges respectively between 1.3 to 1.4 and 3.1. Only a 1-3 molecular layer can thus fit between the GO layers.

Another remarkable feature is that the d(001) spacing and the unit cell volume for the recovered GO after compression/decompression cycle (8.86 ± 0.04 Å and 45.8 ± 0.5 $Å^3$, respectively) are quite similar to those of pristine GO (8.920 ± 0.006 Å and 46.34 ± 0.09 $Å^3$). The similarity of these values seems to exclude the occurrence of a massive reduction process, which would cause a significant decrease of the interlayer d-spacing and, consequently, of the unit cell volume, due to the removal of oxygenated groups on the layers. As shown before, the pressure evolution of the d(010)-spacing reveals only a subtle effect of pressure on the chemical bonds building up the C network of GO, suggesting a strong mechanical resistance of this material. The GO sheets are naturally puckered with respect to the graphite planes, due to the presence of a large amount of sp^3 carbon sites. The reduction of GO and the restoration of sp^2 carbon domains should cause an increase in the a lattice parameter. No increase is observed in our compression, and the d(010)-spacing of pristine GO and of recovered GO/NH_3 are quite the same. However, the asymmetric shape of the (010) peak seems to account for some

kind of perturbation of the chemical bonds structure in the GO layers during compression.

Considering that the confinement is known to alter the transition pressure and temperature of molecular systems and that only few layers can fit between the GO sheets, inserted NH_3 is likely expected not to follow the solidification of its bulk counterpart outside GO. At 1.1 GPa, the molecular insertion is blocked by the crystallization of bulk NH_3, but however the d-spacing values indicate that ammonia is still present between the layers. Ammonia could likely interact with the O-bearing functionalities on the GO layers, and considering its Brønsted-base character, the weak acidity of water, the fact that absorption of gaseous NH_3 in the presence of adsorbed water is strongly enhanced [111], and the known tendency of the GO d-spacing to increase in presence of basic media [98], the reported *auxetic effect* is in perfect agreement and further confirms and supports available literature data.

2.3 High pressure reactivity of GO and simple molecules

Besides of the structural behaviour of GO in the presence of simple inert (Ar, N_2) or interacting (NH_3) molecular systems, the main interest of our study was about the pressure induced reactivity of confined molecules between the GO layers, in the perspective of promoting the N-doping of this carbon based nanostructured material. The reactivity of the GO/Ar, GO/N_2 and GO/NH_3 systems has been fostered by means of pressure, heating and photoirradiation, and the effects have been monitored by FTIR and micro-Raman spectroscopy. More in detail, on the different samples have been performed room temperature compression/decompression experiments (GO/Ar, GO/NH_3), high pressure resistive heating (GO/N_2, GO/NH_3) and high pressure photoirradiation using UV and VIS wavelengths (GO/N_2 and GO/NH_3, with NH_3 both in the liquid and in the solid phase).

2.3.1 Experimental results

Regarding GO/Ar mixtures, only compression/decompression experiments have been carried out, to evaluate possible chemical changes of the layers due to the increased density conditions. GO/Ar samples have been studied by FTIR and Raman spectroscopy during room temperature compression up to 31 GPa and further decompression to ambient conditions. As shown in section 2.1, FTIR spectrum of GO is dominated by three broad absorption regions (800-1500 cm^{-1}, 1500-1800 cm^{-1} and 2600-3800 cm^{-1}). In figure 2.10, upper panel, the pressure evolution of the IR spectra of GO/Ar upon compression is reported. The main effect of the application of pressure on this sample seems to be an intensification of the IR bands centered at 1416 and 1625 cm^{-1}, starting from 0.8 GPa. Every band in the spectrum is subjected to a broadening upon pressure application, and to a blue shift, except for the absorption related to the O-H groups, that tends to have a red shift and presents a broadening towards low frequencies, thus suggesting the strengthening of the H-bond. Above the hydrostatic limit for Ar ($\sim$ 10 GPa) [112], the structure of the absorption profile is progressively lost and the intensity of the infrared signal weakens. This deterioration of the IR spectrum is related to the appearance of cracks on the layers of GO, thus confirming the non-hydrostatic conditions, which prevented the acquisition of spectra below 9.6 GPa during the decompression. Only limited spectral changes are detected on compressing GO/Ar samples: during the compression, we observed an intensity decrease between 1500 and 1800 cm^{-1}, and an intensity increase between 900 and 1400 cm^{-1} up to 31 GPa. These effects are better appreciated in the comparison of the IR spectrum of GO/Ar sample recovered at ambient conditions with the IR spectrum of the starting GO (see figure 2.10, bottom panel, *a* traces). The difference indicates that the slight chemical modifications mainly involve the adsorbed water molecules, with an intensity decrease at 1620 cm^{-1} and in the O-H stretching region, whereas the intensity increase at about 1000 cm^{-1} suggests the formation of new C-O bonds on GO layers (figure 2.10, bottom panel, *b* trace).

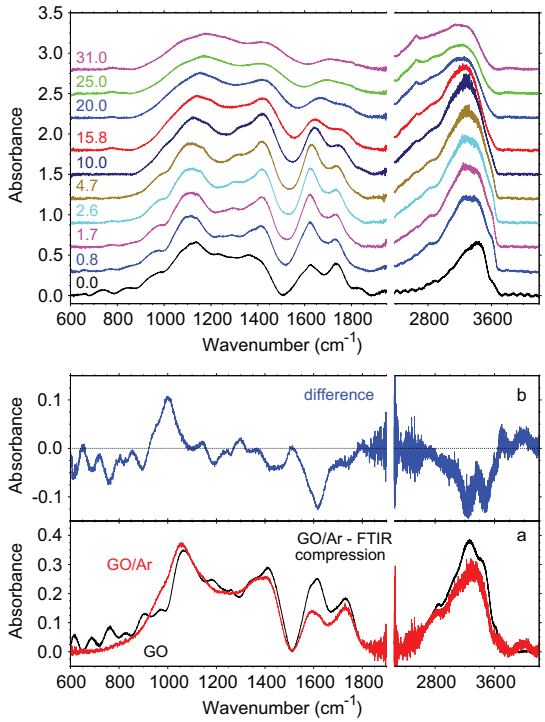

Figure 2.10: *Upper panel: evolution of FTIR spectra of GO/Ar with pressure. Spectra were vertically shifted for the sake of clarity. The wavenumber axis break excludes the frequency region where the saturating absorption of the diamond anvils occurs. Lower panel: (a) FTIR absorption spectra of the GO/Ar recovered sample (red) and of the starting GO (black) at room conditions; (b) difference between recovered GO/Ar and starting GO spectra.*

The Raman spectra of GO/Ar during room temperature compression up to 31 GPa and further decompression to ambient conditions are reported in figure 2.11 together with the pressure evolution of the frequencies for D, G and D' Raman bands.

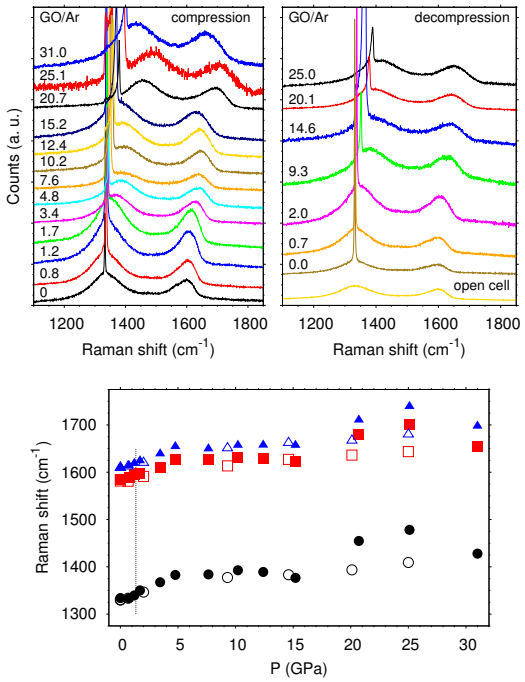

Figure 2.11: *Upper panels: Evolution of Raman spectra of GO/Ar during room temperature compression (left) and decompression (right). Lower panel: pressure dependence of the D (black circles), G (red squares) and D' (blue triangles) Raman bands of GO during compression (full symbols) and decompression (empty circles). The dotted line indicates the solidification pressure of Ar at room temperature.*

The Raman data show a continuous blue shift of the GO bands after the solidification pressure of Ar (1.3 GPa) [101] up to 6 GPa, where a flattening in their frequency occurs. Above 15 GPa, we observed an increase in the frequency of the three bands, that decrease again above 30 GPa. Even in the Raman spectrum, the profile deteriorates after the crystallization of Ar due to non-hydrostatic conditions, thus determining a bigger uncertainty in the frequency of the Raman bands. The I_D/I_G values remains substantially

unaffected after the compression/decompression run in respect to the starting values (3.4 after and 3.2 before).

The reactivity of GO/N_2 samples was studied by FTIR and Raman spectroscopy in two different experiments performed at 1.9 GPa and room temperature, where N_2 is liquid and the molecular insertion between the layers should be easier, at the same time providing sufficiently high density conditions for the reaction to occurs. In the first experiment, reactivity was induced by one-photon excitation of GO, using the 514.5 nm wavelength of an Ar ion laser source. In the second experiment, reactivity was induced by thermal activation of GO. In both the experiments, we used GO films of 10-20 μm thickness produced by drop-casting deposition for obtaining a good intensity transmission (evaluated by FTIR intensity signal). We found that irradiation with power higher than 100 mW and heating at more than 200°C systematically cause the loss of the infrared transmission signal.

In the first experiment, three irradiations of 100 mW and increasing duration (1, 3 and 5 hrs) were performed on GO/N_2 sample. In figure 2.12, the evolution of the FTIR spectra during the irradiation is reported (panel *a*), together with two magnifications (panels *b* and *d*) and the differential spectra after the different irradiations (panel *c*).

The FTIR spectra, acquired after each irradiation, suggest the occurrence of a chemical reactivity: the main feature is the appearance of two sharp bands at 664 and 2350 cm^{-1}, assigned to bending and antisymmetric stretching vibration of CO_2 growing with the irradiation time. A small amount of CO_2 was also present in the starting spectrum, acquired before the first irradiation (black trace in figure 2.12a), and it's probably the effect of the 647.1 nm laser line from a Kr ion laser used to excite the ruby fluorescence. Besides this two features, the differential spectra reported in figure 2.12c show a broad intensity increase between 800 and 1800 cm^{-1}, with peaks centered at 1240 and 1580 cm^{-1}. Furthermore, looking at figure 2.12d, the spectra clearly show the presence of two distinct components of the antisymmetric stretching mode of CO_2. In the experimental conditions

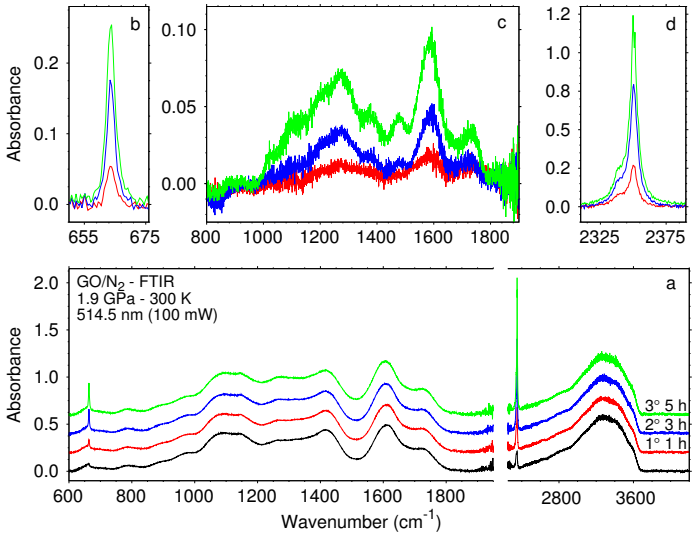

Figure 2.12: *FTIR spectra acquired on GO/N_2 sample during laser irradiation. Lower panel (a): FTIR spectra acquired at the beginning of the reaction (black trace) and after the three successive irradiations (λ=514.5 nm) of the same power (100 mW) and increasing duration (1, 3 and 5 hrs). Spectra were vertically shifted for the sake of clarity. The wavenumber axis break excludes the frequency region where the saturating absorption of the diamond anvils occurs. Upper panels: difference absorption spectra of the spectra acquired after the three irradiations with respect to the spectrum of the starting sample in the bending (b) and stretching (d) regions of CO_2 and in the characteristic absorption region of GO between 800 and 1900 cm^{-1}.*

(1.9 GPa and 300 K), CO_2 is stable in the solid phase I (Pa3), where only one component for the antisymmetric stretching band is expected. Therefore these two bands indicate that CO_2 experiences two different environments in the sample, with different interactions, and are assigned to bulk CO_2 and to CO_2 molecules trapped between the layers. More in detail, the high-frequency side of this composite band (2350.5 cm^{-1}), stronger and narrower, is assigned to bulk CO_2 [113,114], while the broad low-frequency one (2339.9 cm^{-1}) is likely due to the nanoconfined CO_2, trapped between the layers and exposed to several, different interactions with the functional groups of GO

decorating both sides of the interlayer spacing [115]. These interactions are responsible for the broadening and for the low-frequency shift of this band.

The Raman spectra acquired after the three irradiations do not exhibit appreciable changes. However, as for CO_2 in the infrared spectra, an asymmetric band shape of the N≡N stretching mode is observed in the spectra acquired on the top side of GO layer in contact with bulk N_2, compared to the spectra acquired on the bottom side, where a symmetric band shape is observed. The I_D/I_G value changes from 3.3 (at the beginning of the experiment) to 2.8 (at the end of the experiment).

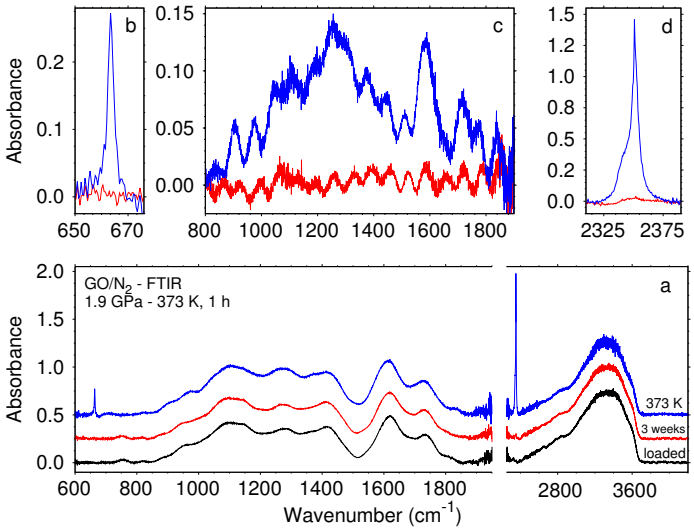

Figure 2.13: *FTIR spectra acquired on GO/N_2 sample during heating experiment. Lower panel (a): evolution of the FTIR spectra of GO/N_2 at 1.9 GPa before heating (black trace), after three weeks (red trace) and after the first heating (373 K, 1 h, blue trace). After the second heating (473 K, 1 h) no IR signal was detectable. The wavenumber axis break excludes the frequency region where the saturating absorption of the diamond anvils occurs. Upper panels: difference absorption spectra with respect to the spectrum of the starting sample in the bending (b) and stretching (d) regions of CO_2 and in the characteristic absorption region of GO between 800 and 1900 cm^{-1}.*

In the second experiment, the reactivity of GO/N_2 sample was induced

by performing two different heating of the same duration (373 K, 1 h and 473 K, 1 h) at the same pressure (1.9 GPa). Both infrared and Raman spectra are substantially identical to those obtained under irradiation. Figure 2.13 shows the FTIR spectra for this experiments. After the second heating (473 K, 1 h), the infrared signal was completely lost. A direct comparison between the difference absorption spectra of the photoirradiated and heated samples indicates a remarkably similar absorption profile (see figure 2.14), thus suggesting that the same reaction channel is accessed by both electronic and thermal excitation of GO.

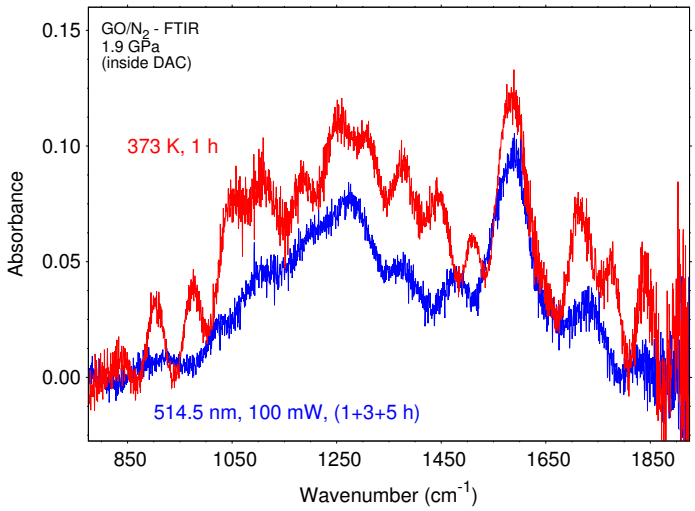

Figure 2.14: *Comparison of the FTIR difference absorption spectra in the 800-1800 cm^{-1} frequency range between the irradiated (blue) and heated (red) samples with respect to the spectra acquired before irradiation and heating at the same pressure (1.9 GPa).*

For the irradiated sample, an infrared spectrum of the recovered GO/N_2 could has been acquired at ambient conditions outside of DAC and compared with the same spectrum of the starting GO. The two spectra and the differential spectrum are reported in figure 2.15. The comparison clearly indicates a remarkably increase of the absorption intensity in the range between 800 and 1800 cm^{-1} and between 2300 and 3600 cm^{-1}.

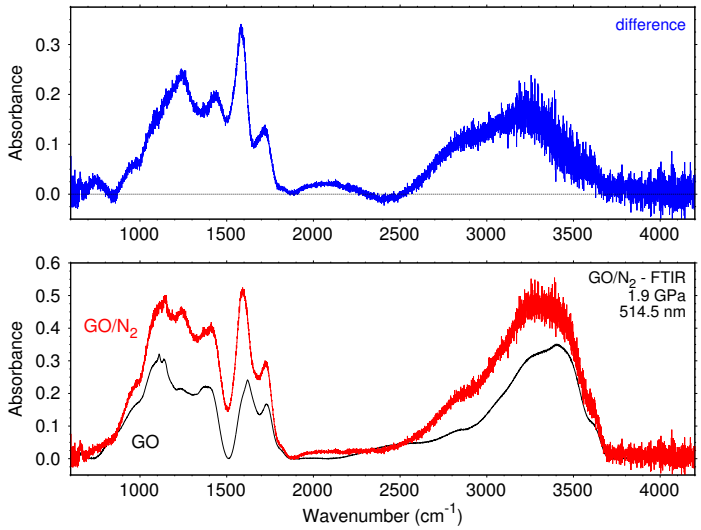

Figure 2.15: *FTIR absorption spectra on the recovered GO/N_2 sample after irradiation and on starting GO and their difference. Lower panel: FTIR absorption spectra of the starting GO before compression and irradiation (black trace) and of the GO/N_2 sample recovered after three irradiations with the same wavelength (λ = 514.5 nm), same power (100 mW) but increasing duration (1 h, 3 hrs, 5 hrs.). The spectra were acquired outside the DAC on a free standing gasket at room conditions. Upper panel: difference absorption spectra between the recovered GO/N_2 irradiated sample and the starting GO.*

The Raman spectra acquired during the thermal reaction are quite similar but, as in the case of the photoirradiated GO/N_2 sample, the I_D/I_G values after heating are slighlty lower than before (2.8 against 3.3, exactly as it was for the photo-induced reaction).

In the case of GO/NH_3, we have studied the high pressure reactivity of the system under static compression only and in combination with controlled photoirradiation, using the 514.5 nm wavelength in the solid phase IV of NH_3 (5.0 GPa) and the near-UV multiline emission centered at ∼350 nm in the liquid phase of NH_3 (0.5 GPa).

In the case of compression/decompression experiments, the high pressure behaviour of GO/NH_3 samples has been studied until 15.1 GPa (Raman)

and until 7 GPa (FTIR). This lower pressure value is related to the limitation imposed by the small sample thickness required for the acquisition of good FTIR spectra, which is responsible for a breaking of the GO sample at higher pressure, preventing further acquisitions. Figure 2.16 reports the FTIR absorption spectra acquired during compression and decompression on GO/NH_3 sample.

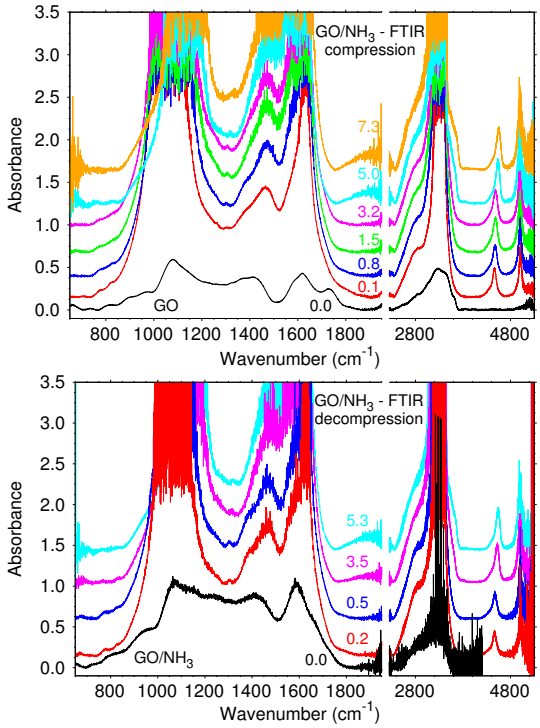

Figure 2.16: *FTIR absorption spectra acquired during compression (upper panel) up to 7.3 GPa and decompression (lower panel) to ambient pressure of a GO/NH_3 sample inside the DAC. Spectra were labeled with the corresponding pressure value. Ambient pressure spectra were acquired on GO before loading NH_3 and applying pressure (upper panel, compression, 0.0 GPa) and on the recovered sample after releasing the pressure (lower panel, decompression, 0.0 GPa.* Spectra were vertically shifted for the sake of clarity. The wavenumber axis break excludes the frequency region where the saturating absorption of the diamond anvils occurs.

The spectra are dominated by the saturating intensity of the fundamental

modes of NH_3, i.e. $\nu_2(A_1)$ at 1062 cm^{-1}, $\nu_4(E)$ at 1630 cm^{-1} and the unresolved $\nu_1(A_1)$ and $\nu_3(E)$ modes at $\sim$3310 cm^{-1}, whose intensity overwhelms the broad and weaker absorptions of GO, and by their combination modes, $\nu_2 + \nu_3$ at 4463 cm^{-1} and $\nu_3 + \nu_4$ at 5007 cm^{-1} [116]. In the comparison with the GO/N_2 samples, the reactive character of NH_3 towards GO is immediately evident even at the lowest applied pressure (0.1 GPa, after the loading), where a decrease in the intensity of the carbonyl bands of GO at $\sim$1740 cm^{-1} is registered, together with the appearance of two new absorptions at 1375 and 1470 cm^{-1}, intensifying and shifting to high frequency with increasing pressure, respectively assigned to (C=O)-O^- and NH_4^+ ions, and the intensification of the absorption between 2300 and 3000 cm^{-1}, on the lower frequency side of the intense N-H stretching region, suggesting the formation of H-bonds after loading of NH_3. No other features related to some kind of reactivity are visible during compression/decompression experiments, and no infrared spectral changes account for the phase transitions from liquid to plastic phase III (Fm3m) of NH_3 at 1.1 GPa [105, 106, 108, 109], whereas an evident high frequency shift and narrowing of the ν_2 mode of NH_3 and, consequently, also of the $\nu_2 + \nu_3$ combination mode, together with the appearance of absorption between 3500 and 3700 cm^{-1}, provide evidence for the phase transition from disordered crystal phase III to the ordered crystal phase IV of NH_3 ($P2_12_12_1$) [109], as visible in the spectrum acquired at 5.0 GPa. The behaviour of the GO/NH_3 sample is substantially reversible during decompression. After the complete releasing of pressure, the bands related to NH_3 and the two bands observed at 1375 and 1470 cm^{-1} are not observable anymore and the absorption profile of the recovered sample is remarkably different with respect to the starting GO. The decrease of the integrated area of the $\nu_2 + \nu_3$ combination mode of NH_3 during the compression/decompression cycle allows to estimate an overall 12% NH_3 consumption (comparison between the spectra acquired at 0.1 GPa in compression and 0.2 GPa in decompression), but the occurrence of chemical reactivity can be better appreciated by looking at the comparison between the infrared spectra of

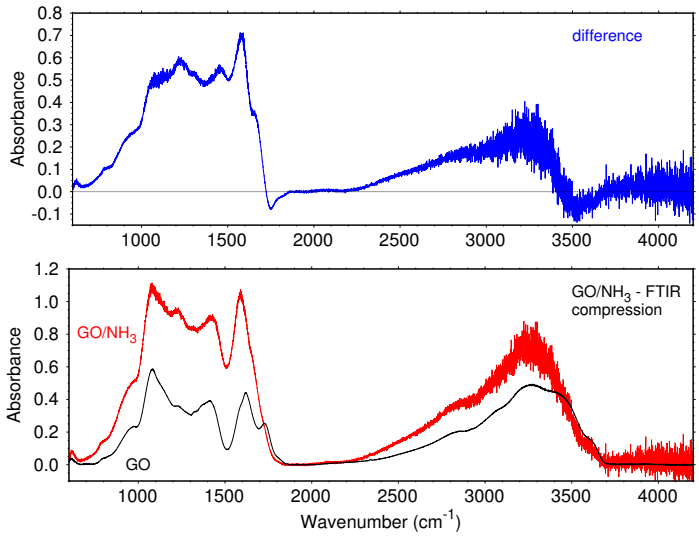

Figure 2.17: *FTIR absorption spectra on the recovered GO/NH_3 sample and starting GO and their difference. Lower panel: FTIR absorption spectra of the starting GO at ambient pressure (black trace) and of the recovered GO/NH_3 sample after compression and decompression (red trace). Upper panel: difference absorption spectrum between recovered GO/NH_3 sample and starting GO (red and black trace of lower panel). The Spectra on upper and lower panel were acquired outside the DAC.*

the recovered GO/NH_3 sample and of the starting GO.

In figure 2.17, the comparison between the infrared spectra of recovered GO/NH_3 and starting GO, and the related difference spectrum, are presented. As it was for GO/N_2 samples, the recovered GO after compression and decompression with NH_3 shows a strong intensity increase in the frequency range between 800 and 1900 cm^{-1} and between 2300 and 3500 cm^{-1}. Furthermore, in comparison to GO/N_2 samples, a sharp intensity drop is clearly observed at 1745 cm^{-1}, in the carbonyl stretching region.

In figure 2.18, the evolution of the Raman spectra in the region of the D, G and D' characteristic bands of GO is reported, together with the pressure evolution of their frequencies. Raman spectra have been measured up to 15.1 GPa and then during decompression to ambient conditions. No evident

changes, except for a frequency shift towards high frequency, can be appreciated, suggesting that the structure of GO is maintained upon compression. The bottom part of the figure shows the frequency evolution of the D, G and D' bands (fitted by Voigt profiles) upon compression (full symbols) and decompression (empty symbols). The points have a smooth and continuous increase during compression, and a reversible behaviour during decompression.

Exploiting photoirradiation to foster reactivity on GO/NH_3 sample, we have performed two experiments: a first one in the solid phase IV of NH_3, and a second one starting from the liquid phase of ammonia. As the first experiment is concerned, the reactivity of the GO/NH_3 system was induced at 5.0 GPa and room temperature, where NH_3 is stable in its solid phase IV, using the 514.5 nm wavelength of an Ar ion laser. This wavelength is one-photon (OP) absorbed by GO. Four irradiations of increasing duration and power have been performed on the GO/NH_3 sample compressed at 5.0 GPa: 100 mW per 1 h, 100 mW per 3 hrs, 300 mW per 1 h and, finally, 500 mW per 1 h. No higher power irradiation or longer duration could be performed without completely losing the infrared signal (always decreasing along these various steps) or irreversibly damaging the thin deposited GO layers. Figure 2.19 reports the sequence of infrared spectra acquired during the various stages of irradiation and, in its bottom part, the comparison between the spectrum of the recovered GO/NH_3 sample at the end of the experiment with respect to the starting GO, and the calculated absorption difference. Infrared spectra are dominated by the saturating absorption due to the modes of NH_3, all out-of-scale except for the combination modes. As in the case of the compression/decompression, the appearance of two new absorption at 1375 and 1470 cm^{-1} and the disappearance, at the same time, of the carbonyl band of GO (1740 cm^{-1}), can be appreciated. In contrast to the result for photoirradiation experiment on GO/N_2 sample, no CO_2 is observed to form. The results of this experiment are quite the same than those of the compression/decompression experiment, and this is confirmed

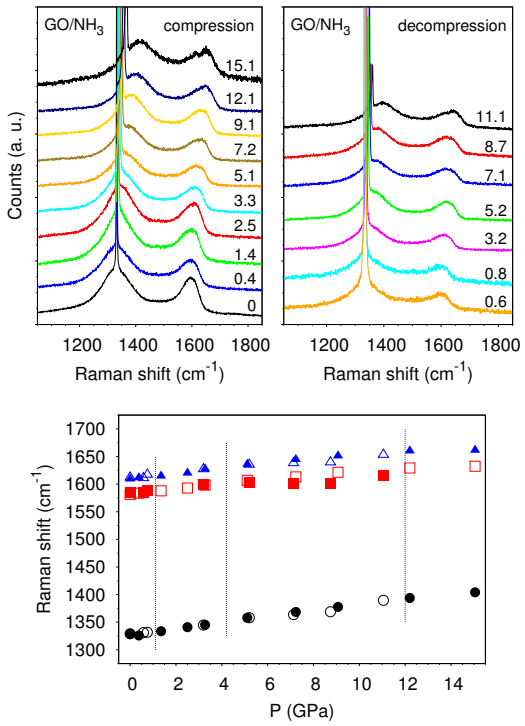

Figure 2.18: *Evolution of Raman spectra of GO/NH_3 during compression and decompression and pressure evolution of the frequency of D, G and D' Raman bands of GO. Upper panels: Raman spectra acquired on the GO/NH_3 sample during compression up to 15 GPa (left) and decompression (right) to ambient pressure. Peak at 1330 cm^{-1} is from the diamond anvils. Lower panel: pressure evolution of the frequency of D (circles), G (squares) and D' (triangles) Raman bands of GO during compression (full symbols) and decompression (empty symbols). The data were obtained by a fit of the Raman spectra using Voigt band profiles. The vertical, dotted lines correspond to the room temperature transition pressure of NH_3 from the liquid to the plastic phase III (1.1 GPa), from phase III to the ordered crystal phase IV (4.2 GPa) and from the phase IV to the phase V (12.0 GPa).*

by the constant value of the integrated area of the $\nu_2 + \nu_3$ combination mode of NH_3, before and after the irradiations, indicating the absence of NH_3 consumption during the experiment. Furthermore, the absorption spectrum of the recovered sample at ambient conditions closely reminds that of the GO/NH_3 samples recovered from compression/decompression, and the difference spectrum reveals an increase of the absorption intensity between 800 and 1700 cm^{-1} ($\sim$143%) and between 2300 and 3500 cm^{-1}, as it was in the experiment with only pressure. No appreciable differences are visible in the Raman spectra, acquired after each irradiation.

In a different reactivity experiment, a GO/NH_3 sample was irradiated at 0.5 GPa and room temperature, where NH_3 is in its liquid phase, using the UVML emission of an Ar ion laser centered at about 350 nm. Besides being one-photon (OP) absorbed by GO, this wavelength should be indeed two-photon (TP) absorbed by NH_3 itself [117, 118]. In figure 2.20a, the FTIR spectra acquired before and after two successive irradiations of the same power (100 mW) and increasing duration (30 mins, 1 h) are reported. In this case, the occurrence of photoinduced chemical reactivity can be appreciated from the absorption difference (figure 2.20b), obtained from the substraction of the spectrum acquired before starting to irradiate at 0.5 GPa from the spectrum acquired after the second irradiation at the same pressure. A systematic intensification can be observed between 1190 and 1300 cm^{-1}, at about 1375 cm^{-1}, between 1450 and 1600 cm^{-1}, between 1660 and 1715 cm^{-1} on both sides of the ν_4 band of NH_3, and between 2600 and 3600 cm^{-1}, in the region of the O-H and N-H vibrations. All these bands are compatible with the formation of single and double C-N bonds that can be obtained from the supposed reactivity of GO layers with the photodissociation products of NH_3 [117,118]. Besides of the increasing absorption intensity in these region, a weakening of the carbonyl bands of GO at $\sim$1740 cm^{-1} and of the fundamental and combination bands of NH_3 between 750 and 985 cm^{-1} (ν_2), between 1715 and 1900 cm^{-1} (ν_4) and at $\sim$4460 cm^{-1} ($\nu_2 + \nu_3$ combination band) is observed. The estimated consumption of NH_3 during the reaction

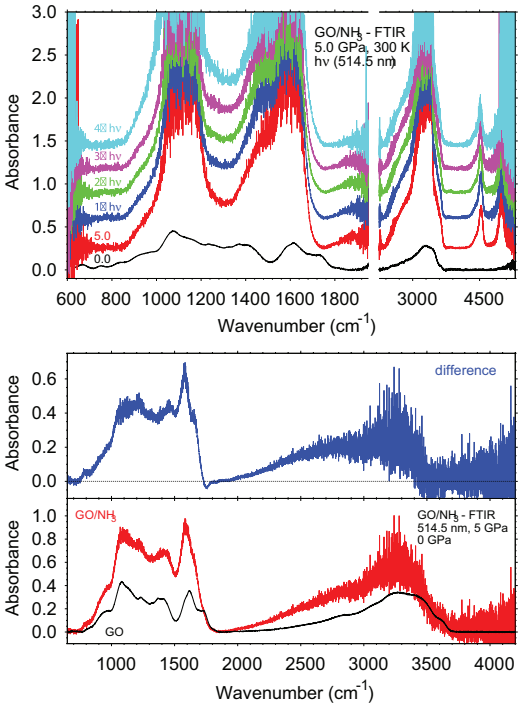

Figure 2.19: *Evolution of FTIR spectra of GO/NH_3 during VIS-photoirradiation in the solid phase IV of NH_3 (5.0 GPa, λ= 514.5 nm) and FTIR absorption spectra on the recovered GO/NH_3 sample and starting GO, and their difference. Upper panel: FTIR absorption spectra acquired on the starting GO at ambient pressure and on the GO/NH_3 sample at 5.0 GPa before irradiation and after each irradiation (blue trace: 100 mW, a h; green trace: 100 mW, 3 hrs; magenta trace: 300 mW, 1 h; cyan trace: 500 mW, 1 h) using the 514.5 nm wavelength emission of an Ar ion laser. Spectra were vertically shifted for the sake of clarity. The wavenumber axis break excludes the frequency region where the saturating absorption of the diamond anvils occurs. Lower panel: bottom part of the figure show the FTIR absorption spectra if the starting GO (black trace) and of the recovered GO/NH_3 sample (red) after the irradiation at ambient conditions outside the DAC; top part of the figure show the difference absorption spectrum obtained by subtracting the spectrum of the starting GO from the spectrum of the recovered sample.*

is about 4%. It's interesting to notice that the intensity of the band at 1470 cm^{-1}, assigned to NH_4^+ ions, doesn't change upon irradiation: this suggests that the proton donor sites on GO are fully deprotonated by the excess NH_3. Also in this case, as it was for the VIS-photoinduced reactivity on GO and solid NH_3, no CO_2 is formed during the reaction. The infrared spectrum of the recovered GO/NH_3 sample is quite different with respect to the other experiments (see figure 2.20c). The comparison between the spectra of the recovered GO/NH_3 sample and of the starting GO shows an intensity increase in the range 800-1600 cm^{-1} (+66%) with peak maxima at about 1240 and 1575 cm^{-1}, and an intensity decrease at 1740 cm^{-1} due to the consumption of carbonyl groups, while a strong intensity decrease is evident between 3300 and 3700 cm^{-1} (more evident on 2.20d). Raman spectra shows no appreciable profile changes for D, G and D' bands of GO.

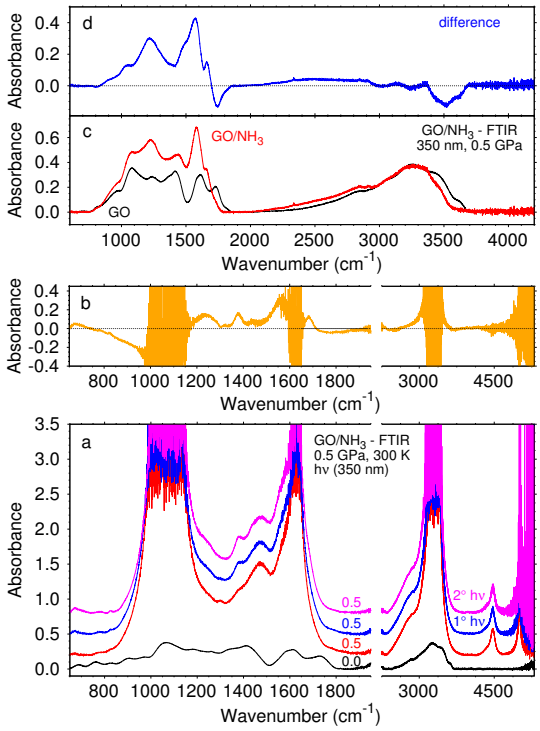

Figure 2.20: *Evolution of FTIR spectra of GO/NH_3 during UV-photoirradiation in the liquid phase of NH_3 (0.5 GPa, λ= 350 nm). (a) FTIR absorption spectra of GO at ambient conditions (black, before loading NH_3) and of the GO/NH_3 sample at 0.5 GPa before irradiation (red) and after two successive irradiation (30', blue; 1 h, magenta) with the same power (50 mW). Spectra were vertically shifted for the sake of clarity. The wavenumber axis break excludes the frequency region where the saturating absorption of the diamond anvils occurs. (b) Difference absorption spectrum obtained by subtracting the red spectrum from the magenta spectrum in figure (a). (c) FTIR absorption spectra of the starting GO sample before loading NH_3 (black) and of the GO/NH_3 sample recovered after the irradiations (red). (d) Difference absorption spectrum obtained by subtracting the spectrum of the starting GO from the spectrum of the recovered sample.*

2.3.2 Reactivity overview

A rapid overview of the results previously described allows to enlight the different features in the reactivity of GO with different simple molecules, differences related to the conditions (pressure, temperature, photoirradiation, heating) and to the molecular systems used as reactants. The samples of GO/Ar and of GO/N_2, studied only with pressure in compression/decompression FTIR (GO/Ar), Raman (GO/Ar and GO/N_2) and XRD (GO/Ar and GO/N_2) experiments, have substantially shown the high pressure stability of GO in the presence of inert systems, extending the literature range which was limited to 8 GPa [119], where a methanol:ethanol (4:1) mixture, which is not chemically or structurally inert towards GO, was used as a compression medium [96], up to a maximum of 31 GPa.

Differently from the simple pressure application, irradiation and heating have been probed to be effective in inducing a reactivity on GO/N_2 mixtures. The FTIR spectra acquired on recovered GO/N_2 samples from both irradiation (1.9 GPa, 5145. nm) and heating (1.9 GPa, 200°C) experiment are quite similar, suggesting the obtainment of really similar products in the two cases. The most evident feature of this reactivity is the appearance of CO_2 related absorption bands, suggesting the decomposition of GO and, accordingly, an increasing of the C:O ratio. The appearance of CO_2 is a typical feature of thermal exfoliation and reduction of GO [120]. The process involves the decomposition of the O-bearing functional groups of GO and the release of CO_2 associated with bond breaking and reconstruction in the basal plane of GO due to the removal of C atoms [121]. The high temperature decomposition mechanism is known to be influenced by the presence of water trapped within the layers [92, 122], and the presence of N_2 or NH_3 in high density conditions has been reported to be effective towards the N-doping of GO during thermal reduction [94].

In the case of the visible irradiation (514.5 nm), the wavelength could be one-photon absorbed by GO, whic has small non negligible absorbance at this wavelength [123], whereas it is not absorbed neither by N_2 nor by

adsorbed water, even through two-photon absorption mechanism. Moreover, the infrared data show the same reaction products both from irradiation and heating, thus suggesting that the electronic transition to the LUMO of GO give rise to the same reaction products as the thermal excitation of the low-frequency vibrational modes.

Ambient pressure studies at temperature values comparable with those used in our studies show a completely different reactivity, largely characterized by the formation of H_2 and CO as main products [92]: in our samples, molecular hydrogen and carbon monoxide have never been detected, and this is not surprising because high pressure conditions can drive chemical reactivity to completely different reaction paths. The reactive enviromnment of our samples, in which dense N_2, trapped between the layers, is found to be very near to those C sites where CO_2 elimination occurs, make highly probable that N_2 itself could be involved in bond reconstruction, as reported in a recent high-pressure study using the same 514.5 nm wavelength [124]. The evolution of the difference absorption spectra during irradiation and heating shows a continuous increase of CO_2 associated with an absorption increase between 800 and 1800 cm^{-1} ($\sim$84%), with higher intensity at 1200 and 1300 cm^{-1}, and at 1585 cm^{-1}. These spectral features are consistent with the insertion of N atoms in extended sp^2 carbon network with the formation of C-N bonds [124,125]. Furthermore, the I_D/I_G ratio values for irradiated and heated GO/N_2 samples significantly decrease, consistently with the release of CO_2 and strengthening the idea of a simultaneous reduction/N-doping of the GO basal planes.

Taking into account NH_3, that is known to interact with the oxygenated functional groups of GO, it should be considered that the presence of adsorbed water on GO and the application of pressure have been proved to be effective in ehnancing the interaction between GO and gaseous NH_3 [84,111,126,127]. NH_3 is a nucleophilic Lewis base, known to attack electron-poor carbon atoms of carbonyl, carboxyl and epoxy groups, besides of having a basic character according to Brønsted, thus tending to deprotonate the al-

cohol and carboxyl groups, generating NH_4^+ and corresponding anions. The reactivity of GO/NH_3 samples is immediately evident with respect to that of GO/N_2, due to this inherent characteristic of ammonia. Some spectral changes are immediately visible (the decreasing in the intensity of the carbonyl stretching region of GO at 1740 cm^{-1} and the appearance of two new bands at 1375 and 1470 cm^{-1}), whereas some others can be appreciated only by comparing the spectra of the recovered sample with that of the starting GO (i.e. the absorption increase at 1670 cm^{-1}, see figure 2.20). Anyway, all these spectral changes are compatible with the conversion of -COOH groups into amide (-CO-NH_2) and ammonium carboxylate ($[NH_4^+][RCOO^-]$) groups and with the formation of amino groups. The formation of amide groups is consistent with the absorption at 1670 cm^{-1}. The band at 1470 cm^{-1} can be assigned to the bending of NH_4^+ (ν_4), whose other absorptions (ν_2 at 1669 cm^{-1}, ν_1 at 3250 cm^{-1} and ν_3 at 3280 cm^{-1}) are covered by the out-of-scale absorptions of NH_3 [128]. The band at 1375 cm^{-1} is compatible with the modes of carboxylate ions, tertiary alcohols (R_3-C-OH) and furthermore with the presence of C-N bonds in amines (-NH_2), likely generated by epoxy ring opening on the GO surface due to nucleophilic attack of NH_3, and in amides. This assignment is in good agreement with the complete absence of CO_2 spectral signatures for the various GO/NH_3 samples with respect to the GO/N_2 ones: the carbonyl groups of GO are indeed chemically converted or stabilized after reacting with NH_3. Furthermore, this assignment also accounts for the constant intensity of the NH_4^+ band at 1470 cm^{-1} during the irradiation with the 350 nm wavelength at 0.5 GPa. The fact that CO_2 is completely absent from the reaction products directly implies that a different reactive process takes place for the GO/NH_3 samples if compared to the GO/N_2 ones.

The fact that NH_3 saturates and stabilizes the oxygenated functional groups of GO also accounts for the very similar spectra of the GO/NH_3 samples recovered after compression/decompression and after irradiation at 5.0 GPa in the ammonia solid phase IV using the 514.5 nm wavelength. For

these two samples, the absorption profile between 1000 and 1600 cm^{-1} closely reminds that of GO/N_2 sample recovered from the irradiation (514.5 nm) and heating (200°C) at 1.9 GPa, except for the different intensities: this suggests that under high pressure conditions the inherent chemical reactivity of NH_3 towards the oxygenated functions of GO is able to modify the structure of GO in such a way that the absorption of the 514.5 nm wavelength by GO does not further affect it.

The irradiation of GO in the presence of liquid NH_3 at 0.5 GPa, using UV wavelengths (350 nm), shows a completely different reactive behaviour (see figure 2.20). The dissociation of NH_3 by two-photon absorption mechanism [117, 118, 129] into $\dot{N}H_2$ and H excited fragments suggests the formation of C-N bonds and amine groups. The recovered spectrum of the GO/NH_3 samples irradiated with 350 nm wavelength are reamarkably different from those of the other GO/NH_3 and GO/N_2 samples. In particular, in UV-photoirradiated GO/NH_3 a larger consumption of carbonyl groups is osberved, together with a higher absorption intensity at 1240 cm^{-1} and 1575 cm^{-1}, a frequency shift of the band at 1585 cm^{-1} and an intensity decrease in the O-H and N-H stretching region (3300-3700 cm^{-1}). This last observation suggests that, besides NH_3, also GO and the adsorbed water are involved in the reaction and are possibly excited by the near-UV radiation, respectively one-photon and two-photon, with this latter generating H and OH excited fragments [34, 35, 130]. The I_D/I_G ratio values, as obtained from the Raman spectra, show an increase in the recovered sample with respect to the starting GO, thus supporting the formation of sp^3 hybridized carbon atoms in the GO layers due to the reactivity with NH_3. Anyway, the reactivity does not affect the persistence and stability of the GO layered structure, as confirmed both by the Raman spectra (the profile signature are always maintained during the whole experiments) and the XRD data (see figures 2.7, 2.8 and 2.9).

The disordered character of GO layers makes it difficult to exaustively assign the IR vibrational spectra of the recovered GO/N_2 and GO/NH_3 samples in terms of group frequencies or local vibrational modes. In addition, the

spectra for the recovered GO/NH_3 product are also largely different from those reported in the literature, referring to GO treated with gaseous NH_3 at ambient pressure [131], and cannot be interpreted only in terms of different oxidation level and relative amount of C:H:O due to the CO_2 removal. In the perspective of a rationalization of the experimental results, the infrared spectra of the recovered GO/N_2 and GO/NH_3 samples have been compared to those of amorphous products recovered from high pressure reactivity of benzene (C_6H_6) [52], containing only C and H atoms, furan (C_4H_4O) [132], containing C, H and O atoms, and *s*-triazine ($C_3H_3N_3$) [133], containing C, H and N atoms. This comparison is reported in figure 2.21.

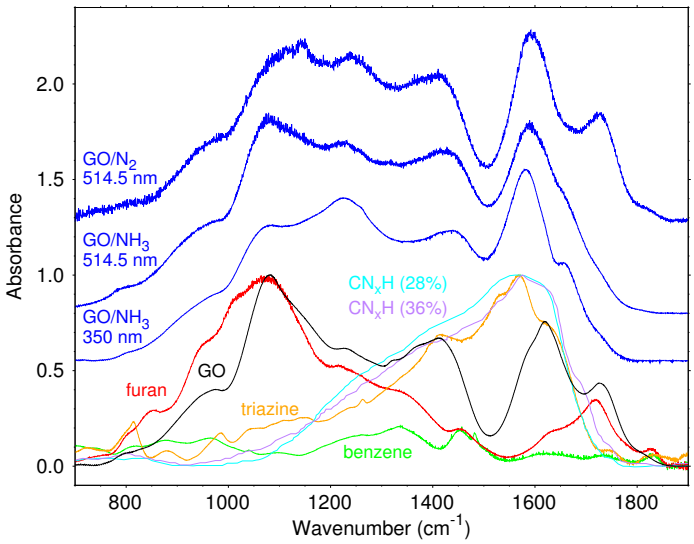

Figure 2.21: *Comparison among the infrared absorption spectra of GO/N_2 (1.9 GPa, 514.5 nm) and GO/NH_3 (5.0 GPa, 514.5 nm; 0.5 GPa, 350 nm) irradiated recovered samples (blue) with respect to starting GO (black) and to the recovered samples of high pressure reactivity of benzene [52] (green), furan [132] (red), s-triazine [133] (orange) and variously composed amorphous hydrogenated carbon nitrides (CN_xH: $x = 28\%$, cyan; $x = 36\%$, purple) adapted from the literature [125]. The spectra were rescaled with respect to their highest absorbance. The spectra for GO/N_2 and GO/NH_3 were vertically translated for the sake of clarity.*

The comparison reports the infrared absorption spectra of the reaction

products recovered from the photoinduced reactivity of GO/N_2 at 1.9 GPa (λ= 514.5 nm), GO/NH_3 at 5.0 GPa (λ= 514.5 nm) and GO/NH_3 at 0.5 GPa (λ= 350 nm) together with the spectrum of the starting GO at ambient conditions and with the spectra of the high pressure reaction products recovered from benzene, furan, s-triazine and variously composed amorphous hydrogenated carbon nitrides (general formula CN_xH). The interesting spectral range between 700 and 1900 cm^{-1} is shown, and each spectrum was normalized to its strongest absorption band.

The infrared spectrum of the recovered sample from the high pressure reaction of benzene, corresponding to an amorphous C:H framework, has its highest absorption between 1200 and 1500 cm^{-1}. Introducing an O atoms (i.e., the recovered sample from the high pressure reaction of furan) determines a consistent intensity increase on the low frequency side of the absorption profile, whereas the introduction of N atoms (i.e., the recovered sample from the high pressure reaction of *s*-triazine) is responsible for an intensity increase on the high frequency side. The spectrum of furan closely reminds that of GO, because of the oxygenated functions present on the two materials, while the recovered spectra from the GO/N_2 and GO/NH_3 photoinduced reactivity experiments show a strongest absorption exactly on the high frequency side of the absorption profile, where *s*-triazine has its "maximum". This is exactly the same frequency range where hydrogenated amorphous carbon nitride (CN_xH), containing C-N and C=N bonds, show their highest absorption value [134]. The comparison clearly shows how the intensity distribution in the spectra of the recovered GO/N_2 and GO/NH_3 samples, peaked on the high frequency side of the absorption profile, can be rationalized through the comparison with the spectra of N-containing systems, thus supporting the incorporation of N atoms into the framework of GO. Furthermore, the intensity increase in the frequency range 800-1600 cm^{-1}, that was observed in all the GO/N_2 and GO/NH_3 samples, has been related to the incorporation of N atoms in pure and hydrogenated amorphous carbon nitride, with an increase of sp^2 carbon content [125], and, in our case, would likely be related to the

incorporation of N into the GO layers. Also the 1270 cm^{-1} intense peak, that is present in the recovered GO/NH_3 sample from UV-photoirradiation at 0.5 GPa but it's not visible in the recovered products of benzene, furan and *s*-triazine, can be compatible with the broad absoprtion centered at about 1250 cm^{-1} in the spectrum of amorphous carbon nitride [125] and likely related to the formation of C-N bonds upon the attack of GO by the photodissociation products of NH_3.

2.4 High pressure polymerization of ethylene in GO

Besides of N-doping of GO layers, another intriguing topic regards the possibility to synthesize new hybrid layered nanocomposite materials with strong directional properties (for instance, a systems made up of alternating conductive and insulating layers) using only physical tools. In this perspective, we have focused on the possibility to induce the polymerization of ethylene between the layers of GO, exploiting the effect of spatial confinement in order to obtain an ordered nanocomposite layered material with specific characteristics.

The structural and chemical changes of ethylene have been investigated in a quite broad range of P and T. In particular, the polymerization under high pressure conditions has been studied both from the liquid phase, in conjunction with UV-photoirradiation [7], and from the solid phase, for effect of the pressure only [8]. The relatively mild pressure/irradiation conditions required to perform the ethylene polymerization allowed to desing and realize an apparatus suitable for extending this synthesis to larger volumes [12]. In order to have the maximum mobility of the monomer molecules, so to favour the insertion between the layers, it was mandatory to perform the synthesis of the new hybrid GO/polyEt nanocomposite starting from the liquid phase of ethylene. Because of the impossibility to perform an *in situ* laser irradiation of the sample on the high pressure beamline where we conducted the pre-

liminary experiments on GO/Et mixtures, it has been necessary to find the correct P,T conditions to perform a high pressure, high temperature spontaneous polymerization of ethylene. For this reason, we performed several preliminary high temperature experiments on fluid ethylene in the perspective of finding the better conditions to synthesize a good quality polymer using only pressure and temperature. In the following section 2.4.1, the high pressure, high temperature experiments on ethylene polymerization will be described.

As a preliminary work, several samples of GO loaded with ethylene was studied. The loading of ethylene was performed both using *Spray loading* technique and simple *Cryo loading* method (-30°C, ∼30 bar of ethylene), see chapter 4.2. GO was loaded both as a thin layer, through drop cast deposition, and as a powder (mainly for XRD experiments). Ethylene polymerization has been performed exploiting only pressure ($P \geq 5$ GPa, starting from solid phase I of ethylene); the joint effect of pressure and mild UV irradiation (0.5 GPa and few mW of the 350 nm wavelength emission of an Ar ion laser, starting from the liquid phase of ethylene); and in the fluid at the high pressure, high temperature conditions described later (1.5 GPa, 423 K). The samples have been investigated by FTIR and Raman spectroscopy, both during the reaction and once released the pressure, and by means of XRD, exploiting the high spatial resolution provided by synchrotron radiation facilities (ESRF, Grenoble). As a preliminary result, we have measured an EOS of the hybrid GO/polyEt nanocomposite material, during a room temperature compression; we have performed XRD studies during high pressure, high temperature polymerization experiments; and we have characterized the recovered sample with Raman spectroscopy. We have found some interesting results, but the data are still under elaboration.

2.4.1 High pressure, high temperature polymerization of ethylene

Polyethylene (polyEt) is probably the most important synthetic polymer. The typical industrial synthesis of polyethylene make use of catalysts and radical initiators, along with high temperature or high pressure conditions in the gas phase or in solution [135]. In this framework, the possibility to synthesize polyethylene from its constituent monomer exploiting only physical tools such as pressure, temperature or laser irradiation is incredibly appealing even in terms of *Green Chemistry*. The technological applications of polyethylene range from medical prosthesis to high-tech fibers, from plastic manifacturing to packaging. The main reason for this incredible variety of possible applications has to be found in the possibility of tuning the mechanical properties of this material by changing its degree of cristallinity, according to the fact that polyethylene is classified by its density and branching: higher the density, higher the cristallinity and more efficient the packing of linear unbranched chains [136]. Another important parameter is the molecular weight: ultrahigh molecular weight (UHMW) polyethylene is an incredibly tough material even though its density is slightly lower than in the more crystalline high molecular weight (HMW) polymer.

Below 10 GPa, the high pressure behaviour of ethylene is well known: in figure 2.22, the phase diagram of ethylene is reported. The characterization of the ethylene phase diagram has been conducted at high pressure by means of NMR (0-2.5 kbar, 100-140 K) [137], isochoric (up to 2.3 GPa and 322 K) [138] and differential scanning calorimetry (up to 2.3 GPa and 300 K) [139]. Two solid phases have been investigated. For pressure and temperature lower than 468 bar and 110.36 K, liquid ethylene solidifies in ordered crystal phase I (monoclinic, space group $P2_2/n$ and two molecules per unit cell), while increasing pressure above 110.36 K ethylene crystallizes in another solid phase, indicated as phase II (plastic phase, characterized by orientational disorder, structure assigned to space group I_{m3m}). At room temperature, the plastic phase II is obtained for compression above 1.9 GPa, while ordered phase I

is obtained upon further compression up to 2.9 GPa [8]. Phase transition between phase II and the ordered crystal phase I has been characterized by FTIR spectroscopy upon the observation of Davydov splittings for most of the modes and upon the frequency discontinuities measured at the transition [8]. On the other hand, the phase transition between fluid ethylene and its disordered-solid phase II has been detected by the frequency discontinuity and the slope change observed in the pressure shift of bending mode of ethylene [8].

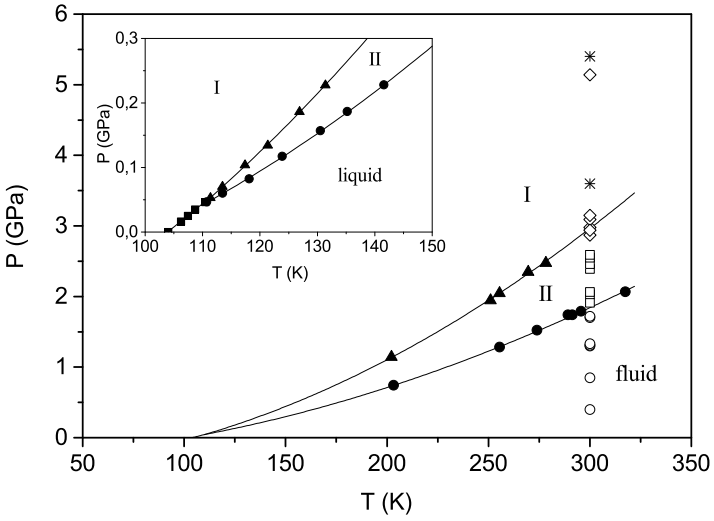

Figure 2.22: *Phase diagram of ethylene. Full symbols indicate the phase boundaries [137–139]. Empty symbols indicate the p,T conditions where ethylene has been studied in ref. [8]. The stars identify the p,T conditions where the polymerization has been studied in ref. [8].*

The occurrence of a spontaneous polymerization in bulk ethylene was first reported at 322 K and 2.3 GPa by Wieldraaijer *et al.* [138]. More recently, the pressure threshold for induced polymerization at room temperature has been studied both in the crystal phase I, at pressure larger than 3 GPa [8], and in the fluid ethylene under near UV irradiation [7]. These last studies allowed to gain important insight about the mechanism of the reac-

tion, and particularly about the relation between the reaction coordinate and the electronic structure of the molecule, in the laser induced reaction, and the crystal structure in the purely pressure induced process. Furthermore, the conditions for the attainment of a polymer with remarkable structural and mechanical characteristics were established. The appeal of a synthetic approach where no solvents, catalysts or radical initiatior are employed stimulated the extension of the high pressure photoinduced synthesis in the fluid to larger volume through the realization of a specifically designed laboratory reactor, described in ref. [12].

The very first studies about purely temperature/pressure or photochemical initiation in a homogeneous ethylene phase were conducted by Buback (between 453 and 523 K, pressure about 0.2 GPa) [140, 141]. Despite the high pressure capability of tuning the reactivity of pure ethylene in the fluid phase, the instability boundaries were not characterized and only a upper limit of 450 K at 0.3 GPa was found while measuring the equation of state of ethylene [142]. Of course, temperature is known to have a relevant effect in producing high quality crystalline polymers, but a deeper knowledge of the instability boundaries would allow to better understand if purely pressure induced reactions can be exploited with current technologies and which are the expected characteristics of the synthesized polymer. Other important informations that could be obtained are about the reaction mechanisms and would allow to span light on how the relevant thermodynamic parameters are modified by pressure.

The instability threshold of fluid ethylene were studied along quasi-isobaric heating cycles, monitoring the appearance of the characteristic absorption bands of the polymer in the infrared spectra. FTIR spectroscopy was used also to check the quality of the sample before setting the initial pressure for the experiments. All ethylene samples were loaded by *Cryo Loading* technique at -30°C and 30 bar of inlet gaseous ethylene. Initial loading pressure was low (0.1-0.5 GPa). Three samples were heated quasi-isobarically at initial pressures of 0.4, 0.8 and 1.4 GPa. Figure 2.23 reports the spectrum of

fluid ethylene and the polymer bands appearing during the heating.

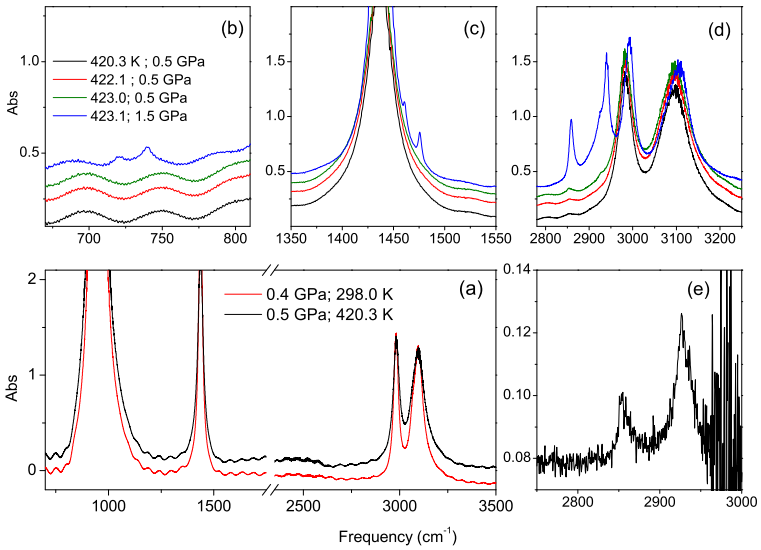

Figure 2.23: *Panel (a): comparison between the FTIR absorption spectra of fluid ethylene along the quasi-isobaric heating experiment performed at 0.4-0.5 GPa at two different temperatures (298.0 K, red curve; 420.3 K, black curve). Panel (b)-(d): FTIR absorption spectra showing the appearance of polyethylene characteristic bands and their intensification with pressure in the regions of CH_2 bending (b), CH_2 rocking (c) and CH stetching (d). Panel (e): difference spectrum in the CH stretching region between the spectra measured at 0.5 GPa at 423 K and 422.1 K, stating the onset of the reaction.*

The spectrum of fluid ethylene is dominated by an out-of-scale absorption at about 950 cm^{-1}, assigned to the ν_7 mode of CH_2 waggins, and three other strong absorption centered at 1437 cm^{-1} (ν_{12}, CH_2 bending), 2982 cm^{-1} (ν_{11}, CH stretching) and 3097 cm^{-1} (ν_9, CH stretching). The heating was performed in 5°C degrees step, measuring a spectrum for each step. The onset of the polymerization reaction was identified through the appearance of the characteristic polymer bands, shown in the panel (b), (c), (d) and (e) of figure 2.23. These bands are the sharp doublet between 2850 and 3000 cm^{-1}, whose high frequency component has an asymmetric shape, assigned

to the CH stretching of saturated carbon atoms, see figure 2.23d and e; the doublet at about 1470 cm^{-1}, on the high frequency side of the ν_{12} band of pure ethylene, assigned to CH_2 bending modes, see figure 2.23b; and the doublet in the region between 700 and 750 cm^{-1}, assigned to CH_2 rocking, see figure 2.23c. These two last doublets appear in an advanced phase of the polymerization, in respect to the stretching bands.

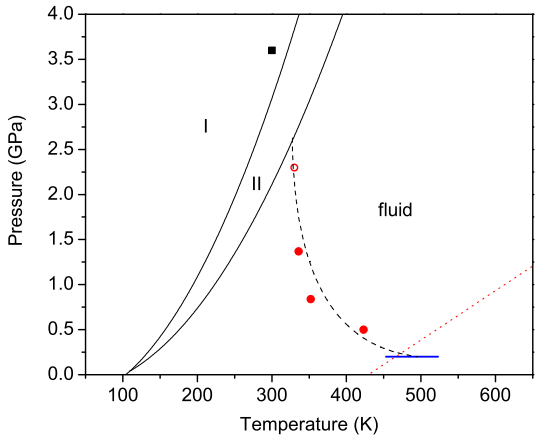

Figure 2.24: *Phase diagram of ethylene and stability boundary of fluid versus the polymerization reaction. Phase I refers to the monoclinic, solid phase of ethylene (space group P21/n, 2 molecules per unit cell) [143], phase II to plastic crystal phase, characterized by orientational disorder (space group I_{m3m}) [143, 144]. The black, full square is the ambient polymerization pressure threshold in solid phase I [8]. The empty red dot is related to the reaction threshold observed in the isochoric measurements of ref. [138, 139], whereas full red dots represent the thresholds measured in the present work. The dashed line across these points is a guide for the eyes, while the blue line indicates the regione where the reaction were studied by Buback at 0.2 GPa [140, 141]. The red dotted line represents the melting line of orthorhombic polyethylene.*

Figure 2.24 reports the onset of the polymerization reaction measured in this way at the three different pressures (0.4, 0.8 and 1.4 GPa) together with other available literature data. The stability boundary of the fluid versus the

polymerization reaction lies well within the P,T region where the polymer is in its stable orthorhombic crystal phase (space group Pnam, two polymeric chains per unit cell). Once it is formed, polyethylene directly crystallizes from the bulk, fluid ethylene. The only exception is for the low pressure region explored by Buback, see ref. [140], where the instability boundary crosses the melting line of polyethylene so that a coexisting, homogeneous liquid phase of both monomer and polymer is expected.

Once the onset of the reaction was identified, the pressure of the sample was rapidly increased to 1.5 GPa where FTIR spectra as a function of time at constant P,T conditions were measured. The reaction kinetics has been studied by measuring the integrated area of the CH bending mode of the polymer as a function of time. The fit was performed using pseudo Voigt band shape to reproduce the absorption profile. Time evolution of integrated area was fitted according to the Avrami model [145–147], originally developed to reproduce crystal growth from a liquid phase and later extended to the study of diffusion controlled solid-state reactions. The general formulation for the Avrami model is given by

$$\frac{A_t}{A_\infty} = 1 - e^{[k(t-t_0)]^n} \tag{2.1}$$

where A_t and A_∞ are the band intensities at the time t and at the end of the reaction; t_0 is the initial time, related to the nucleation step; k is the rate constant and n is a parameter related to the dimensionality of the growth process. Figure 2.25 reports the data collected at 423 K, 1.5 GPa together with the best fit using equation 2.1. k and n values used in the fit for the three kinetics are reported in table 2.1. The reaction rate increases with temperature, while the n values are always smaller than 1, thus suggesting unidimensional diffusion controlled growth of the polymeric chains.

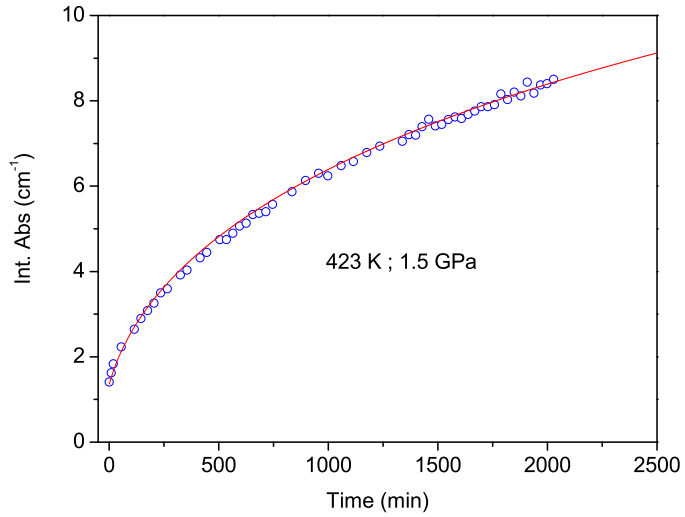

Figure 2.25: *Time evolution of the integrated absorption of CH_2 bending modes of polyethylene at 1476 cm^{-1} measured at 423 K and 1.5 GPa. The evolution has been reproduced according to equation 2.1.*

Temperature, K	***k***	***n***
354	0.002	0.92
414	0.010	0.76
423	0.012	0.50

Table 2.1: *Rate constant and n parameter values as obtained by the fit using equation 2.1 of the time evolution of the integrated absorption of the polymer CH bending modes at 1.5 GPa and the indicated temperature.*

The quality of the product was checked using AD-XRD, FTIR and Raman spectroscopy. Both the vibrational spectra and XRD patterns of the three polymers synthesized at different temperatures are indistinguishable. Figure 2.26 reports the relevant regions of the infrared spectrum of polyethylene recovered at ambient conditions after the synthesis at 423 K and 1.5 GPa.

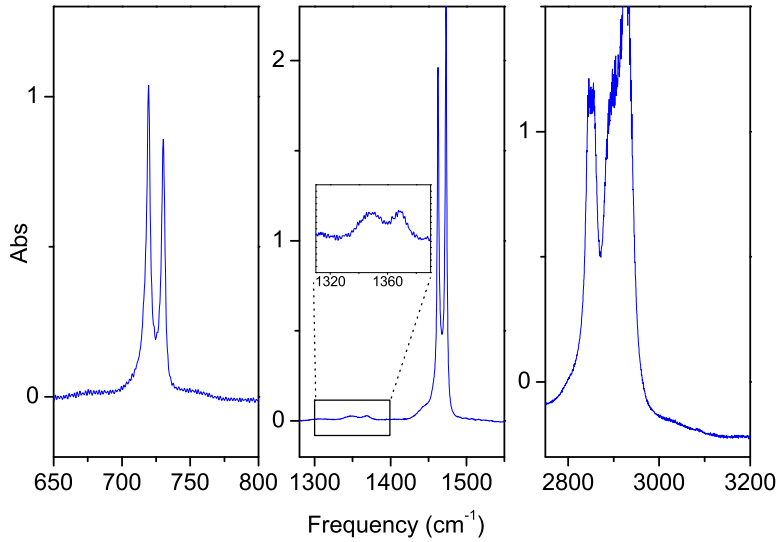

Figure 2.26: *Selected spectral regions of the IR absorption spectrum of recovered polyethylene at ambient conditions. The Davydov components of the CH_2 rocking and bending modes are shown in the left and in the central panel. In the central panel, the inset reports a magnification of the frequency region between 1300 and 1400 cm^{-1}, where the characteristic absorptions of gauche defects, branching and terminations are located. The right panel shows the CH stretching region.*

The two doublets centered at 725 and 1470 cm^{-1} (CH_2 rocking and bending) characterize the ordered crystal, being fully resolved only in high-density polymers. A notable feature is the extremely weak intensity of the absorption bands in the region between 1250 and 1440 cm^{-1} (see inset in figure 2.26, central panel). These absorptions originate from gauche defects, branching and terminations, and are weak when the cristallinity of the polymer is high [148, 149] as in the present case. In addition, no bands related to methyl groups (umbrella modes) are visible, thus excluding a great number of terminations and suggesting a considerable length of the chains. This latter issue is also supported by the lack of absorptions related to CH stretching of sp^2 carbon (see right panel).

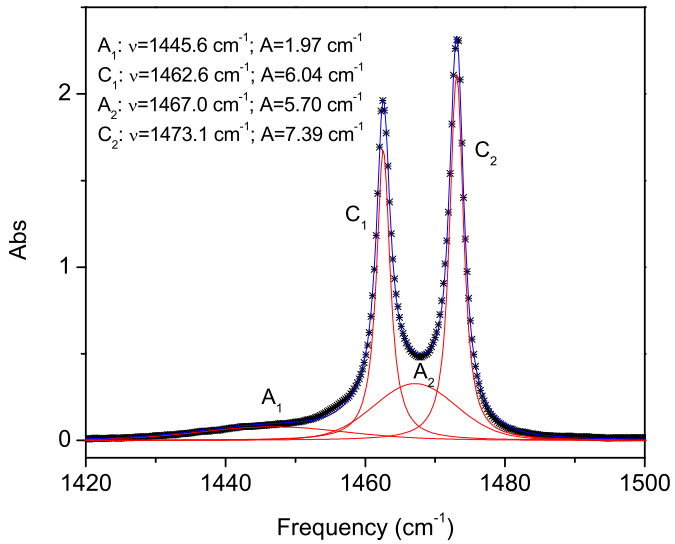

Figure 2.27: *Spectral deconvolution of the CH_2 bending absorption region of polyethylene. C_1 and C_2 refer to the orthorhombic crystal components; A_1 and A_2, particularly broad and weak, account for the amorphous fraction. Peak frequencies and integrated area from the fit are also reported.*

Important informations can be gained from the analysis of the doublet at 1462.6 and 1473.1 cm^{-1}. Figure 2.27 reports the spectral region of this doublet together with the fit, made using four pseudo Voigt bands. In the oriented gas approximation [150], the intensity ratio between these two crystal components should be 1.2333 to have a perfect orthorhombic crystal composed by *trans*-planar chains [148]. Besides the two crystal components, indicated as C_1 and C_2, two other broad bands centered at 1445.6 cm^{-1} and 1467.0 cm^{-1}, due to the amorphous fraction of polymer, and indicated as A_1 and A_2, are always present in the spectra of polyethylene, even if in the present case they are really weak with respect to the crystal components, thus attesting the high crystallinity of the polymer. The intensity ratio between C_1 and C_2 is calculated to be 1.224, really close to the expected value for an ideal crystal.

The Raman spectrum of the polymer synthesized at high temperature is

compared in figure 2.28 with those of commercial low density (LDPE) and high density (HDPE) polymers. Broad bands between 1060 and 1100 cm^{-1} and between 1300 and 1330 cm^{-1}, observable in LDPE and related to the disruption of the long range order due to branching and gauche defects, are barely visible in the high temperature, high pressure synthesized samples (see dotted lines in the figure).

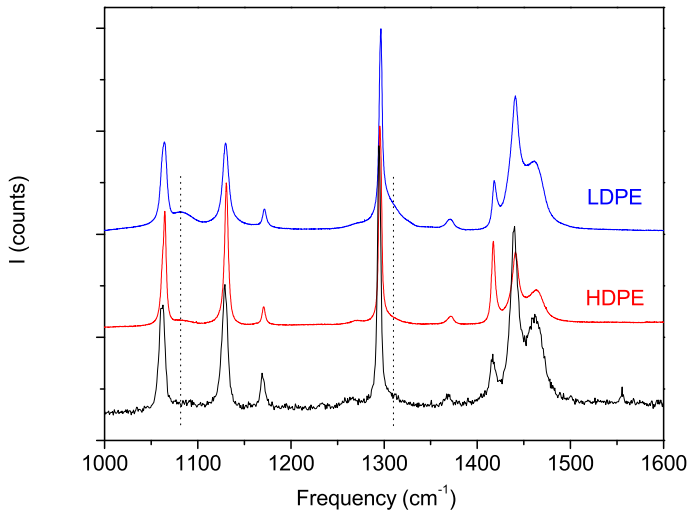

Figure 2.28: *Comparison of ambient conditions Raman spectra of recovered polyethylene from HP, HT synthesis and commercial low density (LDPE) and high density (HDPE) polyethylenes. Black curve: Raman spectrum of the recovered polyethylene from high p,T experiment (340 K, 1.5 GPa). Red curve: Raman spectrum of a commercial sample of high density polyethylene (HDPE). Blue curve: Raman spectrum of a commercial sample of low density polyethylene (LDPE). The two vertical dotted lines indicate the regions where spectral contributions from the amorphous fraction are expected.*

Angle dispersive X-Ray diffraction (AD-XRD) provides the more direct informations about the crystallinity of high temperature, high pressure synthesized polyethylene. Figure 2.29 shows the ADXRD pattern of the recovered polymer from the reaction at 423 K and 1.5 GPa. The two osberved

peaks, at 2θ values of 9.869° and 10.963°, are related to pure orthorhombic polyethylene, and are in the correct relative intensity [151]. The two peaks are assigned to the (110) and (200) reflections, respectively, and are expected at about 9.829° and 10.883° taking into account the standard settings of the orthorhombic Pnam structure, with cell parameters $a = 7.48$ Å, $b = 4.97$ Å, and $c = 2.55$ Å, and with the c axis directed along the chain-axis direction [152]. From the experimental value, the calculated d-spacings are 4.138 Å and 3.730 Å, to be compared with those of HDPE (4.11-4.14 and 3.70-3.75 Å, [153,154]). No other features are visible in the polyethylene XRD pattern. In fact, polyethylene could present here additional contributions, i.e. a broad absorption background related to the amorphous fraction of the polymer [12] and three sharp peaks due to the monoclinic phase (space group A2/m), normally stable above 14 GPa [151] but possibly stabilized at lower pressure due to stress [155].

The polymer obtained upon high temperature, high pressure polymerization presents a really high crystal quality also with respect to the product of laser induced polymerization in the liquid phase of ethylene [7], as shown by the very low amount of defects detectable in the infrared spectrum (see figure 2.26, central panel). The different starting temperature of the experiment (0.4, 0.8 and 1.4 GPa) does not seem to affect the crystal quality of the product, even if a systematic increase of the n value with decreasing temperature could suggest an increase of branching and defects possibly related to the higher reaction rates (see table 2.1).

Deeper insight about the reaction mechanism and other fundamental aspects of the reaction can be gained by the kinetics study. The kinetics were measured at 1.5 GPa at three different temperatures. The pressure value of the kinetics was choosen because of the larger temperature range it could provide, besides of being quite different from the 0.2 GPa value choosen by Buback for the same purpose [140, 141].

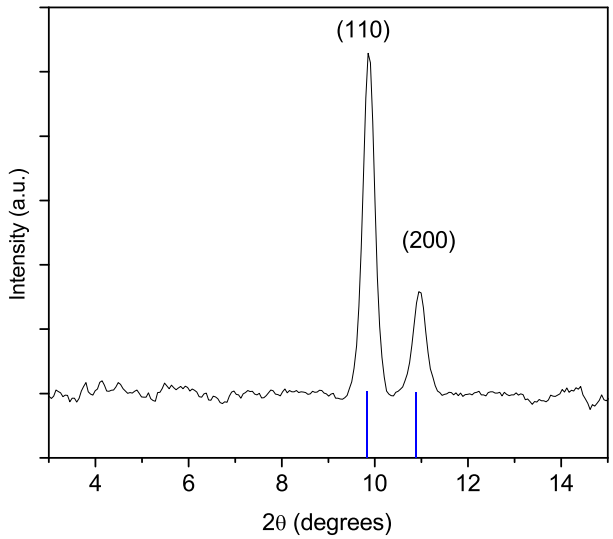

Figure 2.29: *XRD pattern of the recovered polyethylene from high temperature, high pressure polymerization (423 K, 1.5 GPa). The blue lines indicate the position of the expected reflections for an orthorhombic Pnam structure with the cell parameters reported in ref. [152] (a = 7.48 Å, b = 4.97 Å, c = 2.55 Å). The baseline has been corrected by subtracting the background due to the diamond anvils Compton scattering.*

The dependence of the rate constant k upon temperature at constant pressure is given by

$$\left(\frac{\partial \ln k}{\partial T}\right)_P = \frac{E_a}{RT^2} \tag{2.2}$$

and its integration allows to compute the activation energy E_a by the linear relation of $\ln k$ vs $1/T$. Figure 2.30 reports this plot using the rate constant derived from the Avrami model and reported in table 2.1. The computed activation energy value is 31.5 ± 1.1 kJ/mol, much lower than that measured by Buback (136.3 ± 6 kJ/mol at 0.2 GPa) but comparable to the value of 37 ± 8 kJ/mol obtained at 0.2 GPa in the UV photoinduced reaction (see ref. [141]). For having a profitable comparison, one could adopt

the same, extremely simplified analysis procedure used by Buback (see ref. [140,141]), separating the whole activation energy obtained with the fit (E_{tot}) in three different contributions related to initiation (E_i), propagation (E_p) and termination (E_t) steps, respectively:

$$E_{tot} = \frac{1}{2}E_i + E_p - \frac{1}{2}E_t \tag{2.3}$$

Buback adopted a mean value of $E_p - \frac{1}{2}E_t$ equal to 31.4 ± 6 kJ/mol, thus giving an activation energy if the initial step E_i of 209.8 ± 12 kJ/mol. Following this same procedure, in the present case the value of E_i is about 0. An underestimation of this number is quite likely, because a decrease of the activation energy of the propagation step with the increasing pressure can be reasonably expected.

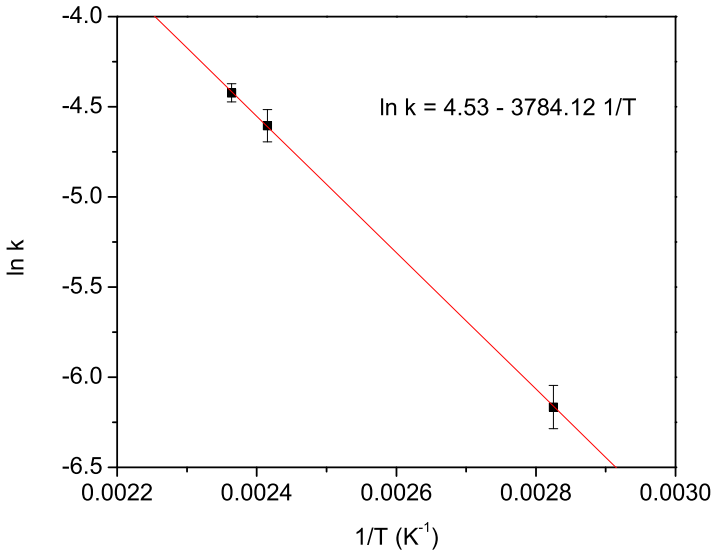

Figure 2.30: *Linear regression of the evolution of* $\ln k$ *as a function of* $1/T$ *at 1.5 GPa. The equation of the fitting curve is also reported. The rate constant values have been obtained by reproducing the evolution with time of the* CH_2 *bending mode bands of polyethylene using the Avrami model.*

Another reasonable cause for the lowering of the activation energy bar-

rier has to be found in the reduced distances and in the minimization of the steric hindrance for the monomers to react. In fact, the pressure increase can determine a consistent reduction in the activation energy for the initiation step, up to a complete annhilation of the energy barrier between reactants and products [156]. In the fluid phase, the activation energy for the initiation step is substantially related to the energy barrier for the internal rotation. The annullment of this term can be imagined as due to the formation of a structured fluid at high denisity, where steric hindrances are enormously minimized and the molecules are already in the most profitable configuration to readily react. A similar occurrence was found in the UV-photoassisted polymerization of ethylene at high temperature (470-500 K) and 0.2 GPa [141], where the activation energy for the initiation step was about 0. The photochemical activation of the reaction is based on a two-photon absorption process to the $\pi\pi^*$ valence state [7]. The population of the antibonding molecular orbital reduces the bond order of the molecule down to one, thus increasing the sp^3 hybridization like character of the involved carbon atoms and causing a stretching of the C-C bond and a twisting of the entire molecule [157, 158]. This rotation of the CH_2 groups along the C-C axis (D_{2d} point group simmetry) allows the minimization of the repulsive interactions with the nearest-neighbour molecules, making of ethylene a classical example of a biradicaloid specimen [159]. High density conditions are capable of driving a very fast reaction of these excited specimen with their nearest neighbours, thus readily and very efficiently starting the polymerization process. A speculated mechanism could be the one in which high temperature and high pressure conditions favour a displacement along the twisting coordinate in the ground state of ethylene, determining a decrease of the π bonding character of the molecule and then the formation of diradicals which efficiently act in triggering a fast reactivity, in other words enormously reducing the initiation and propagation contribution to the activation energy.

Buback adopted a very simple rate law expression to reproduce the absorption (i.e., concentrations) data in its thermal and photoinduced polymer-

ization experiments [140, 141]:

$$v = k\,[C_2H_4]^m \tag{2.4}$$

In equation 2.4, k is the overall reaction rate coefficient, $[C_2H_4]$ the monomer concentration and m the overall reaction order. The parameter m can be determined by a double logarithmic plot, where the logarithm of the overall reaction rate is plotted versus the logarithm of the monomer concentration yielding, by means of a linear fit of the data, to the determination of both overall rate constant and reaction order. In his experiments, Buback found m values at 0.2 GPa ranging from 2 (for the photoinduced reaction) to 2.5 (for the thermal polymerization), thus corresponding to an initiation reaction order of 2 and 3, respectively [140, 141]. The effect of increasing pressure on the polymerization reaction can be better explained by comparing the data for the present study, performed at 1.5 GPa, with those from Buback. The kinetics at three different temperature were analysed following the consumption of the monomer as a function of time through the integrated absorption of the $\nu_5 + \nu_{12}$ and $\nu_2 + \nu_9$ combination bands of ethylene lying at 4518 and 4735 cm^{-1}, respectively. The evolution has been reproduced by a stretched exponential function. Figure 2.31 reports in the left panel an example of the evolution with time of the integrated area relative to the two combination modes, measured during the reaction at 423 K and 1.5 GPa and the corresponding fit. This way, the double logarithm plot on the right panel was produced, allowing to determine the overall reaction order by the slope value of the linear fit. In the present experiment, the value ranges between 8 and 9, much larger than those reported by Buback, and leading to an initiation reaction order between 14 and 16. Despite of the exact meaning of this number, it should be related to the number of molecules involved in the initial step of the reaction and, taking Buback's work as a reference, let think of a process that become more an more cooperative with increasing pressure [160].

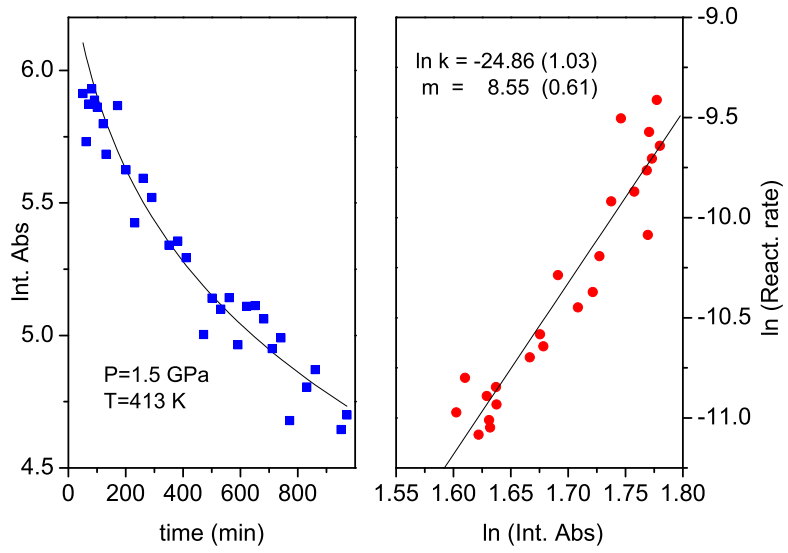

Figure 2.31: *Left panel: time evolution of the total integrated absorbance of the combination bands of ethylene. The fitting curve is a stretched exponential with exponent $\beta = 0.324$. Right panel: log-log plot of the reaction rate vs the integrated absorbance (concentration) of ethylene. The linear regression of these data yields a reaction order greater than 8 (see equation 2.4).*

2.5 Summary

The high pressure structural and reactive behaviour of Graphite Oxide (GO) in the presence of small atoms and molecules (Ar, N_2 and NH_3) have been studied. The effects of the intercalation of small molecules between the layers of GO have been characterized by means of spectroscopic (FTIR, Raman) and structural (XRD) techniques.

The conservation of the structural properties of GO upon compression in GO/Ar, GO/N_2 and GO/NH_3 mixtures is deduced by the preservation of the interlayer d(001)-spacing once released the pressure at the end of the experiment. In fact, in pure GO, the d(001)-spacing reduces of about 10% after compression/decompression. In the case of GO/N_2, the preservation of

the d-spacing constitute a major proof of the insertion of molecular nitrogen between the layers, thus avoiding the formation of interlayer bonding that can alter the structural features of the matrix, while in the case of GO/Ar, more evidently, sharp discontinuities in the EOS of the mixture is visible at the transition pressure between liquid and solid phases of Ar (1.3 GPa, see figures 2.5 and 2.6). In the case of GO/NH_3, the extremely particular behaviour of the mixture clearly shows the presence of ammonia molecules in between the layers: the interlayer d(001)-spacing tends to increase upon compression up to the solidification pressure of ammonia into plastic phase III (about 1.1 GPa), thus suggesting that more and more molecules are introduced between the layers with increasing pressure until NH_3 is in the liquid phase. The negative compressibility of GO/NH_3 mixtures between the lower investigated pressure (0.2 GPa) and the solidification pressure of NH_3 (1.1 GPa) is a major feature of so called *auxetic materials*. Above the solidification pressure of ammonia, the system starts to behave as expected for a material with positive compressibility, but the d(001)-spacing remains always well above the mean value for the pure GO, thus attesting how the layers remain spaced by the now solid, trapped molecules of ammonia. A singular feature is that the EOS for GO/Ar and GO/N_2 mixtures are lower in the graph with respect to pure, compressed GO (see figure 2.5 with regard to a parameter, which has a major influence on the unit cell volume, and to c parameter in the inset). This is another indirect proof of the successful insertion of Ar and N_2 between the layers: these small systems substitute the adsorbed water molecules, that are responsible for the d-spacing value in the pure GO (the value of d(001)-spacing strongly depends on the hydration of the material), thus resulting in a lower interlayer d(001)-spacing (i.e., lower hydration degree) and at the same time avoiding bond cleavage and reformation by someway "insulating" the layers through the formation of an inserted buffer. This allows to recover the initial interlayer d(001)-spacing once released the pressure in membrane.

The fact that GO, with respect to zeolites, is an active system, in which every single layer is decorated by many different oxygenated functional groups,

establishes an important difference from the reactivity point of view. Whereas silicalite was an inert, protecting inorganic scaffold that allowed to perform high-pressure synthesis of specific polymers inside their nanocavities, thus enhancing the capability of ambient pressure recovering of interesting materials, GO is highly reactive because of its several, different oxygenated functionalities, that makes it easy to undergo further functionalization and doping. In particular, N-doping of the GO basal plane is an extremely appealing achievement for diverse technological applications. Samples of GO have been compressed in the presence of two different N-bearing systems, the inert and apolar molecular N_2 and the highly reactive NH_3, a nucleophilic Lewis base with a basic character also according to Brønsted and Lowry. Reactivity was induced by means of pure pressure (compression/decompression experiments), heating and photoirradiation (VIS and UV). Both in the presence of N_2 and NH_3, infrared spectra reveal clear signatures of a reaction, and particularly of N atoms inclusion in the basal plane (in terms of C-N, C=N and -NH_2 functionalities, see figures 2.14, 2.17, 2.20 and 2.19). The results of photoirradiation experiments on GO/NH_3 sample are the most interesting, both starting from the solid phase IV of ammonia (5.0 GPa, with the 514.5 nm wavelength) and from the liquid phase (0.5 GPa, with the 350 nm wavelength). In these last cases, and differently from what was observed in GO/N_2 samples, there is no CO_2 formation and the FTIR spectra account for the conversion of carbonyl groups of GO into other functionalities (amides, -CO-NH_2, ammonium carboxylate groups, [NH_4^+][R-COO^-]) due to the reaction with NH_3 molecules. The constant intensity of the NH_4^+ band at 1470 cm^{-1} during the irradiation with the 350 nm wavelength at 0.5 GPa could be explained in the same way. IR spectra reveal also the presence of amine groups, likely generated through the opening of epoxy rings on GO. In the case of UV-photoirradiation, the recovered spectrum at the end of the reaction is quite peculiar also with respect to the other sample from high pressure ammonia photoinduced reaction, showing a large consumption of carbonyl groups, a higher absorption intensity at 1240 and 1575 cm^{-1}, a fre-

quency shift for the band at 1585 cm^{-1} and an intensity decrease in the O-H and N-H stretching region (between 3300 and 3700 cm^{-1}), thus suggesting that UV laser line is absorbed not only by ammonia (TP absorption) but likely by water molecules (TP absorption) and, of course, GO (OP absorption). The evolution of I_D/I_G ratio values before and after the reaction is significant because supports the formation of sp^3 hybridized carbons on the basal plane of GO.

An assignment of the bands in the recovered samples was not possible in terms of localized vibrational modes. This is likely due to the inherent disorder of the starting GO. Anyway, a comparison is possible between the recovered sample of GO/N_2 and GO/NH_3 experiments with the recovered samples of other high pressure experiment on C-rich sytems (benzene), C:O systems (furan) and C:H:N systems (*s*-triazine and amorphous, variously hydrogenated carbon nitrides). The results, summarized in figure 2.21, clearly show an increased N amount on the recovered sample of GO after reaction in the presence of N_2 and NH_3 with respect to the starting, unreacted GO, thus confirming the insertion of N on the basal plane. This result is particularly appealing because the N-insertion was obtained only by means of physical tools (pressure, irradiation, heating) and without the exploitation of strong and quite dangerous reducing agent as hydrazine, typically used to these purposes.

In order to perform the high pressure synthesis of new hybrid nanocomposite materials with interesting physical characteristics, a first step was the study of polymerization reactions in the confined space provided by the layered structure of GO. In particular, as a reference case study, the polymerization of ethylene between the layers of GO has been studied both with spectroscopic and structural techniques. FTIR and Raman spectroscopy provided informations about the evolution of the reaction, while XRD allowed to understand the behaviour of the system upon compression/decompression. The data from this experiments are currently under elaboration. Furthermore, in order to have the maximum mobility of the monomers and to work in favour-

able P,T conditions for the polymerization, as a preliminary step in this synthesis, the high pressure, high temperature polymerization of bulk ethylene has been studied. This study allowed to gain information on the instability boundaries of liquid ethylene as a function of pressure and temperature (see figure 2.24) and provided also important kinetic data and interesting insights on the reaction mechanism. In particular, kinetic data accounted for a reaction with essentially no initiation energy and that becomes more and more cooperative with increasing pressure: the energy barriers for the initiation step of a reaction are generally lowered by the reduction of the distances and the minimization of the steric hindrance, and in the liquid phase the energy barrier is essentially related to the internal rotation. The annulment of the term E_i in equation 2.3 could therefore be interpreted in terms of formation of a structured fluid where molecules are in the correct configuration for readily starting the reaction. This occurrence is likely related to a displacement in the twisting internal coordinate, favoured by high pressure and high temperature conditions, resulting in the formation of a biradicaloid specimen with lowered steric hindrance and an increased sp^3 hydridization character of the carbon atoms. These reactive radicals efficiently trigger a fast reaction with the nearest-neighbour molecules, that is what data account for. Furthermore, the quality of the polymer synthesized at high P,T conditions is really high, substantially crystalline, orthorhombic polyethylene with no (or extremely low) fraction of amorphous species.

Further experiments are planned to fully elucidate the features of high pressure polymerization between the layers of GO, in the perspective of performing the synthesis of new materials with specific characteristics.

Chapter 3

High pressure chemistry of Phosphorous allotropes

In this chapter, the results concerning high pressure stability and structural behaviour of black Phosphorus (P-black) in the presence of simple atoms and molecules, and about high pressure chemical reactivity of black and red Phosphorus (P-red) towards ammonia will be presented. In fact, a comparison between the reactivity of red and black phosphorus is mandatory to better understand the stability of these two allotropes towards simple molecule in specific pressure, temperature and irradiation conditions, and as a preliminary work for the study of possible molecular insertion and intercalation in the layered structure of black phosphorus. These results are obviously of great importance, from an applicative point of view, as Phosphorene-based materials are concerned. Phosphorene is a recently emerging 2D platform material with a huge variety of possible applications, mainly related to its inherent bandgap that makes it a natural semiconductor.

3.1 Phosphorus and its allotropes

Phosphorus (P) is a key element in chemistry and physics as well as in Life, Earth, planetary and materials science [27]. It belongs to the *pnicto-*

gen group (VA, Group 15 in the periodic table) together with Nitrogen (N), Arsenic (As), Antimony (Sb) and Bismuth (Bi), with external electronic configuration ns^2np^3 and, therefore, most common oxidation states of ± 3, $+5$. In addition, d orbitals can also be involved in the formation of chemical bonds. Phosphorus is an ubiquitous element, widely abundant on Earth and in our organism also (i.e., DNA), but is not found free in nature, frequently occuring in some oxidized state as *phosphate*, at least on Earth [27]: there are more than 300 different known phosphate minerals [161–163] that can be roughly splitted in two distinct groups, **a)** *Apatitic Phosphate Minerals* and **b)** *Non-Apatitic Phosphate Minerals*, being the first ones the major commercial sources of the element due to their great abundance and concentration [27].

The members of Apatite group are common accessory minerals in igneous, sedimentary and metamorphic rocks, of general formulation given by $Ca_{10}(PO_4)_6(F,OH,Cl)_2$. The most common igneous apatite deposits consist mainly of *fluorapatite*, whose general formulation is $Ca_{10}(PO_4)_6F_2$, *chlorapatite*, with general formula $Ca_{10}(PO_4)_6Cl_2$, and *hydroxyapatite*, with general formula $Ca_{10}(PO_4)_6(OH)_2$. Apatite occurs mostly as a sedimentary deposit of approximate composition $Ca_{10}(PO_4)_6F_2$ named *Phosphorite* or "*Phosphate Rock*", being this last a general term used to describe almost all kind of phosphate deposits. Phosphorites are typically dirty white to greenish and made of mainly microcrystalline or amorphous fluorapatite, often found in association with calcium carbonate and other impurities (general formula $Ca_{10-x}(PO_4)_{6-x}(CO_3)_x(F,OH)_2$, with some chance of found up to 25% replacement of PO_4 by CO_3 and up to 10% Ca by Mg) [27]. Another common metal involved in these phosphates is Aluminium (Al).

Non-Apatitic Phosphate Minerals include compounds from the so called Laueite Group, Lazulite Group, Montgomeryte Group, Crandallite Group, Triplite Group and Torbernite Group, that are all isostructural groups of phosphate with different brute formula. They are often found as mutual solid solutions of variuos compositions [27]. Non-phosphorus anions such as

O^{2-}, OH^{-1}, F^{-1}, SiO_4^{4-} and AsO_4^{3-} are often found in these phosphates in stoichiometric proportions, or as occluded materials, and there is also a great variety of possible involved metal cations. Some of these phosphates are an important source of rare earth elements such as Uranium.

Elemental phosphorus exists at ambient pressure as at least three different allotropes, roughly identified by their colour: white, black and amorphous red phosphorus. Several other phosphorus allotropes such as crystalline red, grey, violet or brown phosphorus have been synthesized so far under non-ambient conditions [164]. Among all these allotropes, White Phosphorus (P-white, wP) is the most common one: it is a molecular solid made up of tetrahedric shaped P_4 units, that exist in the crystal structure α-P_4 at ambient conditions, a body-centered cubic α-manganese-like structure [165]. Several studies have found that α structure undergoes a phase transition to a β phase at about -80°C (193 K), and from β to another phase γ at lower temperature [166–170]. β-wP has a triclinic structure, while γ-wP has a monoclinic structure, quite close to an orthorhombic one [171]. P_4 units have been found to have librational disorder in α and β phases, whereas this is not the case in the γ one [171]. P-white is largely available from several synthetic protocols starting from phosphorus minerals, and it is widely used in the phosphorus industry despite of its instability, high reactivity, flammability and toxicity, that could make highly uncomfortable to have to deal with it.

Red Phosphorus (P-red or rP), on the other hand, is a polymeric amorphous solid much more stable and less toxic than molecular P_4. Figure 3.1 reports the structure of a single, polymeric P-red chain. P-red has been characterized by means of Raman, XRD and neutron scattering techniques [172, 173]. This allotrope exhibits an irreversible phase transition to black phosphorus (P-black) at about 6.3 GPa at ambient temperature.

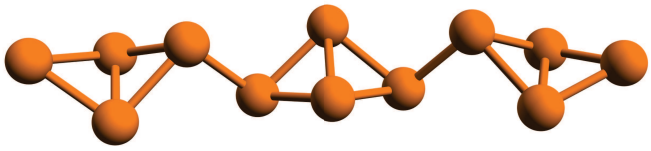

Figure 3.1: *Structure of a single chains of polymeric P-red.*

Being far more stable and less toxic than P-white, the phosphorous red allotrope could be preferably used in industrial and research chemistry, but few technological applications have been found over the decades (matches industry, production of flame retardants in plastics and aluminum phosphide). High pressure reactivity of P-red has been studied in the presence of water [174] and ethanol [175], with the twofold purpose of obtaining large amounts of H_2 from water molecules (a remarkable goal for environmentally friendly synthetic methods based of renewable sources to produce appealing energy vectors) and of elucidating the possibile formation of phosphorous-bearing compounds in terrestrial and space environments (extreme conditions synthesis). In both cases, reactivity has been triggered by means of two-photon absorption of near-UV laser light (350 nm). In the case of P-red/H_2O samples [174], five hours irradiation with 500 mW of 350 nm wavelength laser emission was sufficient to obtain an almost complete consumption of P-red and the contemporary appearance of Raman signature of H_2 and PH_3, together with bands related to various phosphorus-based acids (H_3PO_2, H_3PO_3 and H_3PO_4). On the other hand, mixtures of ethanol and P-red exhibited a very different reactivity in quite similar conditions [175]. First of all, 11 hrs was necessary to observe a first, partial consumption of the starting P-red; only after 21 hrs the P-red consumption was completed. FTIR spectra of the reacted mixtures showed signature that could be related to decomposition products of ethanol (ethane, methane, CO_2 and methyl groups). It is quite remarkable that no characteristic products of pure ethanol reactivity were observed [176], thus suggesting a preferential reactivity of the activated fragments towards P-red. Raman spectra revealed also the presence of

ethylene and diethyl ether, in addition to PH_3 and molecular hydrogen. The only organophosphorous compound identified in the products mixture was triethylphosphate.

Black Phosphorus (P-black or bP) is a crystalline solid. The stable structure at ambient conditions is the orthorhombic A17 (space group *Cmca*, 8 atoms per unit cell) [177, 178]. Upon increasing pressure, orthorhombic P-black undergoes to phase transitions to rhombohedral A7 phase (space group $R\bar{3}m$, two atoms per unit cell), at about 5.5 GPa: A7 is a common structure for all the elements in the VA group of the periodic table. At 10.3 GPa, another phase transition from rhombohedral A7 to simple cubic (sc) phase (space group $Pn\bar{3}m$, one atom per unit cell) has been detected [179]. These three phases have been extensively studied both by means of XRD technique and by Raman spectroscopy in the low-frequency phonon region [180]. At higher pressure, simple cubic (sc) P-black transforms into simple hexagonal structure (sh) (137 GPa), after the transition to an intermediate phase at 107 GPa: this last phase, named P-IV, could present some affinity with a distorted bcc structure (tetragonal, space group *P4/n*, with 10 atoms per unit cell) [181]. This assignment is made taking into account the typical structural sequences of other elements in the VB group, i.e. A7 - (sc) - distorted bcc - bcc [182]. The simple hexagonal (sh) structure (spage group *P6/mmmm*, with only one atom per unit cell) appears at 137 GPa [181]. The relatively small pressure range where P-IV phase exists suggests this last to be an intermediate step in the (sc)-(sh) transition. In this process, the coordination number of phosphorus increases from 6 (sc) to 8 (sh), with a relatively large volume reduction [181]. The (sh) structure does not typically occur in the VB group elements, thus suggesting phosphorus does not exactly follow the typical structural sequence [182]. Furthermore, (sh) structure is relatively rare in the periodic table, and it is reported only for high pressure phases of Si [183, 184] and Ge [183]. At even higher pressure, (sh) structure has been found to transform into bcc structure (between 253 and 262 GPa, space group $Im\bar{3}m$) [185, 186]. Figure 3.2 reports a phase diagram of P-black until

15 GPa, together with literature data from Kikegawa *et al.* [187].

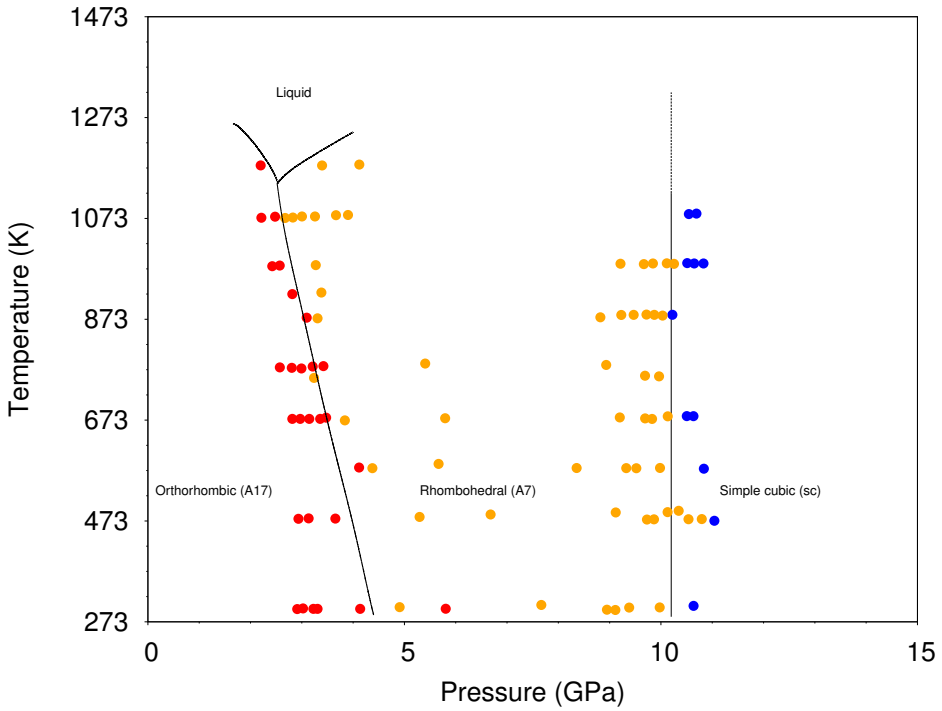

Figure 3.2: *Phase diagram of black phosphorus between 0 and 15 GPa and 273 and 1473 K. Solid lines account for the phase boundaries between orthorhombic A17 and rhombohedral A7 phases, and between rhombohedral A7 and simple cubic (sc) phases. Dotted lines refer to melting of black phosphorus into liquid phase at high temperature. Red circles represent the points where the orthorhombic structure is observed; yellow circles, the points where rhombohedral structure is observed; blue circles, the points where simple cubic structure is observed. Red, yellow and blue circles are taken from experimental data of Kikegawa and coauthors, see ref. [187].*

Both orthorhombic A17 and rhombohedral A7 are layered structure. More in detail, orthorhombic P-black crystals consist of corrugated layers of six-membered rings in chair conformation share edges like in *cis*-deacalin, whereas rhombohedral P-black structure is made of layers of six-membered rings linked in a *trans*-decalin fashion [188]. Figure 3.3 reports the ball-and-stick structures for orthorhombic and rhombohedral P-black. Structural data are

obtained from the works by Cartz and coauthors [189] and Ahuja [190].

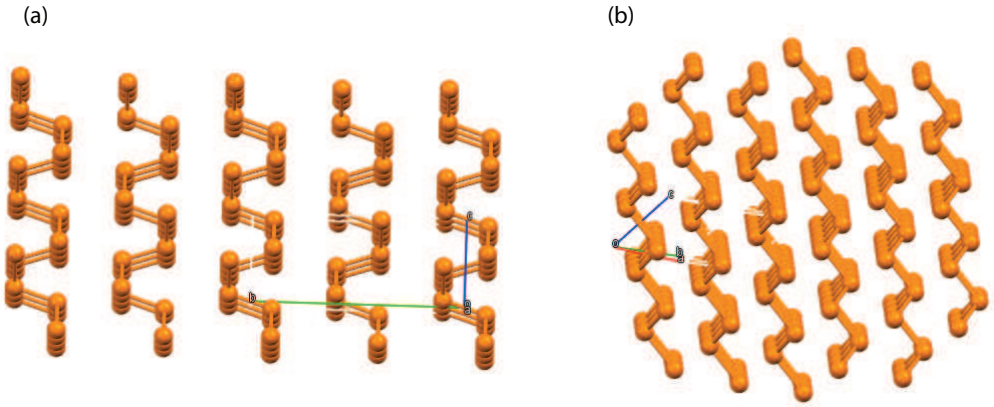

Figure 3.3: *Structures of orthorhombic (a) and rhombohedral (b) P-black. CIF compiled by Cartz (see ref. [189]) and Ahuja (see ref. [190]). The images have been created on Mercury software.*

Boulfelfel and coauthors [188] suggest a possible mechanism of the phase transition between A17 and A7 structures, considering a structural reconstruction starting from compression and layer shuffling that allows the occurrence of interlayer contacts and intralayer bonds until complete transformation to A7 structure. On the other hand, the transition from rhombohedral to simple cubic structure, that are subgroup-group related, involves small antiparallel displacements along the (111) cubic direction, with an increase of rhombohedral angle up to 60°. The ratio between c and a parameter is exactly $\sqrt{6}$ in perfect cubic geometry in absence of any distortion, and so rhombohedral structure could be somewhat considered as a distorted simple cubic structure.

The single layer of P-black, named Phosphorene in analogy with the system Graphite-Graphene, has raised a huge interest in the scientific community in the last couple of years, due to its appealing properties. Phosphorene has in fact an inherent bandgap, that made it suitable for several possible applications in diverse field [29–31]. The synthesis of Phosphorene is extremely challenging, and it is substantially performed in two ways: scotch-

tape-based microcleavage [31] and liquid exfoliation [191, 192]. Phosphorene forms in a honeycomb lattice structure with notable nonplanarity in the shape of structural ridges. One major disadvantage of Phosphorene, and one of the major challenges in its production and use for research purposes, also in view of its high instability towards atmospheric moisture. Phosphorus is in fact highly hygroscopic, and the material has an extremely high surface-to-volume ratio: as a result, Phosphorene reacts very readily with water vapor and oxygen assisted by visible light [193], and its degradation is complete within few hours, making very difficult to deal with it for technical applications.

3.2 High pressure photoinduced reactivity of P-red and P-black with NH_3

The behaviour of P-red and P-black in the presence of a simple, reactive N-bearing molecule has been studied with the purpose to explore the high pressure reactivity of the two allotropes in order to compare the effect of the different structural arrangement on the reaction mechanisms and paths. As a reactant, NH_3 has been selected because of its very well known high-pressure behaviour and phase diagram [109, 194], and, as it was for GO/NH_3 mixtures (see section 2.3), for the possibility to foster a photodissociation of the molecule using near-UV irradiations by a two-photon absorption process. Within the suitable pressure range to establish a comparison between P-red and P-black reactivity, that is from 0 to 6.3 GPa, where P-red spontaneously and irreversibly transforms into P-black, NH_3 undergoes to the transition between liquid phase [108, 109] and the orientationally disordered plastic phase III [105,106] (face-centered cubic, $Fm\bar{3}m$) at about 1.0 GPa, and then to the transition between phase III and ordered phase IV (orthorhombic, $P2_12_12_1$) [109]. NH_3 also presents two low temperature phases, named phase I (cubic, $P2_13$) and II (hexagonal closed-packed structure, $P6_3/mmc$). Figure 3.4 reports a phase diagram for NH_3 between 225 and 500 K, and 0-10 GPa.

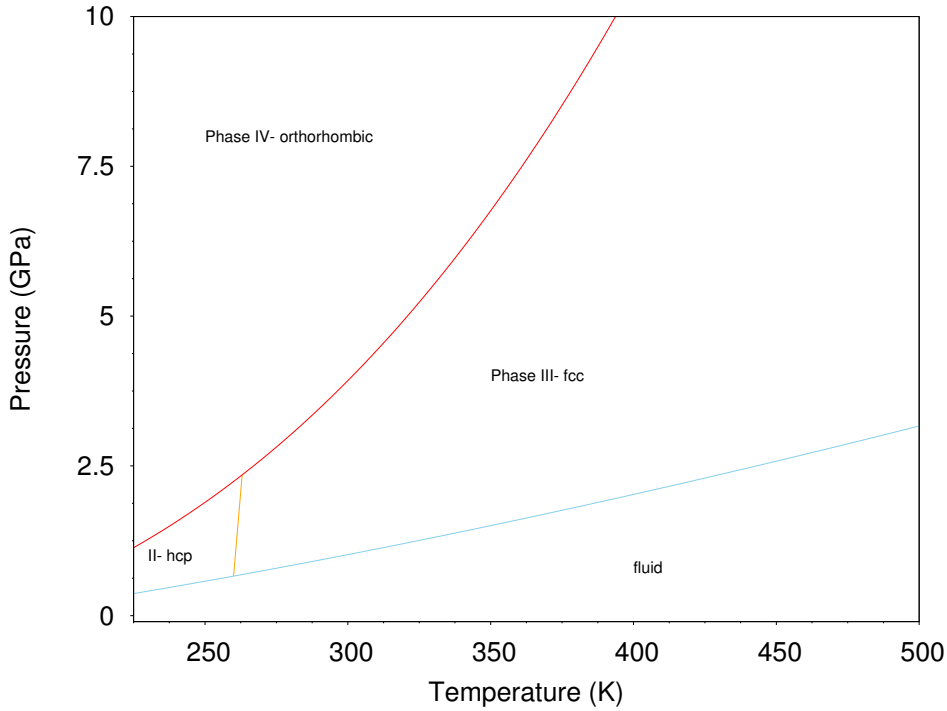

Figure 3.4: *Phase diagram for NH_3 (225-500 K, 0-10 GPa). Melting curve and phase boundaries data are taken from Ninet et al., see ref. [109].*

The first electronic excited state of NH_3 is a quasi bound state with a very weak dissociation barrier to the formation of H and $\dot{N}H_2$ excited fragments [117, 118, 195, 196]. From the fundamental electronic state $\tilde{X}(^1A_1')$, the system can reach the first excited state $\tilde{A}(^1A_2'')$ by a two-photon absorption (the required energy, 216.7 nm, is therefore largely exceeded via two-photon absorption of near-UV 350 nm wavelength). The $\tilde{A}(^1A_2'')$ state is a predissociative state with a weakly bonded planar trigonal structure that, depending on the vibrational excitation, could evolve in a bond cleavage with the production of H (^2S) and $\dot{N}H_2$ fragments, the latter both in their excited, $\tilde{A}(^2A_1)$ or ground state $\tilde{X}(^2B_1)$ [117,195,196]. Figure 3.5 reports a picture of the ground and of the first excited state of NH_3 with the relative dissociated species.

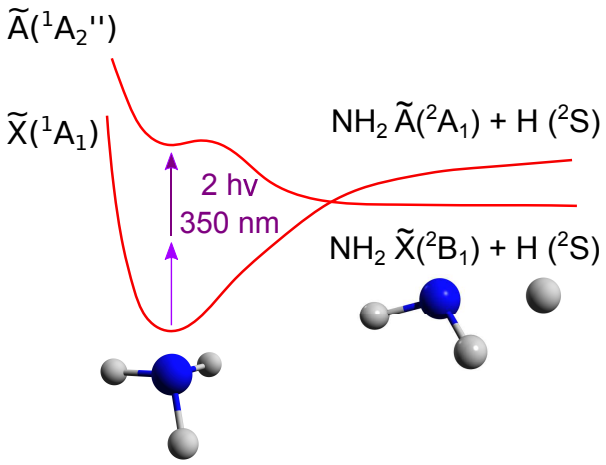

Figure 3.5: *Representation of the ground and first excited state of NH_3.*

The generation of highly reactive fragments in the high density conditions provided by high pressure, and the reduced molecular distances, can bring to a comparable timescale the recombination process, leading to a deactivation of photo-activated species, and the effective intermolecular collisions, leading to an effective reactivity in the sample.

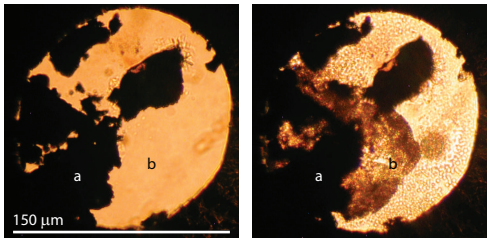

Figure 3.6: *Optical images of P-black/NH_3 sample at the beginning (left) and at the end (right) of the photoinduced reaction. The dimension of the sample are reported in left panel. (a) and (b) on the sample refer to different point where micro-Raman spectra have been acquired.*

P-black sample has been studied in the presence of NH_3, loaded in DAC by *Spray-loading* technique (see section 4.2). Seven irradiations of the same power (500 mW) for a total of 67 hrs, using 350 MLUV-wavelength, have been performed on the sample at room temperature and 0.8 GPa, in the fluid

phase of ammonia (see figure 3.4). Figure 3.6 shows the visual aspect of the sample before any irradiation and at the end of the last irradiation, where the presence of small bubbles can be appreciated, thus suggesting some kind of reactivity in the regions where the initial P-black sample appears to be "consumed" by the reaction. The evolution of the reaction has been monitored by means of FTIR and micro-Raman spectroscopy. Figure 3.7 reports the sequence of FTIR spectra acquired after each irradiation (coloured traces) in comparison with the spectrum of the starting P-red/NH_3 sample. The initial spectrum is dominated by the saturating intensity of the fundamental modes of NH_3: $\nu_2(A_1)$ at about 1058 cm^{-1}, $\nu_4(E)$ at 1630 cm^{-1} and the unresolved $\nu_1(A_1)$ and $\nu_3(E)$ modes at $\sim$3307 cm^{-1}. In the high frequency side of the spectrum, we find the combination modes $\nu_2+\nu_3$ at 4470 cm^{-1} and $\nu_3+\nu_4$ at 5003 cm^{-1} [116]. No FTIR signal possibly related to P-black is visible in the medium infrared spectral region. Immediately after the first near-UV irradiation (500 mW, 1 h, blue trace in fig. 3.7), the appearance of a new band as a shoulder on the high frequency side of ν_2 mode of NH_3 can be appreciated. The band, centered at about 1200 cm^{-1}, intensifies upon further irradiations up to the last spectrum (red trace in fig. 3.7, after a total of 67 hrs of irradiation). The frequency of this band is compatible with the stretching mode of P=N double bonds. Other spectroscopic signatures suggesting newly formed chemical bonds involving phosphorus from P-red and nitrogen from NH_3 can be appreciated, in the course of the irradiations, as a broad absorption in the region 750-900 cm^{-1}, on the low frequency side of ν_2 band of ammonia, ascribable to the stretching of P-N single bonds, and as two broad bands at 1500 and 1550 $cm^{-}1$, possibly related to bending modes of P-NH_2 groups. The comparison of the FTIR spectra before the irradiations (black trace) and after the last irradiation (red trace) allows to estimate, by the ratio of the integrated absorption of combination modes of NH_3, a consumption of this specie during the reaction of about 21% with respect to the starting amount. No other spectral feature related to the formation of other functionalities in the irradiated P-black/NH_3 sample are visible in the FTIR spectra.

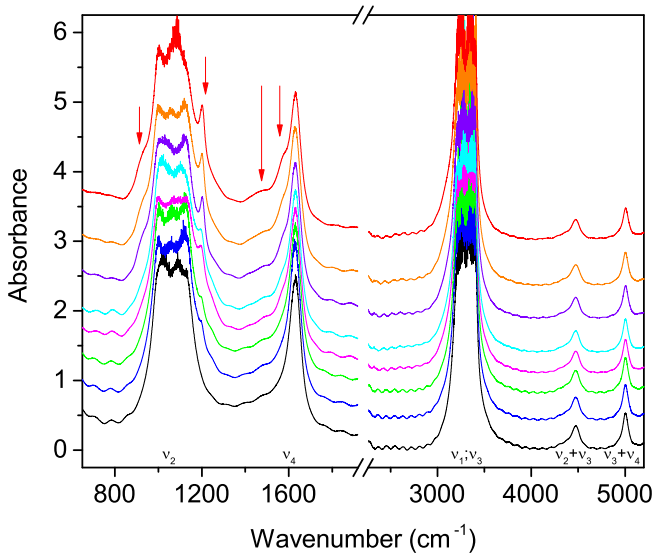

Figure 3.7: *Sequence of the FTIR spectra acquired on P-black/NH_3 sample upon irradiation. Black trace refers to the sample of P-black/NH_3 at the initial pressure of 0.8 GPa before any irradiation; subsequent spectra refer to successive irradiation of the sample with 500 mW of the near-UV 350 nm wavelength for increasing times (1 h, 2 hrs, 7 hrs, 14 hrs, 14 hrs, 14 hrs and finally 15 hrs). The saturating absorption of NH_3 are labelled with their name in greek letters. Spectra were vertically shifted for the sake of clarity. The wavenumber axis break excludes the frequency region where the saturating absorption of the diamond anvils occurs.*

Figure 3.8 reports the Raman spectra acquired before and after irradiations in the (a) and (b) points of the sample (see fig. 3.6) in two spectral regions. In the left panel of figure 3.8, the low frequency phonon region is shown. On P-black, (a) point in the sample, the five Raman active modes of P-black are visible (see black trace): the weak B_{1g} mode at 191.6 cm^{-1} and B^1_{3g} mode at 226.6 cm^{-1}, and the stronger A^1_g (363.4 cm^{-1}), B_{2g} (431.6 cm^{-1}) and A^2_g (459.3 cm^{-1}) modes [180]. Upon irradiation (red trace), minor changes are visible in the region 190-400 cm^{-1}.

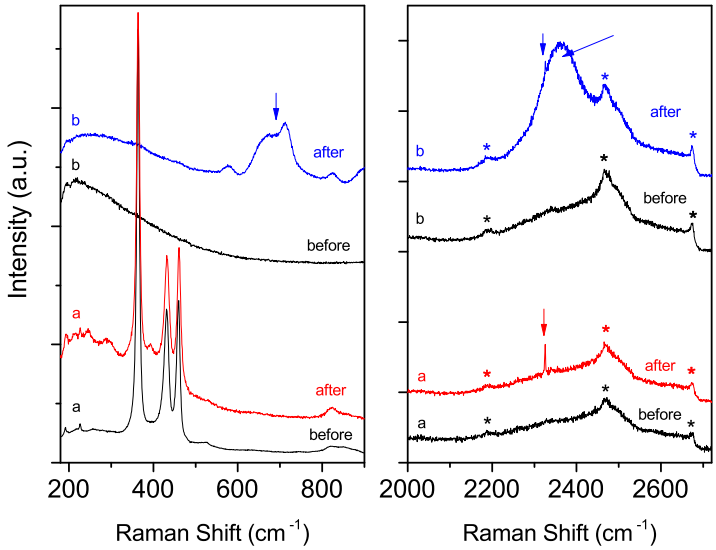

Figure 3.8: *Raman spectra of P-black/NH_3 sample before and after irradiation. Left panel: Raman spectra in the low frequency phonon region on (a) P-black and on (b) bulk NH_3 before (black traces) and after (red and blue traces, respectively) irradiations. Blue arrow indicates the P-H Raman active bending mode. Right panel: Raman spectra in the frequency region between 2000 and 2700 cm^{-1}, acquired on (a) P-black and on (b) former bulk NH_3 and new product, before (black traces) and after (red and blue traces, respectively) irradiations. Red arrow indicates the P-H stretching band of phosphine, while blue arrows indicate P-H stretching from phosphine and P-H stretching from other chemical species. Asterisks refer to Raman peaks from the diamond anvils. Spectra are vertically translated for the sake of clarity.*

On bulk NH_3, point (b), besides of the diffuse scattering due to the fluid ammonia, upon irradiation a broad doublet with peak frequencies of 675 and 710 cm^{-1} appears, together with two broader and weaker bands at 575 and 824 cm^{-1}. This is the region where the bands due to P-H bending modes are expected. In the right panel of figure 3.8, the spectral region between 2000 and 2700 cm^{-1} is shown. In this region, the characteristic sharp Raman band related to P-H stretching of phosphine (PH_3) molecule is

found at 2325.1 cm^{-1} both on P-black (a) and on bulk NH_3 (b), where grainy products of P-black consumption can be seen after irradiation. In this region of the sample, however, the phosphine P-H stretching band is superimposed to a much broader and far more intense Raman band, centered at about 2366 cm^{-1}, generally assigned to P-H stretching modes. No other significant features can be appreciated in Raman spectra of P-black/NH_3 mixtures.

P-red sample has been studied in the presence of NH_3 and in the same conditions than P-black one. 5 irradiations of the same power (500 mW) for a total of 60 hrs, using 350 MLUV-wavelength, have been performed at room temperature and 0.8 GPa, in the fluid phase of ammonia (see figure 3.4). Figure 3.9 shows optical images of the P-red/NH_3 sample at three different stages of the reaction (beginning, after irradiations, after releasing pressure), where the occurrence of chemical reactivity is well evident (as instance, optical images reveal bubbles formation in the sample). In fact, three different regions of the sample have been investigated with all the available techniques: solid region, fluid transparent region and bubbles.

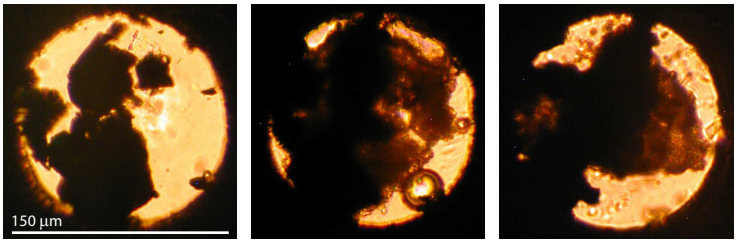

Figure 3.9: *Optical images of P-red/NH_3 sample in three different stages of the photoinduced reaction. Left: before any irradiation. Center: after the irradiation. Right: after releasing pressure.*

Figure 3.10 reports the FTIR spectra acquired after each irradiation on the sample (coloured traces) with respect to the spectrum of the starting P-red/NH_3 mixture (black trace).

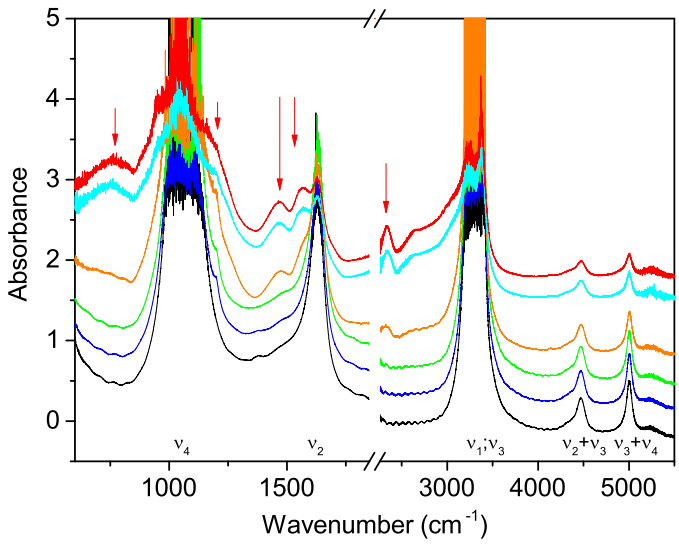

Figure 3.10: *Sequence of the FTIR spectra acquired on P-red/NH_3 sample upon irradiation. Black trace refers to the sample of P-red/NH_3 at the initial pressure of 0.8 GPa before any irradiation; subsequent spectra refer to successive irradiation of the sample with 500 mW of the near-UV 350 nm wavelength for increasing times (5 hrs, 14 hrs, 14 hr, 14 hrs and finally 13 hrs). The saturating absorption of NH_3 are labelled with their name in greek letters. Spectra were vertically shifted for the sake of clarity. The wavenumber axis break excludes the frequency region where the saturating absorption of the diamond anvils occurs.*

The spectrum collected before starting irradiating the sample is dominated by the saturating absorptions due to the vibrational bands of NH_3. After the first irradiation, a shoulder to the $\nu_2(A_1)$ appears at about 1200 cm^{-}1, as it was in the P-black/NH_3 sample. Differently from what happened with the other sample, in this case the other absorption bands in the spectrum increase far more than in the case of P-black/NH_3. During the irradiations, a broad band between 700 and 950 cm^{-1} appears, together with two bands centered at 1500 and 1550 cm^{-1} and another broad one centered at 2345 cm^{-}1. The bands at 700-950, 1200, 1500 and 1550 cm^{-}1 can be confidently assigned to P-N stretching, P=N stretching and P-NH_2 bending mode, re-

spectively, while the absorption band appearing at 2345 cm^{-1} can be assigned to stretching modes of P-H groups. Also in this case, from the comparison of the FTIR spectra before the irradiations (black trace) and after the last irradiation (red trace) it is possible to estimate, by the ratio of the integrated absorption of combination modes of NH_3, its consumption during the reaction to a 72% of the starting amount, far more than in the P-black/NH_3 molecule, thus accounting for a remarkably higher reactivity of the P-red sample with respect to the P-black one.

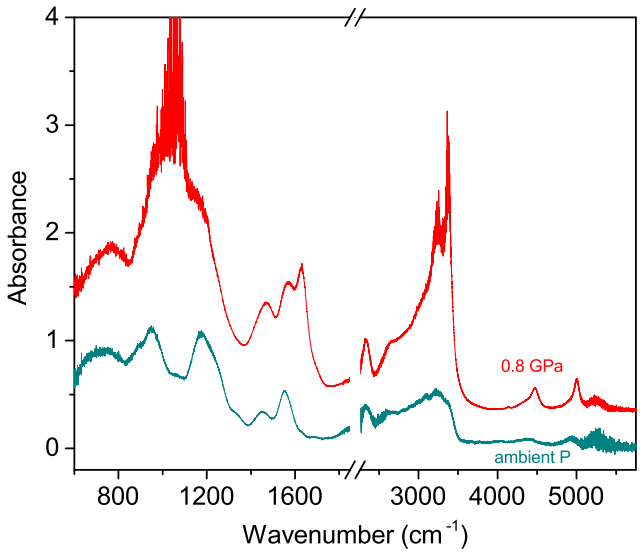

Figure 3.11: *FTIR spectra acquired on P-red/NH_3 sample after the last irradiation at 0.8 GPa (red trace) and on the recovered solid product at ambient temperature (dark cyan trace). Spectra were vertically shifted for the sake of clarity. The wavenumber axis break excludes the frequency region where the saturating absorption of the diamond anvils occurs.*

Differently from P-black/NH_3 sample, the acquisition of a FTIR spectrum of the recovered sample after releasing pressure was here possible. Figure 3.11 reports the FTIR spectrum of the recovered solid product of the reaction between P-red and NH_3 together with the last spectrum acquired under

pressure (0.8 GPa), as a comparison. On opening the cell, the saturating absorption bands of unreacted NH_3 obviously disappear, but the absorption bands related to solid product of P-red/NH_3 reaction remain visible: two asymmetric broad peaks at 985 and 1200 cm^{-1}, a doublet at 1453 and 1556 cm^{-1}, the P-H stretching peak at 2345 $cm^{-}1$ and a broad region from 2600 and 3500 cm^{-1} that could be related to N-H stretching modes.

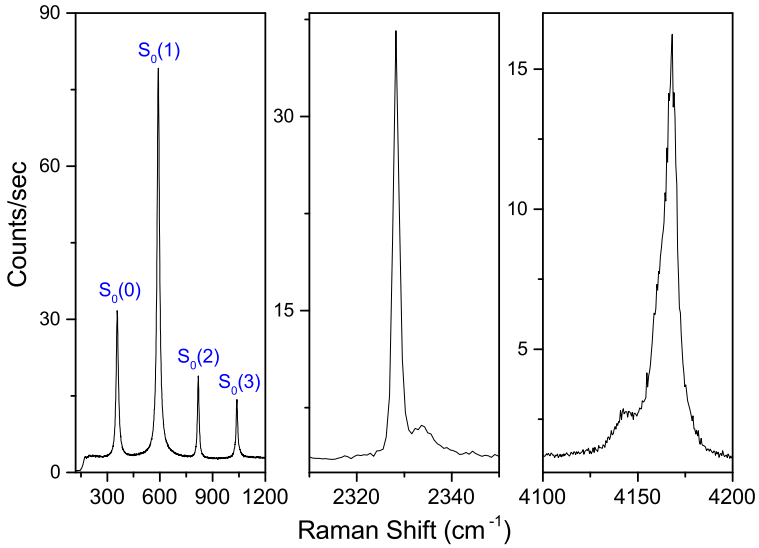

Figure 3.12: *Raman spectra of the "bubbles" region in the P-red/NH_3 sample after irradiations. Left panel: low frequency region, showing the four, intense rotational bands of molecular hydrogen, labelled $S_0(0)$, $S_0(1)$, $S_0(2)$, $S_0(3)$. Central panel: region of P-H stretching, where the intense Raman band from PH_3 is visible. Right panel: high frequency region, showing the intense Raman band related to H-H stretching mode in molecular hydrogen. Integration time: 500 seconds.*

Exploiting the high spatial resolution of the micro-Raman equipment, it was possible to investigate different regions of the sample. Raman spectra were acquired using few mW of 647.1 nm wavelength on bubbles, solid P-red, product region and fluid (bulk) NH_3. Figure 3.12 reports the Raman spectra acquired on the bubbles visible in the optical images of figure 3.9, central panel. In the low frequency region, the four intense rotational bands

of molecular hydrogen, H_2, are visible: $S_0(0)$ at 357.5 cm^{-1}, $S_0(1)$ at 590 cm^{-1}, $S_0(2)$ at 818.1 cm^{-1} and $S_0(3)$ at 1038.6 cm^{-1} [197,198]. Furthermore, at 4167 cm^{-1}, also the H-H stretching band is visible. This confirms the production of H_2 during the photoinduced reaction of P-red and NH_3. As in the case of P-black/NH_3 sample, but to a more extent, Raman spectra confirm also the formation of phosphine, as indicated by the intense Raman band at 2328 cm^{-1}.

Even more interesting results are visible in the region of the sample where P-red was, and where a solid product is formed. In fact, three different Raman profiles, possibly related to three different solid products, are visible in the spectra. Figure 3.13 reports the Raman spectra of the three different products (labeled as P1, P2 and P3) together with the Raman spectra of P-black and P-red to have a direct comparison. Raman spectra of P-black [180] and P-red [173] have been acquired at the beginning of the P-black/NH_3 and of the P-red/NH_3 experiments, respectively. The red trace refer to the spectra of P1 at ambient conditions. First of all, Raman spectrum of P1 shows a completely different profile in the phonon region between 200 and 500 cm^{-1}, more defined under high pressure (0.8 GPa) than at ambient conditions. More in detail, Raman signals are visible at 224 cm^{-1}, followed by a doublet at 281 and 297 cm^{-1}, the most intense peak at 337 cm^{-1}, other less intense peaks at 380 cm^{-1}, 409 cm^{-1} and a doublet at 453 and 471 cm^{-1}. P2 (blue trace in the figure) has a completely different spectrum: a broad, weaker and structured profile between 200 and 400 cm^{-1}, likely due to lattice modes, and two strong and sharp bands at 545 and 725 cm^{6-1}, ascribable to internal modes. Also this product is retained at ambient conditions. Finally, P3 (green traces) presents a broad doublet at 670-725 cm^{-1}, but what is noticeable is that, on releasing pressure and opening the cell, the spectrum disappears and transforms into a profile closely reminding that of H_xPO_y species and particularly H_3PO_3 [174], thus suggesting a metastability of P3 which decomposes in atmosphere.

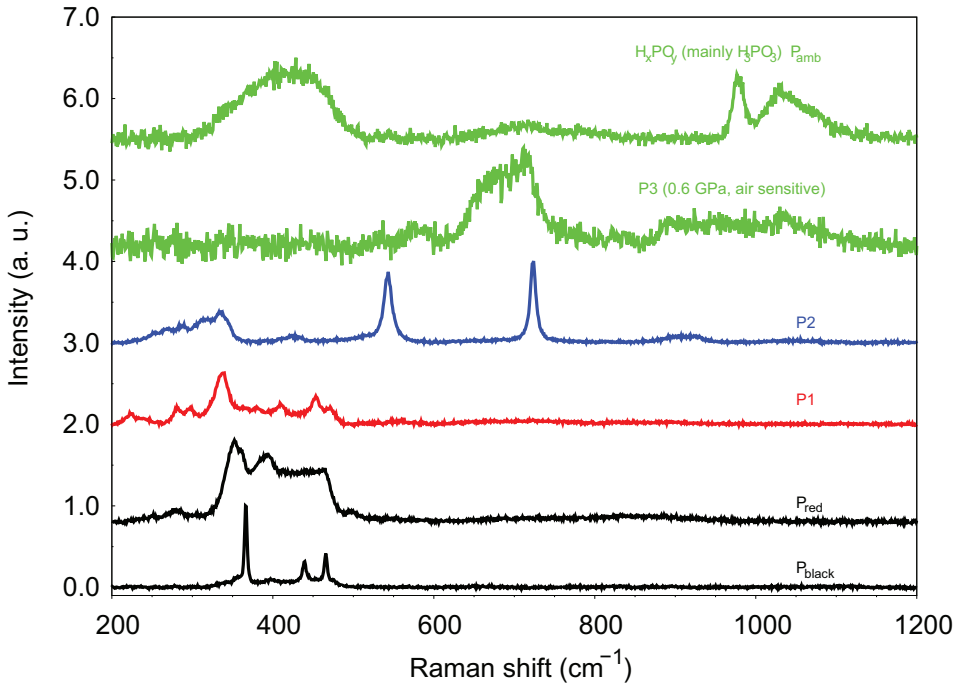

Figure 3.13: *Raman spectra of the three different solid products of P-red/NH_3 photoinduced reaction. From bottom to top: Raman spectra of P-black and P-red (black traces); Raman spectra of P1 at ambient conditions (red trace); Raman spectrum of P2 (blue trace); Raman spectra of air sensitive P3 before and after opening the cell (green traces). The spectra were vertically shifted for the sake of clarity and were normalized to allow a direct comparison.*

Besides of the air sensitive P3, probably amorphous and characterized by P-H functionalities that, in contact with the atmospheric moisture, turns to H_3PO_3 specie, a complete and detailed assignment of the Raman spectra of P1 and P2 is not possible. In order to understand the extension and the regions of formation of the three products, we performed a complete Raman mapping of the sample both under pressure (0.6 GPa, after the last irradiation) and at room pressure conditions, in the spectral regions where phonon bands, P-H groups bands and N-H bands are visible. Figure 3.14 summarizes these results in a visual colormap. In the maps, P1 is highlighted in red, P2 in blue and P3 in green. Unreacted P-red is indicated by yellow squares. It is immediately evident how the P3 is distributed on the edge of

the solid region, where a grainy solid is visible: the edges of the solid part of the sample are the first to deteriorate in contact with the atmospheric moisture, when P3 turns into H_3PO_3 (from green circles to green squares in the colormap). The solid part of the sample seems equally divided in three parts, one with a major presence of P1 (in the center), one mostly P2 and the other one with the residual, unreacted P-red. Besides the phonon region, the high frequency spectral regions gives very interesting hints about the actual structures of P1 and P2. At 0.6 GPa, the Raman spectra acquired on P-H region (between 2000 and 2800 cm^{-1}) showed the presence of phosphine everywhere in the sample (not reported on the map) and some points where P-H stretching of phosphine is present together with a broader P-H stretching band centered at about 2360 cm^{-1}, mainly located in the region of the sample where P2 is found (blue dots). Once opened the DAC, the P-H stretching band disappears almost everywhere on the sample, being likely related to the amorphous P3 fraction that turns into oxyacid derivatives of phosphorous in contact with the atmospheric moisture. The Raman map of the 2000-2800 cm^{-1} spectral region is therefore almost empty, thus stating that there is almost no regions where P-H stretching signal can be found on the recovered sample. More interestingly, the Raman map of the recovered product in the N-H stretching spectral region (2800-3600 cm^{-1}) reveals a clear correspondence in the spatial distribution of the N-H band with the spatial distribution of P2 (blue dots in the top and bottom maps of the right column, figure 3.14). This means that the recovered P2 should feature N-H functionalities in its chemical structure. Summarizing the results, P3 is an amorphous, air-sensitive product characterized by the presence, in its structure, of P-H functionalities, and cannot be recovered at ambient conditions, decomposing with the formation of oxyacids, mainly H_3PO_3. P2 presents narrow bands at 545 and 725 cm^{-1}, and weaker bands centered at 355 cm^{-1}; in addition, the regions where this product is found are also rich in N-H functionalities, thus suggesting the presence of this group in its chemical structure. P1 has a completely different lattice phonon spectrum of both pristine P-black and

P-red, with narrow bands and a complex and detailed structure, and on its spatial region on the sample neither P-H nor N-H Raman signals have been found. Both products 1 and 2 are recoverable at ambient conditions.

According to the crystalline nature of the products of P-red/NH_3 reactivity, additional information for their identification can be provided by XRD. A synchrotron XRD mapping have been executed on the solid portion of the sample both at 0.6 GPa and at ambient conditions. In figure 3.15, a comparison has been established between the Raman spectra in the phonon region of the P-red/NH_3 sample, with the identification of the three different products described above, and the XRD patterns acquired on a mesh at ID27 (ESRF). The mesh was 100x80 with a spacing of 10 μm, for a total of 80 patterns of 20 seconds duration each one, on the solid part of the sample and therefore, differently from the Raman maps, not considering the whole sample area, that would have required much longer acquisition times. XRD patterns reveal no significant differences in the region where P1 and P2 were identified from the Raman spectrum, so there are no features able to distinguish between the two spectroscopically labelled product, thus suggesting the idea that one of these sample is probably amorphous and, therefore, gives no XRD peaks. However, the XRD patterns corresponding to a crystalline product are found in a region with a good superimposition with the points where only P2 was found at Raman, even if a 100% reliability of the assignment cannot be ensured due to likely errors in the motor movements while performing the acquisitions, and to difficulties in establish an exact correspondence between the two different maps (Raman and XRD). The single XRD 2D images reveal single spots signals and no rings all over the sample, thus suggesting the presence of a highly oriented polycrystalline reaction product: furthermore, the peak intensities are not always the same, and this is clearly an effect related to the orientation of the crystal domains. Figure 3.16 reports an example of a typical integrated XRD pattern acquired on the recovered P-red/NH_3, together with the related 2D diffraction image.

Summarizing the results obtained in these two experiments concerning

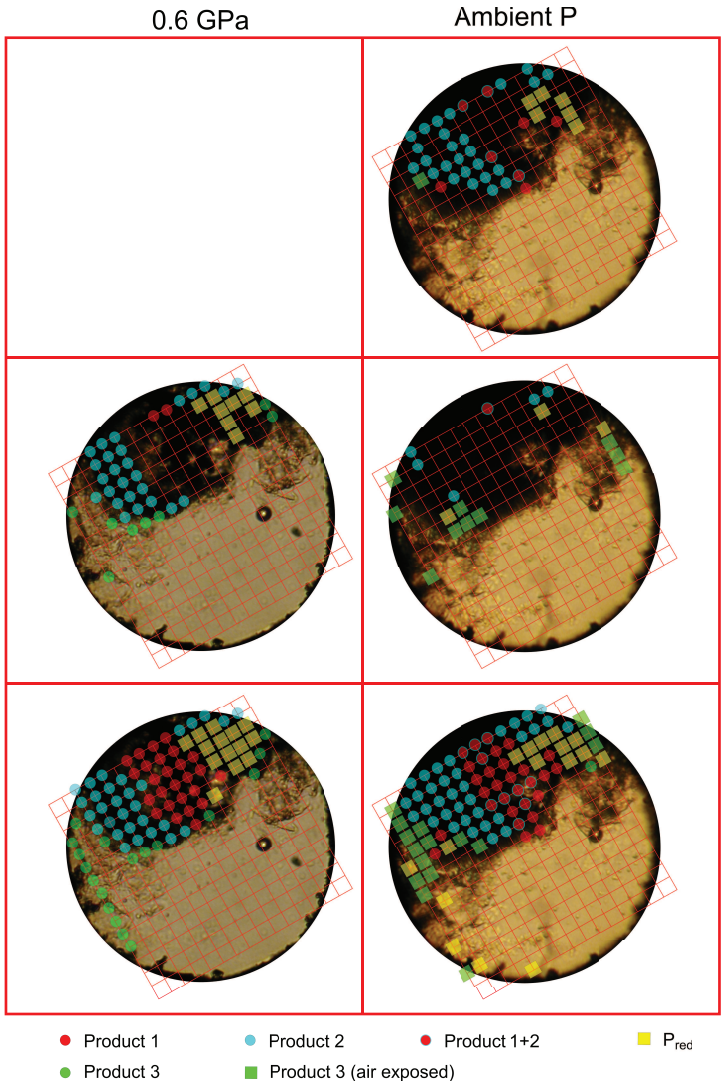

Figure 3.14: *Visual representation of micro-Raman mapping on the P-red/NH_3 sample in three different spectral regions under pressure (0.6 GPa, left column) and at ambient conditions (right column). Bottom row shows the results for the low frequency region of the spectra (phonon region); central row, the results for the frequency region between 2000 and 2800 cm^{-1}, where P-H stretching bands are found; top row, the results for the frequency region between 2800 and 3600, where N-H stretching bands are found. The color legend is reported in the figure.*

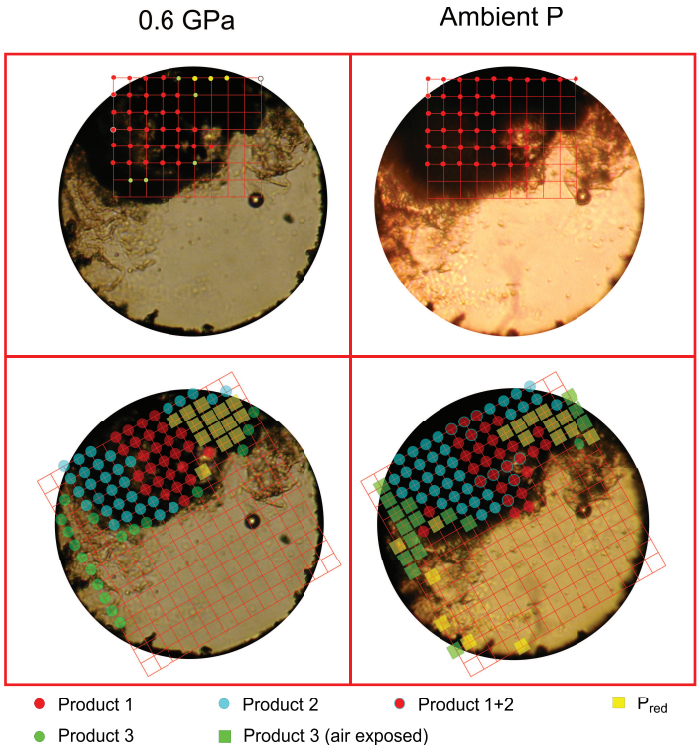

Figure 3.15: *Comparison between the visual representation of micro-Raman mapping on the P-red/NH_3 sample in the low frequency region under pressure (0.6 GPa) and at ambient conditions, and the XRD mapping on the same sample at the same conditions. Left column: maps acquired under pressure (0.6 GPa); right column: maps acquired at ambient conditions. Bottom row: representation of Raman mapping; top row: representation of XRD mapping. The color legend is reported in the figure.*

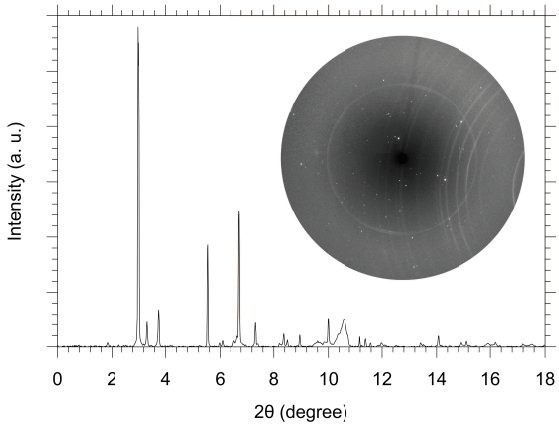

Figure 3.16: *Example of one of the integrated XRD patterns acquired on the recovered sample of P-red/NH_3 together with its related 2D image. Data acquired at ID27, ESRF (λ = 0.3738 Å).*

the reactivity of NH_3 with P-black and P-red, several interesting features have to be discussed. First of all, our experiments show how P-black is far less reactive than P-red, as expected (due to its well known higher stability): the FTIR spectra acquired on P-black/NH_3 attest for a consumption of about 21% of the starting, loaded NH_3. Reactivity is attested by the appearance of absorption bands related to mostly P=N, but also P-N and P-NH_2 functional groups (see figure 3.7). Raman spectra on the P-black/NH_3 sample suggest the formation of a small amount of phosphine and the appearance of some products involving P-H bonds in its chemical structure. More generally, our results highlight for a substantial conservation of the P-black layered structure upon the explored reaction conditions, thus suggesting that the high pressure functionalization occurs on the surface while preserving the single phosphorene layers. XRD patterns, acquired on the recovered P-black/NH_3 mixture and here not reported, confirm the stability of the layered structure, showing the characteristic Bragg peaks from orthorhombic P-black at ambient conditions.

P-red shows instead a much higher and complex high pressure, photoinduced reactivity with NH_3. FTIR spectra attest for a huge consumption

of the starting ammonia (about 72%, see figure 3.10) and for the formation of several new absoprtion bands in a shorter time (a total of 60 hrs of irradiation) than in the case of P-black/NH_3 mixtures. P-red, being an amorphous, polymeric material made up of P-chains, provides much more surface to the attack from NH_3 with respect to P-black, and this could help to explain the differencies in the extent of the photoinduced reactions of the two allotropes in the same P,T,hν conditions. In any case, the reaction ends up in a mixture of heterogeneous products: fluid PH_3 and H_2 (the latter found only in the P-red/NH_3 sample, see figure 3.12), and three different solid products, labeled P1, P2 and P3, found in the Raman spectra (see figure 3.13) acquiring in different region of the sample by exploiting the high spatial resolution provided by the micro-Raman setup (see section 4.4). P3, characterized by the presence of P-H functional groups in its chemical structure, was found to be air-sensitive, completely transforming into mainly H_3PO_3 upon cell opening and exposure to atmospheric moisture. P1 and P2 are, instead, solid products recoverable at ambient conditions, but their assignment and correct identification is not possible at the moment. P1 is characterized by a complex low frequency phonon region, completely different from that of the starting P-red, and no P-H or N-H groups have been detected by Raman spectroscopy in the region where it was found. On the other hand, P2 is characterized by the presence of two very strong and sharp Raman bands at 545 and 725 cm^{-1}, together with a far less intense lattice phonon region. Raman mapping in the regions where P2 was found attests for the presence of N-H groups on this solid product. The assignment of these two extended solid products, involving P-N and P=N functionalities in their structures, has been tried through a comparison with the literature data about various phosphorous nitride imides (of general formulation given by HP_xN_y) and phosphorous nitrides (general formula P_xN_y). FTIR spectra of P-red/NH_3 mixtures showed similarities with the FTIR spectra of phosphorous nitride imides of general formula HP_xN_y, and particularly HPN_2 [199]. Raman spectra, thanks to the high spatial resolution of our equip-

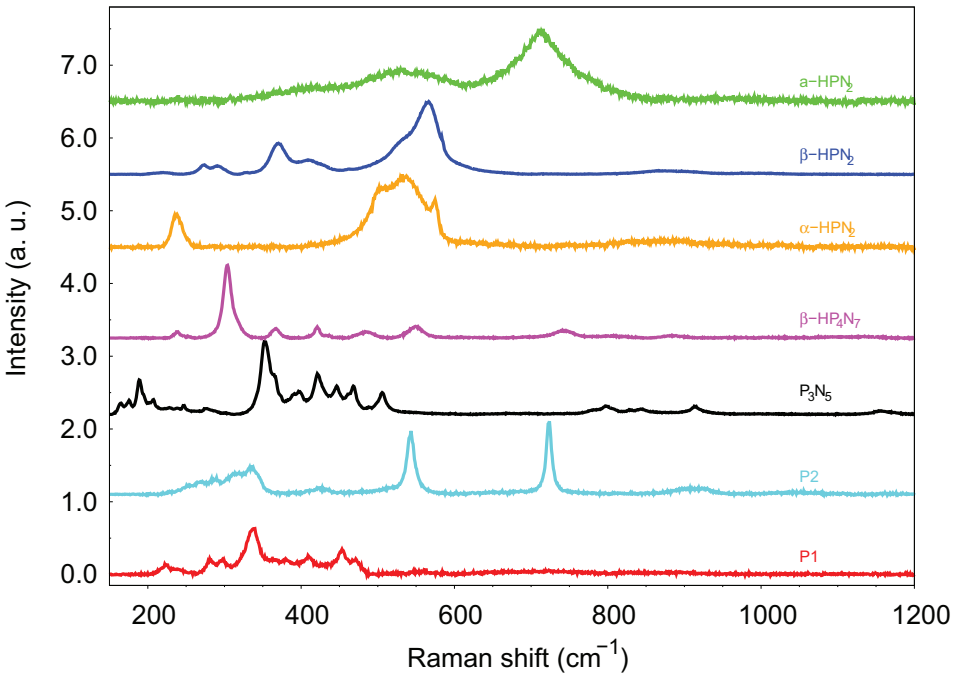

Figure 3.17: *Comparison between the Raman spectra of recovered solid products of P-red/NH_3 photoinduced reaction with the Raman spectra of model P_xN_y and HP_xN_y compounds. Red: P1; cyan; P2; black: P_3N_5; magenta: β-HP_4N_7; orange: α-HPN_2; blu: β-HPN_2; green: a-HPN_2. Spectra were vertically shifted for the sake of clarity.*

ment, allowed to identify at least three different products. To complete the assignment, we have therefore compared the Raman spectra of our products with those of some of this PN compounds. Figure 3.17 reports the Raman spectra of P1 and P2 together with those of P_3N_5 [200–204], β-HP_4N_7 [205] and of three different allotropes of HPN_2, and in particular the crsytalline α-HPN_2 [199] and β-HPN_2 [206] and the amorphous a-HPN_2 [199]. P1 shows a lattice phonon region closely reminding that of P_3N_5 [200], consistently with the absence of Raman signals that could be referred to P-H and N-H functionalities (see Raman maps of figure 3.14). For what is about P2, its two sharp bands at 545 and 725 cm^{-1} closely remind the Raman spectrum of β-HP_4N_7 [205], even if with different intensities and a less defined lattice phonon region.

XRD mapping of the solid region in the P-red/NH_3 sample was performed to find structural signatures that could be helpful for a reasonable product assignment. The results of the mesh mapping of the sample (sse figure 3.15) suggest the presence of a crystalline phase inside the cell, that can be recovered at ambient conditions, and give no hints about the presence of two different solid besides of the fact that one of these two could be amorphous. In fact, the XRD powder data are essentially the same in every point of the grid, and a significant superimposition between crystal patterns found in XRD mapping and the Raman signature for the so called P2 were found. These could mean that, to some extent, both products can be crystalline and contribute to the XRD spectrum, but diffraction data are not sufficient to distinguish between them as Raman data were. To find a correct assignment for the reaction product, a comparison between the XRD data acquired on P-red/NH_3 sample and literature data for P_xN_y and HP_xN_y structures is mandatory. The XRD pattern from the recovered product of the photoinduced reaction between P-red and NH_3 is due to spot signals in the 2D image, thus suggesting the presence of a highly oriented crystalline solid in the form of a multi-grains mixture of not sufficiently broad orientational distribution. For the sake of comparison, a summation over all the integrated powder XRD patterns collected in the grid points have been performed both for the data acquired under pressure (0.6 GPa) and for the data acquired after opnening the cell (at ambient conditions) to roughly average between grain orientations. In figure 3.18, the comparison between the summation of XRD patterns of the recovered product at 0.6 GPa and at P_{amb} and the XRD patterns from P-black [179], β-HP_4N_7 [205], α- and γ-P_3N_5 [200–204] and α- and β-HPN_2 [199,206] is reported. The XRD data for the HP_xN_y and the P_xN_y compounds have been found in the COD database or reconstructed from the CIF data reported in literature. Looking at the XRD pattern of the recovered P-red/NH_3 sample, both at 0.6 GPa and at ambient conditions, the strong reflection at 2θ values of 10.58 is due to the gasket and is the only observed rings in the 2D diffraction image. The most interesting part

of the XRD patterns in the recovered sample of P-red/NH_3 lies in the low angle region, between 3.0° and 4.0°, where the solid product has three sharp diffraction peaks that are not found in any other of the compared systems. In fact, two of these peaks, at 2θ values of about 3.0° and 3.8° Å, do not match with any of the other considered products. The only two products having reflections below 5.0° are γ-P_3N_5 and β-HP_4N_7: in both cases, there is a single peak at an angle of 3.40°, in a pretty good agreement with the central peak in the three-peaks structure of the recovered product (that lies at 2θ about 3.35°). Furthermore, γ-P_3N_5 and β-HP_4N_7 present also very intense Bragg reflections between 2θ 5.0 and 5.5° and in between 2θ 6.5 and 7.0°, where the recovered sample has a very intense peak (slightly asymmetric, at 2θ of about 5.20°) and a doublet (at 2θ values of 6.71 and 6.83°). At the moment, no other assignment has been made on the recovered product, but it would be really interesting to find a connection between the low angle peaks exhibited by the recovered product of the high pressure, photoinduced reaction of P-red and NH_3 and some other PN product synthesized at high pressure, so to establish a correlation between the high density conditions and the particular structure of the resulting products. Single crystal XRD (SC-XRD) measurements have been performed on the recovered P-red/NH_3 product at ID27 beamline, ESRF, but the results are currently under elaboration and no more details can be added to this discussion.

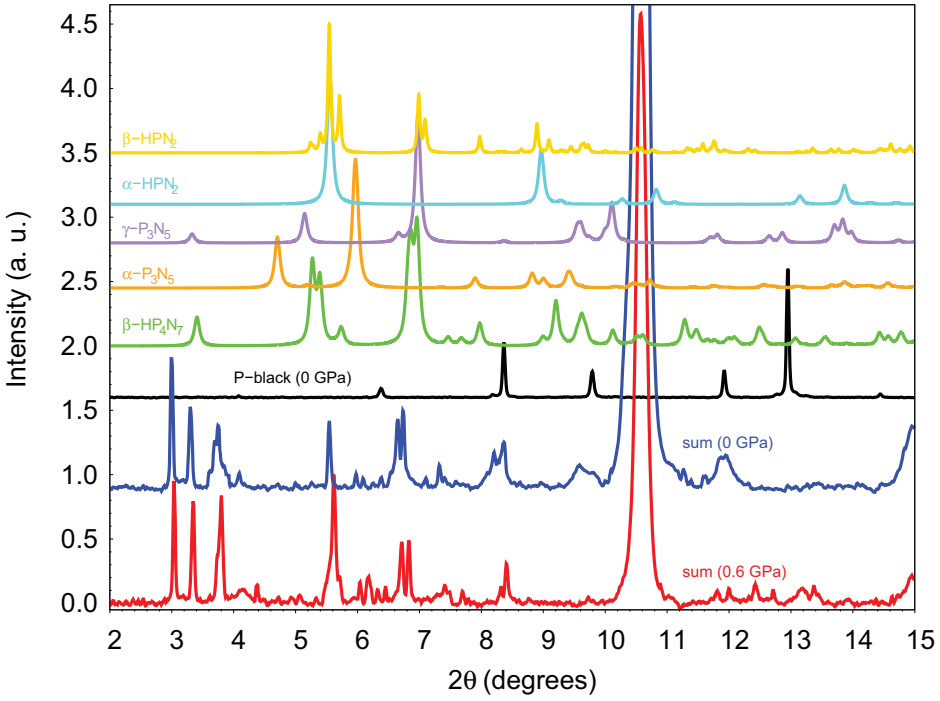

Figure 3.18: *Comparison between XRD data on the recovered P-red/NH_3 sample and XRD patterns of P-black and other PN products. The XRD patterns from the recovered sample at two different pressure (0.6 GPa, red trace, and ambient pressure, blue trace) have been obtained as a summation over all the integrated powder XRD patterns collected in the grid points to roughly average between grain orientations. P-black XRD pattern at ambient conditions (black trace), measured at ESRF, and β-HP_4N_7, α- and γ-P_3N_5 and α- and β-HPN_2 XRD patterns are also reported as a comparison. XRD patterns were vertically shifted for the sake of clarity.*

3.3 High pressure behaviour of P-black in the presence of small molecules

The high pressure behaviour of P-black in the presence of small atoms and molecules (He, H_2) has been studied by means of synchrotron XRD technique. These studies have the twofold purpose to highlight the high pressure stability of P-black upon compression and to find evidencies of simple molecules insertion between the layers. This could be indeed relevant in view of high pressure functionalization of the layers or the synthesis of new nanocomposite materials. He and H_2 were loaded in DAC by means of *Gas-loading*, in the presence of a small P-black crystal and of a ruby chip as a pressure gauge. The experiments were designed in the perspective of favouring the insertion of He atoms and H_2 molecules between the layers of P-black by exploiting high density conditions in combination with excellent performances as compression medium. Figure 3.19 reports the experimental melting curves of He and H_2 together with a simplified phase diagram for P-black. The curves elucidate the better P,T conditions to have the conjunction of high density and good mobility (fluid phase) for the two systems to profitably occupy the space between the layers. The melting curve indicates how both He and H_2 should be in the fluid phase before the first phase transition in P-black, thus allowing to profitably modify density conditions before their crystallization in order to favour the insertion process. Experimental data for the melting curves reported in figure 3.19 are taken by the work of Datchi and coauthors, see reference [100].

P-black/He and P-black/H_2 samples were studied during room temperature compression/decompression up to 28 GPa and 17 GPa, respectively. In these pressure ranges, P-black shows two phase transitions, from the starting orthorhombic phase (A17, space group *Cmca*, 8 atoms per unit cell) to the rhombohedral one (A7, space group $R\bar{3}m$, two atoms per unit cell), at 5.5 GPa, and then from the rhombohedral to the simple cubic phase (sc, space group $Pn\bar{3}m$, one atom per unit cell), at about 10.3 GPa. In figure 3.20 the

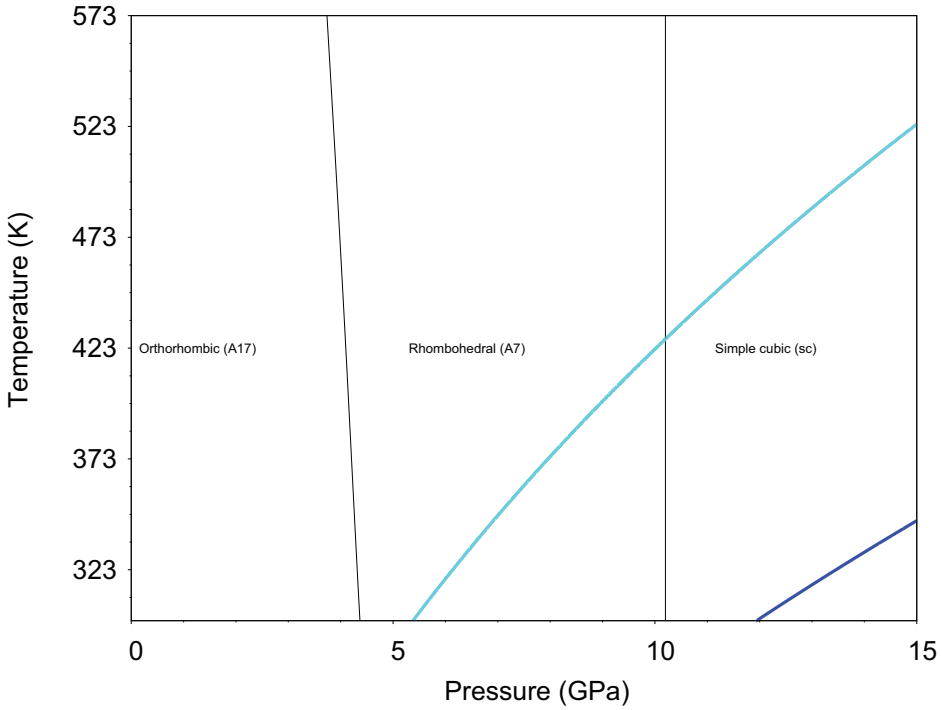

Figure 3.19: *Experimental melting curves for He and H_2 and simplified phase diagram of P-black. Cyan curve: experimental melting line for H_2 [100]; blue curve: experimental melting line for He [100].*

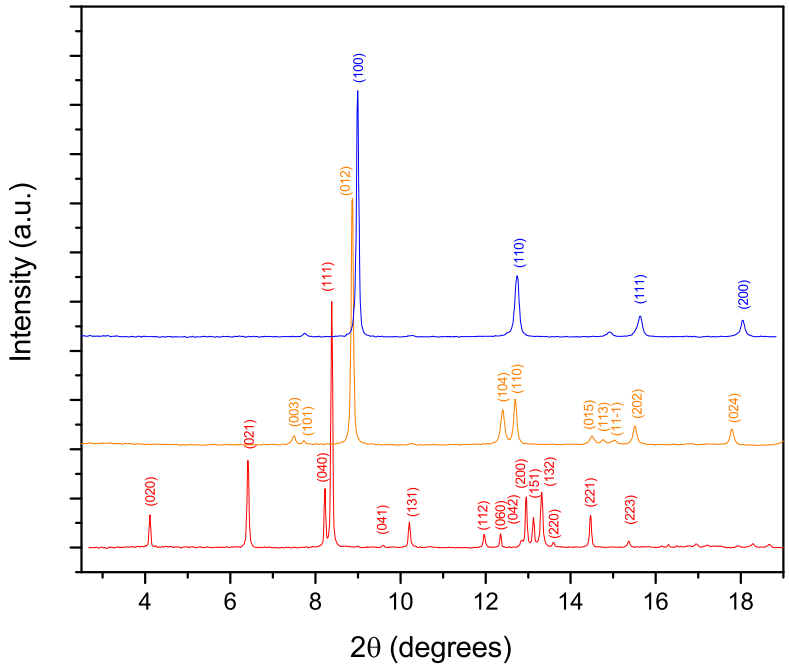

Figure 3.20: *Integrated XRD patterns for P-black in A17, A7 and sc crystal phases, together with the peak assignment. From bottom to top: red trace, experimental integrated XRD pattern for P-black in the orthorhombic phase (0.22 GPa); orange trace, experimental integrated XRD pattern for P-black in the rhombohedral phase (6.53 GPa); blu trace, experimental integrated XRD pattern for P-black in the simple cubic phase (11.23 GPa); Peak assignment is reported in the same colour of the referring phase. In the rhombohedral A7 phase, indices are assigned in terms of a hexagonal lattice. The integrated patterns were vertically translated for the sake of clarity.*

characteristic experimental integrated XRD patterns of P-black in this three phases, together with the Bragg reflections assignment, are reported.

The experimental patterns acquired in the three phases and showed in figure 3.20 are in agreement with available literature data [189, 190]. More in detail, in the orthorhombic phase the Bragg peaks shift towards higher 2θ values, thus suggesting a decrease in the interlayer spacing with pres-

sure. $(040)_o$ and $(111)_o$ reflections get nearer to each other and convolute in an unique Bragg peak at about 2 GPa, while $(042)_o$ reflection moves, with respect to $(200)_o$, from lower to higher 2θ values between 0.22 and 1.50 GPa. $(200)_o$ reflection is the only one that doesn't shift and maintain its position upon increasing pressure. A common feature for the XRD pattern acquired on P-black/He and P-black/H_2 samples regards the intensity ratios between the peaks, that abruptly change during the experiment due to random orientation of the P-black crystallites. At the phase transition between orthorhombic and rhombohedral phases, two new reflections appear, indexed as $(104)_r$ and $(110)_r$ in terms of a hexagonal lattice, whereas the $(020)_o$ and $(021)_o$ reflections from orthorhombic phase disappear. The integrated XRD pattern for the simple cubic phase is much simpler than the previous two. The phase transition to (sc) phase is attested by the appearance of the $(200)_c$ Bragg peak. During the transition, the $(104)_r$ and $(110)_r$ reflections shift towards each other and the $(110)_c$ peak appears, superimposed to the two reflections from the rhombohedral phase. The reflections indexed as $(101)_r$, $(015)_r$ and $(024)_r$ from the rhombohedral phase disappear, while reflections indexed as $(012)_r$, $(110)_r$ and $(202)_r$ continuously turn into $(100)_c$, $(110)_c$ and $(111)_c$, respectively. This is the expected behaviour for the A7 to (sc) transition, due to the fact that rhombohedral space group is a subgroup of the simple cubic one.

The room temperature compression/decompression of P-black/He sample has been studied up to a maximum pressure of 27.5 GPa. The XRD patterns acquired during the compression steps are the same reported in figure 3.20 above. The first phase transition of P-black from the orthorhombic A17 to the rhombohedral A7 phase occurs at about 4.6 GPa. Due to some hysteresis in the sample despite of the hydrostatic pressure compression medium, the Bragg reflections from the A17 phase are still visible for about 2 GPa into the rhombohedral one. The second phase transition from rhombohedral A7 to simple cubic (sc) phase presents at 10.2 GPa. By the equations connecting the d-spacing of the Bragg peaks to the Miller indices, the values of the cell

parameters and of the volume of the three phases can be computed. In figure 3.21, the evolution of cell parameters for the orthorhombic phase of P-black during room temperature compression/decompression in the presence of He are reported. Figure 3.22 reports, instead, the evolution with pressure of the volume per atom for the same phase, and the comparison with literature data.

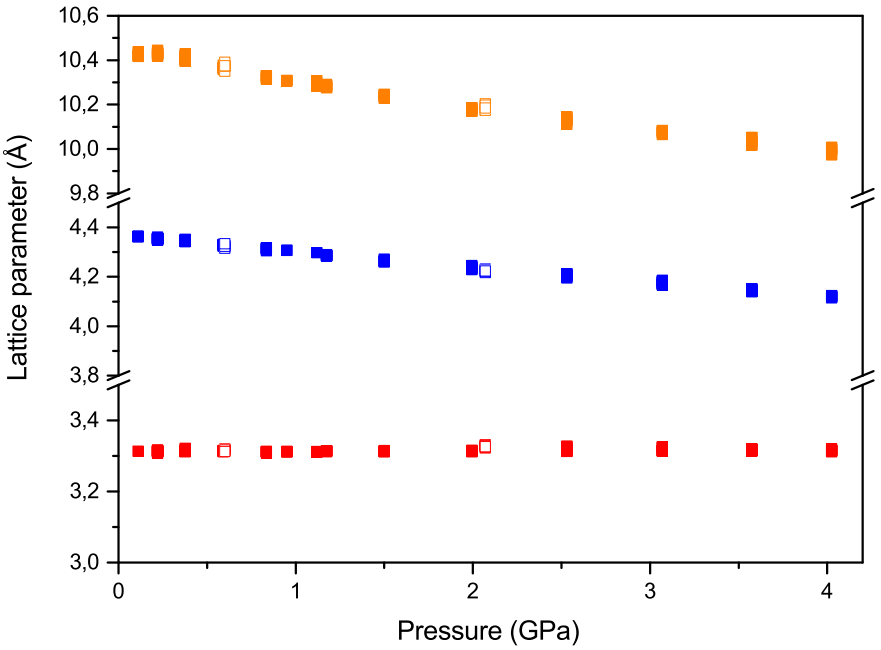

Figure 3.21: *Evolution with pressure of cell parameters for the orthorhombic phase of P-black during room T compression in the presence of He. Red: "a" parameter in compression (full squares) and decompression (open squares). Orange: "b" parameter in compression (full squares) and decompression (open squares). Blue: "c" parameter in compression (full squares) and decompression (open squares). The error in the fit procedure is negligible, while the error in the pressure measurements by ruby fluorescence method is considered to be ±5%.*

The computed volume per atom evolution with pressure for P-black/He sample in the orthorhombic phase is in very good agreement with previous

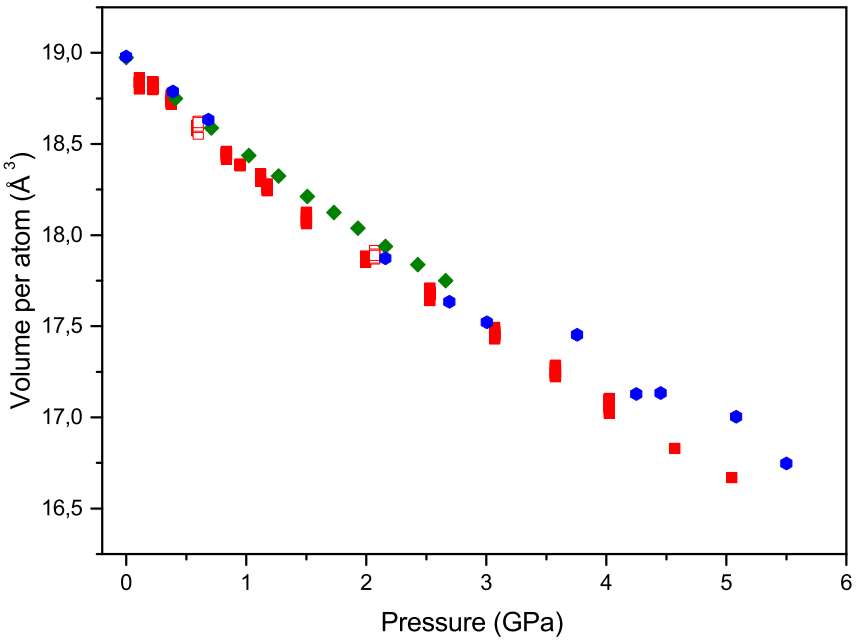

Figure 3.22: *Evolution with pressure of volume per atom for the orthorhombic phase of P-black during room T compression in the presence of He. Red: experimental data for P-black/He sample during compression (full squares) and decompression (open squares). Blu hexagons: experimental data from Kikegawa and Iwasaki, see reference [179]. Green diamonds: experimental data from Cartz and coauthors, see reference [189].*

literature data by Kikegawa *et al.* [179] and Cartz *et al.* [189]. In figure 3.23, the evolution of cell parameters for the rhombohedral phase of P-black during room temperature compression/decompression in the presence of He are reported. Figure 3.24 reports, instead, the volume per atom evolution with pressure for the same phase, and the comparison with literature data.

Figure 3.24 shows a comparison between experimental data in P-black/He sample and the available literature data from Kikegawa *et al.* [179] and Clark *et al.* [207]. Data quality for experimental P-black/He points is far better than the literature ones, characterized by a greater uncertainty. Finally,

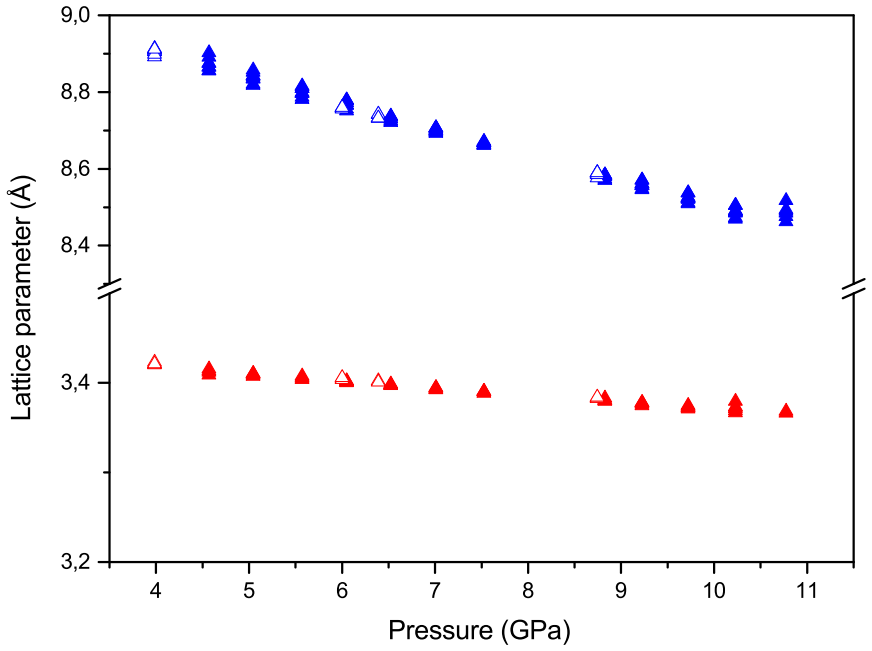

Figure 3.23: *Evolution with pressure of cell parameters for the rhombohedral phase of P-black during room T compression in the presence of He. Red: "a" parameter in compression (full triangles) and decompression (open triangles). Blue: "c" parameter in compression (full triangles) and decompression (open triangles).*

in figure 3.25, the evolution of the cell parameter a for the simple cubic phase of P-black during room temperature compression/decompression in the presence of He are reported. Figure 3.26 reports, instead, the volume per atom evolution with pressure for the same phase, and the comparison with literature data.

In the case of simple cubic phase for P-black, as it was evident also for the rhombohedral cell volume, the experimental data obtained during room temperature compression in the presence of He show a very high quality with respect to literature data. More in detail, the pressure evolution of volume per atom is particularly smooth if compared to the data from Clark *et al.* [207] but, mainly, from Kikegawa *et al.* [179]. In the latter case, the far less

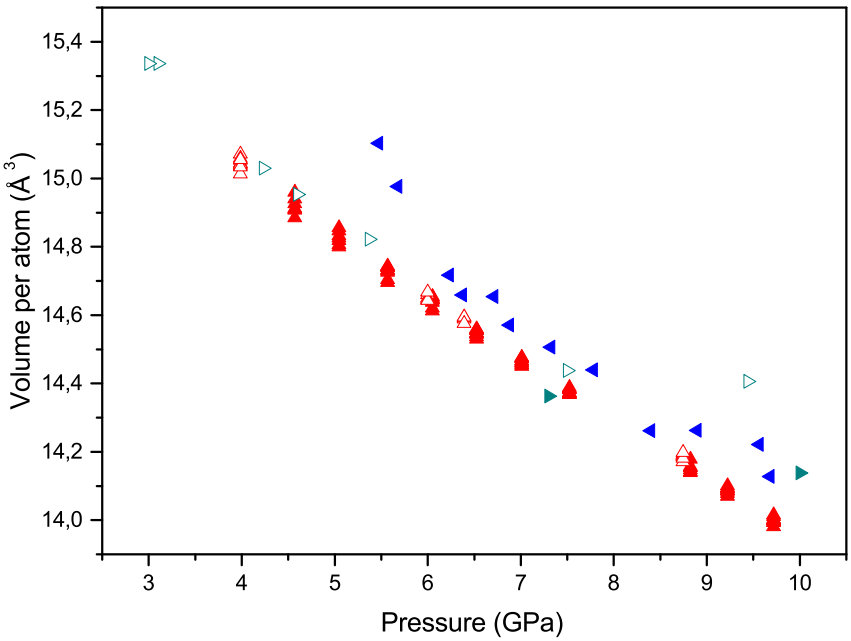

Figure 3.24: *Evolution with pressure of volume per atom for the rhombohedral phase of P-black during room T compression in the presence of He. Red: experimental data for P-black/He sample during compression (full triangles) and decompression (open triangles). Blu right-rotated triangles: experimental data from Kikegawa and Iwasaki, see reference [179]. Cyan left-rotated triangles: experimental data from Clark and Zaug during compression (full) and decompression (open), see reference [207].*

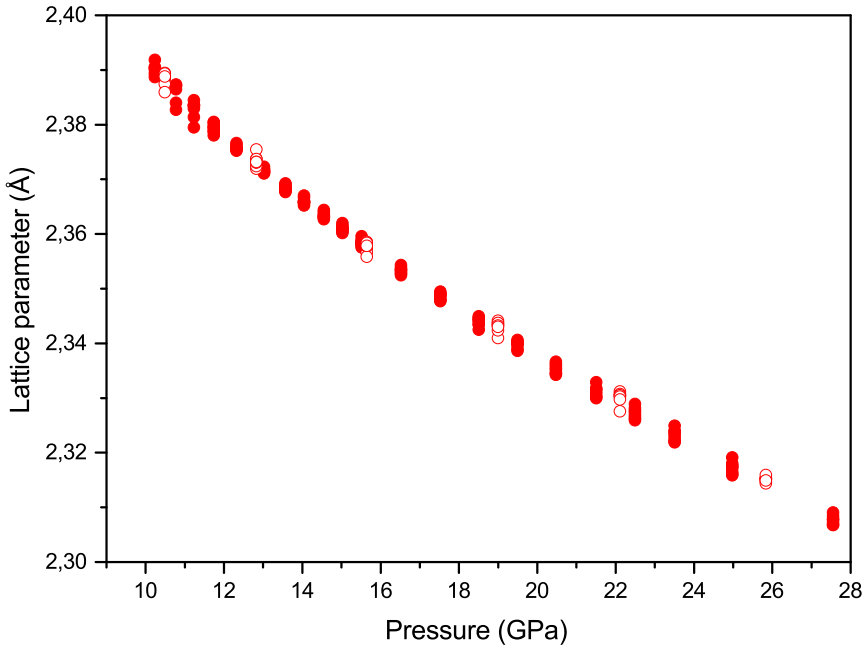

Figure 3.25: *Evolution with pressure of cell parameter "a" (red) for the simple cubic phase of P-black during room T compression in the presence of He. Full circles: values computed during compression. Open circles: values computed during decompression.*

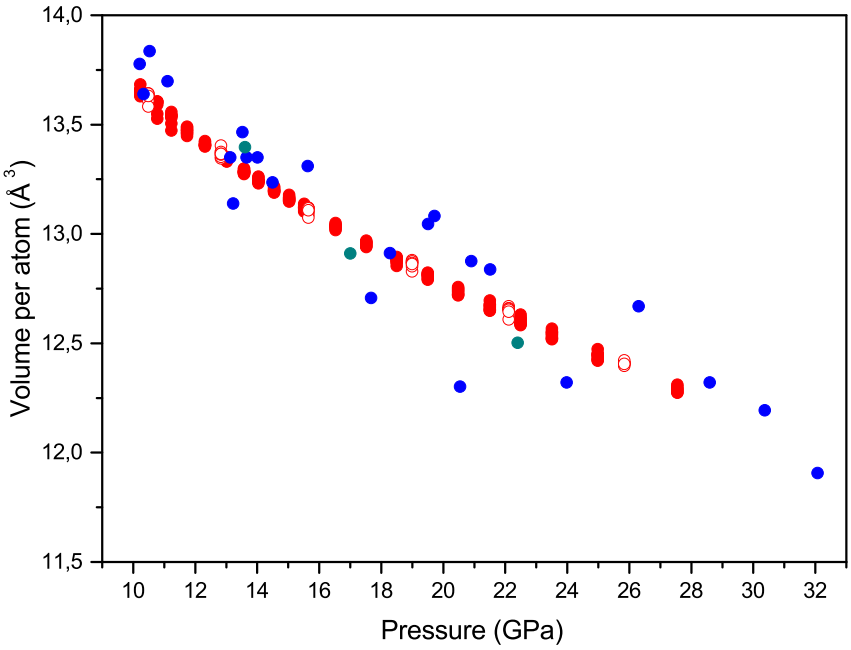

Figure 3.26: *Evolution with pressure of volume per atom for the simple cubic phase of P-black during room T compression in the presence of He. Red: experimental data for P-black/He sample during compression (full circles) and decompression (open circles). Blu circles: experimental data from Kikegawa and Iwasaki, see reference [179]. Cyan circles: experimental data from Clark and Zaug, see reference [207].*

spread of the calculated volume per atom values can be related to the good hydrostaticity of He as a pressure transmitting medium in the investigated pressure range with respect to sodium chloride (NaCl), used by Kikegawa *et al.* [179].

The volume per atom of orthorhombic, rhombohedral and simple cubic phases of P-black, calculated from the measured lattice parameters as a function of pressure, has been reproduced by the Vinet equation of state [208, 209]:

$$P = 3k_0 \frac{1 - f_v}{f_v^2} exp\left[\frac{3}{2}(k' - 1)(1 - f_v)\right] \tag{3.1}$$

The *strain* f_v is expressed as

$$f_v = \left(\frac{V}{V_0}\right)^{\frac{1}{3}} \tag{3.2}$$

whereas K_0 and K' are the *bulk modulus* and its firts derivative, respectively. Treating V_0 as an adjustable parameter for the three phases, where it was possible, K_0 and K' have been computed, yielding V_0= 18.91±0.02 Å^3, k_0= 33.3±1.3 GPa and k'= 3.1±0.6 for the orthorhombic A17 phase; V_0= 15.88±0.02 Å^3, k_0= 69.1±2.4 GPa and k'= 1.8±0.4 for the rhombohedral A7 phase; V_0= 14.92 Å^3, k_0= 89.7±0.8 GPa and k'= 4.7±0.1 for the simple cubic sc phase. In figure 3.27, the pressure dependence of the atomic volume of P-black at 300 K across the three mentioned phases in the P-black/He experiment is reported, together with the Vinet equation of state fit. The main error on experimental data was found to be a 5% uncertainty in the pressure measurement, whereas the error due to the fitting procedure was found to be negligible. The experimental data for the P-black/He room temperature compression/decompression experiment were of a very good quality, allowing to measure a reliable equation of state with respect to the literature data. In the comparison with the main literature sources, we found a very good agreement for what is concerned with the orthorhombic A17 and the rhombohedral A7 phases, for which our calculated V_0 and k_0 values nicely agree

with data from Kikegawa *et al.* [179] and Clark *et al.* [207]. As the simple cubic sc phase is concerned, our experimental data attest for a *bulk modulus* of 89.7±0.8, that is in better agreement with the values from Kikegawa and coauthors (k_0=95±5 GPa, see ref. [179]) than with the data from Clark *et al.* [207] and Akahama *et al.* [181].

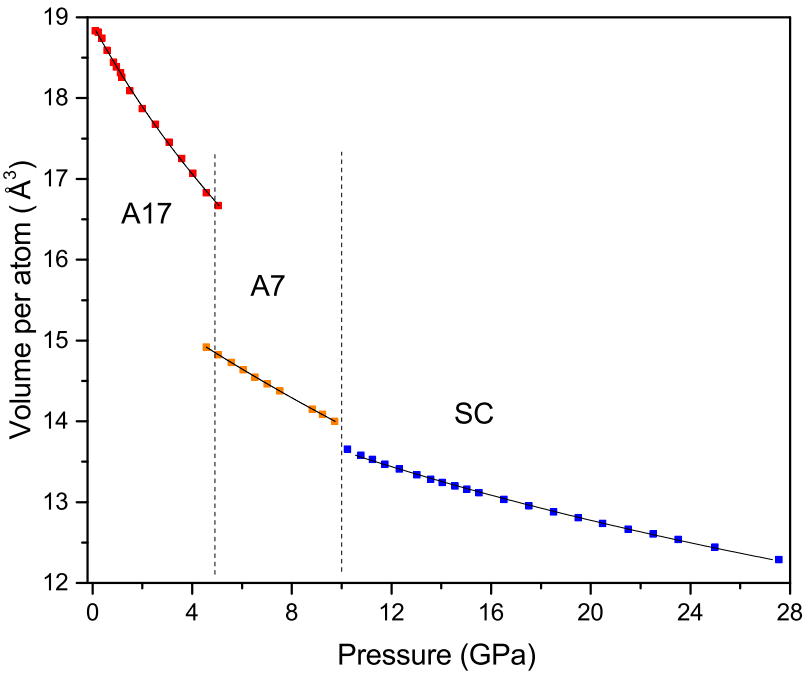

Figure 3.27: *Pressure dependence of the atomic volume of Phosphorus at 300 K in the P-black/He experiment and least-squares fit of the Vinet equation of state to the experimental data. Red squares refer to data in the orthorhombic A17 phase; orange square, to data in the rhombohedral A7 phase; blue square, to data in the simple cubic sc phase. Solid lines represent the results of the least-squares fit of the equation 3.1 to the experimental data (see table 3.1).*

Besides the high quality of the V vs P data and the substantial agreement with the available literature data, another interesting feature emerges from compression of P-black with He. Although no evident signature of He inclusion between the layers could be derived from these data, the XRD patterns across the phase transition between rhombohedral and simple cubic phase of P-black show some anomalies. As shown in figure 3.28, two Bragg reflections from rhombohedral phase, indexed as $(003)_r$ and $(113)_r$ in terms of a hexagonal lattice and labeled with asterisks, survive through the transition. The two Bragg peaks remain visible in the integrated patterns up to the maximum investigated pressure of 28 GPa (in figure, the magenta curve represent an XRD pattern acquired at 21.5 GPa, magnificated by a factor 30, where the two reflections are still visible), well beyond the transition threshold. No hysteresis is reported in literature for A7 $\longrightarrow$ sc transition [187], thus suggesting the retention of some fraction of the hexagonal structure into the cubic one. The two Bragg peaks allow to obtain the volume per atom for the residual rhombohedral phase in the simple cubic one at least up to 22 GPa. The other structural features attest for a normal transition between the two phases: the appearance of the $(200)_c$ reflection at 10.2 GPa, at 2θ value of about 18° as a low angle shoulder of the rhombohedral $(024)_r$ reflection and, between 10.2 and 11.2 GPa, the complete disappearance of the $(104)_r$ Bragg peak from rhombohedral phase at 2θ value of about 12.5°.

The room temperature compression/decompression of P-black/H_2 sample has been studied up to a maximum pressure of 17 GPa. A severe deformation of the gasket prevented the achievement of higher pressures. The XRD patterns acquired during the compression steps are the same reported in figure 3.20. In this case, differently from P-black/He sample, the first phase transition of P-black from the orthorhombic A17 to the rhombohedral A7 phase occurs at about 5.0 GPa, whereas the second phase transition from rhombohedral A7 to simple cubic (sc) phase takes place at 11.0 GPa. Both this values are slightly larger than in the P-black/He sample. The integrated XRD patterns from P-black/H_2 show exactly the same behaviour than those

acquired on P-black/He, even if they have a lower S/N ratio, making difficult to correctly assign all the Bragg peaks. This fact diminish the number of reflections that can be used to compute lattice parameters and unit cell volume for P-black in the course of this experiment. In figure 3.29, the whole volume per atom evolution with pressure for the P-black/H_2 sample is reported, together with the same curve measured for P-black/He. From their comparison, it can be seen that the pressure evolution of the two volumes is perfectly indistinguishable, and also that minor hysteresis can be appreciated for P-black/H_2 around the orthorhombic to rhombohedral phase transition, differently from what observed on P-black/He. The reflections from the orthorhombic phase survive into the rhombohedral one for no more than 0.5 GPa, and only one of the reflections, the $(111)_o$, can be correctly assigned, but it's not sufficient to calculate the unit cell volume. Figure 3.30 briefly summarizes the lattice parameters evolution through the three phases of P-black in the presence of H_2. No major differences with respect to the P-black/He sample were found.

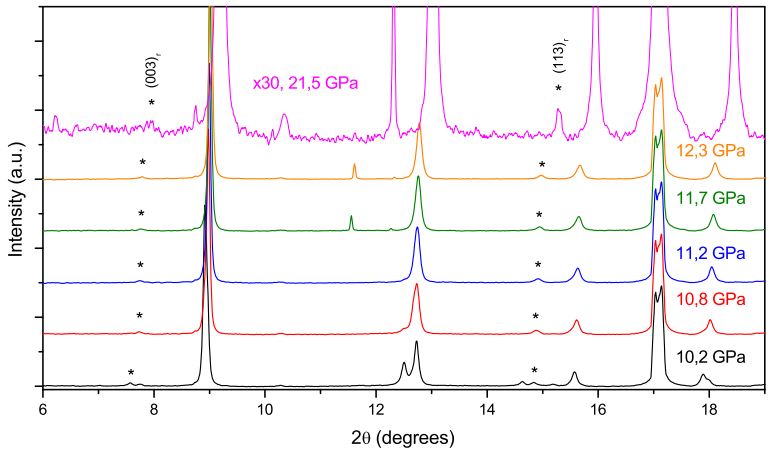

Figure 3.28: *Detail of the integrated XRD pattern of P-black/He across the rhombohedral-simple cubic phase transition (10.2 GPa- 12.32 GPa) and at the P = 21.5 GPa. Asterisks mark the surviving $(003)_r$ and $(113)_r$ reflections (indexed in terms of a hexagonal lattice) of the rhombohedral phase in the simple cubic phase across the transition. The reflections are retained up to the maximum investigated pressure. Magenta curve, referring to 21.5 GPa, have been magnified by a factor 30. Reflection $(113)_r$ and $(003)_r$ are still visible. Integrated XRD patterns were vertically translated for the sake of clarity.*

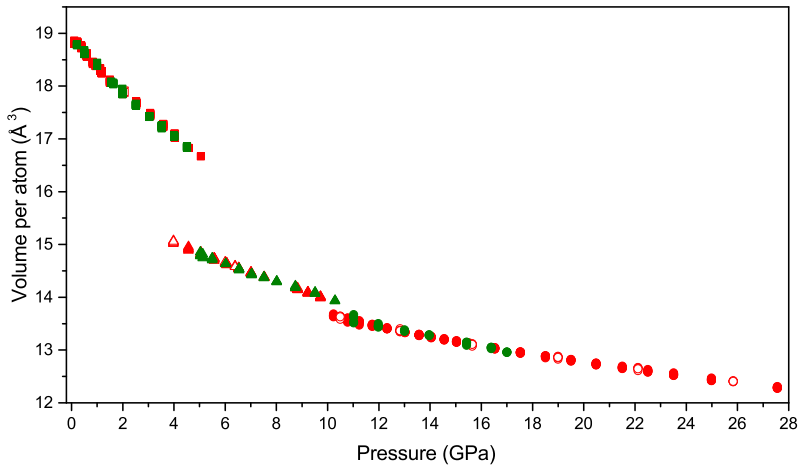

Figure 3.29: *Evolution of the volume per atom with increasing pressure for the three phases of P-black in the room temperature compression experiments of P-black/He and P-black/H_2. The orthorhombic, rhombohedral and simple cubic volume points are indicated by squares, triangles and dots, respectively. Red symbols: volume per atom of P-black during room temperature compression (full symbols) and decompression (open symbols) in the P-black/He experiment. Green symbol: volume per atom of P-black during room temperature compression (full symbols) in the P-black/H_2 experiment. No data were acquired on decompression to ambient conditions for P-black/H_2.*

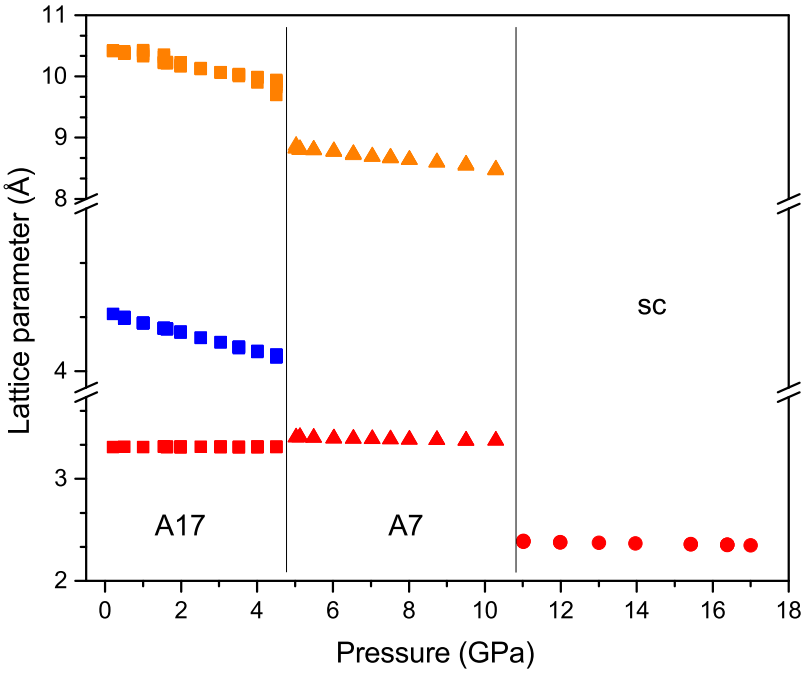

Figure 3.30: *Evolution with pressure of the P-black cell parameters across the three phases of P-black during room T compression in the presence of H_2 (0.2-17 GPa). Squares, triangles and dots refer to orthorhombic, rhombohedral and simple cubic phases, respectively. Red symbols: "a" parameter; blue symbols: "b" parameter; orange symbols: "c" parameter. The two vertical solid lines approximately indicate the transition boundaries of P-black.*

From the volume per atom of orthorhombic, rhombohedral and simple cubic phases of P-black, calculated from the measured lattice parameters, and as a function of pressure, a least-squares fit of the volumetric data to the equation 3.1 has been performed. Treating V_0 as an adjustable parameter for the three phases, where it was possible, the values of *bulk modulus* have been computed, yielding V_0= 18.91±0.02 Å^3, k_0= 32.4±1.4 GPa and k'= 3.3±0.7 for the orthorhombic A17 phase; V_0= 15.81 Å^3, k_0= 70.3±1.1 GPa and k'= 2.5±0.3 for the rhombohedral A7 phase; V_0= 15.06 Å^3, k_0= 90.3±2.3

GPa and k'= 3.1±0.4 for the simple cubic sc phase. In figure 3.31, the pressure dependence of the atomic volume of P-black at 300 K across the three mentioned phases in the P-black/H_2 experiment is reported, together with the fit based on the Vinet equation of state. The results of the fit have been summarized in table 3.1 and compared with those relative to the P-black/He sample and literature data.

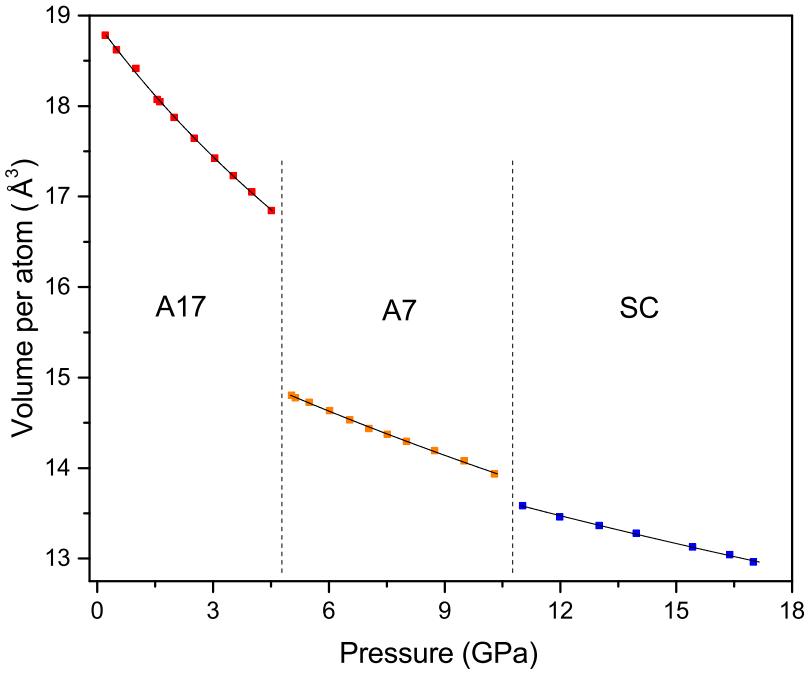

Figure 3.31: *Pressure dependence of the atomic volume of Phosphorus at 300 K in the P-black/H_2 experiment and least-squares fit of the Vinet equation of state to the experimental data. Red squares refer to data in the orthorhombic A17 phase; orange square, to data in the rhombohedral A7 phase; blue square, to data in the simple cubic sc phase. Solid lines represent the results of the least-squares fit of the equation 3.1 to the experimental data (see table 3.1).*

Exp	**PTM**	**Phase**	V_0 (Å^3)	k_0 (GPa)	k'
P-black/He	He	A17	18.91±0.02	33.3±1.3	3.1±0.6
P-black/H_2	H_2	A17	18.91±0.02	32.4±1.4	3.3±0.7
Kikegawa *et al.* [179]	NaCl	A17	19.03	36±2	4.5±0.5
Clark *et al.* [207]	methanol:ethanol:water	A17	18.98±0.08	34.7±0.5	-
P-black/He	He	A7	15.88±0.02	69.1±2.4	1.8±0.4
P-black/H_2	H_2	A7	15.81	70.3±1.1	2.5±0.3
Kikegawa *et al.* [179]	NaCl	A7	16.6±0.2	46±4	3.0±0.6
Clark *et al.* [207]	methanol:ethanol:water	A7	15.97±0.02	65.0±0.6	-
P-black/He	He	sc	14.92	89.7±0.8	4.7±0.1
P-black/H_2	H_2	sc	15.06	90.3±2.3	3.1±0.4
Kikegawa *et al.* [179]	NaCl	sc	15.2±0.2	95±5	2.1±0.8
Clark *et al.* [207]	methanol:ethanol:water	sc	15.33±0.02	72.5±0.3	-
Akahama *et al.* [181]	no	sc	15.5	70.7±0.9	4.69±0.1

Table 3.1: *Initial volume (V_0), bulk modulus (K_0) and its pressure derivative (K') at ambient conditions for the A17, A7 and sc phases of P-black from P-black/He and P-black/H_2 experiments, ant their comparison with literature data from the work of Kikegawa, Akahama and Clark.*

From this comparison results that our V_0 and k_0 values are in very good agreement with literature data [179, 181, 207] for all the three phases of P-black. The computed values seem to be highly reliable due to the very good quality of the experimental data even if, for both P-black/He and P-black/H_2 equation of states, a comparison with an equation of state for P-black in the presence of a non-penetrating pressure transmitting medium with the same data quality and in a comparable pressure range is mandatory to better understand if insertion of He or H_2 occurs.

As it was in the case of P-black/He, even in the P-black/H_2 experiment there are signatures of a retention of some rhombohedral reflections into the simple cubic phase after the transition threshold (about 11 GPa). Figure 3.32 show some of the integrated XRD patterns of P-black/H_2 sample across the phase transition and up to the maximum pressure of 17 GPa. Once the transition is completed, two reflections from the rhombohedral phase, indexed as $(113)_r$ and $(024)_r$ in terms of a hexagonal lattice, are visible within the

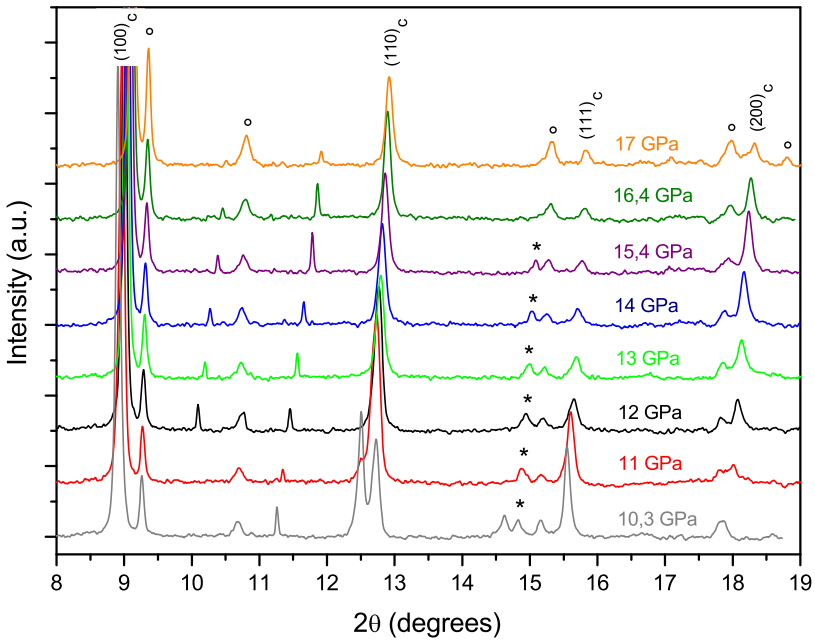

Figure 3.32: *Detail of the integrated XRD pattern of P-black/H_2 across the rhombohedral-simple cubic phase transition and up to the maximum investigated pressure (10.3 GPa- 17 GPa). In parenthesis, the reflections from simple cubic phase and their indices are reported. Open dots mark reflection due to Au from the protecting golden ring of the Rhenium gasket. Asterisks mark the $(113)_r$ reflection (indexed referring to hexagonal lattice) surviving in the simple cubic phase. The other rhombohedral reflections that is retained through the transition to simple cubic phase, $(024)_r$ in terms of hexagonal lattice, is overwhelmed by one of the reflections from Au.*

pattern of the new, simple cubic phase. The reflection $(113)_r$ is highlighted in fig. 3.32 by an asterisk. Unfortunately, the reflection $(024)_r$ is overwhelmed by a reflection of Au from the golden ring protecting the Rhenium gasket from the penetration of dense H_2 at high pressure. The superimposition between these last two reflections prevents the calculation of the volume for the residual rhombohedral phase in the simple cubic one.

In summary, the results obtained in the two room temperature compression/decompression experiments of P-black/He and P-black/H_2 are in good agreement with the previous literature data, but generally exhibit a major quality. In particular, the data acquired on P-black/He sample show a remarkably high quality, that allows to correctly compute the volume and cell parameter for P-black exploiting a great number of assigned reflections. The major quality of our experimental data reflects in a very accurate fit of the pressure dependence of atomic volume using the Vinet equation of state (eq. 3.1), yielding highly reliable values for the volumes, extrapolated at ambient conditions, and for the *bulk moduli* of each phase. The evolution of volume per atom with pressure both in the case of P-black/He and P-black/H_2 samples don't show any peculiar characteristic possibly related to He or H_2 inclusion between the layers of P-black, that could have determined some variation in the equation of state of the resulting material. Nevertheless, the data allow to gain some insights about the presence of confined He and H_2 between the layers of P-black. Interesting informations are provided by the persistence of some reflections of the rhombohedral phase into the simple cubic one, well beyond any possible hysteresis-related mechanism, in addiction to the fact that hysteresis phenomena are not reported for the rhombohedral $\longrightarrow$ simple cubic transition [187]. This peculiar feature, evident both in P-black/He and P-black/H_2 samples, suggests some kind of retention of the hexagonal structure from the rhombohedral phase into the simple cubic structure well above the transition pressure of 10-11 GPa (up to 28 GPa in P-black/He and 17 GPa in P-black/H_2). In the case of P-black/He, the two reflections from the rhombohedral structure are very well visible in all the pressure range up to 28 GPa, and allow to compute the volume of the residual rhombohedral phase into the cubic one. Figure 3.33 reports a detail of the volume per atom evolution with pressure of P-black/He sample where the behaviour of the residual rhombohedral phase in the simple cubic one is highlighted. The pressure evolution of the volume for the residual A7 phase shows a smooth decrease instead of a sharp discontinuity (as in the case of

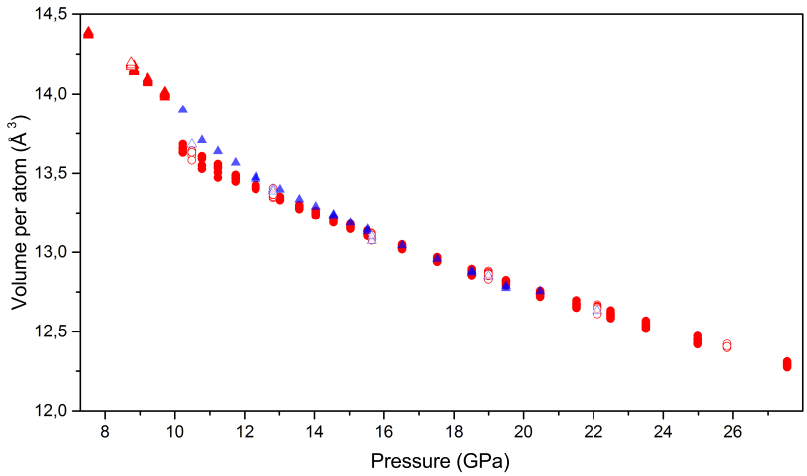

Figure 3.33: *Evolution of the atomic volume in P-black/He sample across the rhombohedral-simple cubic phase transition. Triangles and dots refer to rhombohedral and simple cubic phase, respectively. Red symbols: P-black/He atomic volume evolution with pressure across the phase transition. Violet symbols: pressure evolution of atomic volume of the residual rhombohedral phase into the simple cubic one.*

V_{rhombo}-V_{sc} comparison for the massive phase) along the phase transition, but the values tend to match those for the volume per atom of simple cubic phase at higher pressure.

The couple of rhombohedral residual reflections in the simple cubic phase of P-black compressed in the presence of He allow to evalute a and c parameters and to compute the c/a ratio. This ratio has a well known pressure trend, that is perfectly followed by our data up to the phase transition. The c/a ratio decreases from an initial value of 2.60 and tends to the minimum value of $\sqrt{6} = 2.45$, but it is well known that the structure undergoes the phase transition before reaching that limit [179, 187]. Beyond the phase transition, and considering the values of a and c parameters for the residual rhombohedral phase, we found that c/a ratio assumes exactly the 2.45 limit value, remaining constant. This means that the residual rhombohedral phase is

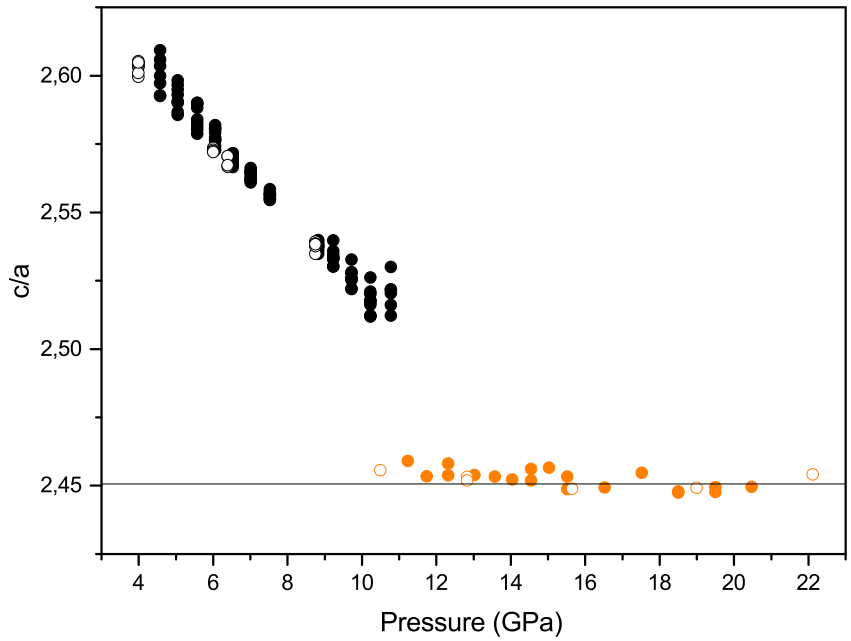

Figure 3.34: *Pressure evolution of the ratio between "c" and "a" cell parameters for the residual rhombohedral phase into the simple cubic phase of P-black/He sample. Black dots: c/a ratio for the rhombohedral phase during compression (full symbols) and decompression (empty symbols). Orange dots: c/a ratio for the residual rhombohedral phase after the transition to simple cubic during compression (full symbols) and decompression (empty symbols).*

subject to a huge strain so to maintain the typical c/a ratio value expected for the simple cubic phase without transforming into this last one at least throughout the whole investigated pressure range (from 10 to 28 GPa into the simple cubic phase). In figure 3.34, the c/a ratio evolution with pressure for the residual rhombohedral phase is reported.

A similar behaviour is reasonably expected in the P-black/H_2 sample, where two rhombohedral reflections remain visible well beyond the A7 $\rightarrow$ sc phase transition. Unfortunately, one of these two Bragg peaks, the one indexed as $(024)_r$ with respect to the hexagonal lattice, is overwhelmed by

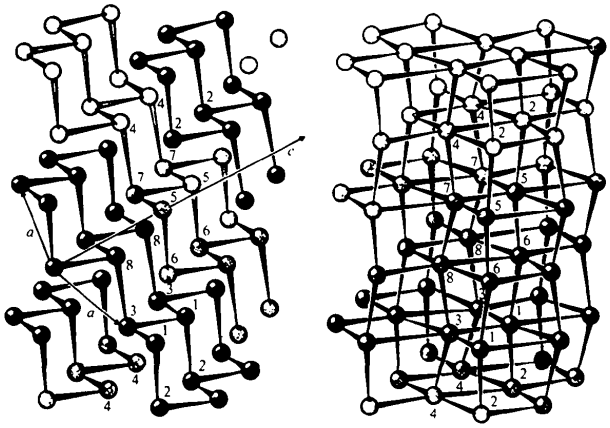

Figure 3.35: *Atomic arrangements in rhombohedral (A7) and simple cubic (sc) P-black. Left: rhombohedral (A7) P-black. Right: simple cubic (sc) P-black. To better elucidate the structural relation of the sc phase with the A7 phase, most of the atoms are shown not exactly positioned on the cubic lattice. Figure taken from the work of Kikegawa and coauthors, see ref. [179].*

a reflection due to the Au of the protecting golden ring of the gasket, thus avoiding to use both reflections to correctly compute unit cell volume and, even more important, the c/a ratio for the residual rhombohedral phase into the simple cubic one. No other significant data can be obtained by the integrated XRD patterns of P-black/H_2, but, as in the case of P-black/He, the retention of the rhombohedral reflections into the simple cubic phase is a strong evidence of the persistence of the A7 phase, likely related to some kind of deactivation of the transition rearrangement mechanism due to the insertion of guest molecules between the P-black layers at lower pressure. This mechanism is indeed based on the formation of new interlayer bonds (see figure 3.35) that is at least partially deactivated by the presence of confined He and H_2.

However, it is not possible to estimate the actual amount of confined He and H_2 and, for extension, to compute the amount of P-black that is not converted to simple cubic phase after the transition threshold. These speculations are directly related to the question about the amount of confined

He and H_2, and the P,T conditions of their inclusion between the layers. The total amount of rhombohedral phase could likely be small, thus suggesting that He and H_2 could be intercalated between the layers due to random defects on the P-black structure and surfaces whereas, in case the amount of rhombohedral would be higher, a massive inclusion of He and H_2 due to the high density conditions would be revealed. In this latter case, however, some more evident modifications in the unit cell volume (and in the equation of state) could reasonably be expected, that has not been detected during our experiments.

3.4 Summary

The high pressure behaviour of two Phosphorous allotropes, polymeric P-red and crystalline P-black, in the presence of small atoms and molecules (He, H_2, NH_3) has been studied. More in detail, a comparison between the high pressure, photoinduced reactivity of P-red and P-black in the presence of NH_3 has been established, so to evaluate their stability and their tendency to react, and the products have been characterized by means of FTIR and micro-Raman spectroscopy and XRD techniques. Furthermore, the possibility of pressure-driven insertion of small atoms or molecules between the layers in the crystal structure of P-black has been investigated by XRD techniques.

The high pressure reactivity of P-red towards simple molecules, triggered by two-photon absorption of near-UV wavelengths, is very well known [174, 175]. NH_3 has a a low-lying predissociative electronic excited state that can be reached by two-photon absorption of a 350 nm wavelength, yielding two excited NH_2 and H fragments that are able to trigger a chemical reaction with P-red and P-black. Reaction has proceeded to a different extent in the case of P-black and P-red, reflecting the different stability of the two allotropes: in the case of the red one, we found a high cosumption of the starting ammonia (evaluated by the decreasing integrated absorption of combination bands of NH_3 in the infrared spectra) and clear spectroscopic

signatures of the formation of new products bearing P-N, P=N and P-NH_2 functionalities. In the case of P-black, in the same experimental conditions, we found instead an overall good stability of the layered structure to high pressure, photoinduced reactivity, with only minor evidences of the formation of reaction products and a calculated lower consumption of the starting ammonia (see figures 3.7 and 3.10 for a comparison). The different reactivity can be confidently ascribed to the much larger P/NH_3 interface in the case of P-red, being unlikely the NH_3 penetration between the layers of P-black. The more interesting results have been obtained on the P-red/NH_3 mixture, where an heterogeneous product has been found, made up of fluid bubbles, an amorphous part and a solid, crystalline fraction. Micro-Raman spectroscopy revealed that the fluid bubbles, well visible in the optical images of the sample (see figure 3.9), were mainly constituted by molecular hydrogen and phosphine (see figure 3.12), that are by-products of the main reactive process as it was for P-red/water and, to a less extent, P-red/ethanol samples [174, 175]. The amorphous fraction of the product, mainly identified by micro-Raman measurements and labelled as P3 in the text, showed P-H functionalities and has been found to be totally unstable if exposed to atmospheric conditions, readily transforming into mainly H_3PO_3 (see figure 3.13). A correct assignment of the solid, crystalline products labelled as P1 and P2 has not been possible even if some hints have been provided by the comparison of micro-Raman (figure 3.14) and synchrotron XRD mapping (figure 3.15) of the reaction products at 0.6 GPa and at ambient conditions. The micro-Raman maps, measured in different spectral regions, allowed to spatially distinguish the different products permitting useful correlations for their assignment. P1 presents Raman bands only in the lattice phonon region, whereas in the points of the sample where characteristic Raman signals related to P2 were found, also N-H stretching bands were observed, thus suggesting that P2 could feature N-H functionalities in its chemical structure. By comparing the FTIR and Raman spectra acquired on P-red/NH_3 sample with some FTIR and Raman spectra of two classes of P,N products of gen-

eral formula P_xN_y and HP_xN_y, we did not find any full correspondence with the known products (HPN_2, HP_4N_7, P_3N_5), however some minor similarities between P2 and HP_4N_7 have been evidenced(figure 3.17. XRD mapping of the solid product region of the P-red/NH_3 revealed only one kind of XRD pattern, related to some highly oriented polycrystalline sample, but did not allowed to distinguish P1 and P2. Furthermore, some low angle reflections, visible in the reaction product of P-red/NH_3 mixtures, are not found in any of the compared P_xN_y and HP_xN_y products, despite of some other minor similarities with some of those species, as showed in figure 3.18. Unfortunately, no further informations could be gained by structural and spectroscopical techniques. At the moment, the refinement of synchrotron SC-XRD data acquired on P-red/NH_3 reaction product is in course, in the perspective of enlightening the actual structure of the crystalline product.

The high stability of P-black, attested once again by its very low reactivity towards NH_3, opens the way to possible simple atoms and molecules inclusion between the layers also in perspective of achieving single Phosphorene layers and, possibilty, their functionalization. To better understand the possibility of intercalation between the layers, the high pressure, room temperature compression/decompression of P-black in the presence of He and H_2 has been studied by means of synchrotron XRD technique. The very high quality of experimental data with respect to available literature data, allowed to measure the pressure evolution of unit-cell-volume and atomic volume, besides of that of lattice parameters, for all the three investigated phases of P-black, the orthorhombic A17, the rhombohedral A7 and the simple cubic sc. The fit of the equation of state of P-black in its three different phases, performed using Vinet equation of state, constituted a remarkable refinement of the available literature data [179, 181, 207]. From the integrated XRD patterns of P-black/He and, to a less extent, of P-black/H_2 samples, a major evidence of the inclusion of the two pressure transmitting media between the layers could be gained. This evidence were related to the retention of some Bragg peaks from the rhombohedral phase into the simple cubic one up to very

high pressures, ruling out, also due to the high hydrostaticity of the pressure transmitting media employed, any possible metastability of the low pressure phase. This phenomenon were not due to hysteresis, that is not known in the A7 $\rightarrow$ sc transition, and it lasted for all the investigated pressure range, well beyond the transition threshold boundaries. In fact, in P-black/He samples the Bragg peaks from rhombohedral phase persisted into the simple cubic one up to the maximum investigated pressure of 28 GPa, and in the P-black/H_2 sample they were visible up to 17 GPa, where a severe deformation of the gasket prevented the achievement of higher pressures (see figure 3.28 and 3.32). In the case of P-black/He, the experimental data were of very high quality, thus allowing to calculate the volume of the residual rhombohedral phase into the simple cubic (fig. 3.33) up to 22 GPa and, even more important, to estimate the c/a ratio for the rhombohedral phase in the simple cubic one (fig. 3.34). From this last plot, it is possible to detect is how, in the case of P-black/He and differently from what is observed in previous P-black literature, the c/a ratio assumes exactly the value of $\sqrt{6} = 2.45$. Generally, the c/a ratio tends to this value in the rhombohedral phase, towards the transition to simple cubic, but the transition occurs before it can be reached. Our experimental results thus suggests the A7 $\rightarrow$ sc phase transition wa inhibited unless in some portions or domains of the sample, and that some rhombohedral domains stay undefinitely stable, even if very highly strained, embedded in the surrounding, simple cubic structured crystal. It is likely that the inclusion of He atoms between the layers of P-black at some point of the room temperature compression would have triggered this mechanism, thus resulting in the unusual persistence of rhombohedral phase domains at pressures where, typically, P-black is well inside its simple cubic phase. A similar phenomenon also happens in the case of P-black/H_2, where two other Bragg reflections due to the rhombohedral phase are visible at very high pressure (until the maximum pressure of 17 GPa), but unfortunately, due to some superimposition of Au-reflections from protecting ring on the Rhenium gasket, it was not possible to calculate the volume of the residual

A7 phase or the c/a ratio. It was also not possible to evaluate how much of the rhombohedral phase remained in the simple cubic one, a mandatory information to elucidate if the deactivation of the transition mechanism was related to a massive inclusion of He and H_2 or just to a partial inclusion due to the presence of defects on the structure and surfaces of P-black. Taking into account the van der Waals radii of He and H_2 and roughly comparing them with the available space to enter the layered structure of P-black in its orthorhombic and rhombohedral phases, a massive inclusion of the two pressure transmitting media is unlikely, even if both He and H_2 are well known for their high capability to diffuse into crystal lattice of several materials at high pressure (as instance, diamond). However, the intensity of the XRD peaks seems to support the inclusion of small amounts of He and H_2 through the lattice defects. As a future perspective, literature data reports that the interplanar spacing in P-black increase with increasing temperature [187]: another way to foster the atomic and molecular inclusion between the layers would be to perform the same experiments at higher temperature, exploiting the larger interlayer spacing.

Chapter 4

Experimental Setup and Techniques

Here the instrumental setup and experimental techniques used for the studies presented in this thesis will be discussed in detail.

4.1 Diamond Anvil Cell

Diamond Anvil Cell (DAC) (see figure 4.1) is a specifically designed device that allows to apply pressure in the range from 0.1 to 100 GPa on small volume samples. DAC allows to work in a temperature range from 10 to 1300 K (resistive heating). The sample chamber is drilled on a metallic gasket, preindented between the anvils, that allows to confine the samples laterally. Gasket are drilled by spark erosion or even laser drilling. Sample dimensions typically range from 100 to 200 μm (diameter) per 50 μm (thickness). Diamond anvils guarantee the optical access through the sample at the same time allowing optical spectroscopy (FTIR, Raman) and X-ray diffraction experiments to be performed. Depending on sample and experiments, several materials are suitable to be used as anvils (sapphire, tungsten carbide, synthetic diamonds etc.). Pressure can be monitored by Ruby fluorescence method, adding a small ruby chip as a sensor; alternative methods consist

in the use of Samarium salts (that perform better at high temperatures), internal standards or even of the pressure shift of the D band of diamond in the Raman spectrum. DACs used during the experiment presented in this thesis are membrane Diamond Anvil Cells (mDACs): the membrane allows to remotely control pressure by inflating it with He, making possible to perform compression/decompression experiment in the evacuated sample chamber of the FTIR spectrometer, for instance.

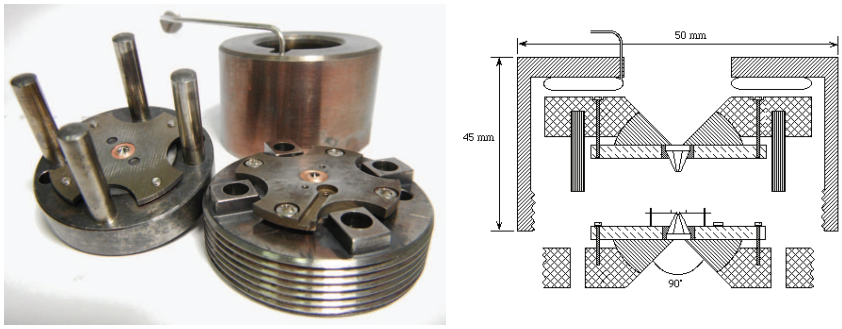

Figure 4.1: *Picture and schematization of a membrane Diamond Anvil Cell (mDAC). On the left, a picture of an opened mDAC; on the right, a schematization of the cell.*

4.2 Loading techniques

The loading of heterogeneous sample is a complex part of the sample preparation in *diamond anvil cell* (DAC). Typically, solid and liquid sample can be directly loaded between the anvils, inside the gasket sample chamber, and then the cell is closed and pressure is externally applied by a *Pressure Driving System* (PDS). The loading of gas compounds could be instead a little bit tricky, and the good method to achieve it strictly depends on the nature of the gas itself (and, particularly, on its freezing point). There are two main techniques for the loading of gas sample, named *cryo-loading* and *gas-loading*, respectively.

Cryo-loading is a suitable technique for gases with a freezing point above the temperature of liquid nitrogen (77 K). The DAC, with slightly spaced dia-

monds (about 100 μm) is placed in a vessel and directly connected with the external pressure driving system. The vessel is evacuated from atmospheric moisture, and immersed in a cryogenic bath. Depending on the thermodynamic conditions needed for the gas condensation, the cryogenic bath could be liquid nitrogen (77 K) or some other refrigerated cooling bath (for temperature between 300 and 240 K). Inside the vessel, the gas to be loaded is letting flow and, when the temperature reached the freezing point, it starts to condensate. When the level of the liquefied gas covers the DAC, pressure is applied on the membrane and the sample is sealed between the diamonds. All samples of Ar (190 K, 1 bar), N_2 (77 K, 2-3 bar) and Ethylene (in a cryogenic bath with 243 K and 30 bar) in these experiments have been loaded by this method.

Gas-loading is used for gases with a lower boiling point than that of molecular nitrogen. Gas-loading is a room temperature technique: it just consists in loading the gas at a huge pressure (1000-3000 bar), usually exploiting double cycle compressor. The DAC is inside a Copper-Beryllium vessel, and both membrane and the vessel itself are filled with the gas to be loaded. At the loading pressure, the vessel circuit begins to be emptied in respect to the membrane circuit, so to maintain a difference in pressure that is going to be, at room conditions, the sealing pressure of the DAC. Gas-loading has been used for the loading of methane clathrate hydrates sample, by obtaining a small bubble of methane inside a drop of bidistillated water; other gas typically loaded by means of gas-loading are H_2, He and Ne. H_2 and He samples for this thesis have been gas-loaded in ESRF.

In the most part of our experiments we have used a different technique, named *Spray-loading*. Spray-loading (see figure 4.2) consists in condensating really small quantities of the gas directly on the diamond, and then closing the cell. It's a useful technique when the condensed gas could be dangerous in large amounts. The DAC is cooled down in a cryogenic bath (typically using liquid nitrogen), with the diamond spaced so to allow a small capillary to reach the center of the sample chamber. The gas will flow through a

dedicated line from the bottle to the capillary, and from there directly on the bottom diamond. Once the desired quantity of gas has been condensed on the sample chamber, the capillary is removed, the cell is manually closed and a pressure on membrane is applied. We have used this technique for the loading of Acetylene, Ammonia and some of the Ethylene samples loaded with Silicalite, GO and P-red.

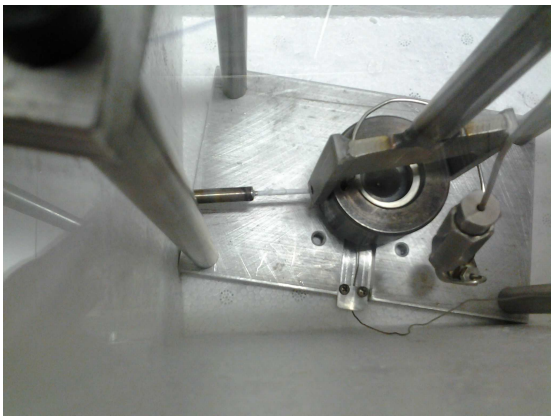

Figure 4.2: *Detail of the Spray-loading procedure.*

In all the cases, small ruby chips have been added as pressure gauges [210].

4.3 FT-IR

Samples confined in DAC can be accessed by spectroscopic and structural techniques. The Fourier Transform Infrared Spectroscopy (FTIR) is the election technique to follow modifications and chemical reactivity by measuring absorption and reflection spectra. For a brief overview of the basic principles of this technique, see ref. [211]. All the infrared measurements presented in this work were performed on a Bruker IFS-120HR spectrometer (see figure 4.3), specifically modified for high pressure experiments [212].

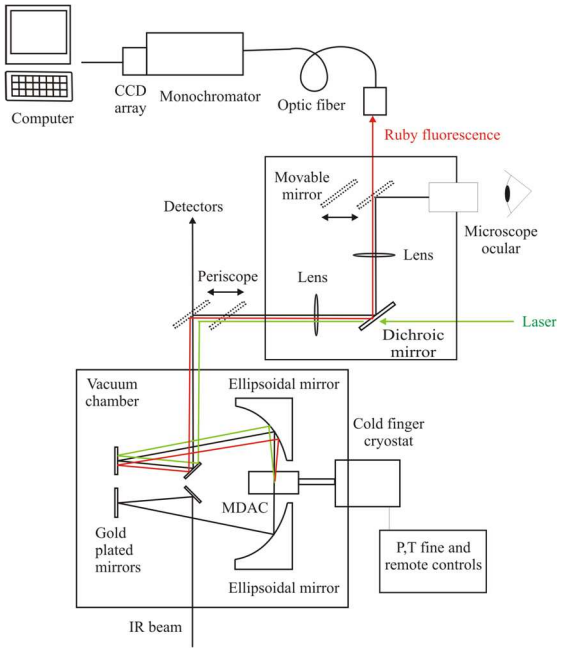

Figure 4.3: *Schematic representation of the modified Bruker IFS-120HR.*

In principle, the FTIR apparatus perform very well in a broad spectral range from far IR to the near UV, e.g. from 5 to 25000 cm^{-1}. The instrument is equipped with three source lamps, tungsten (visible/near infrared), Globar (medium infrared) and an Hg lamp (far infrared); three different interchangeable kind of beam splitters, Mylar (of different thickness), KBr and CaF_2; and four detectors, a bolometer (10-600 cm^{-1}), a mercury-cadmium-tellurium semiconductor (MCT, 500-6000 cm^{-1}), an indium antimonide semiconductor (InSb, 1850-9000 cm^{-1}) and a silicon diode (9000-32000 cm^{-1}). Optimal combinations of sources, beam splitters and detectors allow to investigate the different spectral regions. Anyway, for samples confined in a DAC, the lowest accessible frequency is limited by the diffraction losses due to the small sample chamber (gasket hole), that actually behaves like a diaphragm for the incident light. In the best condition, the low frequency limit is equal to 30-50 cm^{-1}. The whole spectrometer operates under vacuum or in an inert, N_2 atmosphere, so to remove the strong absorption due to atmospheric CO_2 and moisture. The Bruker IFS-120 HR has a moving mirror with an

arm of 3.0 m. This setup is necessary if you have to measure fine rotational structure of vibrational transitions in gaseous systems, but it gives a much higher resolution than needed for high pressure measurements, where bands are typically much broader than at room conditions. The spectrometer has been specifically modified to overcome the technical limitations due to the small sample dimensions (samples in DAC have dimensions ranging in the hundreds μm). Typically, with the DAC, an IR microscope has to be used in order to fit the IR beam dimensions to the small gasket hole. The size of the beam spot that can be achieved is strictly related to the properties of the light source: using synchrotron radiation, it's possible to obtain an almost diffraction-limited small spot (see section 4.3.1), while using a lamp the size of the spot is determined by the size of the source image through the microscope. In the case of our Bruker, it has been modified with a *beam condenser optical bench* (see figure 4.4) equipped with ellipsoid mirrors for focusing the IR spot on the DAC. The demagnification ratio of the ellipsoid mirrors is of about a factor of 4 resulting in a waist on the focus of the same dimensions of the sample determining an effective enhancement of the transmission through the diamond anvil cell larger than one order of magnitude [213].

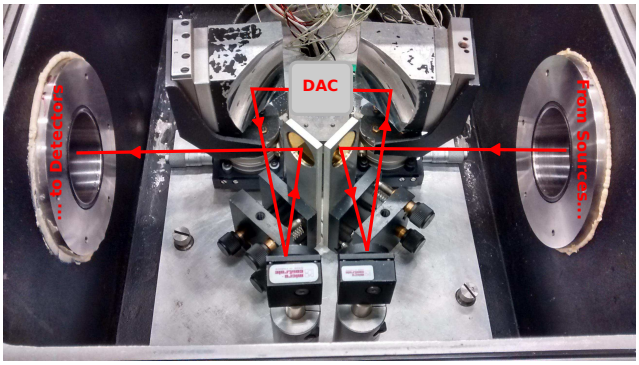

Figure 4.4: *The beam condenser optical bench in the modified sample chamber of Bruker IFS-120HR. The red line is a guide for the eye, indicating the IR-beam path through the DAC.*

Our setup allows to measure FTIR spectra in a wide temperature range.

Temperature as low as 20 K are achieved through a closed cycle double step helium compression cryostat (DE204SL by APD Cryogenics) that is coupled with the spectrometer. High temperatures (600-700 K) can be reached using a resistive heater that envelops the cell and that can be remotely controlled from outside, using as a feed-back of the temperature a thermocouple inserted either inside the heater itself or inside the cell, fixed near the gasket. The pressure can be regulated remotely by a capillary connecting the pressure regulator outside the instruments to the membrane of the MDAC inside the sample chamber, via a vacuum feed-through. The pressure can be measured in situ by the ruby fluorescence method, using a microscope that focuses few mW of the second harmonic of a CW Nd/Yag laser onto the ruby chip and collects the fluorescence in a back scattering geometry, exploiting the same modified optical bench.

4.3.1 Synchrotron FT-IR

Some of the FTIR measurements in this thesis have been performed using synchrotron radiation in ELETTRA (Trieste). The advantage of synchrotron radiation could be summarized in the higher brilliance of the source, that allows to work with IR spots of dimensions near to the diffraction limit. In the case of *SISSI* beamline in ELETTRA, the beam from the *accumulation ring* is splitted in two halves. The one suitable for solid state physics studies goes through a commercial BRUKER Vertex-70v Spectrometer, coupled with an IR microscope Hyperion-2000. The Vertex-70v is equipped to cover the whole spectral range between 5 and 20000 cm^{-1} with the combination of Quartz lamp, Hg lamp and Globar as sources, MCT, Si bolometer, DTGS and Si-diode as detectors and Si, KBr or CaF_2 as beam splitters. Hyperion-2000 has an accessible frequency range from 100 to 13000 cm^{-1}, with 15x and 36x available objective, and a spatial resolution depending from the wavelength. Samples in DAC are held on a specific support under the microscope, and the IR spot can be reduced down to a minimum of 10 μm using a spatial filter. In the case of our experiments, we used 20 μm and 30 μm spots on

the sample, with spectral resolution of 1 cm^{-1} and a sampling rate of 20 KHz. A detailed description of the instrumental setup and performances of the beamline SISSI can be found in ref. [214].

4.4 Micro-Raman setup

Raman measurements on this thesis were performed using a custom setup specifically designed to have a high spatial resolution in diamond anvil cell [213, 215] (figure 4.5). High spatial resolution is a fundamental prerequisite to work with heterogeneous materials.

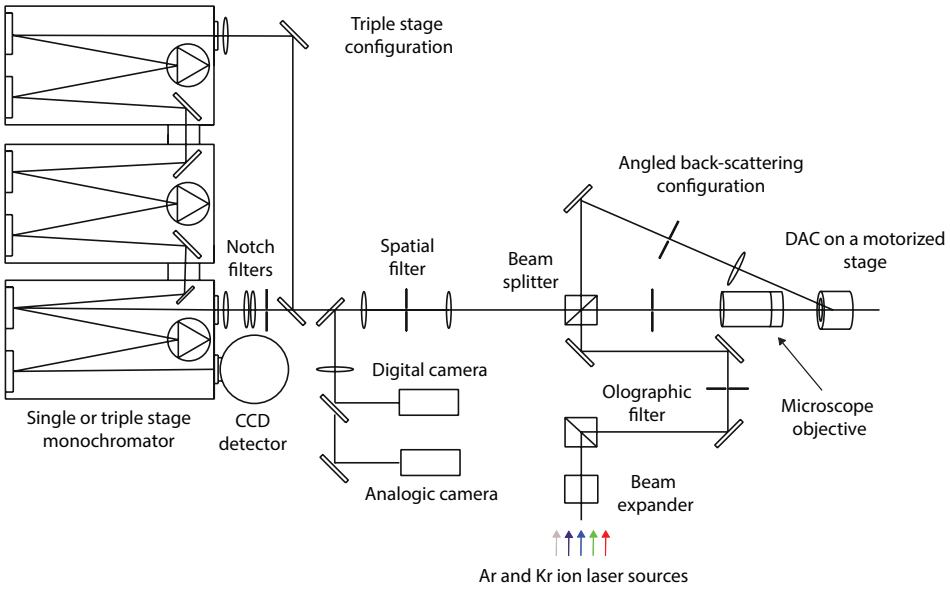

Figure 4.5: *Schematic representation of the micro-Raman setup at LENS.*

The 647.1 nm line of a continuous wave Kr ion laser (INNOVA 300, Coherent) is typically used as laser source: this wavelength has been used for all the experiments presented in this thesis. Anyway, the Kr ion laser provides several different lines and, furthermore, a second laser, a continuous wave Ar Ion laser (Innova Sabre, Coherent) is suitable to provide other laser wavelength for Raman spectroscopy (in particular 514.5 nm and 488 nm). A *beam expander* allows to expand the beam from the laser output and to send

it to a *50% beam splitter*. The reflected part of the beam is focused onto the sample in DAC through a *20x microscope objective* (Mitutoyo, F = 20 mm). The same objective recollect the scattered radiation in a *back scattering configuration* and send it to the same beam splitter, where the transmitted part goes to the detector. The combination of the beam expander with the short working distance of the microscope objective allows to obtain the best transverse resolution, with a focal spot ranging, depending on the alignment, between 2 and 5 μm. Optical access to the sample is provided on this same line just by switching to the camera using a dedicated mirror on the path of scattered beam. There are two available cameras, the first one digital (allowing to acquire photos and videos of samples during the experiments) and the other one analogical (allowing to see the sample). Another possibility for the collection consists in using an *angled quasi-backscattering geometry*, where the the incident beam is focused by another lens and there is no need to use a beam splitter. In this case, the Raman and the fluorescent background signal coming from the anvils are greatly reduced, but the limited aperture of the DAC and the size of the collecting micro-objective strongly reduce the numerical aperture of the focusing lens, decreasing the transverse resolution and the Raman signal coming from the sample. Whatever scattering configuration is adopted, a *spatial filter* of the collected optical path is mandatory. This filter consists of two confocal lens that produce and collimate, respectively, an image of the sample magnified by a factor 10. Between these two lenses, in the image plane, there is a 25 μm pinhole. This pinhole selects the part of the image that is illuminated by the laser spot, allowing to reduce the background signal of the diamond anvils by achieving a spatial resolution of about 1 μm on the focal plane with an effective depth of field of about 20 μm. The clean, collimated beam is sent to two super plus *notch filters*, which avoid every residue of the excitation wavelength, and then focused onto the slit of the last stage of a *Triple Stage Monochromator* (Acton SpectraPro 2500i). This last stage is equipped with three different, interchangeable gratings (300, 900 and 1800 grooves/mm), with a maximum

spectral resolution of about 0.7 cm^{-1}. This single grating monochromator needs to be used in combination with the two super plus notch filters, and in this configuration we have a high throughput because of the very few optical elements included in the monochromator (two lenses and a grating). The notch filters remove the quasi-elastic Rayleigh component of the scattered signal which, otherwise, would overwhelm the inelastic one. Unfortunately, this two notch filters has a large rejection band, completely removing the signal within a spectral region up to 200 cm^{-1} around the zero Raman frequency. This drawback prevents the analysis of the low-energy Raman modes, such as low-energy phonons or the continuous, collision-induced spectrum of fluid materials. In order to access this low frequency part of the spectrum, after the spatial filter the collected signal can be sent to the entrance slit of the first stage of the *Triple Stage Monochromator* that, operating in a *subtractive mode*, could allow to go down in frequency to a minimum of 5 cm^{-1}. In this operating mode, the scattered signal enters stage 1, which is a single monochromator, and is dispersed by the diffraction grating; the dispersed light enters stage 2, through a slit which cut out the Rayleigh component. Stage 2 is completely identical to stage 1, but the grating is rotated in the opposite phase and its job is to counter-disperse the signal, recomposing it into a white beam. This cleaned beam enters stage 3 where it is dispersed on the last diffraction grating, and the dispersed signal goes to the detector. The total throughput of this configuration is about one order of magnitude lower than in the single stage operating mode, and this make this last option largely preferable unless one doesn't have to look at the low frequency region of the spectrum. The frequency resolution of the spectrometer depends only on the third stage. It is related to **a)** the focusing length of the mirrors (500-750 mm), **b)** the grooves/mm of the grating (between 300 and 2500), **c)** the wavelength and **d)** the pixel size of the CCD (usually about 20 μm). Whatever configuration is adopted, the Raman signal is collected and analysed by means of a 1024x1024 pixel *liquid nitrogen cooled CCD detector* (Princeton Instrument), placed on the exit of the stage 3. Operating tem-

perature of this CCD is about -120°, and the CCD covers a spectral region between 200 and 1000 nm, with a very high efficiency (over 90%). Detector noise is determined by the read-out device, and typically amounts to only few electrons per pixel. A recent development of the Raman instrumentation was about the automatization of some elements. First of all, the sample holder is completely remote-controlled by a custom, home made software, allowing to translate the DAC on the three directions with an accuracy within 1 μm and to perform high spatial resolution Raman mapping of the samples. Then, other elements are remotely controlled to simplify the optical alignment procedure and the switching between the different configurations: the pinhole can be moved in and out of the beam path, and a mirror can be switched in three positions that send the signal either to the cameras (for visual inspection of the sample), to stage 3 in a single monochromator configuration, and to stage 1 in the triple monochromator configuration. It is also possible to automatically move a filter array that allows to reduce laser power on the sample, and to look at the laser spot during the alignment procedure. The Raman setup can be profitably used also for low temperature and high temperature measurements. In the first case, a dedicated closed cycle cryostat with a Cu cold-tip in which the DAC can be placed is coupled to the instrument, allowing to fastly switch from the regular sample holder to the cryostat cold-tip. High temperature measurements can be performed using resistive heaters, and a specifically designed, water cooled vacuum chamber that allows to reach temperature up to 1000 K.

The Ar ion laser can be profitably used to perform irradiation cycles on samples in DAC. The samples can be irradiated both on the same support used for the Raman measurements and on a specific support placed in front of the laser output. Lenses of various focal lengths (f= $50, 100, 200$ mm) have been used to focus the laser spot, depending on the sample dimensions in DAC and in order to minimize light losses. Available wavelengths ranges from multiline UV emission (centered at about 350 nm) to green (514.5 nm). Powers between 50 and 500 mW on the sample have been used.

4.5 Vibrational Data Analysis

Vibrational data obtained from FTIR and micro-Raman spectroscopy have been analyzed to gain information, for instance, about integrated areas or pressure dependence of peak positions. Areas and band positions have been estimated through analytical fitting procedures. The fits have been performed using Fityk and Origin softwares, by means of Levenberg-Marquardt algorithms. Typical band shapes were Voigt and Pseudo-Voigt. The softwares used to analyze data allowed to compute and compare all the fitting parameters (band center, area, height and FWHM). Where band areas were fitted to compute I_D/I_G ratios (see section 2.3) or for kinetic studies (see section 2.4.1), care was devoted to a proper consideration of lineshape FWHM in the comparing of peaks intensities and integrated areas all along the fitting procedure.

4.6 X-Ray Diffraction techniques

The LENS diffractometer is a custom setup dedicated to X-ray diffraction (XRD) measurements in diamond anvil cell (see figure 4.6).

The X-ray beam is produced by a Molybdenum micro source (Xenox-GeniX Mo Small Spot), with characteristic wavelength of 0.719317 Å. The beam goes through a focusing optics, where multilayered elliptical reflectors focus the 60 μm beam coming from the source to a 160 μm spot with a divergence of about 0.2°. A portion of the magnified beam spot is selected by a *spatial pin hole*, this way empowering the quality of the light that will probe the sample. Three *pin holes* are available with 50, 100 and 200 μm diameters, depending on the intensity/resolution ratio needed for the experiments. The pin hole position is motorized, and this allows to better align it on the beam. All the allignment procedures on the instrument are automatically driven by an homemade software (compiled in MatLab), and the most important part of the entire procedure is the *X-ray pin diode detector*. This is an Indium and Germanium film-covered diode that collects the X-ray photon transmitted by

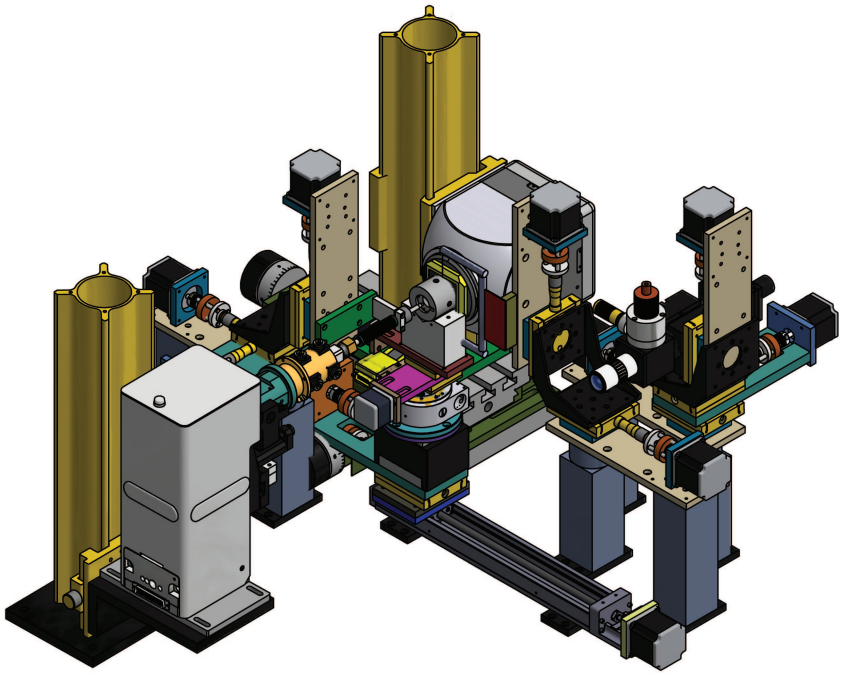

Figure 4.6: *Schematic representation of the XRD custom setup at LENS.*

the sample and allows to center it on the three axis and on the beam. The sample in DAC (or the calibrant) is held on a specific support that can be moved on the x, y and z axis and that can be rotated and oscillated to perform averaged powder diffraction acquisitions. The alignment procedure is an iterative process that allows to center the DAC on the y and z axis, and then to obtain the better x (focus) by comparing three different acquisition at three different angle (0, $+\theta$ and $-\theta$). Increasing θ values allows to increase the precision of the good focus evaluation. The DAC rotation axis should be also placed on the beam-path. During all this procedures, the *X-ray pin diode detector* collects the transmitted radiation, and the converted electrical signal is sent to the software that drives the alignment process. Once the sample is aligned, the pin diode detector can be moved off ot the beam path, and the scattered X-ray diffraction can be collected on the *image detector*. The image detector consists of a phosphorus screen coupled with a Peltier cooled CCD

detector (PI-SCX4300). The operating temperature of the CCD is about -50°. Acquisition times ranging from 15 to 60 minutes are mandatory to perform good XRD acquisitions. The 2D diffraction patterns acquired this way can be analyzed and integrated using FIT2D [216] and Dioptas [217] softwares. The calibration standards used for our experiments are CeO_2 or LaB_6.

Furthermore, the DAC support is mounted on a rail that allows to switch from the X-ray Diffraction configuration to another position where an integrated *Pressure by Ruby Luminescence (PRL)* system is present. This system allows to measure pressure in diamond anvil cell using the ruby fluorescence method. The PRL is equipped with a green, small diode laser (514.5 nm) and an analogic camera that allows visual inspections of the sample.

4.6.1 Synchrotron XRD at ESRF

In order to investigate different regions in nanocomposites sample, it's useful to exploit high spatial resolution techniques that can be provided by synchrotron radiation facilities. We have performed several Angle Dispersive X-ray Diffraction (AD-XRD) experiments at the ID27 and ID09 high pressure beamlines in ESRF, Grenoble.

For ID27, the operating wavelength used for our experiment was λ = 0.3738 Å. The signal can be collected on a Mar345 Flat Panel detector, on a CCD detector (MAR CCD165) or on a PerkinElmer image plate. The nominal spot size on the sample was between 2 and 5 μm, allowing mesh acquisitions and an accurate mapping of different regions in nanocomposite samples. The beamline equipment allows to perform high temperature measurements using resistive heaters in a water-cooled vacuum chamber. Pressure can be monitored in situ by a dedicated PRL, and the pressure driving system can be remotely controlled via software. An accurate description of the experimental setup in the ID27 beamline can be found in reference [218].

Regarding the ID09 beamline, presently renamed as ID15B, the used wavelength was λ = 0.415352 Å, while the detector was a MAR555 flat

panel. The local spot size of the beam is about 10 μm. Pressure can be monitored in situ by a dedicated PRL, and the pressure driving system can be remotely controlled via software.

Conclusions

The application of an external high pressure is shown to be a powerful method to finely tune the structural and reactive properties of simple molecular system due to their "softness" or, in other words, to their high compressibility. By reducing their molar volume while increasing their density, high pressure allows molecular systems to explore different regions of their potential energy surfaces and, significantly, previously inaccessible new local or global energy minima. This effect produces phase transition to new dense states, amorphization, ionization processes or, more drastically, to a complete reorganization of the chemical bonds leading to the formation of new products. High pressure is an appealing tool to achieve these interesting transformations also because, together with temperature effect and laser irradiation, allows to overcome energy barriers for the formation of products such as polymers without the use of catalysts, radical initiators or other reactants, thus suggesting its importance in the context of the so called *green chemistry methods*.

In the framework of high pressure chemical reactivity, the behaviour of ordinary matter under extreme confinement is an almost unexplored topic, although confined conditions are certainly frequent in nature and could find applications in geophysics, gas storage and, more interestingly, in the synthesis of new materials with specific and tunable characteristics. The combined effect of high density and extreme confinement conditions is known to have the capability of driving chemical reactivity through preferential reaction coordinates, where a limited number of nearest neighbours and the interaction

with the walls allow to obtain specific reaction products with high selectivity. Low dimensionality drastically affects the geometrical constraints of chemical reactions, thus completely modifying the reaction mechanisms and, significantly, their final products. From a theoretical point of view, the study of the behaviour of ordinary matter under extreme confinement provides insight about the modification of reaction mechanisms, i.e. how the effect of reduced space and reduced dimensionality affects the various, different steps of chemical reactions, enlightening the specific role of the confining matrix and of the reaction conditions (high pressure, high temperature, laser irradiation related effects). From an applicative point of view, the capability to drive a totally selective chemical reactivity exploiting the low dimensionality provided by specific matrices would be an important starting point towards the synthesis of appealing nanocomposite materials for applications in the fields of nanosensors, nano-optics, nano-electronics and nano-photonics. A slight change in the reaction conditions could favour the fine tuning of the interesting properties of these new materials, and a deeper knowledge of the mechanisms that regulates this peculiar reactivity would allow to design and synthesize new products characterized by the desired features. Among the different possible model systems for the study and understanding of these mechanisms, we investigated nanocomposite inclusion materials based on C/Si constituents, nanostructured carbon-based materials and two different allotropes of elemental Phosphorus, P-red and P-black.

Among the nanocomposite inclusion materials, C/Si based systems, where a Si-based structure provides a space for small hydrocarbon molecules to undergoes polymerization in highly confined conditions, are of prominent interest. The experiments conducted on the high pressure polymerization of model hydrocarbons (acetylene, C_2H_2) and simple molecules (carbon monoxide, CO) inside the nanocavities of two different synthetic, non catalytic and electrically neutral, pure SiO_2 zeolites, Silicalite (MFI) and ZSM-22 (TON), characterized by a 3D and a 1D internal network respectively, allowed to draw important conclusions about the reduced dimensionality effect on chemical

reactivity. First of all, confined molecules showed exactly the same behaviour of their bulk counterpart, undergoing chemical transformations upon the same experimental P,T conditions (pressure threshold were substantially unaltered) and in absence of any catalyst or initiator. Nevertheless, the confinement due to the zeolite internal walls selected preferential reaction paths thus allowing the obtainment of more ordered polymers with specific geometrical features in respect to their bulk counterparts. Another important feature regarded the zeolite hosts themselves, and particularly the tuning of some of their properties (as, for instance, thermal expansion coefficients), that can be related to the fine tuning of the amount of polymerized materials inside the nanocavities. The most remarkable point in this study has to be found in the fact that Silicalite and ZSM-22 are non-catalytic matrices. Therefore, their influences on the reactive behaviour of the confined molecules has to be searched only in the reduced dimensionality provided by their nanocavities. In fact, different internal nanocavities, related to the different structures of the two zeolite crystals, selected different isomers for the confined polymers, and accounted for increased ordering in the polymeric chains and, from the "inorganic framework point of view", for the different filling degree of the pores. The high quality of the polymeric chains obtained under nanocavities confinement should allow to preserve their specific properties (as instance, monodimensional conductivity for ideal polyacetylene chains), and the protecting scaffold provided by the zeolites was fundamental to recover products like polyacetylene and polyCO at ambient conditions without altering their structural and chemical conformations due to the contact with atmospheric moisture. In fact, the products of acetylene and carbon monoxide polymerization were impossible to recover in the bulk processes due to their great instability to air-exposure.

Nanostructured carbon-based materials are another interesting class of systems that allowed to deepen the understanding of confinement effects on simple molecules structure and reactive properties. The experiments conducted on Graphite Oxide (GO) had the twofold purpose to determine the

better conditions for obtaining the inclusion of simple atomic and molecular systems in its layered structure, and to foster the functionalization of the single sheets of Graphene Oxide. Differently from the aforementioned zeolites, GO is an active substrate in all the investigated processes: the great number of oxygen-bearing functions, randomly decorating the basal planes of GO and their edges, played a fundamental role in the interaction with Ar, N_2 and NH_3 both from structural and from reactive point of view. The inclusion of these three simple systems between the GO layers determined a retention of the structural features of GO up to high pressure and, in the case of NH_3, a giant auxetic behaviour was revealed. In fact, chemical affinity between GO layers and ammonia molecules determined a continuous insertion of NH_3 molecules with pressure up to their solidification, thus attesting for a tendency of GO to increase its d-spacing in order to accommodate molecules that could establish strong interactions with its oxygenated functional groups. At ambient conditions, the recovering of the initial structural features upon compression/decompression was an important signature of the structural stabilization of the GO layered structure by the intercalated atoms and molecules. From the reactive point of view, the fostering of an N-doping of the GO layers, in the perspective of technological applications, was an extremely appealing goal of these experiments. The high pressure behaviour of differently reactive N-bearing molecules, N_2 and NH_3, towards the GO layers was investigated in conjunction with thermal excitation and laser irradiation. Besides the high stability of the layered structure, GO/NH_3 samples exhibited a remarkably pronounced reactivity leading to the incorporation of N atoms on the GO basal plane. This was possible because of the complex network of GO functional groups, that allowed a great number of possible reactions to be triggered and, consequently, a huge variety of possible N-functions to be incorporated on the layers. No assignment of the reaction products was possible in terms of localized vibrational modes. Different spectral features accounted for the inclusion of the same reaction products between the GO layers, as for instance in the case of CO_2, thus suggesting

how the reactivity could be profitably triggered both on the surface than in the confined space but, in any case, revealing how the GO functionalized layers played a crucial role in every step of this processes.

As a last class of materials, the high pressure stability of Phosphorous allotropes has been considered. More in detail, a comparison has been established between the high pressure photoinduced reactivity of amorphous, polymeric P-red and crystalline, layered P-black. This study has allowed to underline the high stability of P-black towards NH_3 upon several irradiation with near-UV wavelengths and, on the other hand, the peculiar and pronounced reactivity of P-red, yielding a complex mixture of heterogeneous products (solid and fluid ones) that could in part be recovered at ambient conditions and whose correct assignment is under elaboration. The remarkable difference in the reactivity of these two phosphorous allotropes could be explained taking into account the reaction mechanism and the extension of the P/NH_3 interface. In fact, the reactivity is triggered by two-photon dissociation of NH_3 and since this molecule cannot enter between the layers of P-black, the reactivity with P-black only occurs at the surfaces. On the other hand, the stability of P-black is an important feature in view of succeeding with the insertion of small atoms and molecules between its layers and, in perspective, to promote the single Phosphorene layer functionalization. Recent, theoretical studies about phosphorous hydrides are the proof of a renewed interest of the scientific community towards non-metal hydrides in general and, more specifically, towards the Phosphorene sheets functionalization for tailored, practical applications. The experiment conducted on room temperature compression/decompression of P-black in the presence of He and H_2 allowed to better describe and understand the high pressure behaviour of P-black and its equation of state and, furthermore, provided evidences for He and H_2 inclusion between the layers in the orthorhombic and rhombohedral phases. In fact, the high density induced inclusion of He and H_2 were able to partially deactivate the transition mechanism from the rhombohedral A17 to the simple cubic sc phase. The presence of the guest atoms and

molecules were responsible for a partial retention of Bragg reflections related to the rhombohedral phase of P-black well beyond the transition threshold to simple cubic phase, in conditions where no transition hysteresis were reported in available literature data and no metastability of the low pressure phase can be expected also because of the high hydrostaticity of the pressure transmitting media. Another remarkable feature we found is related to the high strain of the residual rhombohedral domains of the P-black crystal into the simple cubic phase. It is not clear if the He and H_2 inclusion could possibly be related to the presence of few defects on the surface and edges of the P-black crystal, or if a massive penetration of the two fluids between the layers structure occurred, resulting in some kind of steric hindrance for the complete transition to the sc phase. In fact, an estimate of the amount of the residual rhombohedral phase with respect to the simple cubic one was not possible. However, the inclusion of He and H_2 and the partial deactivation of the transition mechanism through high pressure phases of P-black remarked the capability of confined systems to strongly affect the behaviour of the confining matrix.

Subnanometric confinement is a common circumstance experienced by a great variety of molecular systems throughout the whole universe, under largely varying P,T, hν conditions. The experiments conducted on three different classes of materials and presented in this work, together with other studies on clathrate hydrates not discussed here, helped to unveil several aspects of the reduced dimensionality interactions in guest-host systems. The main achievements were related to the successful attempt to highlight the importance of the structural features of subnanometric spaces provided by the host matrices, reflecting in a largely different behaviour of the guest molecules. Confined polyacetylene in 3D and 1D zeolites, as instance, exhibited remarkably different structural properties. On the other hand, the nature and chemical conformation of the host systems account for the different role played by the matrices in presence of intercalated atoms and molecules. Synthetic, pure-SiO_2 zeolites were in fact inert, non catalytic inorganic scaffold

that simply provided reduced space for polymerization reaction to occur with a pronounced selectivity. In contrast GO, characterized by its several oxygenated functions, established favourable interactions with some inclusion candidates yielding peculiar behaviours under high pressure that leaded to interesting structural (*auxetic* behaviour) and reactive (incorporation of N-atoms in the basal plane) results. The effects of confinement have been exploited for the synthesis of nanocomposite compounds with specific and tunable characteristics. PASIL, pCOSIL and, mostly, their 1D analogous PA/TON and pCO/TON are good examples of nanocomposite products with strong directional properties (as 1D-nanoconductivity) and of high energy density materials. N-doped GO, as obtained from photoinduced reactivity of GO and NH_3, can be useful materials for catalysis. Finally, the possibility to obtain single Phosphorene layers in view of their functionalization opens countless possibilities in technological applications. Other interesting products could be obtained by these high pressure routes, i.e. by embedding and separating conducting or semi-conducting layers within electrically insulating matrices (the idea lying behind the GO/polyEthylene experiment), and there is a wide range of diverse possibility for developing new synthesis and exploring entire new classes of useful materials for several technological applications.

The mutual interactions between guest molecules and the host systems are a key parameter for the complete understanding of the behaviour of confined systems, and the three classes of materials taken into account in this work allowed to investigate purely reduced dimensionality-oriented mechanism and, also, functional groups-mediated interactions. The knowledge of this peculiar aspects of high pressure reactivity under extreme confinement conditions could help to elucidate several, intriguing phenomena on our planet and universe and could possibly be exploited for driving the synthesis of new materials for tailored applications.

List of Publications

1. D. Scelta, M. Ceppatelli, M. Santoro, R. Bini, F. A. Gorelli, A. Perucchi, M. Mezouar, A. van der Lee, J. Haines, "High Pressure Polymerization in a Confined Space: Conjugated Chain/Zeolite Nanocomposites," *Chem. Mater.*, vol. 26, pp. 2249-2255, 2014.

2. M. Ceppatelli, D. Scelta, G. Tuci, G. Giambastiani, M. Hanfland, R. Bini, "Lattice expansion of graphite oxide by pressure induced insertion of liquid ammonia," *Carbon*, vol. 93, pp.484-491, 2015.

3. M. Santoro, K. Dziubek, D. Scelta, M. Ceppatelli, F. A. Gorelli, R. Bini, J-M. Thibaud, F. Di Renzo, O. Cambon, J. Roquette, P. Hermet, A. van der Lee, J. Haines, "High Pressure Synthesis of All-Transoid Polycarbonyl $[\text{-(C=O)-}]_n$ in a Zeolite," *Chem. Mater.*, vol. 27, pp. 6486-6489, 2015.

4. M. Ceppatelli, D. Scelta, G. Tuci, G. Giambastiani, M. Hanfland, R. Bini, "High-Pressure Chemistry of Graphene Oxide in the Presence of Ar, N_2, and NH_3," *J. Phys. Chem. C*, vol. 120, pp. 5174-5184, 2016.

5. M. Santoro, D. Scelta, K. Dziubek, M. Ceppatelli, F. A. Gorelli, R. Bini, G. Garbarino, J-M. Thibaud, F. Di Renzo, O. Cambon, P. Hermet, J. Roquette, A. van der Lee, J. Haines, "Synthesis of 1D Polymer/Zeolite Nanocomposites under High Pressure," *Chem. Mater.*, vol. 28, pp. 4065-4071, 2016.

6. D. Scelta, M. Ceppatelli, R. Bini, "Pressure induced polymerization of

fluid ethylene," *J. Chem. Phys.*, vol. 145, p. 164504.

7. D. Scelta, M. Ceppatelli, R. Bini, M. Peruzzini, "High pressure chemistry of red and black phosphorus and ammonia under near-UV irradiation", *submitted*

8. D. Scelta, M. Ceppatelli, R. Bini, M. Peruzzini, "Equation of state of P-black in the presence of He and H_2", *submitted*

Bibliography

[1] R. Bini and V. Schettino, *Materials Under Extreme Conditions - Molecular Crystals at High Pressure*. Imperial College Press, 2013.

[2] V. Schettino, R. Bini, M. Ceppatelli, L. Ciabini, and M. Citroni, "Chemical reactions at very high pressure," in *Advances in Chemical Physics* (S. A. Rice, ed.), vol. 131, pp. 105–242, John Wiley & Sons, Inc., 2005.

[3] R. L. Mills, B. Olinger, and D. T. Cromer, "Structure and phase diagram of N_2 and CO to 13 GPa by X-ray diffraction," *J. Chem. Phys.*, vol. 84, p. 2837, 1986.

[4] J. Bernstein, *Polymorphism in Molecular Crystals*. Oxford: Oxford University Press, 2002.

[5] M. I. Eremets, A. G. Gavriliuk, I. A. Trojan, D. A. Dzivenko, and R. Boehler, "Single-bonded cubic form of nitrogen," *Nat. Mater.*, vol. 3, 2004.

[6] M. Ceppatelli, M. Santoro, R. Bini, and V. Schettino, "Fourier transform infrared study of the pressure and laser induced polymerization of solid acetylene," *J. Chem. Phys.*, vol. 113, no. 14, pp. 5991–6000, 2000.

[7] D. Chelazzi, M. Ceppatelli, M. Santoro, R. Bini, and V. Schettino, "High-pressure synthesis of crystalline polyethylene using optical catalysis," *Nat. Mater.*, vol. 3, 2004.

[8] D. Chelazzi, M. Ceppatelli, M. Santoro, R. Bini, and V. Schettino, "Pressure-induced polymerization in solid ethylene," *J. Phys. Chem. B*, vol. 109, no. 46, pp. 21658–21663, 2005. PMID: 16853812.

[9] M. Santoro, F. A. Gorelli, R. Bini, G. Ruocco, S. Scandolo, and W. A. Crichton, "Amorphous silica-like carbon dioxide," *Nature*, vol. 441, 2006.

[10] L. Ciabini, M. Santoro, F. A. Gorelli, R. Bini, V. Schettino, and S. Raugei, "Triggering dynamics of the high-pressure benzene amorphization," *Nat. Mater.*, vol. 6, 2007.

[11] T. C. Fitzgibbons, M. Guthrie, E.-s. Xu, V. H. Crespi, S. K. Davidowski, G. D. Cody, and J. V. Alem, Nasim; Badding, "Benzene-derived carbon nanothreads," *Nat. Mater.*, vol. 14, 9 2015.

[12] M. Ceppatelli and R. Bini, "Light-induced catalyst and solvent-free high pressure synthesis of high density polyethylene at ambient temperature," *Macromol. Rapid Comm.*, vol. 35, no. 8, pp. 787–793, 2014.

[13] C.-G. Wu and T. Bein, "Conducting polyaniline filaments in a mesoporous channel host," *Science*, vol. 264, no. 5166, pp. 1757–1759, 1994.

[14] C.-G. Wu and T. Bein, "Conducting carbon wires in ordered, nanometer-sized channels," *Science*, vol. 266, no. 5187, pp. 1013–1015, 1994.

[15] K. Kageyama, J. Tamazawa, and T. Aida, "Extrusion polymerization: Catalyzed synthesis of crystalline linear polyethylene nanofibers within a mesoporous silica," *Science*, vol. 285, no. 5436, pp. 2113–2115, 1999.

[16] A. R. Lewis, G. J. Millar, R. P. Cooney, and G. A. Bowmaker, "trans-polyacetylene on sodium and cesium mordenites: a resonance Raman spectroscopic study," *Chem. Mater.*, vol. 5, no. 10, pp. 1509–1517, 1993.

[17] G. J. Millar, G. F. McCann, C. M. Hobbis, G. A. Bowmaker, and R. P. Cooney, "Spectroscopic investigation of the polymerization of pyrrole and thiophene within zeolite channels," *J. Chem. Soc., Faraday Trans.*, vol. 90, pp. 2579–2584, 1994.

[18] K. Tajima and T. Aida, "Controlled polymerizations with constrained geometries," *Chem. Commun.*, pp. 2399–2412, 2000.

[19] T. Aida and K. Tajima, "Photoluminescent silicate microsticks containing aligned nanodomains of conjugated polymers by sol gel-based in situ polymerization," *Angew. Chem. Int. Ed.*, vol. 40, no. 20, pp. 3803–3806, 2001.

[20] M. Ikegame, K. Tajima, and T. Aida, "Template synthesis of polypyrrole nanofibers insulated within one-dimensional silicate channels: hexagonal versus lamellar for recombination of polarons into bipolarons," *Angew. Chem. Int. Ed.*, vol. 42, no. 19, pp. 2154–2157, 2003.

[21] K. Tajima, G. Ogawa, and T. Aida, "Novel molecularly hybridized polyethylene/silica composite materials: Polymerization of ethylene with supported titanocenes by mesoporous silicates," *J. Polym. Sci. A Polym. Chem.*, vol. 38, no. S1, pp. 4821–4825, 2000.

[22] M. Krutyeva, A. Wischnewski, M. Monkenbusch, L. Willner, J. Maiz, C. Mijangos, A. Arbe, J. Colmenero, A. Radulescu, O. Holderer, M. Ohl, and D. Richter, "Effect of nanoconfinement on polymer dynamics: Surface layers and interphases," *Phys. Rev. Lett.*, vol. 110, p. 108303, Mar 2013.

[23] M. Fichtner, "Nanoconfinement effects in energy storage materials," *Phys. Chem. Chem. Phys.*, vol. 13, pp. 21186–21195, 2011.

[24] M. Santoro, F. A. Gorelli, R. Bini, A. Salamat, G. Garbarino, C. Levelut, O. Cambon, and J. Haines, "Carbon enters silica forming a

cristobalite-type CO_2-SiO_2 solid solution," *Nat. Commun.*, vol. 5, 4 2014.

[25] R. M. Hazen, A. P. Jones, and J. A. Baross, *Carbon in Earth.* Reviews in mineralogy and geochemistry, v. 75, Mineralogical Society of America and Geochemical Society, 1 ed., 2013.

[26] A. K. Geim and K. S. Novoselov, "The rise of graphene," *Nat. Mater.*, vol. 6, 2007.

[27] D. E. G. Corbridge, *Phosphorus Chemistry, Biochemistry and Technology, Sixth Edition.* CRC Press, 6 ed., 2013.

[28] X. Ling, H. Wang, S. Huang, F. Xia, and M. S. Dresselhaus, "The renaissance of black phosphorus," *Proc. Natl. Acad. Sci. USA*, vol. 112, no. 15, pp. 4523–4530, 2015.

[29] S. Fukuoka, T. Taen, and T. Osada, "Electronic structure and the properties of phosphorene and few-layer black phosphorus," *J. Phys. Soc. Jpn.*, vol. 84, no. 12, p. 121004, 2015.

[30] L. Kou, C. Chen, and S. C. Smith, "Phosphorene: Fabrication, properties, and applications," *J. Phys. Chem. Lett.*, vol. 6, no. 14, pp. 2794–2805, 2015. PMID: 26266865.

[31] H. Liu, A. T. Neal, Z. Zhu, Z. Luo, X. Xu, D. Tománek, and P. D. Ye, "Phosphorene: an unexplored 2d semiconductor with a high hole mobility," *ACS Nano*, vol. 8, no. 4, pp. 4033–4041, 2014. PMID: 24655084.

[32] E. Dendy Sloan Jr. and C. Koh, *Clathrate Hydrates of Natural Gases, Third Edition (Chemical Industries Series).* Chemical Industries Series 119, CRC Press, 3 ed., 2007.

[33] J. S. Loveday and R. J. Nelmes, "High-pressure gas hydrates," *Phys. Chem. Chem. Phys.*, vol. 10, pp. 937–950, 2008.

[34] M. Ceppatelli, R. Bini, and V. Schettino, "High-pressure photodissociation of water as a tool for hydrogen synthesis and fundamental chemistry," *Proc. Natl. Acad. Sci. USA*, vol. 106, no. 28, pp. 11454–11459, 2009.

[35] M. Ceppatelli, R. Bini, and V. Schettino, "High-pressure reactivity of clathrate hydrates by two-photon dissociation of water," *Phys. Chem. Chem. Phys.*, vol. 13, pp. 1264–1275, 2011.

[36] N. Goldman, E. J. Reed, L. E. Fried, I.-F. William Kuo, and A. Maiti, "Synthesis of glycine-containing complexes in impacts of comets on early earth," *Nat. Chem.*, vol. 2, 2010.

[37] C. Pruteanu, "How does high density impact miscibility?." Oral contribution to Joint AIRAPT 25th and EHPRG 53rd meeting, held in Madrid (August 30th- September 4th), 2015.

[38] G. Artioli, C. Lamberti, and G. L. Marra, "Neutron powder diffraction study of orthorhombic and monoclinic defective silicalite," *Acta Crystallogr. Sect. B-Struct. Sci.*, vol. 56, pp. 2–10, Feb 2000.

[39] B. Marler, "Silica-ZSM-22: synthesis and single crystal structure refinement," *Zeolites*, vol. 7, no. 5, pp. 393 – 397, 1987.

[40] F. D. Renzo, F. Remoué, P. Massiani, F. Fajula, F. Figueras, and C. T. Des, "Crystallization kinetics of zeolite TON," *Zeolites*, vol. 11, no. 6, pp. 539 – 548, 1991.

[41] J. Haines, C. Levelut, A. Isambert, P. Hébert, S. Kohara, D. A. Keen, T. Hammouda, and D. Andrault, "Topologically ordered amorphous silica obtained from the collapsed siliceous zeolite, Silicalite-1-F: A step toward "perfect" glasses," *J. Am. Chem. Soc.*, vol. 131, no. 34, pp. 12333–12338, 2009. PMID: 19705916.

[42] J. L. Guth, H. Kessler, and R. Wey, "New route to pentasil-type zeolites using a non alkaline medium in the presence of fluoride ions," in *New*

Developments in Zeolite Science and Technology- Proceedings of the 7th International Zeolite Conference (A. I. Y. Murakami and J. Ward, eds.), vol. 28 of *Studies in Surface Science and Catalysis*, pp. 121 – 128, Elsevier, 1986.

[43] J. Haines, O. Cambon, C. Levelut, M. Santoro, F. Gorelli, and G. Garbarino, "Deactivation of pressure-induced amorphization in Silicalite SiO_2 by insertion of guest species," *J. Am. Chem. Soc.*, vol. 132, no. 26, pp. 8860–8861, 2010.

[44] B. Coasne, J. Haines, C. Levelut, O. Cambon, M. Santoro, F. Gorelli, and G. Garbarino, "Enhanced mechanical strength of zeolites by adsorption of guest molecules," *Phys. Chem. Chem. Phys.*, vol. 13, pp. 20096–20099, 2011.

[45] M. Santoro, F. A. Gorelli, R. Bini, J. Haines, and A. van der Lee, "High-pressure synthesis of a polyethylene/zeolite nano-composite material," *Nat. Commun.*, vol. 4, 3 2013.

[46] S. Park, R.-W. G. Kunstleve, H. Graetsch, and H. Gies, "The thermal expansion of the zeolites MFI, AFI, DOH, DDR, and MTN in their calcined and as synthesized forms," in *Progress in Zeolite and Microporous MaterialsPreceedings of the 11th International Zeolite Conference* (S.-K. I. Hakze Chon and Y. S. Uh, eds.), vol. 105 of *Studies in Surface Science and Catalysis*, pp. 1989 – 1994, Elsevier, 1997.

[47] K. Aoki, Y. Kakudate, M. Yoshida, S. Usuba, K. Tanaka, and S. Fujiwara, "Raman scattering observations of phase transitions and polymerizations in acetylene at high pressure," *Solid State Commun.*, vol. 64, no. 10, pp. 1329 – 1331, 1987.

[48] K. Aoki, Y. Kakudate, S. Usuba, M. Yoshida, K. Tanaka, and S. Fujiwara, "High-pressure Raman study of liquid and crystalline C_2H_2," *J. Chem. Phys.*, vol. 88, no. 8, pp. 4565–4568, 1988.

[49] K. Aoki, S. Usuba, M. Yoshida, Y. Kakudate, K. Tanaka, and S. Fujiwara, "Raman study of the solid-state polymerization of acetylene at high pressure," *J. Chem. Phys.*, vol. 89, no. 1, pp. 529–534, 1988.

[50] A. Anderson, B. Andrews, and B. H. Torrie, "Raman and far infrared spectra of crystalline acetylene, C_2H_2 and C_2D_2," *J. Raman Spectrosc.*, vol. 16, no. 3, pp. 202–207, 1985.

[51] M. Sakashita, H. Yamawaki, and K. Aoki, "FT-IR study of the solid state polymerization of acetylene under pressure," *J. Phys. Chem.*, vol. 100, no. 23, pp. 9943–9947, 1996.

[52] L. Ciabini, M. Santoro, R. Bini, and V. Schettino, "High pressure reactivity of solid benzene probed by infrared spectroscopy," *J. Chem. Phys.*, vol. 116, no. 7, pp. 2928–2935, 2002.

[53] N. M. Balzaretti, C. A. Perottoni, and J. A. H. da Jornada, "High-pressure Raman and infrared spectroscopy of polyacetylene," *J. Raman Spectrosc.*, vol. 34, no. 4, pp. 259–263, 2003.

[54] M. McIntire, L. Zhao, V. Kobryanskii, and E. Chronister, "High-pressure Raman spectroscopy of nanoparticle polyacetylene in a poly(vinyl-butyral) matrix," *J. Raman Spectrosc.*, vol. 42, no. 6, pp. 1435–1441, 2011.

[55] L. S. Lichtmann, E. A. Imhoff, A. Sarhangi, and D. B. Fitchen, "Resonance Raman spectra of cis $(CH)_x$ and $(CH)_x$," *J. Chem. Phys.*, vol. 81, no. 1, pp. 168–184, 1984.

[56] H. Takeuchi, Y. Furukawa, I. Harada, and H. Shirakawa, "Vibrational analysis of polyacetylene and copoly(acetylene+acetylene-d_2): In-plane vibrations of trans-polyene chains," *J. Chem. Phys.*, vol. 84, no. 5, pp. 2882–2890, 1986.

[57] H. Teramae, T. Yamabe, and A. Imamura, "Ab initio studies on the geometrical and vibrational structures of polymers," *J. Chem. Phys.*, vol. 81, no. 8, pp. 3564–3572, 1984.

[58] F. B. Schügerl and H. Kuzmany, "Optical modes of trans-polyacetylene," *J. Chem. Phys.*, vol. 74, no. 2, pp. 953–958, 1981.

[59] I. Harada, Y. Furukawa, M. Tasumi, H. Shirakawa, and S. Ikeda, "Spectroscopic studies on doped polyacetylene and β-carotene," *J. Chem. Phys.*, vol. 73, no. 10, pp. 4746–4757, 1980.

[60] J. Tao and A. Sleight, "The role of rigid unit modes in negative thermal expansion," *J. Solid State Chem.*, vol. 173, no. 2, pp. 442 – 448, 2003.

[61] M. Santoro, F. Gorelli, J. Haines, O. Cambon, C. Levelut, and G. Garbarino, "Silicon carbonate phase formed from carbon dioxide and silica under pressure," *Proc. Natl. Acad. Sci. USA*, vol. 108, no. 19, pp. 7689–7692, 2011.

[62] M. Santoro, D. Scelta, K. Dziubek, M. Ceppatelli, F. A. Gorelli, R. Bini, G. Garbarino, J.-M. Thibaud, F. Di Renzo, O. Cambon, P. Hermet, J. Rouquette, A. van der Lee, and J. Haines, "Synthesis of 1D polymer/zeolite nanocomposites under high pressure," *Chem. Mater.*, vol. 28, no. 11, pp. 4065–4071, 2016.

[63] D. Scelta, M. Ceppatelli, M. Santoro, R. Bini, F. A. Gorelli, A. Perucchi, M. Mezouar, A. van der Lee, and J. Haines, "High pressure polymerization in a confined space: Conjugated chain/zeolite nanocomposites," *Chem. Mater.*, vol. 26, no. 7, pp. 2249–2255, 2014.

[64] A. I. Katz, D. Schiferl, and R. L. Mills, "New phases and chemical reactions in solid CO under pressure," *J. Phys. Chem.*, vol. 88, p. 3176, 1984.

[65] R. L. Mills, D. Schiferl, A. I. Katz, and B. Olinger, "New phases and chemical reactions in solid CO under pressure," *J. Phys. (Paris), Colloq.*, vol. 45, pp. C8–187, 1984.

[66] M. Lipp, W. J. Evans, V. Garcia-Baonza, and H. E. Lorenzana, "Carbon monoxide: spectroscopic characterization of the high-pressure polymerized phase," *J. Low Temp. Phys.*, vol. 111, no. 3, pp. 247–256, 1998.

[67] M. J. Lipp, W. J. Evans, B. J. Baer, and C. S. Yoo, "High-energy-density extended CO solid," *Nat. Mater.*, vol. 4, p. 211, 2005.

[68] W. J. Evans, M. J. Lipp, C. S. Yoo, H. Cynn, J. L. Herberg, R. S. Maxwell, and M. F. Nicol, "Pressure-induced polymerization of carbon monoxide: Disproportionation and synthesis of an energetic lactonic polymer," *Chem. Mater.*, vol. 18, p. 2520, 2006.

[69] D. T. Cromer, D. Schiferl, R. LeSar, and R. L. Mills, "Room-temperature structure of carbon monoxide at 2.7 and 3.6 GPa," *Acta Crystallogr., Sect. C: Cryst. Struct. Commun.*, vol. C39, p. 1146, 1983.

[70] S. Bernard, G. L. Chiarotti, S. Scandolo, and E. Tosatti, "Decomposition and polymerization of solid carbon monoxide under pressure," *Phys. Rev. Lett.*, vol. 81, p. 2092, 1998.

[71] N. Rademacher, L. Bayarjargal, W. Morgenroth, B. Winkler, J. Ciezak-Jenkins, I. G. Batyrev, and V. Milman, "The local atomic structures of liquid CO at 3.6 GPa and polymerized CO at 0 to 30 GPa from high-pressure pair distribution function analysis," *Chem. - Eur. J.*, vol. 20, p. 11531, 2014.

[72] M. Ceppatelli, A. Serdyukov, R. Bini, and H. J. Jodl, "Pressure induced reactivity of solid CO by FTIR studies," *J. Phys. Chem. B*, vol. 113, p. 6652, 2009.

[73] J. Sun, D. D. Klug, C. J. Pickard, and R. J. Needs, "Controlling the bonding and band gaps of solid carbon monoxide with pressure," *Phys. Rev. Lett.*, vol. 106, p. 145502, Apr 2011.

[74] M. Santoro, K. Dziubek, D. Scelta, M. Ceppatelli, F. A. Gorelli, R. Bini, J.-M. Thibaud, F. Di Renzo, O. Cambon, J. Rouquette, P. Hermet, A. van der Lee, and J. Haines, "High pressure synthesis of all-transoid polycarbonyl $[\text{-(c=o)-}]_n$ in a zeolite," *Chem. Mater.*, vol. 27, no. 19, pp. 6486–6489, 2015.

[75] D. R. Dreyer, S. Park, C. W. Bielawski, and R. S. Ruoff, "The chemistry of graphene oxide," *Chem. Soc. Rev.*, vol. 39, pp. 228–240, 2010.

[76] F. K. P. Michio Inagaki Ph.D., *Materials Science and Engineering of Carbon: Fundamentals, Second Edition.* Butterworth-Heinemann, 2 ed., 2014.

[77] A. Talyzin, V. Solozhenko, O. Kurakevych, T. Szabó, I. Dékány, A. Kurnosov, and V. Dmitriev, "Colossal pressure-induced lattice expansion of graphite oxide in the presence of water," *Angew. Chem., Int. Ed.*, vol. 47, p. 8268, 2008.

[78] B. C. Brodie, "On the atomic weight of graphite," *Phil. Trans. R. Soc. Lond.*, vol. 149, pp. 249–259, 1859.

[79] L. Staudenmaier, "Verfahren zur Darstellung der Graphitsäure," *Ber. Dtsch. Chem. Ges.*, vol. 31, no. 2, pp. 1481–1487, 1898.

[80] U. Hofmann and E. König, "Untersuchungen über Graphitoxyd," *Z. Anorg. Allg. Chem.*, vol. 234, no. 4, pp. 311–336, 1937.

[81] W. S. Hummers and R. E. Offeman, "Preparation of graphitic oxide," *J. Am. Chem. Soc.*, vol. 80, no. 6, pp. 1339–1339, 1958.

[82] D. C. Marcano, D. V. Kosynkin, J. M. Berlin, A. Sinitskii, Z. Sun, A. Slesarev, L. B. Alemany, W. Lu, and J. M. Tour, "Improved synthesis

of graphene oxide," *ACS Nano*, vol. 4, no. 8, pp. 4806–4814, 2010. PMID: 20731455.

[83] D. R. Dreyer, A. D. Todd, and C. W. Bielawski, "Harnessing the chemistry of graphene oxide," *Chem. Soc. Rev.*, vol. 43, pp. 5288–5301, 2014.

[84] M. Ceppatelli, D. Scelta, G. Tuci, G. Giambastiani, M. Hanfland, and R. Bini, "Lattice expansion of graphite oxide by pressure induced insertion of liquid ammonia," *Carbon*, vol. 93, pp. 484 – 491, 2015.

[85] U. Hofmann and R. Holst, "Über die Säurenatur und die Methylierung von Graphitoxyd," *Ber. Dtsch. Chem. Ges. (A and B Series)*, vol. 72, no. 4, pp. 754–771, 1939.

[86] G. Ruess, "Über das Graphitoxyhydroxyd Graphitoxyd," *Monatsh. Chem. Verw. Tl.*, vol. 76, no. 3, pp. 381–417, 1947.

[87] W. Scholz and H. P. Boehm, "Untersuchungen am Graphitoxid. VI. betrachtungen zur Struktur des Graphitoxids," *Z. Anorg. Allg. Chem.*, vol. 369, no. 3-6, pp. 327–340, 1969.

[88] T. Nakajima, A. Mabuchi, and R. Hagiwara, "A new structure model of graphite oxide," *Carbon*, vol. 26, no. 3, pp. 357 – 361, 1988.

[89] T. Nakajima and Y. Matsuo, "Formation process and structure of graphite oxide," *Carbon*, vol. 32, no. 3, pp. 469 – 475, 1994.

[90] A. Lerf, H. He, M. Forster, and J. Klinowski, "Structure of graphite oxide revisited," *J. Phys. Chem. B*, vol. 102, no. 23, pp. 4477–4482, 1998.

[91] T. Szabó, O. Berkesi, P. Forgó, K. Josepovits, Y. Sanakis, D. Petridis, and I. Dékány, "Evolution of surface functional groups in a series of progressively oxidized graphite oxides," *Chem. Mater.*, vol. 18, no. 11, pp. 2740–2749, 2006.

[92] M. Acik, C. Mattevi, C. Gong, G. Lee, K. Cho, M. Chhowalla, and Y. J. Chabal, "The role of intercalated water in multilayered graphene oxide," *ACS Nano*, vol. 4, no. 10, pp. 5861–5868, 2010. PMID: 20886867.

[93] R. S. Park, Sungjin; Ruoff, "Chemical methods for the production of graphenes," *Nat. Nanotech.*, vol. 4, 2009.

[94] X. Li, H. Wang, J. T. Robinson, H. Sanchez, G. Diankov, and H. Dai, "Simultaneous nitrogen doping and reduction of graphene oxide," *J. Am. Chem. Soc.*, vol. 131, no. 43, pp. 15939–15944, 2009. PMID: 19817436.

[95] A. Talyzin, S. Luzan, T. Szabó, D. Chernyshev, and V. Dmitriev, "Temperature dependent structural breathing of hydrated graphite oxide in H_2O," *Carbon*, vol. 49, no. 6, pp. 1894 – 1899, 2011.

[96] A. V. Talyzin, B. Sundqvist, T. Szabó, I. Dékány, and V. Dmitriev, "Pressure-induced insertion of liquid alcohols into graphite oxide structure," *J. Am. Chem. Soc.*, vol. 131, p. 18445, 2009.

[97] A. V. Talyzin and S. M. Luzan, "Pressure-induced insertion of liquid acetone into the graphite oxide structure," *J. Phys. Chem. C*, vol. 114, no. 15, pp. 7004–7006, 2010.

[98] A. V. Talyzin, B. Sundqvist, T. Szabó, and V. Dmitriev, "Structural breathing of graphite oxide pressurized in basic and acidic solutions.," *J. Phys. Chem. Lett.*, vol. 2, no. 4, pp. 309–313, 2011.

[99] D. Kim, D. W. Kim, H.-K. Lim, J. Jeon, H. Kim, H.-T. Jung, and H. Lee, "Intercalation of gas molecules in graphene oxide interlayer: The role of water," *J. Phys. Chem. C*, vol. 118, no. 20, pp. 11142–11148, 2014.

[100] F. Datchi, P. Loubeyre, and R. LeToullec, "Extended and accurate determination of the melting curves of argon, helium, ice (H_2O), and hydrogen (H_2)," *Phys. Rev. B*, vol. 61, pp. 6535–6546, Mar 2000.

[101] E. H. Abramson, "Melting curves of argon and methane," *High Pressure Res.*, vol. 31, no. 4, pp. 549–554, 2011.

[102] G. J. Hanna and M. D. McCluskey, "Equation of state and refractive index of argon at high pressure by confocal microscopy," *Phys. Rev. B*, vol. 81, p. 132104, Apr 2010.

[103] W. L. Vos and J. A. Schouten, "Improved phase diagram of nitrogen up to 85 kbar," *J. Chem. Phys.*, vol. 91, no. 10, pp. 6302–6305, 1989.

[104] R. Bini, L. Ulivi, J. Kreutz, and H. J. Jodl, "High-pressure phases of solid nitrogen by Raman and infrared spectroscopy," *J. Chem. Phys.*, vol. 112, no. 19, pp. 8522–8529, 2000.

[105] M. Guthrie, C. A. Tulk, J. Molaison, and A. M. dos Santos, "Local structural motifs and extended-range order in liquid and solid ammonia under pressure," *Phys. Rev. B*, vol. 85, p. 184205, May 2012.

[106] R. B. Von Dreele and R. C. Hanson, "Structure of NH_3-III at 1.28 GPa and room temperature," *Acta Crystallogr. Sect. C-Cryst. Struct. Commun.*, vol. 40, pp. 1635–1638, Oct 1984.

[107] S. Klotz, M. Gauthier, J. M. Besson, G. Hamel, R. J. Nelmes, J. S. Loveday, R. M. Wilson, and W. G. Marshall, "Techniques for neutron diffraction on solidified gases to 10 GPa and above: Applications to ND_3 phase IV," *Appl. Phys. Lett.*, vol. 67, no. 9, pp. 1188–1190, 1995.

[108] T. Kume, M. Daimon, S. Sasaki, and H. Shimizu, "High-pressure elastic properties of liquid and solid ammonia," *Phys. Rev. B*, vol. 57, pp. 13347–13350, Jun 1998.

[109] S. Ninet and F. Datchi, "High pressure–high temperature phase diagram of ammonia," *J. Chem. Phys.*, vol. 128, no. 15, 2008.

[110] A. Harlow, G. Wiegand, and E. Franck, "The density of ammonia at high pressures to 723 K and 950 MPa," *Ber. Bunsenges. Phys. Chem.*, vol. 101, no. 10, pp. 1461–1465, 1997.

[111] M. Seredych, J. A. Rossin, and T. J. Bandosz, "Changes in graphite oxide texture and chemistry upon oxidation and reduction and their effect on adsorption of ammonia," *Carbon*, vol. 49, no. 13, pp. 4392 – 4402, 2011.

[112] S. Klotz, J.-C. Chervin, P. Munsch, and G. L. Marchand, "Hydrostatic limits of 11 pressure transmitting media," *J. Phys. D Appl. Phys.*, vol. 42, no. 7, p. 075413, 2009.

[113] R. C. Hanson and L. H. Jones, "Infrared and Raman studies of pressure effects on the vibrational modes of solid CO_2," *J. Chem. Phys.*, vol. 75, p. 1102, 1981.

[114] Vetter. Diploma Thesis of Schaeferjohann, U. FB Physik, University of Paderborn), 2001.

[115] S. Eigler, C. Dotzer, A. Hirsch, M. Enzelberger, and P. Müller, "Formation and decomposition of CO_2 intercalated graphene oxide," *Chem. Mater.*, vol. 24, p. 1276, 2012.

[116] M. Sakashita, H. Yamawaki, H. Fujihisa, and K. Aoki, "Phase study of NH_3 to 100 GPa by infrared absorption," *The Review of High Pressure Science and Technology*, vol. 7, pp. 796–798, 1998.

[117] A. Bach, J. M. Hutchison, R. J. Holiday, and F. F. Crim, "Vibrational spectroscopy and photodissociation of jet-cooled ammonia," *J. Chem. Phys.*, vol. 116, no. 12, pp. 4955–4961, 2002.

[118] W. Lai, S. Y. Lin, D. Xie, and H. Guo, "Full-dimensional quantum dynamics of $\tilde{A}$-state photodissociation of ammonia: Absorption spectra," *J. Chem. Phys.*, vol. 129, no. 15, 2008.

[119] L. Xu and L. Cheng, "Graphite oxide under high pressure: A Raman spectroscopic study," *J. Nanomater.*, vol. 2013, p. 1, 2013.

[120] A. Kaniyoor, T. T. Baby, T. Arockiadoss, N. Rajalakshmi, and S. Ramaprabhu, "Wrinkled graphenes: A study on the effects of synthesis parameters on exfoliation-reduction of graphite oxide," *J. Phys. Chem. C*, vol. 115, no. 36, pp. 17660–17669, 2011.

[121] A. Bagri, C. Mattevi, M. Acik, Y. J. Chabal, M. Chhowalla, and V. B. Shenoy, "Structural evolution during the reduction of chemically derived graphene oxide," *Nat. Chem.*, vol. 2, p. 581, 2010.

[122] M. Acik, G. Lee, C. Mattevi, A. Pirkle, R. M. Wallace, M. Chhowalla, K. Cho, and Y. Chabal, "The role of oxygen during thermal reduction of graphene oxide studied by infrared absorption spectroscopy," *J. Phys. Chem. C*, vol. 115, p. 19761, 2011.

[123] Q. Lai, S. Zhu, X. Luo, M. Zou, and S. Huang, "Ultraviolet-visible spectroscopy of graphene oxides," *AIP Adv.*, vol. 2, p. 032146, 2012.

[124] M. Ceppatelli, M. Pagliai, R. Bini, and H. J. Jodl, "High-pressure photoinduced synthesis of polynitrogen in δ and η nitrogen crystals substitutionally doped with CO," *J. Phys. Chem. C*, vol. 119, no. 1, pp. 130–140, 2015.

[125] A. C. Ferrari, S. E. Rodil, and J. Robertson, "Interpretation of infrared and Raman spectra of amorphous carbon nitrides," *Phys. Rev. B: Condens. Matter Mater. Phys.*, vol. 67, pp. 155306–1, 2003.

[126] M. Seredych and T. J. Bandosz, "Mechanism of ammonia retention on graphite oxides: Role of surface chemistry and structure," *J. Phys. Chem. C*, vol. 111, p. 15596, 2007.

[127] W. H. Slabaugh and B. C. Seiler, "Interactions of ammonia with graphite oxide," *J. Phys. Chem.*, vol. 66, p. 396, 1962.

[128] J. M. Price, M. W. Crofton, and Y. T. Lee, "Vibrational spectroscopy of the ammoniated ammonium ions $NH_4^+(NH_3)_n$ (n = 1–10)," *J. Phys. Chem.*, vol. 95, p. 2182, 1991.

[129] M. Ashfold, C. Bennett, and R. Dixon, "Predissociation dynamics of $\tilde{A}$-state ammonia probed by two-photon excitation spectroscopy," *Chem. Phys.*, vol. 93, p. 293, 1985.

[130] M. Ceppatelli, R. Bini, and V. Schettino, "High-pressure reactivity of model hydrocarbons driven by near-UV photodissociation of water," *J. Phys. Chem. B*, vol. 113, p. 14640, 2009.

[131] H. R. Thomas, S. P. Day, W. E. Woodruff, C. Vallés, R. J. Young, I. A. Kinloch, G. W. Morley, J. V. Hanna, N. R. Wilson, and J. P. Rourke, "Deoxygenation of graphene oxide: Reduction or cleaning?," *Chem. Mater.*, vol. 25, p. 3580, 2013.

[132] M. Ceppatelli, M. Santoro, R. Bini, and V. Schettino, "High pressure reactivity of solid furan probed by infrared and Raman spectroscopy," *J. Chem. Phys.*, vol. 118, no. 3, pp. 1499–1506, 2003.

[133] M. Citroni, S. Fanetti, and R. Bini, "Pressure and laser-induced reactivity in crystalline s-triazine," *J. Phys. Chem. C*, vol. 118, no. 19, pp. 10284–10290, 2014.

[134] P. Hammer, R. Lacerda, R. D. Jr., and F. Alvarez, "Comparative study on the bonding structure of hydrogenated and hydrogen free carbon nitride films with high n content," *Diam. Relat. Mater.*, vol. 9, no. 3–6, pp. 577 – 581, 2000.

[135] M. D., *Introduction to Industrial Polyethylene*. Wiley-Scrivener, Wiley, 1 ed., 2010.

[136] A. Peacock, *Handbook of Polyethylene - Structures, Properties and Applications*. Plastics Engineering, CRC Press, 1 ed., 2000.

[137] N. Trappeniers and F. Ligthart, "Proton spin relaxation in ethylene. A new high pressure phase," *Chem. Phys. Lett.*, vol. 19, no. 4, pp. 465 – 470, 1973.

[138] H. Wieldraaijer, J. A. Schouten, and N. J. Trappeniers, "Investigation of the phase diagrams of ethane, ethylene, and methane at high pressures," *High Temp.- High Press.*, vol. 15, no. 1, pp. 87 – 92, 1983.

[139] L. van der Putten, J. A. Schouten, and N. J. Trappeniers, "A differential scanning calorimetry study of ethylene and propane up to 10 kbar: the phase diagram of ethylene up to 23 kbar," *High Temp.- High Press.*, vol. 18, no. 3, pp. 255 – 264, 1986.

[140] M. Buback, "The high pressure polymerization of pure ethylene," *Makromolekul. Chem.*, vol. 181, no. 2, pp. 373–382, 1980.

[141] M. Buback, "Spectroscopic investigation of the high pressure ethylene polymerization," *Z. Naturforsch. A*, vol. 39, no. 4, pp. 399–411, 1984.

[142] J. Smukala, R. Span, and W. Wagner, "New equation of state for ethylene covering the fluid region for temperatures from the melting line to 450 K at pressures up to 300 MPa," *J. Phys. Chem. Ref. Data*, vol. 29, no. 5, pp. 1053–1121, 2000.

[143] W. Press and J. Eckert, "Structure of solid ethylene-d_4," *J. Chem. Phys.*, vol. 65, no. 11, pp. 4362–4364, 1976.

[144] G. J. H. Nes and A. Vos, "Single-crystal structures and electron density distributions of ethane, ethylene and acetylene. III. Single-crystal X-ray structure determination of ethylene at 85 K," *Acta Crystallogr. Sect. B-Struct. Sci.*, vol. 35, pp. 2593–2601, Nov 1979.

[145] M. Avrami, "Kinetics of phase change. I. General theory," *J. Chem. Phys.*, vol. 7, no. 12, pp. 1103–1112, 1939.

[146] M. Avrami, "Kinetics of phase change. II. Transformation-time relations for random distribution of nuclei," *J. Chem. Phys.*, vol. 8, no. 2, pp. 212–224, 1940.

[147] M. Avrami, "Granulation, phase change, and microstructure kinetics of phase change. III," *J. Chem. Phys.*, vol. 9, no. 2, pp. 177–184, 1941.

[148] G. Zerbi and M. Del Zoppo, *Vibrational Spectra as a Probe of Structural Order/Disorder in Chain Molecules and Polymers*, pp. 87–206. Wiley-VCH Verlag GmbH, 2007.

[149] S. Krimm, *Infrared spectra of high polymers*, pp. 51–172. Berlin, Heidelberg: Springer Berlin Heidelberg, 1960.

[150] J. C. Decius and H. R. M., *Molecular Vibrations in Crystals*. McGraw-Hill, 1977.

[151] L. Fontana, D. Q. Vinh, M. Santoro, S. Scandolo, F. A. Gorelli, R. Bini, and M. Hanfland, "High-pressure crystalline polyethylene studied by X-ray diffraction and *ab initio* simulations," *Phys. Rev. B*, vol. 75, p. 174112, May 2007.

[152] D. L. Dorset, "Applications of direct methods for structure determination to problems in electron and X-ray fibre diffraction of polymers," *Rep. Prog. Phys.*, vol. 66, no. 3, p. 305, 2003.

[153] S.-R. Hu, T. Kyu, and R. S. Stein, "Characterization and properties of polyethylene blends I. linear low-density polyethylene with high-density polyethylene," *J. Polym. Sci. Part B Polym. Phys.*, vol. 25, no. 1, pp. 71–87, 1987.

[154] J. E. Mark, *Physical Properties of Polymers Handbook*. Springer, 2 ed., 2007.

[155] K. Russell, B. Hunter, and R. Heyding, "Monoclinic polyethylene revisited," *Polymer*, vol. 38, no. 6, pp. 1409 – 1414, 1997.

[156] J. Spooner, B. Yanciw, B. Wiebe, and N. Weinberg, "Reaction profiles and energy surfaces of compressed species," *J. Phys. Chem. A*, vol. 118, no. 4, pp. 765–777, 2014. PMID: 24372515.

[157] R. J. Sension and B. S. Hudson, "Vacuum ultraviolet resonance Raman studies of the excited electronic states of ethylene," *J. Chem. Phys.*, vol. 90, no. 3, pp. 1377–1389, 1989.

[158] R. P. Krawczyk, A. Viel, U. Manthe, and W. Domcke, "Photoinduced dynamics of the valence states of ethene: a six-dimensional potential-energy surface of three electronic states with several conical intersections," *J. Chem. Phys.*, vol. 119, no. 3, pp. 1397–1411, 2003.

[159] J. M. Martin Klessinger, *Excited States and Photochemistry of Organic Molecules*. VCH (New York), 1995.

[160] D. Scelta, M. Ceppatelli, and R. Bini, "Pressure induced polymerization of fluid ethylene," *J. Chem. Phys.*, vol. 145, no. 16, 2016.

[161] T. J. Brown, C. E. Wrighton, N. E. Idoine, E. R. Raycraft, R. A. Shaw, D. E. A., J. Rippingale, and T. Bide, *World Mineral Production 2010-14*. Keyworth, Nottingham, England: British Geological Survey, 1 ed., 2016.

[162] M. C. Mew, ed., *World Survey of Phosphate Deposits*. British Sulphur Corporation Limited, 4 ed., 1980.

[163] J. O. Nriagu and P. B. Moore, *Phosphate Minerals*. Springer-Verlag Berlin Heidelberg, 1 ed., 1984.

[164] S. Böcker and M. Häser, "Covalent structures of phosphorus: A comprehensive theoretical study," *Z. Anorg. Allg. Chem.*, vol. 621, no. 2, pp. 258–286, 1995.

[165] D. E. C. Corbridge and E. J. Lowe, "Structure of white phosphorus: Single crystal X-ray examination," *Nature*, vol. 170, 10 1952.

[166] P. W. Bridgman, "Two new modifications of phosphorus," *J. Am. Chem. Soc.*, vol. 36, no. 7, pp. 1344–1363, 1914.

[167] H. Spiess, R. Grosescu, and H. Haeberlen, "Molecular motion studied by NMR powder spectra. II. Experimental results for solid P_4 and solid $Fe(CO)_5$," *Chem. Phys.*, vol. 6, no. 2, pp. 226 – 234, 1974.

[168] A. Simon, H. Borrmann, and H. Craubner, "Crystal structure of ordered white phosphorus (β-P)," *Phosphorus Sulfur Relat. Elem.*, vol. 30, no. 1-2, pp. 507–510, 1987.

[169] A. Simon, H. Borrmann, and J. Horakh, "On the polymorphism of white phosphorus," *Chem. Ber.*, vol. 130, no. 9, pp. 1235–1240, 1997.

[170] H. Östmark, S. Wallin, N. Hore, and O. Launila, "Raman spectra of P_4 at low temperatures," *J. Chem. Phys.*, vol. 119, no. 12, pp. 5918–5922, 2003.

[171] H. Okudera, R. E. Dinnebier, and A. Simon, "The crystal structure of γ-P_4, a low temperature modification of white phosphorus," *Z. Kristallogr.*, vol. 220, 03 2005.

[172] P. Jóvári and L. Pusztai, "On the structure of amorphous red phosphorus," *Appl. Phys. A*, vol. 74, no. 1, pp. s1092–s1094, 2002.

[173] J. M. Zaug, A. K. Soper, and S. M. Clark, "Pressure-dependent structures of amorphous red phosphorus and the origin of the first sharp diffraction peaks," *Nat. Mater.*, vol. 7, 2008.

[174] M. Ceppatelli, R. Bini, M. Caporali, and M. Peruzzini, "High-pressure chemistry of red phosphorus and water under near-UV irradiation," *Angew. Chem. Int. Ed.*, vol. 52, no. 8, pp. 2313–2317, 2013.

[175] M. Ceppatelli, S. Fanetti, and R. Bini, "Photoinduced reactivity of red phosphorus and ethanol at high pressure," *J. Phys. Chem. C*, vol. 117, no. 25, pp. 13129–13135, 2013.

[176] M. Ceppatelli, S. Fanetti, M. Citroni, and R. Bini, "Photoinduced reactivity of liquid ethanol at high pressure," *J. Phys. Chem. B*, vol. 114, no. 47, pp. 15437–15444, 2010. PMID: 21053928.

[177] A. Brown and S. Rundqvist, "Refinement of the crystal structure of black phosphorus," *Acta Crystallogr.*, vol. 19, pp. 684–685, Oct 1965.

[178] K. J. Chang and M. L. Cohen, "Structural stability of phases of black phosphorus," *Phys. Rev. B*, vol. 33, pp. 6177–6186, May 1986.

[179] T. Kikegawa and H. Iwasaki, "An X-ray diffraction study of lattice compression and phase transition of crystalline phosphorus," *Acta Crystallogr. Sect. B-Struct. Sci.*, vol. 39, pp. 158–164, Apr 1983.

[180] Y. Akahama, M. Kobayashi, and H. Kawamura, "Raman study of black phosphorus up to 13 GPa," *Solid State Commun.*, vol. 104, no. 6, pp. 311 – 315, 1997.

[181] Y. Akahama, M. Kobayashi, and H. Kawamura, "Simple-cubic–simple-hexagonal transition in phosphorus under pressure," *Phys. Rev. B*, vol. 59, pp. 8520–8525, Apr 1999.

[182] H. Iwasaki and T. Kikegawa, "Structural Systematics of the High-Pressure Phases of Phosphorus, Arsenic, Antimony and Bismuth," *Acta Crystallogr. Sect. B-Struct. Sci.*, vol. 53, pp. 353–357, Jun 1997.

[183] H. Olijnyk, S. Sikka, and W. Holzapfel, "Structural phase transitions in Si and Ge under pressures up to 50 GPa," *Phys. Lett. A*, vol. 103, no. 3, pp. 137 – 140, 1984.

[184] J. Hu and I. Spain, "Phases of silicon at high pressure," *Solid State Commun.*, vol. 51, no. 5, pp. 263 – 266, 1984.

[185] Y. Akahama, H. Kawamura, S. Carlson, T. Le Bihan, and D. Häusermann, "Structural stability and equation of state of simple-hexagonal

phosphorus to 280 GPa: phase transition at 262 GPa," *Phys. Rev. B*, vol. 61, pp. 3139–3142, Feb 2000.

[186] H. Katzke and P. Tolédano, "Displacive mechanisms and order-parameter symmetries for the A7-incommensurate-bcc sequences of high-pressure reconstructive phase transitions in Group VA elements," *Phys. Rev. B*, vol. 77, p. 024109, Jan 2008.

[187] T. Kikegawa, H. Iwasaki, T. Fujimura, S. Endo, Y. Akahama, T. Akai, O. Shimomura, T. Yagi, S. Akimoto, and I. Shirotani, "Synchrotron-radiation study of phase transitions in phosphorus at high pressures and temperatures," *J. Appl. Crystallogr.*, vol. 20, pp. 406–410, Oct 1987.

[188] S. E. Boulfelfel, G. Seifert, Y. Grin, and S. Leoni, "Squeezing lone pairs: the A17 to A7 pressure-induced phase transition in black phosphorus," *Phys. Rev. B*, vol. 85, p. 014110, Jan 2012.

[189] L. Cartz, S. R. Srinivasa, R. J. Riedner, J. D. Jorgensen, and T. G. Worlton, "Effect of pressure on bonding in black phosphorus," *J. Chem. Phys.*, vol. 71, no. 4, pp. 1718–1721, 1979.

[190] R. Ahuja, "Calculated high pressure crystal structure transformations for phosphorus," *Phys. Status Solidi B*, vol. 235, no. 2, pp. 282–287, 2003.

[191] A. H. Woomer, T. W. Farnsworth, J. Hu, R. A. Wells, C. L. Donley, and S. C. Warren, "Phosphorene: synthesis, scale-up, and quantitative optical spectroscopy," *ACS Nano*, vol. 9, no. 9, pp. 8869–8884, 2015. PMID: 26256770.

[192] Z. Guo, H. Zhang, S. Lu, Z. Wang, S. Tang, J. Shao, Z. Sun, H. Xie, H. Wang, X.-F. Yu, and P. K. Chu, "From black phosphorus to phosphorene: Basic solvent exfoliation, evolution of Raman scattering, and

applications to ultrafast photonics," *Adv. Funct. Mater.*, vol. 25, 12 2015.

[193] A. Favron, E. Gaufrès, F. Fossard, A.-L. Phaneuf-L'Heureux, N. Y.-W. Tang, P. L. Lévesque, A. Loiseau, R. Leonelli, S. Francoeur, and R. Martel, "Photooxidation and quantum confinement effects in exfoliated black phosphorus," *Nat. Mater.*, vol. 14, 5 2015.

[194] J. S. Loveday, R. J. Nelmes, W. G. Marshall, J. M. Besson, S. Klotz, and G. Hamel, "Structure of deuterated ammonia IV," *Phys. Rev. Lett.*, vol. 76, pp. 74–77, Jan 1996.

[195] D. H. Mordaunt, M. N. R. Ashfold, and R. N. Dixon, "Photodissociation dynamics of $\tilde{A}$ state ammonia molecules. I. State dependent μ-ν correlations in the $NH_2(ND_2)$ products," *J. Chem. Phys.*, vol. 104, no. 17, pp. 6460–6471, 1996.

[196] V. Vaida, M. I. McCarthy, P. C. Engelking, P. Rosmus, H. Werner, and P. Botschwina, "The ultraviolet absorption spectrum of the $\tilde{A}\,{}^1A_2' \leftarrow \tilde{X}\,{}^1A_1$ transition of jet-cooled ammonia," *J. Chem. Phys.*, vol. 86, no. 12, pp. 6669–6676, 1987.

[197] U. Bafile, L. Ulivi, M. Zoppi, and F. Barocchi, "Depolarized-light-scattering spectrum of normal gaseous hydrogen at low density and a temperature of 297 K," *Phys. Rev. A*, vol. 37, pp. 4133–4144, Jun 1988.

[198] L. Ulivi, M. Zoppi, L. Gioè, and G. Pratesi, "Molecular hydrogen internuclear distance in high-pressure fluid and solid phases at room temperature," *Phys. Rev. B*, vol. 58, pp. 2383–2386, Aug 1998.

[199] W. Schnick and J. Lücke, "Darstellung, Kristallstruktur und IR-spektroskopische Untersuchung von Phosphor(V)-nitrid-imid, HPN_2," *Z. Anorg. Allg. Chem.*, vol. 610, no. 4, pp. 121–126, 1992.

[200] S. Vepřek, Z. Iqbal, J. Brunner, and M. Schärli, "Preparation and properties of amorphous phosphorus nitride prepared in a low-pressure plasma," *Philos. Mag. B*, vol. 43, no. 3, pp. 527–547, 1981.

[201] W. Schnick, J. Lücke, and F. Krumeich, "Phosphorus nitride P_3N_5: synthesis, spectroscopic, and electron microscopic investigations," *Chem. Mater.*, vol. 8, no. 1, pp. 281–286, 1996.

[202] K. Landskron, H. Huppertz, J. Senker, and W. Schnick, "High-pressure synthesis of γ-P_3N_5 at 11 GPa and 1500 °C in a multianvil assembly: a binary phosphorus(V) nitride with a three-dimensional network structure from PN_4 tetrahedra and tetragonal PN_5 pyramids," *Angew. Chem. Int. Ed.*, vol. 40, no. 14, pp. 2643–2645, 2001.

[203] K. Landskron, H. Huppertz, J. Senker, and W. Schnick, "Multianvil-Synthese, Pulver-Röntgenstrukturanalyse, 31P-MAS-NMR- und FTIR-Spektroskopie sowie Materialeigenschaften von γ-P_3N_5, einer Hochdruckphase von binärem Phosphor(V)-nitrid mit verzerrt quadratischen PN_5-Pyramiden und PN_4-Tetraedern," *Z. Anorg. Allg. Chem.*, vol. 628, no. 7, pp. 1465–1471, 2002.

[204] S. Horstmann, E. Irran, and W. Schnick, "Synthesis and crystal structure of phosphorus(V) nitride α-P_3N_5," *Angew. Chem. Int. Ed. in English*, vol. 36, no. 17, pp. 1873–1875, 1997.

[205] D. Baumann and W. Schnick, "High-pressure polymorph of phosphorus nitride imide HP_4N_7 representing a new framework topology," *Inorg. Chem.*, vol. 53, no. 15, pp. 7977–7982, 2014. PMID: 25036732.

[206] A. Marchuk, F. J. Pucher, F. W. Karau, and W. Schnick, "A high-pressure polymorph of phosphorus nitride imide," *Angew. Chem. Int. Ed.*, vol. 53, no. 9, pp. 2469–2472, 2014.

[207] S. M. Clark and J. M. Zaug, "Compressibility of cubic white, orthorhombic black, rhombohedral black, and simple cubic black phosphorus," *Phys. Rev. B*, vol. 82, p. 134111, Oct 2010.

[208] P. Vinet, J. R. Smith, J. Ferrante, and J. H. Rose, "Temperature effects on the universal equation of state of solids," *Phys. Rev. B*, vol. 35, pp. 1945–1953, Feb 1987.

[209] P. Vinet, J. H. Rose, J. Ferrante, and J. R. Smith, "Universal features of the equation of state of solids," *J. Phys. -Condens. Mat.*, vol. 1, no. 11, p. 1941, 1989.

[210] K. Syassen, "Ruby under pressure," *High Pressure Res.*, vol. 28, no. 2, pp. 75–126, 2008.

[211] W. Demtröder, *Atoms, Molecules and Photons: An Introduction to Atomic, Molecular and Quantum Physics*. Graduate Text in Physics, Springer-Verlag Berlin Heidelberg, 2 ed., 2010.

[212] R. Bini, R. Ballerini, G. Pratesi, and H. J. Jodl, "Experimental setup for fourier transform infrared spectroscopy studies in condensed matter at high pressure and low temperatures," *Rev. Sci. Instrum.*, vol. 68, no. 8, pp. 3154–3160, 1997.

[213] M. Santoro, "Optical spectroscopy at high pressure," in *High-Pressure Physics* (J. Loveday, ed.), Scottish Graduate Series, pp. 111–129, Chapman and Hall/CRC, 1 ed., 2012.

[214] S. Lupi, A. Nucara, A. Perucchi, P. Calvani, M. Ortolani, L. Quaroni, and M. Kiskinova, "Performance of SISSI, the infrared beamline of the ELETTRA storage ring," *J. Opt. Soc. Am. B*, vol. 24, pp. 959–964, Apr 2007.

[215] M. Ceppatelli, F. A. Gorelli, J. Haines, M. Santoro, and R. Bini, "Probing high-pressure reactions in heterogeneous materials by Raman spectroscopy," *Z. Kristallogr. - Crystalline Materials*, vol. 229, 01 2014.

[216] A. P. Hammersley, S. O. Svensson, M. Hanfland, A. N. Fitch, and D. Hausermann, "Two-dimensional detector software: from real detector to idealised image or two-theta scan," *High Pressure Res.*, vol. 14, no. 4-6, pp. 235–248, 1996.

[217] C. Prescher and V. B. Prakapenka, "Dioptas: a program for reduction of two-dimensional X-ray diffraction data and data exploration," *High Pressure Res.*, vol. 35, no. 3, pp. 223–230, 2015.

[218] M. Mezouar, W. A. Crichton, S. Bauchau, F. Thurel, H. Witsch, F. Torrecillas, G. Blattmann, P. Marion, Y. Dabin, J. Chavanne, O. Hignette, C. Morawe, and C. Borel, "Development of a new state-of-the-art beamline optimized for monochromatic single-crystal and powder X-ray diffraction under extreme conditions at the ESRF," *J. Synchrotron Radiat.*, vol. 12, pp. 659–664, Sep 2005.

List of Tables

List of Figures

Acknowledgements

"First thought, best thought." This was the phrase that poet Allen Ginsberg used to describe spontaneous and fearless writing, a way of telling the truth that arises from naked and authentic experience. I'm not good at all in writing acknowledgements, so I decided I will write this last part of my PhD. thesis following that rule.

First of all, I would like to thank Roberto Bini for his support, encouragement and guidance all over these years. His help and his advices have been valuable beyond words. A huge thanks goes to Matteo, who shared with me all the infinite research work hiding behind these few (?) pages. I owe a great debt of gratitude to Roberto and Matteo for all they have done for me.

I would also like to thank all the people in the *High Pressure Chemistry and Physics Group* for all the constructive discussions, for their collaboration and help and for a lot of other, very precious things: Mario, Federico, Samuele, Margherita, Marcelo, Naomi and Kamil, the least I can do is to thank you for all. In these years, a lot of other people and students shared their time with me, trying to load some "ridiculously impossible samples" and, from time to time, having unexpected success in these (and other) attempts. An affectionate thanks goes to all of them.

A final word of thanks (and a very special one) goes to my family, my friends and Irene, for supporting me during all this period and, mostly, for putting up with me. I mean, for sure you know what I'm talking about.

Thanks to all of you.